Università degli Studi di Pavia
Dottorato di Ricerca in Fisica - XXXIV Ciclo

R&D on Triple-GEM detectors for the optimal and safe operation in the CMS experiment

Davide Fiorina

Tesi per il conseguimento del titolo

Università degli Studi di Pavia
Dipartimento di Fisica

Dottorato di Ricerca in Fisica - XXXIV Ciclo

R&D on Triple-GEM detectors for the optimal and safe operation in the CMS experiment

Davide Fiorina

Submitted to the Graduate School of Physics in partial fulfillment of the requirements for the degree of

DOTTORE DI RICERCA IN FISICA

DOCTOR OF PHILOSOPHY IN PHYSICS

at the

University of Pavia

University Supervisor: Prof. Paolo Vitulo

Cover: Giacomo Borlone de Buschis, *Trionfo e danza della morte*, Clusone (BG), Italy.

R&D on Triple-GEM detectors for the optimal and safe operation in the CMS experiment

Davide Fiorina

Ph.D Thesis - University of Pavia

Pavia, Italy, 24 dicembre 2021

Gionto (e sonto) per nome chiamata morte
ferisco a chi tocherà la sorte;
no è homo chosì forte
che da mi no po' a schanmoare.
Gionto la morte piena de equaleza
sole voi ve volio e non vostra richeza
e digna sonto da portar corona
perché signorezi ognia persona.

-Cartouches waved by the Death

CONTENTS

INTRODUCTION

During this decade, the CERN Large Hadron Collider (LHC) will be upgraded to collide protons beams at centre of mass energy of 14 TeV and instantaneous luminosities up to $7.5 \times 10^{34}\,\mathrm{cm}^{-2}\mathrm{s}^{-1}$. In order to deal with higher events rate and complexity, the LHC experiments need to be upgraded. In particular the Compact Muon Solenoid (CMS) experiment will introduce improvements in the data acquisition and trigger infrastructure along side with upgrades of the sub-detectors systems. As concerning the CMS muon spectrometer, new detection stations based on the triple-GEM technology will be installed to enhance the muon reconstruction redundancy (GE1/1 and GE2/1) and to extend the angular acceptance (ME0).

This thesis took place in the framework of such GEM based upgrades. The work was mainly focused on ensuring the correct operation of GEM detectors in the CMS framework. One of the goal was to ensure that such detectors can survive and return to operate also if the wrong gas mixture is supplied. Moreover, this work aimed to test and develop a reliable GEM layout for the CMS GEM detectors to let them operate at their peak performance also in the harsh background particle environment foreseen in the CMS end-caps.

The first chapter will give a general overview of the LHC and the CMS detector with some details about the GEM based upgrades. The second chapter will introduce some basic concepts about the particle interactions with the matter and the physical processes behind gaseous detectors operations. Also a brief historical overview of the major gaseous detectors technologies will be given.

The third chapter will focus on the work done to develop a reliable system for gases concentrations detection in the gas mixture supplied to CMS GEM detectors (nominally Ar/CO_2 (70/30)). The R&D tests performed to

reach the necessary knowledge level to use a GEM detector for determining the relative ratio of the two gases will be described.

The fourth chapter will present the results that convinced the CMS Group to change the GEM foil design to exploit the maximum performance of the technology in the high hit rate environment. The results, along with the new design, will be described up to the current R&D stage.

The fifth chapter will discuss the advanced aging tests performed to test the radiation hardness and the aging mechanisms taking place in GEM detector when exposed to heavy irradiation and gas contamination. Many experiments were performed also to test different variables that play a role in the aging of both Wire Chambers and GEM detectors.

CHAPTER 1

LHC AND THE CMS EXPERIMENT

With this chapter a brief overview of the Large Hadron Collider (LHC) machine and its experiments is given. Particular attention will be put on the Compact Muon Solenoid (CMS) experiment and its future upgrades.

1.1 LHC

The Large Hadron Collider (LHC) [1] is the largest, ever build, proton-proton and heavy ion collider. The accelerator is based at CERN [2], Geneva and it was designed to study particle physics at the TeV scale. The accelerator collides proton with a centre of mass energy of $\sqrt{s} = 14\,\text{TeV}$ at an instantaneous luminosity of $\mathcal{L} = 1 \times 10^{34}\,\text{cm}^{-2}\text{s}^{-1}$ or lead ions at energies up to $\sqrt{s} = 1.7\,\text{TeV/nucleon}$ at a luminosity of $\mathcal{L} = 1 \times 10^{31}\,\text{cm}^{-2}\text{s}^{-1}$. LHC first run took place in 2008 and it first effective operation in 2010. Since then, two successful data taking runs took place (Run 1 and Run 2) along with the two major Long Shutdown (LS1 and LS2) and one Extended Year End Technical Stop (EYETS), such shutdown periods allowed for accelerator and detector upgrades. The year of writing (2021) correspond to the last year of LS2 and it will be followed by the Run 3 data taking before the LS3 shutdown. After that period, the High-Luminosity LHC (HL-LHC) upgrade will be implemented, increasing the nominal luminosity to $5 \div 7.5\,\text{cm}^{-2}\text{s}^{-1}$. An integrated luminosity of $4000\,\text{fb}^{-1}$ is expected to be reached after the LS3 (Phase 2). This will allow to precisely test the

Standard Model and confirm potential inconsistencies. The most updated LHC schedule is displayed in Fig. 1.1.

Figure 1.1: Last available update of the Large Hadron Collider project schedule (September 2021) [3].

1.1.1 LHC Machine

LHC accelerator is a synchrotron accelerator and collider. It is installed in a 26.66 km tunnel that is $45 \div 170$ m deep below the Swiss and France territories, between the Geneva lake and the Jura mountains. LHC consists in eight straight sector interleaved by eight arcs, the sections magnets are kept at a temperature of 1.9 K with the use of superfluid helium. Two beams are circulating in the same pipe in opposite directions and they are made interacting in four collision points were the experiments are placed. A Toroidal LHC Apparatus (ATLAS) [4] and Compact Muon Solenoid (CMS) [5] are general purpose experiments build to study the standard model and the physics beyond it. LHC beauty experiment (LHCb) [6] is meant to study the physics of the beauty quark and, in general, the CP violation mechanism. A Large Ion Collider Experiment (ALICE) [7] is built to exploit heavy ion collision to study the quark gluon plasma.

Protons are obtained by ionizing hydrogen gas and are accelerated with various facilities before entering in LHC (see Fig. 1.2). The extraction energy of protons is 750 keV and they are accelerated and divided in bunches by the LINAC2 and after by the BOOSTER up to 1.1 GeV. The beam is fed to the Proton Synchrotron (PS) and afterwards the Super Proton Synchrotron (SPS) where, at an energy of 450 GeV they are injected in the LHC machine. The machine design provides two proton beams, circulating in opposite directions, consisting in 2808 bunches of 1.15×10^{11} particles each. During Run 2 the spacing between such bunches reached the nominal value of 25 ns. This is equivalent to 40 MHz collision rates at the interaction points, also known as bunch crossing (BX). Particles are accelerated using radio frequency (RF) cavities running at 400.8 MHz and the beams are steered with superconducting Nb-Ti dipoles. The relation between the

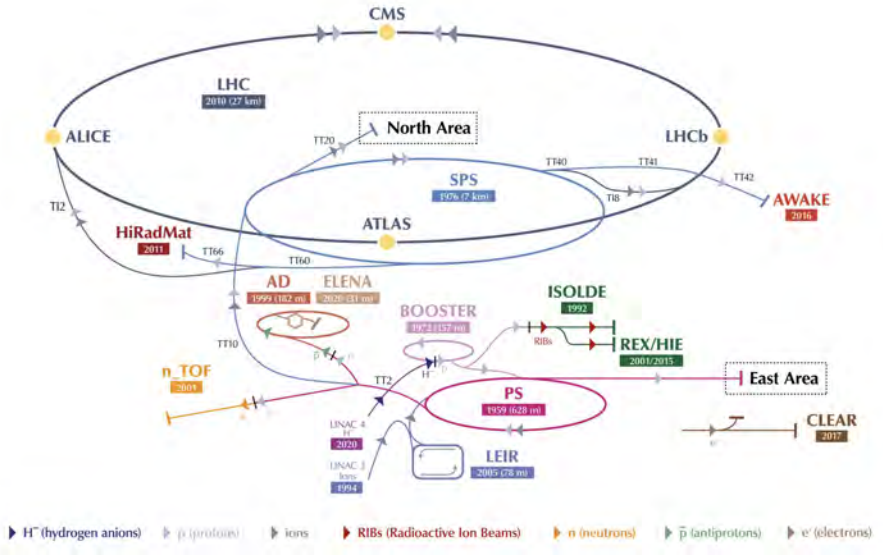

(a) *CERN accelerator complex [8].*

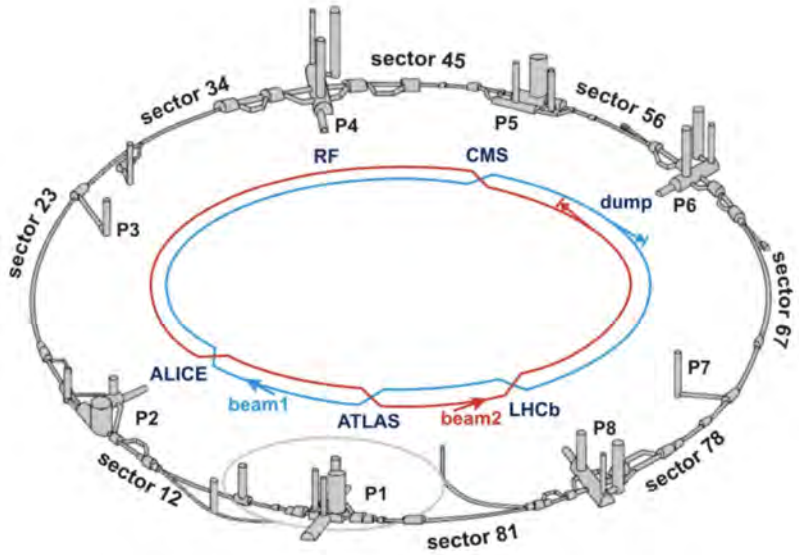

(b) *LHC sectors [9].*

Figure 1.2: The CERN acceleration chain is schematically presented on the top. The LHC sectors are shown on the bottom.

particle momentum p and the required magnetic field B to constrain the beam in the circumference radius $\rho \approx 4.3\,\text{km}$ (with corrections due to the presence of bending magnets only in portions of the beam pipe length) is given by:

$$p[\text{GeV}] = 0.3\frac{q}{e}B[\text{T}]\rho[\text{km}],$$

where q and e are respectively the particle charge and the elementary

charge. For bending 7 TeV protons a field of 8.3 T is required with a current of around 12 kA . Additionally to the steering magnets, 23 Nb-Ti superconducting quadrupoles Focalizing-Defocalizing (FODO) [10] cells are installed along with sextupoles and octupoles. Such modules are necessary to reduce the spread of the proton beam, in particular near the interacting points.

The luminosity for two beams impinging on each other that contain respectively N_1 and N_2 particles and are Gaussian spread along the transverse direction of the beam with variances σ_x and σ_y can be written as:

$$\mathcal{L} = \frac{N_1 N_2 k_b f}{4\pi\sigma_x\sigma_y} F,$$

where k_b is the number of bunches, f is the revolution frequency and F is a correction factor to take into account the non-zero crossing angle between the two beams. The expected rate R of event for a certain process that has a cross section σ is:

$$R = \sigma\mathcal{L}$$

Since the global cross section of protons at $\sqrt{s} = 13\,\text{TeV}$ is around 80 mb , the interaction rate at the 2018 peak luminosity ($\mathcal{L} = 2.1 \times 10^{34}\,\text{cm}^{-2}\text{s}^{-1}$) was 1.7×10^9 events/s corresponding to around 37 interaction per each bunch crossing, i.e. pile-up events. The total numbers of events N in a period T can be written as:

$$N = \sigma L = \sigma \int_0^T \mathcal{L} dt,$$

where L is the integrated luminosity during the period. This is often measured as the inverse of a cross section, usually fb^{-1}. Fig. 1.3 shows respectively the peak luminosity and the integrated one delivered to both CMS and ATLAS experiments during the firsts two runs of LHC. During Run 1 the nominal luminosity ($1 \times 10^{34}\,\text{cm}^{-2}\text{s}^{-1}$) was approached but not reach, however during Run 2 the reached luminosity was up to the double. For Run 3 the same luminosity will be delivered with a small increase of the centre of mass energy from $\sqrt{s} = 13\,\text{TeV}$ to $\sqrt{s} = 14\,\text{TeV}$.

1.1.2 HL-LHC Upgrade

After Run 3 in 2025 , two and a half years of long shutdown (LS3) are foreseen to allow for the infrastructure installation required fo the HL-LHC project [12]. New RF cavities and beam collimators will be installed to have a cleaner beam. To free some space along the circumference, shorter superconducting dipole magnets made of Nb_3Sn will be used, capable to reach magnetic fields up to 12 T. An upgrade of the injection chain will lead to a doubling of the particles per injected bunch in the same volume. This

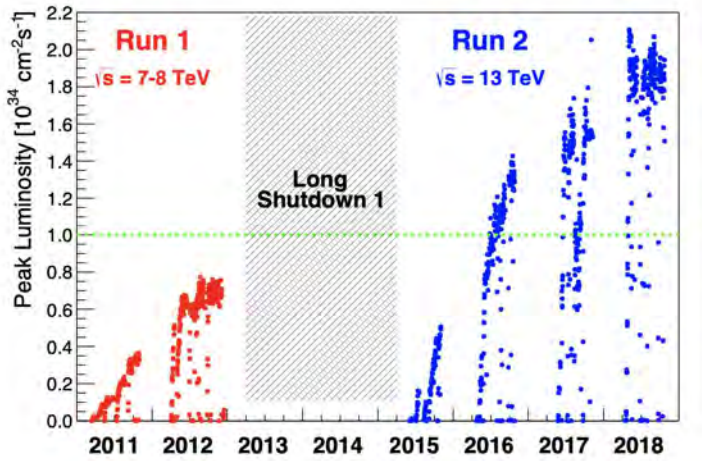

(a) *Peak instantaneous luminosity.*

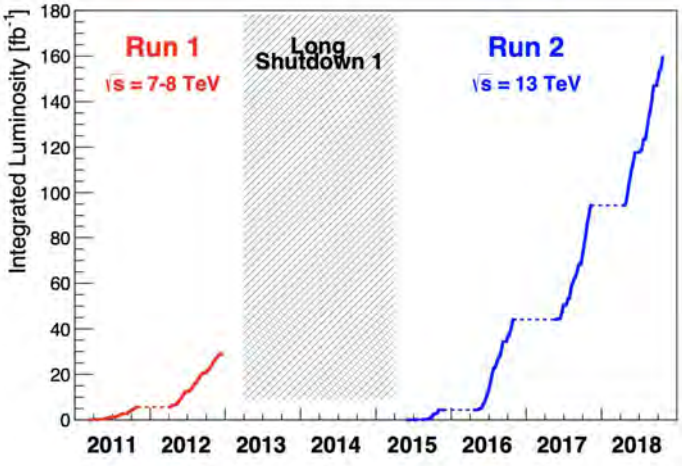

(b) *Integrated luminosity.*

Figure 1.3: Peak instantaneous luminosity (left) and integrated luminosity (right) delivered to the ATLAS and CMS experiments in the first two runs of LHC [11].

improvement can potentially deliver to the experiments a peak luminosity up to $20 \times 10^{34}\,\mathrm{cm}^{-2}\mathrm{s}^{-1}$, that is hardly manageable by the detectors. For this reason a levelling of the luminosity is foreseen to provide more constant value of $5 \div 7.5 \times 10^{34}\,\mathrm{cm}^{-2}\mathrm{s}^{-1}$ for a longer time. HL-LHC will start the Phase 2 of the data taking and, in around 10 years of operation at such luminosity, the delivered integrated luminosity to both ATLAS and CMS will be $4000\,\mathrm{fb}^{-1}$.

1.2 CMS Experiment

As already mentioned, Compact Muon Solenoid (CMS) is a multi purpose detector installed in one of the four point of LHC, Point 5 (P5). The surface buildings include the control room and the surface experimental area (SX5). The underground experimental cavern (UXC55) is placed 90÷100 m under the the surface and host the detector. The nearby Underground Service Cavern (USC55) accommodate the detector and sub-detectors services. Fig. 1.4 shows scheme and arrangement of the P5 infrastructure.

CMS is composed by several layers of high-granularity synchronized detectors, each of them is meant for identification of different particles produced during the collisions and for the measurement of their properties. Information about the particles momentum can be achieved by bending their trajectories with a magnet. CMS mounts a solenoidal magnet generating a magnetic field of about 4 T. The almost 4π coverage of the detector allows also to measure the missing energy, i.e. the energy that exit the detector because of non interacting particles, such as the neutrinos.

1.2.1 CMS Design and Characteristics

Fig. 1.5 shows a schematic view of the CMS detector. The whole detector weights around 14 000 t, it has a cylindrical shape with 21.6 m length and 14 m diameter. The structure is divided in three main modules, i.e. the central barrel and the two end-caps. The detector follows the cylindrical symmetry intrinsically present because of the collisions that permits to cover the largest variety of generated particles trajectories. The Cartesian coordinates adopted by CMS is right handed with the origin situated in the collision point. The x axis points radially from the LHC centre, the y axis is orthogonal to the ground and directed upwards while the z axis points tangentially to the beam pipe. The x-y plane is referred to as the transverse plane and the particle energy and momentum projection through this plane are usually referred to as E_T and p_T. Also a spherical coordinates system is often used, the azimuthal angle ϕ is defined on the transverse plane starting from the x axis while the polar angle θ is referred to the z axis. It is a custom habit to represent the θ angle through the pseudorapidity η that is defined as:

$$\eta = -\ln\tan\frac{\theta}{2} = -\frac{1}{2}\left(\frac{|\bar{p}| + p_z}{|\bar{p}| - p_z}\right),$$

where $|\bar{p}|$ is the module of the particle four-momentum and p_z its projection along the beam axis. CMS is built with concentric layers of subdetectors each of them with a specific role in particle properties measure-

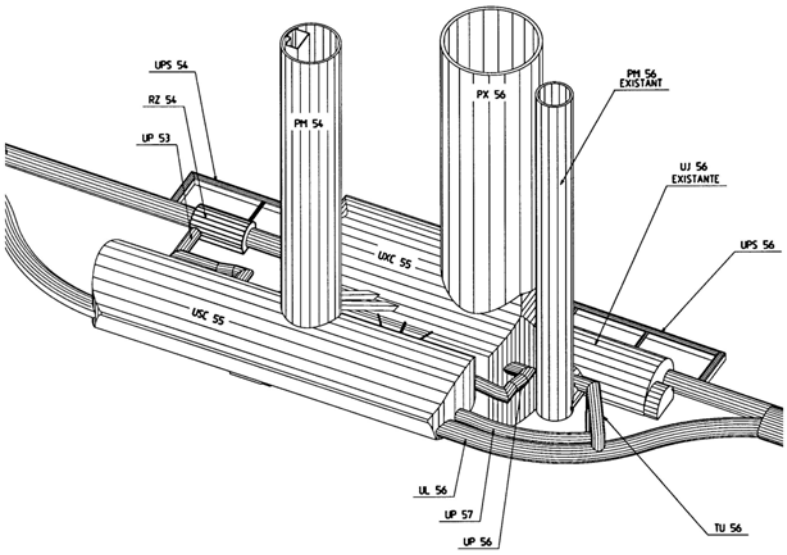

(a) *Scheme of Point 5 caverns and shafts.*

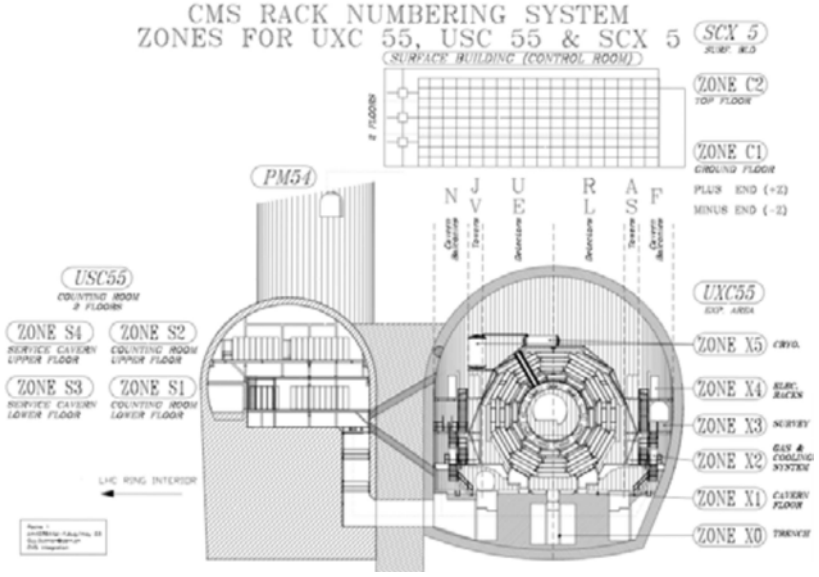

(b) *Point 5 arrangement.*

Figure 1.4: LHC Point 5 caverns [13].

ments. Fig. 1.6 shows a CMS longitudinal view that highlights the sub-detectors layers. In the inner part of the detector a tracker system is placed that measures the charged particles trajectories and the secondary interactions vertexes. Outside the tracker, but still inside the solenoid, are concentrically placed the electromagnetic and hadronic calorimeters. The first aims to measure the energy of photons and electrons, while the second of the hadronic particles and jets. Outside the magnet are placed gaseous detectors that focus on the muon tracking and reconstruction. In

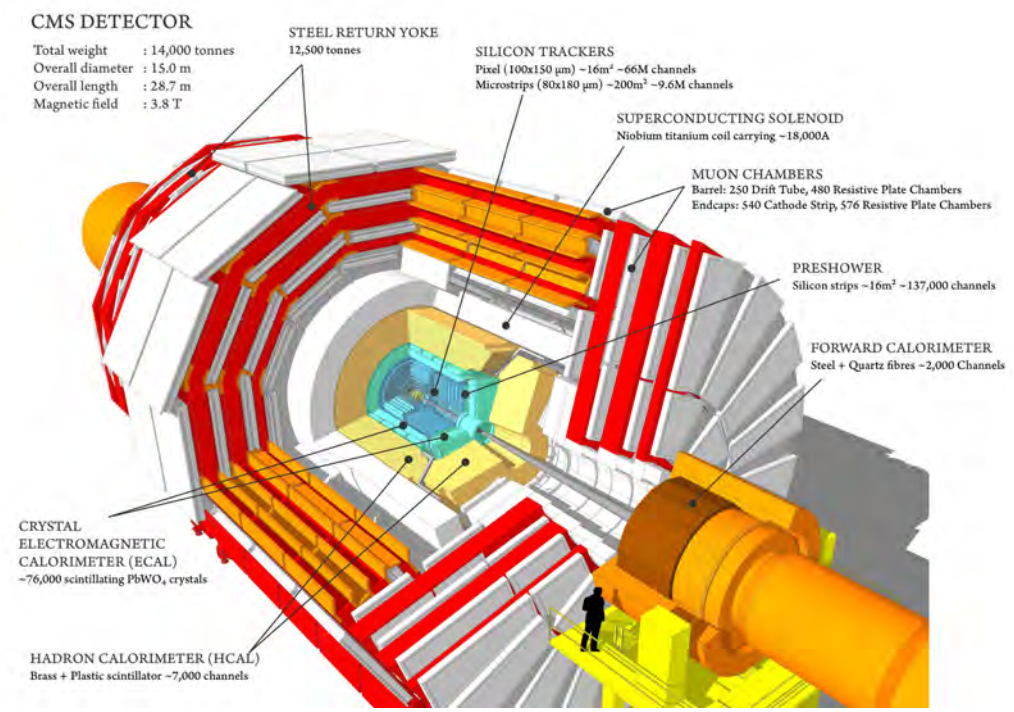

Figure 1.5: Schematic depiction of the CMS detector [14], with labels indicating the main characteristics of the whole detector and the various sub-detectors. More details about the sub-detectors will be given in the text.

the following a brief description of the subsystems will be given.

1.2.2 Silicon Tracker

The silicon tracker is the innermost sub-system of CMS [16, 17]. It is 5.8 m long with a diameter of 2.8 m and it covers the pseudo-rapidity region up to $\eta = 2.5$. Because of the very high particle rate in this region a high granularity is required to have low detector occupancy and high spatial resolution. The tracker barrel region is instrumented with four tracking layers of silicon pixel in the innermost region. The outer part mounts silicon strips detectors arranged in four layer in the inner part and six in the outer one. The end-caps follows the same structure with two pixel layer followed by three layer of strips in the inner part and nine more strips layers in the outer region. The overall system consists of about 66 millions pixels and 10 millions strips. The whole system is operated at $-20\,^{\circ}\mathrm{C}$ to minimize the radiation induced damage on the detector. For low energy or low transverse momentum hadrons ($1\,\mathrm{GeV/c} < p_T < 10\,\mathrm{GeV/c}$) the reconstruction efficiency is around 85%. For higher energies ($p_T >$

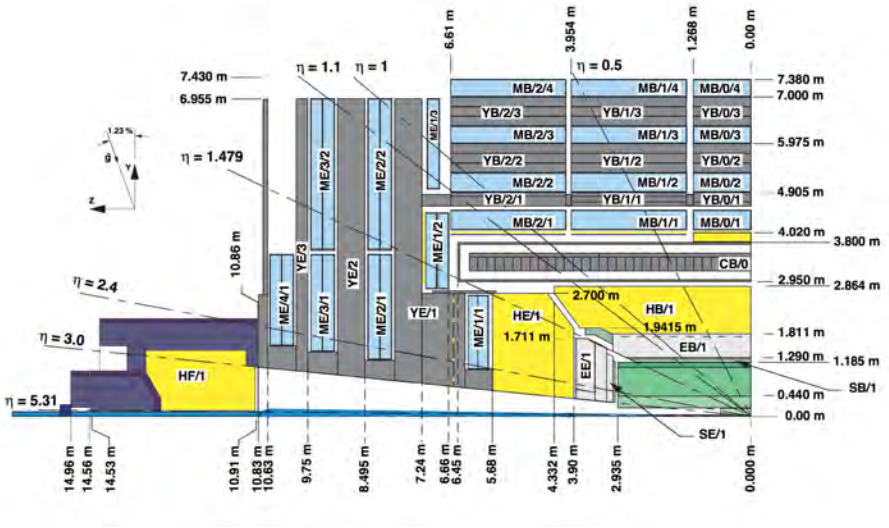

Figure 1.6: CMS detector longitudinal view [15]. Sub-detectors highlighted in different colours with η ranges. The first letter in the labels refers to the subsystem: 'M' indicates the muon subsystem, 'Y' the iron yoke, 'C' the cryostat of the magnet, 'H' the hadron calorimeter, 'E' the electronic calorimeter and 'S' the electronic calorimeter pre-shower. The second letter in the labels refers to the detector position: 'B' stands for barrel, 'E' for end-cap and 'F' for forward. Finally, the two numbers in the muon subsystem refer to the position of each chamber. In the barrel, the first number indicates the wheel, and the second one the station. In the end-caps, the first number refers to the disk, and the second one to the ring. The numbers increase moving away from the interaction point.

10 GeV/c), it becomes 95%. For electrons the efficiency is estimated to be around 90%, and 98% for muons. In the region $|\eta| < 1.6$, the precision on the muon transverse momentum measurement is ($\delta p_T/p_T < 2\%$ up to $p_T = 100\,\text{GeV/c}$).

1.2.3 Electromagnetic Calorimeter

The electromagnetic calorimeter (ECAL) [18] measures electron and photons energies and works in synergy with the hadronic calorimeter for jet energies. The calorimeter consists in a homogeneous and hermetic scintillation detectors made of $PbWO_4$ inorganic crystals. The material was chosen for its small Molière radius (22 mm) and radiation length (X_0=8.9 mm) along with the high radiation hardness and the short scintillation decay time (10 ns). The crystals dimensions are $2.2 \times 2.2 \times 23$ cm (25.8 X_0) in the barrel and $2.9 \times 2.9 \times 22$ cm (24.7 X_0) in the end-caps. A total of 75848

crystals composes the calorimeter that covers the pseudorapidity region $|\eta| < 3.0$. The scintillation light is read by avalanche photodiode in the barrel region and photo triodes in the end-caps. Such technologies are required to sustain the intense magnetic field inside the solenoid and readout the relatively small light emitted by the crystal. Indeed, the scintillation yield in $PbWO_4$ is around 4.5 photons per deposited MeV at 18 °C. Since the yield depends on the crystal temperature a dedicated system was installed to maintain it stable within 0.1 °C. The ECAL energetic resolution is determined by three main terms: a stochastic term (S), a noise term (N) and a constant term (C) that contains other uncertain among with the calibration one. The ECAL resolution is then [19]:

$$\frac{\sigma_E}{E} = \frac{S}{\sqrt{E}} \oplus \frac{N}{E} \oplus C = \frac{2.8\%}{\sqrt{E[\text{GeV}]}} + \frac{12.8\%}{E[\text{GeV}]} + 0.3\%.$$

1.2.4 Hadron Calorimeter

The hadron calorimeter (HCAL) [20] aims to measure the energies of hadronic jets and to estimate the missing transverse energy of the events E_T^{miss}. Such detector is a sampling calorimeter made by alternating layers of brass and plastic scintillators. The scintillation light is carried out by wavelength shifting fibres and waveguides and is readout by Hybrid Photo Diodes (HPD). However, HPDs have been substituted with silicon photomultipliers during LS2 to improve the calorimeter performance during Run 3. Two calorimeter modules are placed in the barrel and end-caps regions nominally HB and HE. An additional outer layer HO was placed outside the magnet. Such modules cover all the pseudo-rapidity region up to 3.2 with a thickness equivalent to 11.8 interaction lengths. In addition to that the forward calorimeter HF extends the angular acceptance up to $|\eta| < 5.2$. Because of the intense background in this region, the HF calorimeter has steel plates as attenuator materials and quartz fibres for the sampling part that detects the Cherenkov light produced by the passing particles. The HCAL energy resolution is given by:

$$\frac{\sigma_E}{E} = \frac{S}{\sqrt{E}} \oplus C = \frac{100\%}{\sqrt{E[\text{GeV}]}} + 4.5\%.$$

1.2.5 Solenoid Magnet

CMS exploits a superconducting solenoidal magnet [21]. It is 12.9 m long and 5.9 m of diameter, providing a magnetic field up to 4 T in the inner barrel and a residual 2 T in the return yoke. At nominal regime the current flowing is around 19 kA in the 2168 turns, providing a inner field of 3.8 T.

The superconductivity is assured by liquid helium cooling that maintains the magnet at 4.5 K. Fig. 1.7 shows a map of the magnetic field when the magnet is operative. Such field provides the bending of particle trajectories

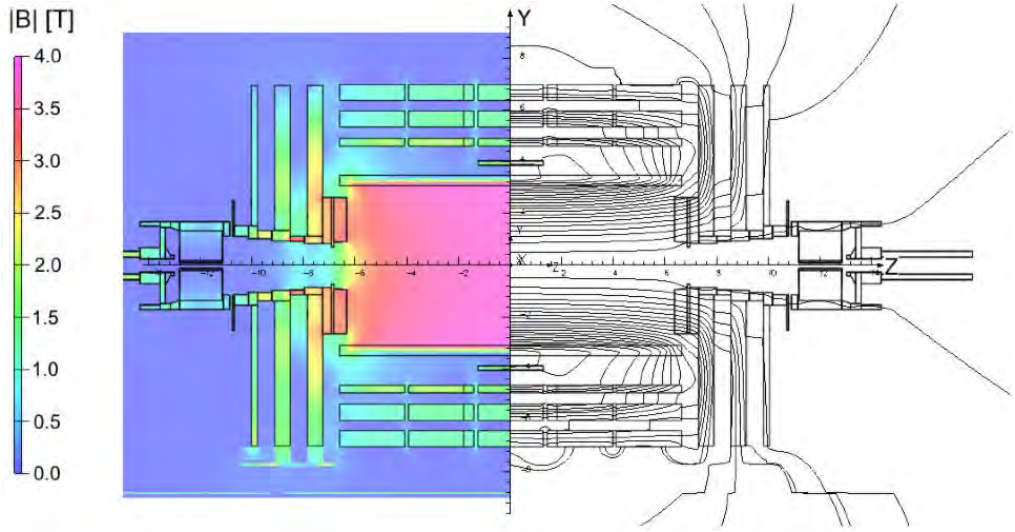

Figure 1.7: Map of the magnetic field generated by the superconducting solenoid in the CMS detector [22]. The value of $|B|$ is shown on the left, the field lines are shown on the right. Each field line represents a magnetic flux increment of 6 Wb.

in the transverse plane, obtaining less than 5% of charge misidentification for muons with $p_T < 200\,\text{GeV}$, $\delta p/p \approx 1\%$ for $p_T = 100\,\text{GeV}$ and less than 10% for $p_T < 1\,\text{TeV}$ for combined inner tracker and muon system measurements.

1.2.6 Muon System

The particles that pass through all the aforementioned sub-detectors without being stopped are usually muons with $p_T \geq 3\,\text{GeV}$. The muon system [23] is the outermost group of sub-detectors that aims to track and measure the transverse momentum such particles. It consists in four stations both in the barrel and in the end-caps and exploits three different gaseous detectors technologies. Fig. 1.8 shows the status of the muon system before LS2. The technologies exploited in the muon system will be briefly described in the following. In particular, the muon system improves the muon p_T resolution of CMS when such particles have $p_T > 200\,\text{GeV}$ (see Fig.1.9).

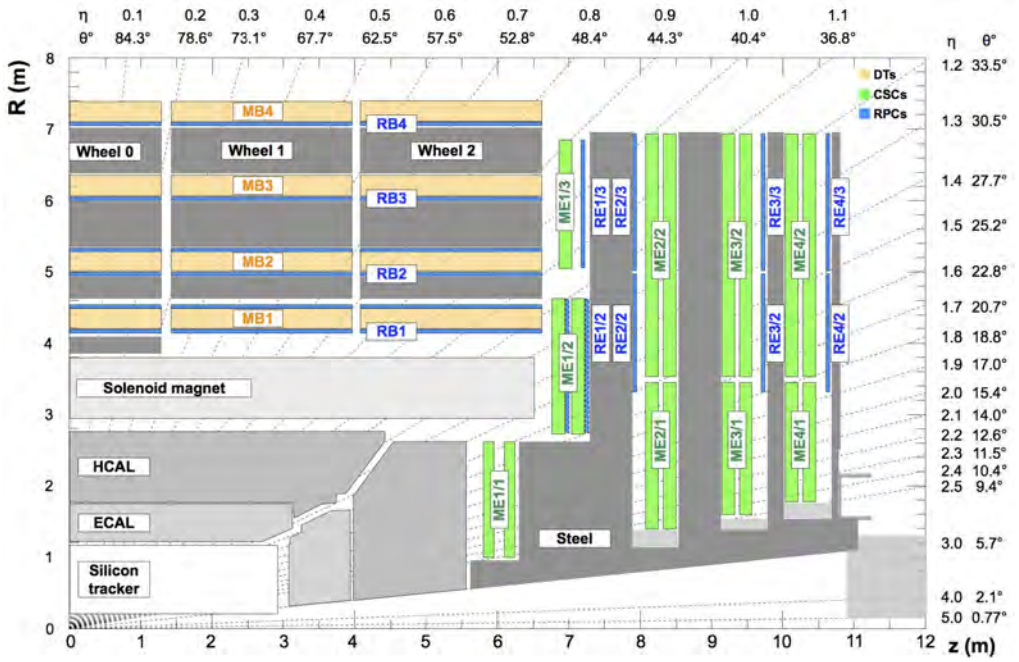

Figure 1.8: CMS muon system longitudinal view. The muon sub-detectors are highlighted in different colours [24].

1.2.6.1 Drift Tubes (DT)

Drift Tubes Chambers (DTs) [25] are employed in the barrel region ($|\eta| < 1.2$) where the occupancy is low and there is a low residual magnetic field in between the yoke iron. This subsystem consists of 5 wheels and 12 azimuthal sectors, see Fig. 1.10. Four concentric rings (stations) of DT are installed on each wheel and each station consists of one DT detector, except in sector 4 and 10 where the MB4 station mounts two chambers. A DT detector is composed of multiple drift cells (see Fig. 1.11) operating with Ar/CO_2 (85/15) gas mixture. A single cell has a transverse size of $42 \times 13\,\text{mm}$ and it uses a $50\,\mu\text{m}$ gold plated steel wire as anode at its centre. In order to correctly shape the electric field, two cathode strips are present on the side walls and other two strips above and below it. The operating voltages for wire, cathode and strips are respectively $3600\,\text{V}$, $-1200\,\text{V}$ and $1800\,\text{V}$. With this design the electron drift velocity is rather constant around $55\,\mu\text{m/s}$ that correspond to a maximum drift time in the cell of $385\,\text{ns}$. Four staggered layers of parallel cells form a Super Layer (SL). A DT chamber consists of two SLs with wires extending along the z axis that measure the $R - \phi$ coordinate (in the bending plane), and an orthogonal SL that measures the $r - z$ coordinate. All the DT chambers have a length of $2.5\,\text{m}$, imposed by the dimensions of the wheels, while their width varies, ranging from $1.9\,\text{m}$ to $4.1\,\text{m}$. Taking into account all

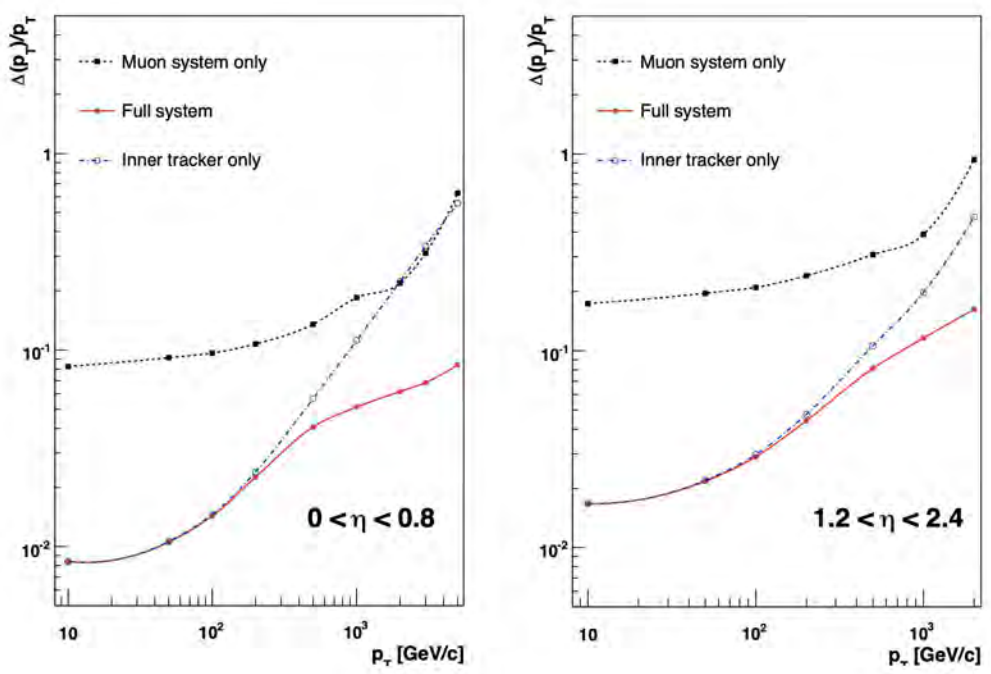

Figure 1.9: Muon transverse momentum resolution as a function of p_T for the inner tracker only, the muon system only and the two systems combined. The results for the barrel are shown on the left, the ones for the end-cap are shown on the right [5].

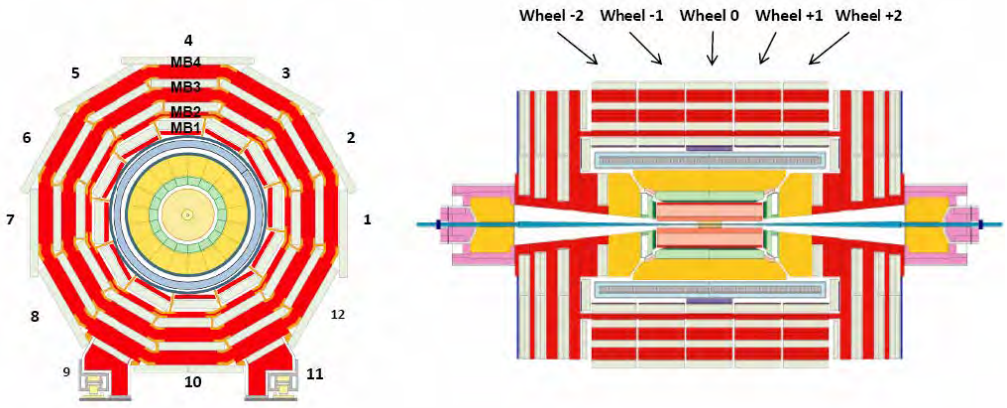

Figure 1.10: Drift Tubes Chambers in CMS: disposition of wheels, sectors and stations in the CMS detector [25].

the systematics the DT detectors, up to Run 2, exhibited a muon efficiency greater than 98% with spatial resolution of around 200 µm [24]. In the θ projection the spatial resolution decreases with the angle passing from 200 µm in the central wheel to 600 µm to the most external ones. On the ϕ

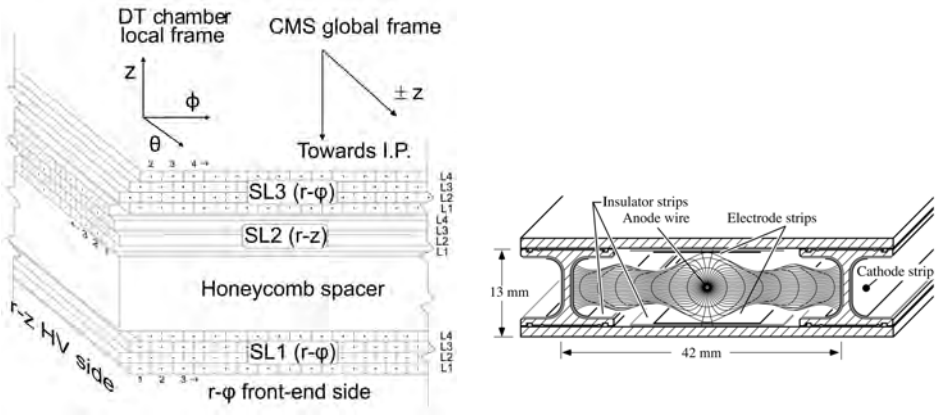

(a) *Schematic view of a DT chamber.*

(b) *Schematic view of a DT cell.*

Figure 1.11: On the left, schematic view of a DT chamber. On the right, section of a drift tube cell showing the drift and isochronous lines. [15].

projection the $4+4$ SLs, with their offline reconstruction algorithms, reach a overall ϕ resolution of 100 µm.

1.2.6.2 Cathode Strips Chambers (CSC)

Faster and more radiation resistant Cathode Strip Chambers (CSCs) have been chosen for the two end-caps ($0.8 < |\eta| < 2.4$) to cope with higher particle fluxes and non uniformities in the magnetic field [26]. Fig. 1.12 shows the disposition and the principle of operation of the trapezoidal CSCs detectors. CSC are based on the Multi Wire Proportional Chamber concept and cover the CMS end-caps with four disks (stations). The disk nearest to the interaction point is divided in three rings while the others in two. All the rings, except ME1/3, have staggered, overlapping neighbouring chambers that cover about 10° each. A CSC detector consists of six layers of anode wires enclosed between two planes of cathodes strips, the gas volume is filled with an $Ar/CO_2/CF_4$ (40/50/10) gas mixture. All the chambers mounts anode wires perpendicular to the readout cathode strips except ME1/1 that has inclined wire at an angle of 29° to compensate for the large Lorentz angle because of the relatively high residual magnetic field ($> 3\,T$). The cathode is grounded while the wires operate at 3600 V, they are both readout and give respectively the radial and azimuthal coordinate of the particles. The cathode readout exploits a collected charge weighted mean to improve the resolution along ϕ. CSCs demonstrated azimuthal track resolution of $70 \div 150$ µm and radial resolution of $1.9 \div 6.0$ mm [23].

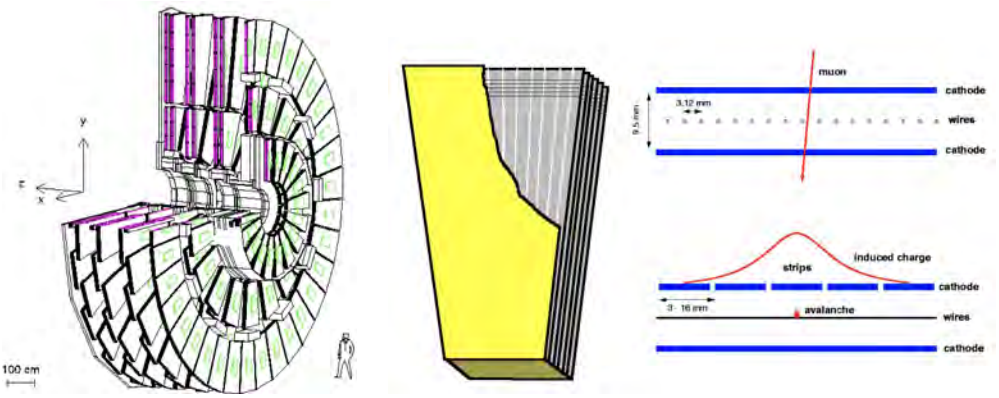

(a) *CSC arrangement in the CMS muon end-cap [27].*

(b) *Schematic view and principle of operation of a CSC chamber [28].*

Figure 1.12: On the left, arrangement of the CSC subsystem in the CMS endcaps. On the right, schematic view of a CMS CSC chamber (non-ME1/1) with radial strips and perpendicular wires, and principle of operation of a CSC chamber.

1.2.6.3 Resistive Plate Chambers (RPC)

Resistive Plate Chambers (RPCs) complement DTs and CSCs in both end-caps and barrel regions up to $|\eta| < 2.1$ [29]. Because of their fast response and excellent time resolution, they improve the precision in the determining of the bunch crossing (BX) of creation of the muons at the trigger level. Six RPC detection layers are installed in the barrel region, four in the inner side of all the DT stations and two in the outer size of MB1 and MB2. Four layers are also present in the end-caps, placed in the outer side of the CSC detector except for the second disk. CMS uses double-gap RPC, with 2 mm gap formed by two parallel High Pressure Laminate (HPL) electrodes with a bulk resistivity of about $1 \div 6 \times 10^{10}\,\Omega\,\mathrm{m}$. A Copper readout plane of strips is placed between the two gaps (see Fig. 1.13). They are operated at around 9.5 kV in avalanche mode with a gas mixture composed by R-134a/isobutane/SF_6 (95.2/4.5/0.3) with a humidity of 40% at $20 \div 22\,^{\circ}\mathrm{C}$. Measured spatial resolution resolution is $0.81 \div 1.32$ cm in the barrel and $0.86 \div 1.28$ cm in the end-cap, time resolution of the order of 2 ns.

1.2.7 Trigger System

As mentioned before, the LHC design luminosity is $1 \times 10^{34}\,\mathrm{cm}^{-2}\mathrm{s}^{-1}$ and 37 average collisions per BX. Since the data size of a proton-proton collision event in CMS is of the order of 1 MB and the event production rate is 40 MHz, it's technically impossible, up to now, to save every event produced

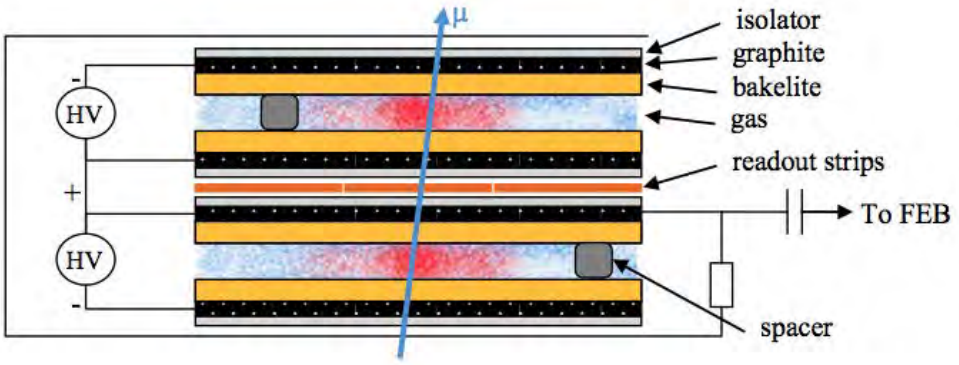

Figure 1.13: Schematic view of a CMS RPC chamber [30]. The acronym FEB stands for Front-End Board.

in CMS, since it would mean to save $\sim 40\,\mathrm{TB\,s^{-1}}$. For these reason it is practical to select only events that may have potential interest for the physics search. The events selection reduces the rate of stored events at some hundreds of Hz. The trigger system is divided in two steps that progressively selects the events and reduces the rate (see Fig. 1.14).

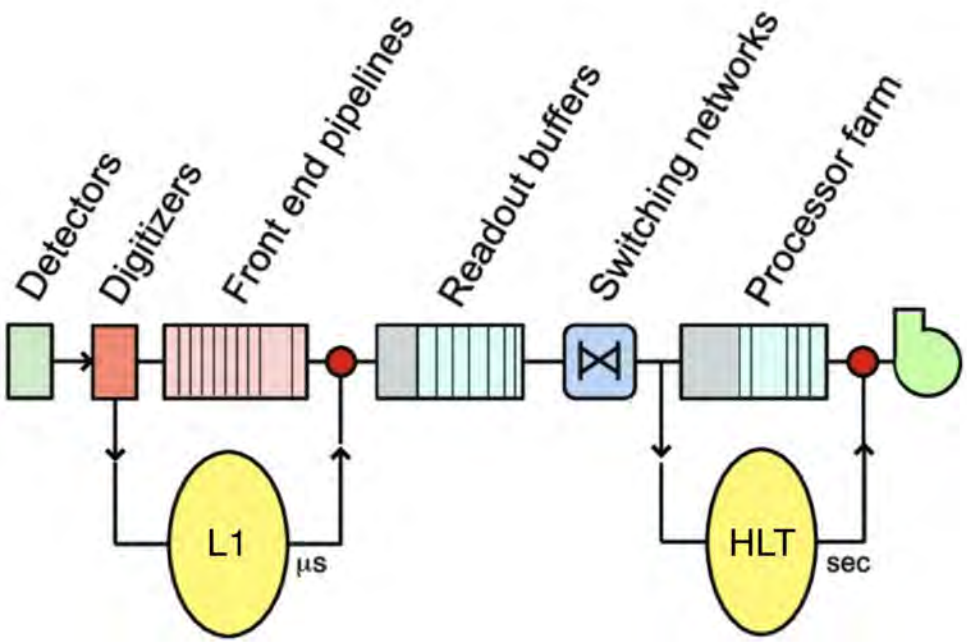

Figure 1.14: Scheme of the CMS trigger system [31].

1.2.7.1 L1 Trigger

This is a detectors level trigger which combines the informations from the calorimeters and the muon system (see Fig. 1.15). Best candidates are compared to p_T and E_T threshold and then accepted or rejected. Tracker informations are not included (up to Run 2) because of the too many channels which will slow down the triggering process. The aim of L1 trigger is

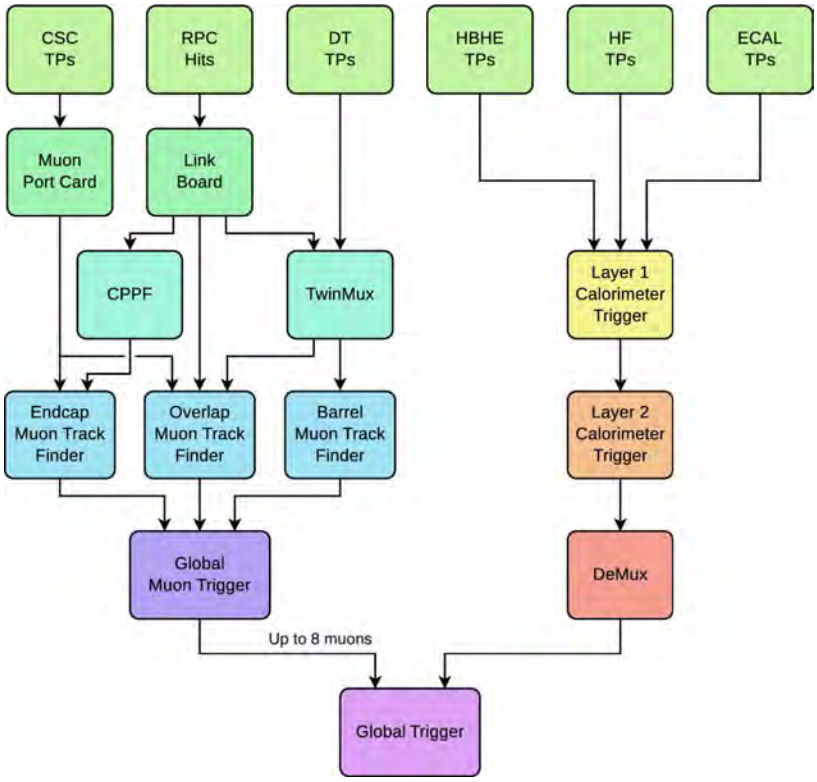

Figure 1.15: Block diagram of the CMS Level 1 trigger system [32]. The acronym TP stands for Trigger Primitive, while CPPF stands for Concentration Pre-Processing and Fan-out.

to reduce the event rate from 40 MHz to 100 kHz and it has not more than 3.2 µs to make a decision.

1.2.7.2 High Level Trigger (HLT)

This trigger is a complex software algorithm which select events candidates on the base of the event topology defined by the interested physics. It runs on a processor farm and reduces the event rate to an average of 400 Hz [33].

1.3 CMS Upgrades

In order to cope with increasing performance of the accelerator and exploit the technology improvements CMS subsystems periodically upgrade themself.

1.3.1 Phase 1 Upgrades

Most of the following upgrades are already completed or will be finished during LS2:

- *Tracker*: Pixel detectors will be replaced and the front-end electronics will be improved in order to maintain the maximum tracking efficiency.
- *Calorimeters*: In HCAL the photo-detectors will be substituted with silicon photo-multiplier. These will improve the light detection by increasing the efficiency and the signal-to-noise ratio. They are also immune to magnetic fields.
- *Muon systems*: The CSC system was arranged with a fourth layer of detectors and an extension of the RPC system. During LS1 The ME4/2 station was mounted and the RPC detection coverage was extended up to $|\eta| = 1.6$. The detector system foreseen for Phase 1 is shown in Fig. 1.16, the GEM based upgrade is presented in the next section.

1.3.1.1 GE1/1

The main upgrade in the muon system is the installation of the first station of GEM based detectors (more information will be given in the next chapter) named GE1/1; this has taken place during LS2. It consists of positioning 36 GEM based detectors in each of CMS end-caps covering the pseudorapidity region $1.60 < |\eta| < 2.15$, enhancing the redundancy of the muon hits in this region. Also it will permit to largely reduce the fraction of soft muons with overestimated momentum and the trigger rate for a given p_T threshold, while maintaining a high trigger efficiency. Fig. 1.17 shows pictures of an assembled GE1/1 detector.

1.3.2 Phase 2 Upgrades

In a similar way many upgrades are foreseen for LHC Phase 2:

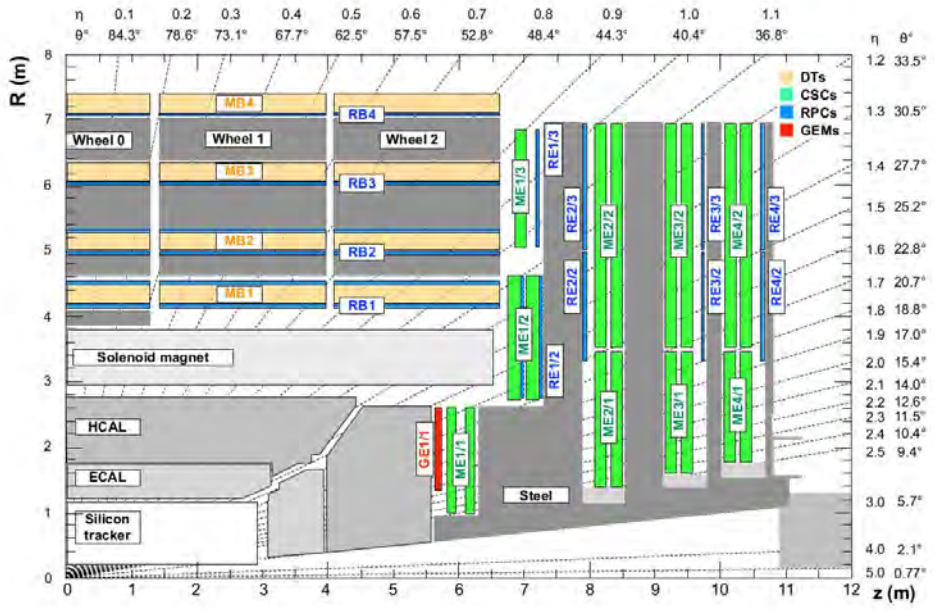

Figure 1.16: A quadrant of the CMS longitudinal cross section showing the foreseen system for Phase 1.

Figure 1.17: Photos of GE1/1 detector. On top the single layer of the chamber, on bottom front and side view of an assembled detector.

- *Tracker*: The entire tracking system will be replaced in order to overcome the radiation damages, furthermore the granularity of the detector will be increased by a factor ≈ 4. One more layer of detectors

in the end-caps will improve the redundancy and the total coverage will increase up to $|\eta| = 4$. During all Phase 2 tracker will participate to L1 trigger in order to ensure the required rate reduction.

- *Calorimeters*: A High Granularity Calorimeter (HGCAL) will replace the end-caps system and will include both EM and hadronic components, in particular it will alternate metallic absorber (W/Cu for EM part and CuZn/Cu for the hadronic one) and silicon sensors.

- *Muon systems*: New detectors based on the RPC technology called iRPC will be installed, increasing the detection coverage up to $|\eta| < 2.4$, the projects names are RE3/1 and RE4/1. Other two GEM-based projects will be installed during LS2: GE2/1 and ME0; they will be discussed in the next two sections.

As the previous upgrades, a big effort will be done to improve or replace the readout electronics, the data acquisition systems and the beam monitoring. Technical details can be found in [34].

1.3.3 GE2/1

This new detector system consists of positioning 18 super-chambers per end-caps in the region $1.6 < |\eta| < 2.4$, see Fig. 1.19. Each super-chamber is composed of two triple-GEM layer of trapezoidal shape, covering 20° in ϕ, as shown in Fig. 1.18. Each GE2/1 chamber covers an area of $1.45\,\mathrm{m}^2$ for a total active area of $105\,\mathrm{m}^2$. Every chamber is segmented in four modules in R each containing 12 sectors and each sector is read by 128 radial strips. This means that each chamber has about six thousand strips, their pitch varies from 0.5 mm to 1.2 mm. The nominal voltage is around 3200 V that means an effective gas gain of 2×10^4. The expected spatial resolution varies, from inner to outer radius, from 200 µm to 410 µm. Each sector of every chamber is read out by a front-end ASIC chip. This chip consists of 128 channel each containing a charge sensitive preamplifier, a shaper and a constant fraction discriminator; resulting in a time resolution, with the detector of 7.5 ns. The connection with the off-detector electronics is provided by an Opto-Hydrid board (OH), which contains a GigaBit Transceiver (GBTx), an FPGA and the optical receiver and transmitter (VTRx and VTTx).

GE2/1 will add an additional detection layer which covers the pseudo-rapidity region $|\eta| < 2.4$, previously only covered by CSC chambers. In the region covered also by GE1/1 the number of hit for a traversing muon will increase to eight. The main advantages provided by GE2/1 project are:

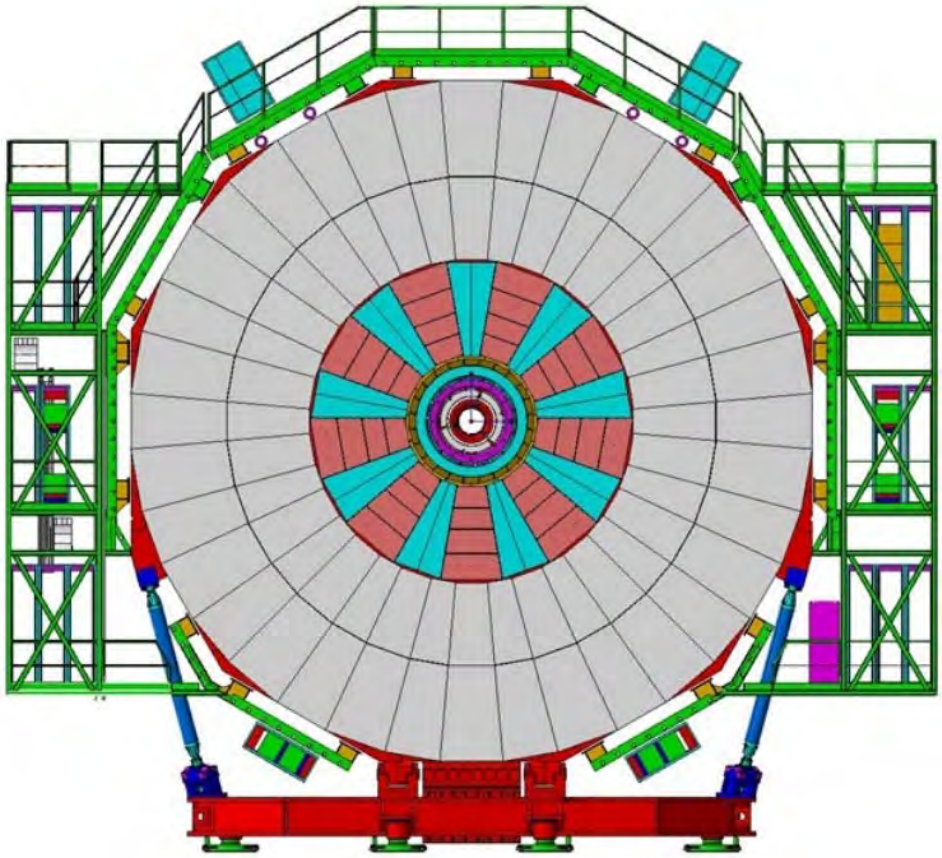

Figure 1.18: Location of the 18 GE2/1 detectors (blue and red) on the back of the yoke disks YE±1. The two chambers of neighbouring super chambers overlap in ϕ, to avoid acceptance holes [28].

- In order to estimate the momentum of a muon at L1 trigger level, a precise measurement of the the position of the track segments in the CSCs are required. Adding a layer of GEM chamber will increase the local lever arm for the segment reconstruction by more than a factor two with respect to the CSC system only. Furthermore, due to the lack of iron yoke between GE2/1 and ME2/1, multiple scattering is negligible. This combination of GEM and CSC can give a good measurement of the muon direction within a single station. This better estimation will provide a less fraction of soft muons with overestimated momentum, resulting in a trigger rate reducing for a fixed p_T threshold.

- The enhanced redundancy provided by GE2/1 will increase the robustness of the track reconstruction already at the L1 trigger level.

- Also in the case of displaced vertices for which the vertex constrain

cannot be exploit, an additional lever arm can be useful. The muon stations in the end-caps can provide a stand-alone muon momentum reconstruction already at L1 trigger level.

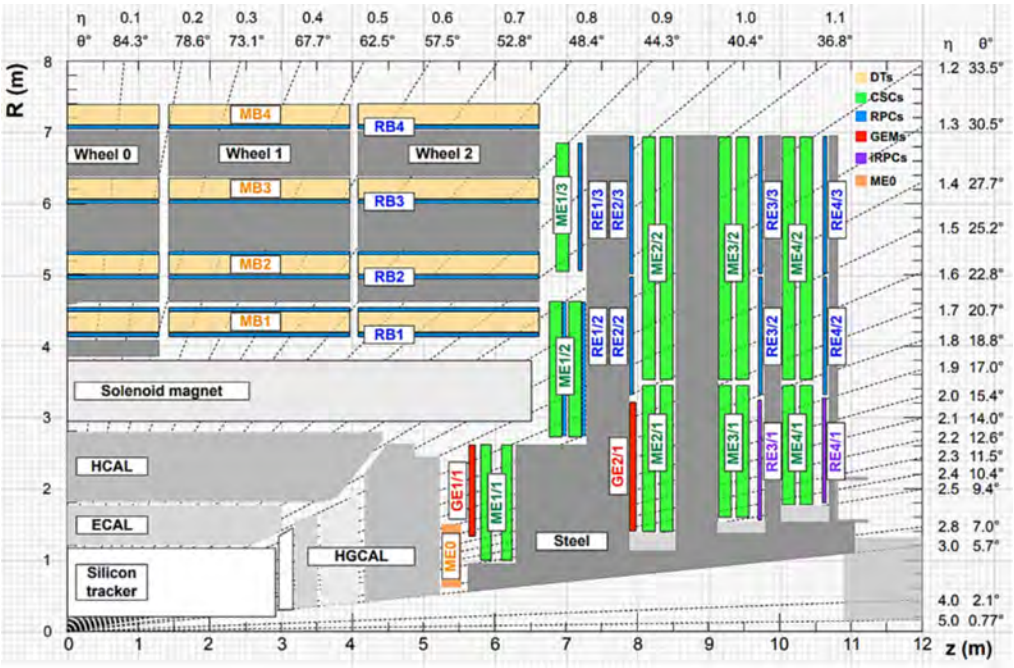

Figure 1.19: A quadrant of the CMS longitudinal cross section showing the foreseen system for Phase 2.

1.3.4 ME0

This detector system consists of positioning 18 modules per end-caps, each of them made of 6 layers of triple-GEM detectors of trapezoidal shape, thus a total of 216 chambers are needed. The station will be installed behind the new HGCAL calorimeter exploiting the space freed by this upgrade, see Fig. 1.20. The covered region extends in $2.0 < |\eta| < 2.8$, which is the maximum possible range due to mechanical constrain. This increases the total acceptance of the muon spectrometer. The system will overlap with the exiting CSCs systems and with the new RPCs stations (up to $|\eta| = 2.4$). The total active area of ME0 upgrade is $105\,\mathrm{m}^2$. The segmentation of a single chamber layer is 8 rings in $|\eta|$ and 3 sectors in $|\phi|$, each of the latter subdivided into 128 radial strips. The construction details are the same of the GE2/1 chambers, while the spatial resolution is more accurate: 160 µm in the inner radius and 390 µm in the outer one. The electronics readout and the data transfer and communication systems will be the same as the GE2/1 station.

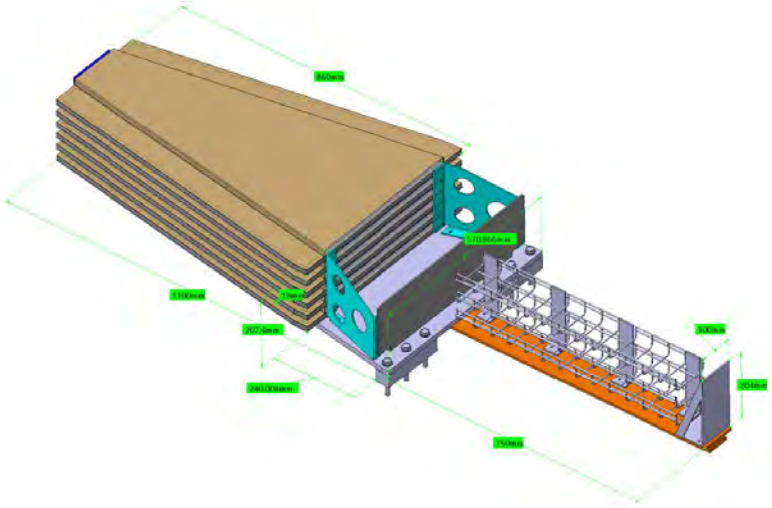

Figure 1.20: Layout of ME0 stack with six triple-GEM layers including cable trays shown in the lower right part of the figure. The six layers are staggered such that the active areas of adjacent stacks overlap in ϕ [28].

The main motivation for this new project is to extend the muon acceptance region. This will improve the physics performance in many physical channel such as multi-muon final states and very forward particle production. In particular, ME0 will improve performance in many ways:

- The ME0 detector will add up to six hit per track and increase the lever arm for momentum determination. This will suppress the L1 trigger rate, due to soft muons with overestimated p_T, by a factor 10.
- In the region $2.15 < |\eta| < 2.40$ (not covered by GE1/1) ME0, together with ME1/1, will ensure the second muon direction measurement. The first one is provided by the tandem GE2/1-ME2/1. This will enable stand-alone trigger of muon resulting from the decay of long-living particles.
- ME0 will be the only station which covers the high pseudorapidity region $2.40 < |\eta| < 2.80$. Its six layers will provide an efficient muon tagging and neutrons background rejection. For example even for momenta down to $p_T = 3\,\text{GeV}$ the identification efficiency is simulated to be up to 95%. A stand-alone ME0 based trigger is not feasible, but it will contribute to the Level-1 cross-trigger (in particular with low p_T muons) and in HLT.
- ME0 will be fundamental to completely exploit the upgraded tracker trigger capabilities. Indeed this detector is not able to identify particles as muons, then muon detectors are needed to completely use the tracker capabilities.

More technical details about the development, the assembling and the commissioning of these projects can be found in [28].

A resume of the main parameters regarding the GEM based detectors that will instrument the CMS muon spectrometer are shown in Tab. 1.1.

GEM station:	**GE1/1**	**GE2/1**	**ME0**
$\|\eta\|$ range:	$1.60 \div 2.15$	$1.60 \div 2.40$	$2.00 \div 2.80$
Number of chambers:	144	72	216
Number of channels:	442368	442368	663552
Number of layers:	2	2	6
Total area (m^2):	54	105	64
Spatial resolution (µm):	$200 \div 340$	$200 \div 410$	$160 \div 390$
Time Resolution (ns):	8	8	8

Table 1.1: Resume of the main parameters for the GEM-based detectors upgrades foreseen in the next years.

CHAPTER 2

GASEOUS DETECTORS

This chapter will give an overview of the basic concepts to understand the behaviour of gaseous particle detectors. A general description of the interactions processes between the radiation particles and the matter will be given. Particular attention will be paid to the processes playing a role in the detection of muons and soft X-rays, which are the particles detected in the CMS end caps and during the R&D activities. A description of the physics behind charge diffusion and multiplication will follow, to consolidate the basis for the understanding of the detectors designs. Finally, an historical overview of the detector technologies developed during the years with their pros and cons will close the chapter. Particular attention will be given to the detectors under analysis in this thesis: the triple-GEM.

The informations and figures presented in this chapter are adapted from [35–41]

2.1 Particles Ionization in Matter

Ionizing particles interact with matter via the four fundamental forces of nature. The electromagnetic force is responsible for the physical processes that give the largest amount of energy deposition for charged particles and photons. In this section, the mechanisms involved in the energy release, useful for detection of fast charged particles and soft X-rays, are described.

2.1.1 Charged Particles

The largest amount of energy dissipated by charged particles in matter is due to the Coulombian interaction between the projectile field and the target atom or molecule. The slowing down of the particle in matter is mainly due to inelastic interaction of excitation and ionization. Fig. 2.1

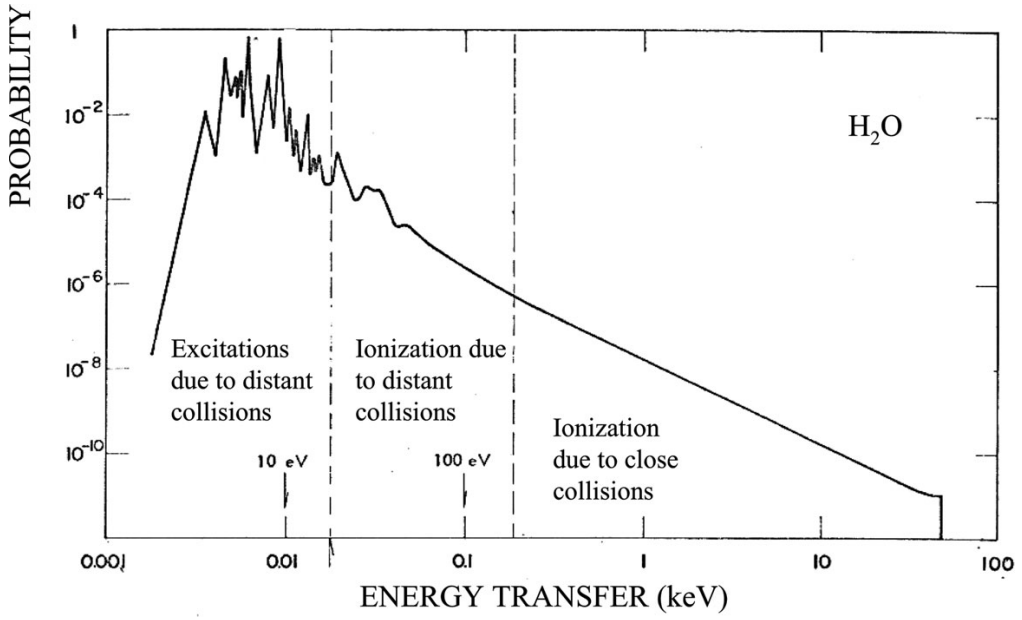

Figure 2.1: Collision probability of fast electrons in water as a function of the energy transfer [42].

shows the interaction probability of a fast electron in water as a function of the energy transfer. In the region from some eV up to some tens of eV the multiple excitation lines of the target molecules and atoms give a relatively complex structure. This is the region of distant interactions, since they require a large impact parameter. The molecules and atoms can rearrange in non-radiative ways, get excited and be ionized with subsequent emission of free electron-ion pairs or de-excitation photons. At higher energies the collision probability decreases exponentially up to the maximum kinematically allowed energy transfer. The results of such interactions are the creation of excited species and the release of free electrons and ions. Despite the low probability, very large energy deposition events (also called "delta electrons") play an important role on the statistic of the energy loss. Photons and electrons created by the primary particle interactions may further excite and ionize the medium contributing to increase or decrease the ionization yield of the energy deposition.

The so called Rutherford expression gives the probability for a particle with velocity β and unit charge to release an energy between ϵ and $\epsilon + d\epsilon$

in a material with density ρ along the path dx:

$$\frac{\partial^2 N}{\partial x \partial \epsilon} = K \frac{Z}{A} \frac{\rho}{\beta^2} \frac{1}{\epsilon^2}, \quad K = \frac{4\pi N e^2}{mc^2}, \tag{2.1}$$

where e and m are the electron charge and mass, Z and A the atomic and mass number of the target material and N the Avogadro number. This formula comes from a semi-classical argument and nicely predicts the behaviour of particles with intermediate velocities. To predict a wider range of experimental data, different corrections were made [43, 44]. In a more general formulation, the stopping power, i.e. the differential energy loss, is written accordingly to the Bethe-Bloch formula:

$$\frac{dE}{dx} = -\rho \frac{2KZ}{A\beta^2} \left[\ln \frac{2mc^2\beta^2}{I(1-\beta^2)} - \beta^2 - \frac{C}{Z} - \frac{\delta}{2} \right]. \tag{2.2}$$

The C/Z term is the so called inner shell correction that takes into account the screening of the Coulombian field on the deepest electron layers. On the other hand the $\delta/2$ term indicates the density effect, an effect that appears at relativistic velocities because of a collective interaction between the projectile field and the medium. Fig. 2.2 shows the qualitative trend of the

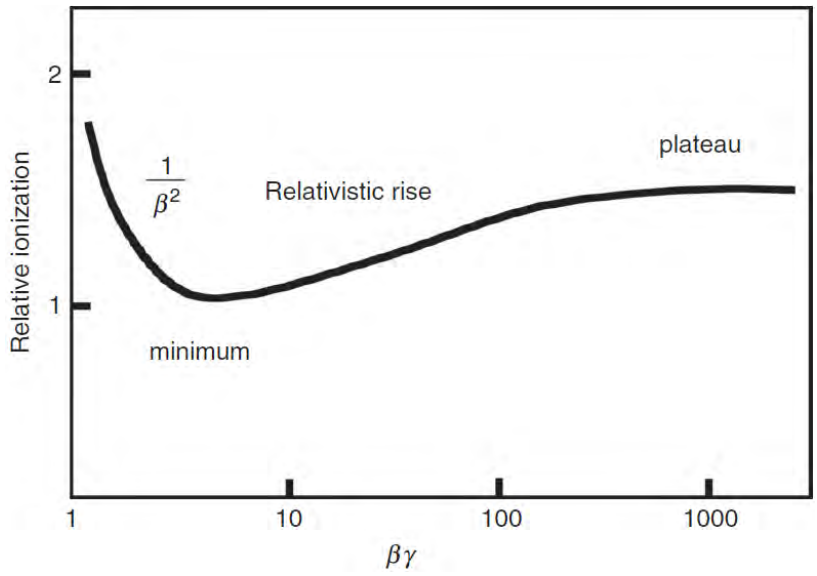

Figure 2.2: Ionization energy loss of charged particles as a function of velocity [35].

ionization energy loss of charged particles in matter. The energy deposited decreases with the velocity, it reaches a minimum when approaching the speed of light and then it starts to slightly increase up to a constant value (the so called Fermi plateau).

At very high particle energies, other mechanisms start playing a role: bremsstrahlung, Cherenkov and transition radiation. These effects contribute little to the overall energy deposition, but for electrons where bremsstrahlung becomes important also at low energies. Fig. 2.3 shows the global mass

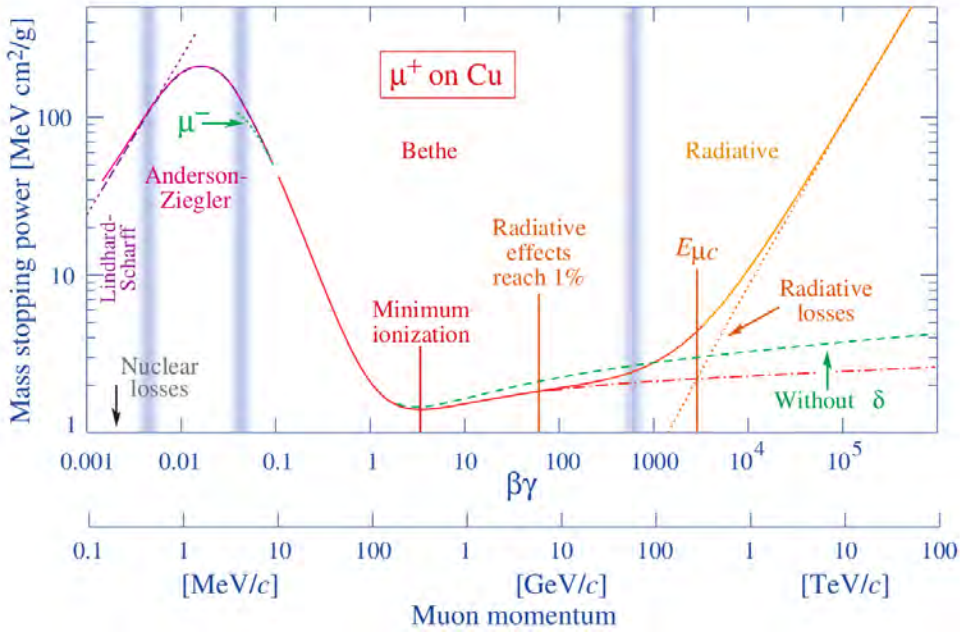

Figure 2.3: Global mass stopping power for a positive muon in Cu as a function of $\beta\gamma$. Solid lines represents the total stopping power [39].

stopping power of a positive muon on a Copper layer. It is clear that for muons the radiative losses are not important at momentums lower than some hundreds GeV. In particular, muons have an energies loss near the minimum for a large range of energy. Most of the cosmic muons and the ones produced in hadron collisions are in this range. Hence muons are usually called Minimum Ionizing Particle (MIP) because their energy loss is almost constant, near $2\,\mathrm{MeVcm}^2/\mathrm{g}$.

It is useful to calculate the average energy deposit per unit path for a muon in a Ar/CO_2 (70/30) gas mixture, since it is the one used for CMS triple-GEM. A good estimation for can be found using the Bragg's Rule:

$$\left\langle \frac{dE}{dx} \right\rangle_{Ar/CO_2} = \rho_{mix}\left[0.7\left\langle \frac{dE}{\rho dx} \right\rangle_{Ar} + 0.3\left\langle \frac{dE}{\rho dx} \right\rangle_{CO_2}\right] = 2.76\,\mathrm{keV/cm}, \quad (2.3)$$

where:

$$\rho_{mix} = 0.7\rho_{Ar} + 0.3\rho_{CO_2} = 1.716 \times 10^{-3}\,\mathrm{g/cm}^3.$$

Using Eq. 2.3, the average energy deposited by a muon impinging perpen-

Element	ρ (g/cm^3)	$\left\langle \frac{dE}{dx} \right\rangle$ (MeVcm^2/g)
Ar	1.662×10^{-3}	1.519
CO_2	1.842×10^{-3}	1.819

Table 2.1: Density and minimum stopping power used for calculations. Gases are evaluated at 1 bar and 20 °C [45].

dicularity in the 3 mm drift gap of a GEM detector is:

$$< E >= \left\langle \frac{dE}{dx} \right\rangle_{Ar/C0_2} 0.3\,\text{cm} = 828\,\text{eV}. \tag{2.4}$$

This value may be larger in case of non perpendicular muons, the scale factor is $1/\cos\theta$ where θ is the angle between the perpendicular and the trajectory. A summary on the used data is shown in Tab. 2.1.

The number of primary ionizations due to independent Coulomb interactions follow the Poisson statistics. The probability P_k^n to have k ionizations with an average n is:

$$P_k^n = \frac{n^k}{k!} e^{-n}.$$

The average number of primary eletron-ions pairs N_T produced may be estimated via:

$$N_T = \frac{\Delta E}{W_I}, \tag{2.5}$$

where ΔE is the energy deposited in the active volume and W_I the average energy required to produce a pair in the medium. Many useful parameters for the gases used in detectors are shown in Tab. 2.2. The average energy required to produce an electron-ion pair in gas mixtures may be computed with the Bragg's rule, for Ar/CO_2 (70/30):

$$W_I = 0.7W_I^{Ar} + 0.3W_I^{CO_2} = 28.4\,\text{eV}, \tag{2.6}$$

meaning that the average number of pairs produces in the 3 mm drift gap of a triple-GEM for perpendicular impinging MIP is:

$$n_0^{MIP} = 29,$$

obtained by merging Eq. 2.4 and Eq. 2.6.

For particles interacting many times in a certain volume the distribution of deposited energy and primary number are Gaussian because of the Central Limit Theorem. However, many gaseous detectors have sensible volumes relatively small and the number of ionizations is not large enough

Gas	**Density,** g/cm^3	$\mathbf{E}_x$ eV	$\mathbf{E}_I$ eV	$\mathbf{W}_I$ eV	$\mathbf{dE/dx}\vert_{min}$ keVcm^{-1}	$\mathbf{N}_P$ cm^{-1}	$\mathbf{N}_T$ cm^{-1}
He	0.179	19.8	24.6	41.3	0.32	3.5	8
Ne	0.839	16.7	21.6	37	1.45	13	40
Ar	1.66	11.6	15.7	26	2.53	25	97
Xe	5.495	8.4	12.1	22	6.87	41	312
$\mathbf{CH_4}$	0.667	8.8	12.6	30	1.61	28	54
$\mathbf{C_2H_6}$	1.26	8.2	11.5	26	2.91	48	112
$\mathbf{iC_4H_{10}}$	2.49	6.5	10.6	26	5.67	90	220
$\mathbf{CO_2}$	1.84	7.0	13.8	34	3.35	35	100
$\mathbf{CF_4}$	3.78	10.0	16.0	54	6.38	63	120

Table 2.2: Properties of noble and molecular gases at normal temperature and pressure (NTP: 20 °C, one atm). E_x, E_I : first excitation, ionization energy; W_I : average energy per ion pair; $dE/dx|_{min}$, N_P , N_T : differential energy loss, primary and total number of electron-ion pairs per cm, for unit charge minimum ionizing particles [39].

to give a Gaussian distribution. This is the case of triple-GEM detectors with 3 mm drift gap. In these situations, the energy loss distribution present a high energy tail, because of delta electrons emissions caused by large amount of energy transferred to the medium. The distribution takes the name of the Russian scientist Landau and is written as:

$$f(\lambda) = \frac{1}{\sqrt{2\pi}} e^{\frac{1}{2}\left(\lambda + e^{-\lambda}\right)},$$

where the variable λ is the normalized deviation from the most probable energy loss ΔE_{MP} :

$$\lambda = \frac{\Delta E - \Delta E_{MP}}{\xi}, \quad \xi = K \frac{Z}{A} \frac{\rho}{\beta^2} x.$$

In general, the width of the distribution is close to the most probable value. A practical example of this distribution, measured on a CMS triple-GEM detector, can be found in Fig. 2.4.

2.1.2 Interaction of Photons

Photons interacts via electromagnetic force with the target atoms. Being neutral particles, photons do not release continuously their energy like charged particles but they interact in single encounters, with or without release of secondary particles. Gases are usually transparent to photons with energies lower than the excitation and ionization levels of the atoms.

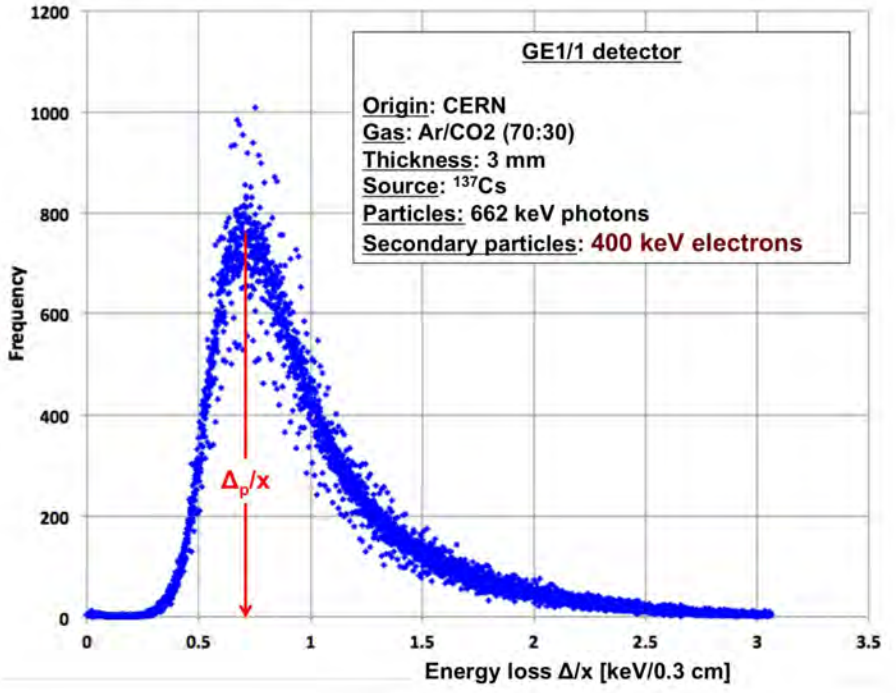

Figure 2.4: Energy distribution of 400 keV electrons in a GEM detector. The electrons are produced from Compton scattering of 662 keV photons with Copper in front of the gas volume [46].

For such photons, up to visible and near ultra-violet energies, elastic interactions with the medium are the most probable. This process, also called coherent or Rayleigh scattering, does not remove the photon from the beam.

At energies higher than some keV the photon starts to excite or ionize the medium. If the photon is completely absorbed during the interaction the process is called photoelectric effect, while if the photon release just a part of its energy the process is called inelastic or Compton scattering. When the energy of the impinging photon is higher than 1.022 MeV, its interaction with the nuclear Coulombian field (or the electron field for higher energies) may lead to the production of electron-positron pairs than may further ionize the medium. For this thesis purpose only photoelectric and Compton effects are described.

Because of their nature, photons are removed from the beam after they interact. If a monochromatic photon beam of N_0 particles impinges on a target the differential number of photon dN lost in a material thickness dx is:

$$dN = -\mu N_0 dx,$$

where μ is the linear attenuation coefficient, that depends on the material

and the photon energy and is related to the cross section of the process. From the previous relation the Lambert-Beer formula can be obtained:

$$N(x) = N_0 e^{-\mu x}. \tag{2.7}$$

Hence the absorption of photon in the matter follows a negative exponential law. This relation is exact if only photoelectric effect occurs, indeed this is the only process that completely removes the photon from the beam. If Compton effect is not negligible, a correction called "build-up factor" has to be taken into account depending on the geometry of the system. Tabulated data usually give the mass attenuation coefficient μ/ρ values that are less dependent on the target material than μ. If photons are subjected to multiple processes the attenuation coefficient are summed linearly. Fig. 2.5 shows the μ/ρ values for photons of different energies when interacting in gaseous Ar/CO_2 (70/30) mixture. With this expression it is possible to quantify the intrinsic efficiency of a gaseous detector given the photon energy and the gas mixture. For a CMS triple-GEM irradiated with 5.9 keV photons from a ^{55}Fe source the fraction of the beam that interacts in the 3 mm drift gap is 0.621, being $\mu_{Ar/CO_2\ (70/30)}(5.9\,\text{keV}) = 0.323\,\text{cm}^{-1}$ [47].

2.1.2.1 Photoelectric effect

As already mentioned, the process where a photon is completely absorbed during a single interaction by a target electron is called photoelectric effect. This can happen only if the energy of the impinging photon E_γ is higher than one of the E_i electrons binding energies. The absorption cross section has a resonance when the photon has the same energy of the shell and decreases with the energy (see Fig. 2.5). For this reason the highest cross section for soft X-rays is on the inner electron shells. The electron, usually called photoelectron, is freed with an energy $E_\gamma - E_i$ since the atom recoil can be neglected. The angular distribution of the emitted photoelectron is showed in Fig. 2.6 for different impinging energies. The plots shows that the electron is emitted perpendicularly to the photon direction for low energy, with lower deviation angle at higher energies.

After the ionization, the hit atom can return to the ground level by filling the vacant shell in two different ways:

- via Auger process: the vacancy is filled by an upper shell electron and the energy is transferred to the even upper shell releasing that electron. For example a vacancy on the K shell may be filled with a L shell electron with the successive emission of a M shell electron (the Auger electron) with energy:

$$E_{Auger} = E_K - E_L - E_M.$$

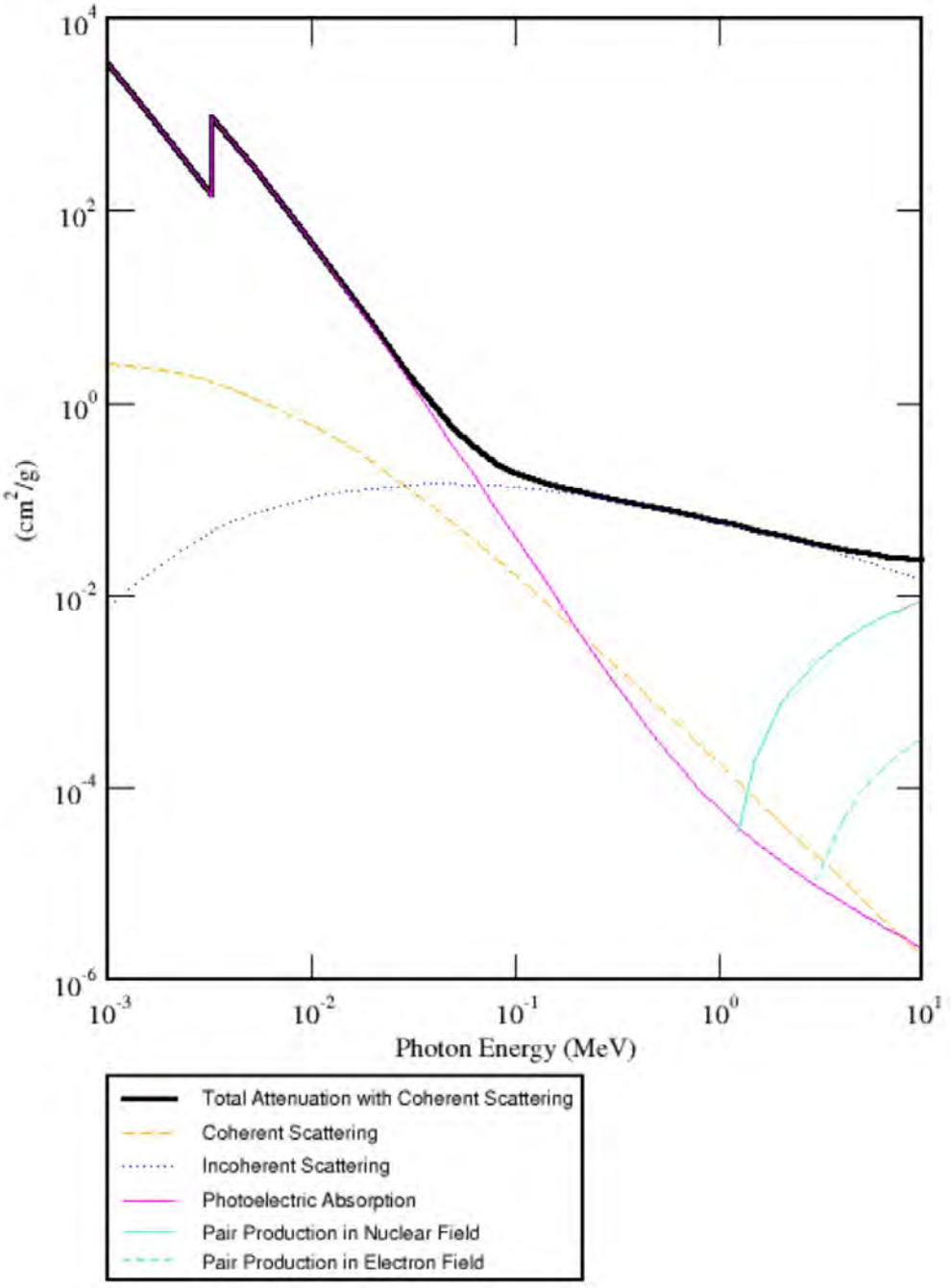

Figure 2.5: Mass attenuation coefficient for the various photons interactions processes in Ar/CO_2 (70/30) [47].

Since usually the L and M shell energies are much smaller than the K one the Auger electron has energy near the vacant shell one E_K.

- via fluorescence: the vacancy is filled by an electron of an outer shell.

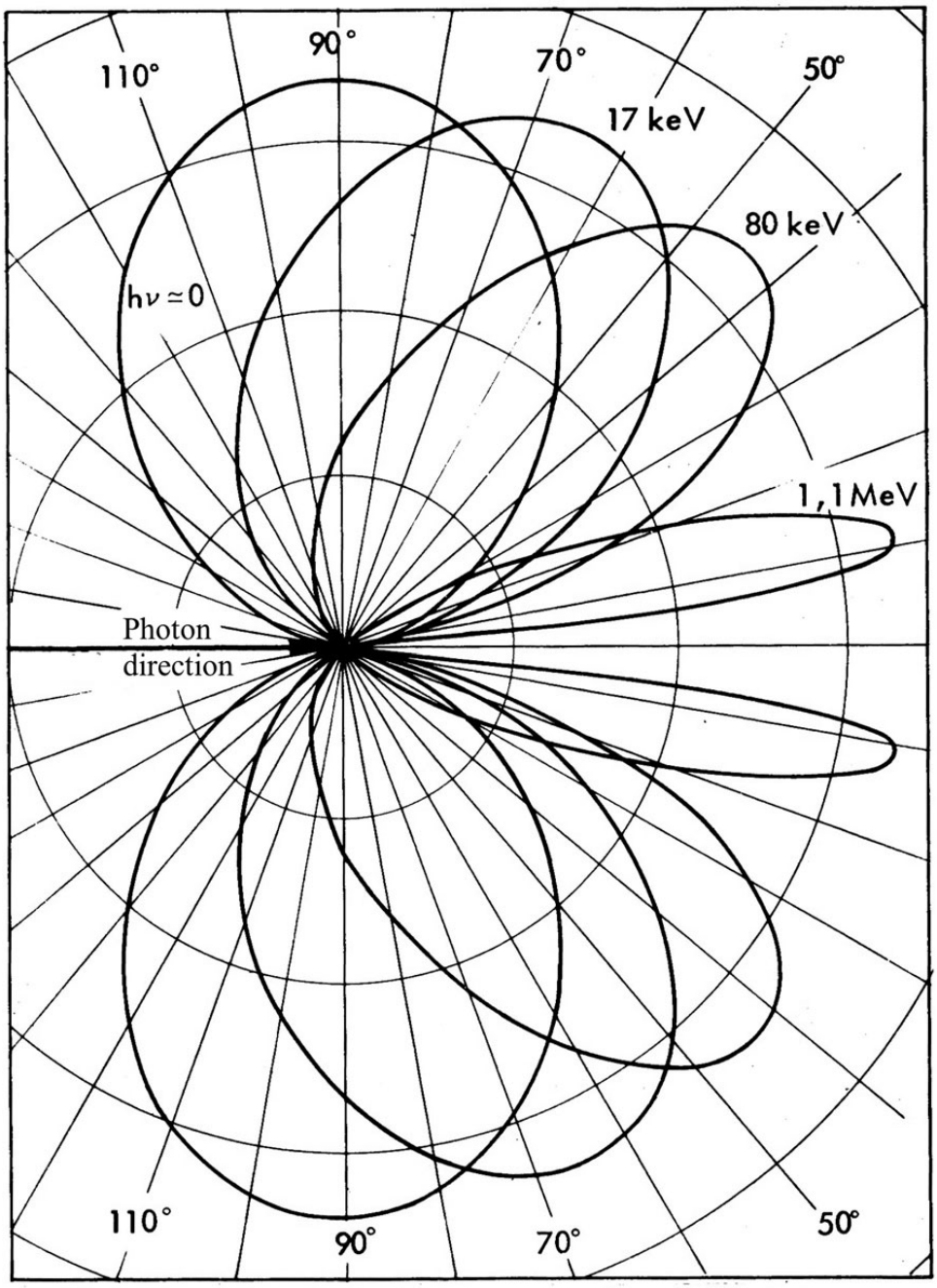

Figure 2.6: Angular distribution of photoelectrons for increasing values of the photon energy [48].

This result in an emission of a photon of energy equal to the difference of the two shells energies.

An Argon based mixture can emit characteristic photons after its ioniza-

tion. Tab. 2.3 shows the typical Argon transition lines; the weighted average of their energies gives: $\langle E_{Ar} \rangle = 2.9845\,\text{keV}$. Argon L-lines have

Transition Line	**Relative Intensity**	**Energy** keV
Kα_2	50	2.9956
Kα_1	100	2.9577
Kβ_1	10	3.1905
Kβ_3	10	3.1905

Table 2.3: Most energetic characteristic X-rays line energies for Argon. A relative intensity of 100 is given to the most probable transition. [49]

energies of the order of 200 eV [50], however they are not so relevant because of their low energy and the very low probability to extract L shell electrons during photoelectric absorption.

The characteristic X-rays emitted after the Argon rearrangement can escape the detector volume because of their relatively long mean free path in gas, but the same can not happen for Auger electrons. If this happens, an energy $\langle E_{Ar} \rangle$ will be not detected. In X-rays spectroscopy with Argon based mixtures this effect appears in the form of a peak with energy $\langle E_{Ar} \rangle$ lower than the expected one. However, this effect is relatively small: about 8% of the photoelectric absorptions is accompanied by the emission of a photon, while in 92% of the events, together with the photoelectron, one or more electrons are produced by the Auger mechanism [35].

As in the case of charged particles, the mean number of primary charges released in the detector volume may be estimated using Eq. 2.5. However, while for charged particles the fluctuations are dominated by the Landau statistics, for X-rays where the deposited energy is relatively large, the fluctuations follows the Poisson statistics with a dispersion $\sqrt{N_T}$. Experimentally, it was observed that the actual resolution of many detectors is better than the one expected with a Poisson dispersion. In particular the Fano factor F (<1) was introduced to take into account the lower fluctuation observed. Hence the effective variance is:

$$\sigma^2_{N_T} = F N_T. \tag{2.8}$$

The fact that Fano factors smaller than 1 are observed for some detectors can be considered a consequence of the partitioning process of the original energy carried in by the incident particle. However, the Fano factor can be calculated accurately using microscopic techniques so that they no longer need to be treated as free variables in simulations [51].

2.1.2.2 Compton effect

Compton scattering starts to become the dominant process when the photon energy is above the highest electron shell level of the target material. The incoming photon interacts with a quasi-free electron and it is deflected at an angle θ with respect to its original direction. The portion of energy transferred to the electron varies in a large range because all the scattering angles are possible. From the momentum and energy conservation during the scattering, the photon energy after the collision can be written as:

$$h\nu' = \frac{h\nu}{1 + \frac{h\nu}{m_e c^2}(1 - \cos\theta)},$$

with symbols defined in Fig. 2.7. The amount of energy transferred goes

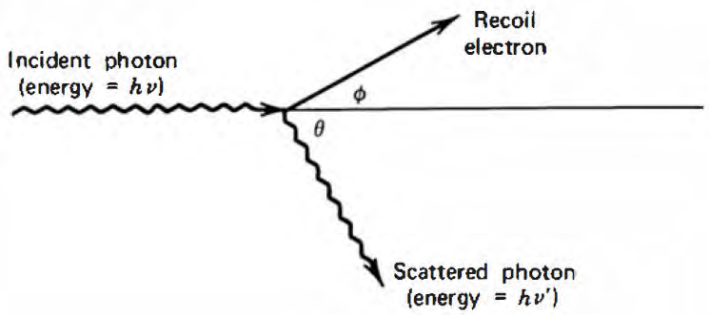

Figure 2.7: Compton effect kinematics [35].

from a very small fraction of the initial energy to a maximum that is always lower than the initial photon energy. The differential cross section and the angular distribution are predicted from quantum mechanics and can be found in [52, 53]. Fig. 2.8 shows the angular distribution of scattered photons and illustrates the strong tendency for forward scattering at high values of the photon energy.

2.2 Gaseous Detectors Operating Principles

As explained in the previous section, the main effect of energy depositing in gas is the creation of free charges. This section will describe the behaviour of such charges with and without the presence of an electric field, and how these mechanisms are used to detect signals in gaseous particles detectors.

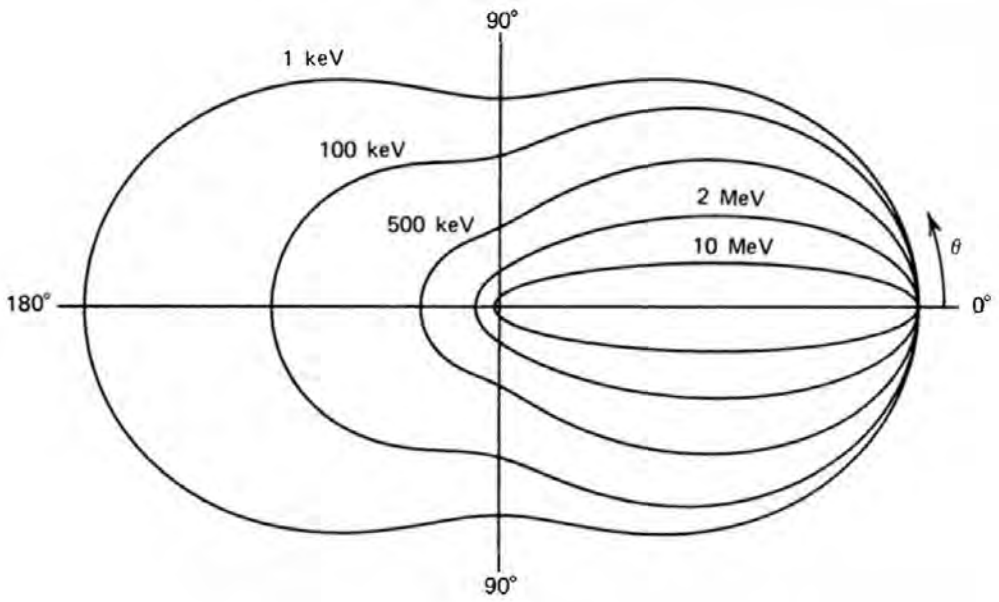

Figure 2.8: A polar plot of the number of photons (incident from the left) Compton scattered into a unit solid angle at the scattering angle θ. The curves are shown for the indicated initial energies [35].

2.2.1 Charges Diffusion and Drift in Gases

The ions and the electrons in gas diffuse like neutral particles if no electric field is present. Their behaviour is described by the classic kinetic theory of gases. The Maxwell-Boltzmann law provides the probability of a particle to have a certain energy ϵ:

$$F(\epsilon) = 2\sqrt{\frac{\epsilon}{\pi\,(kT)^3}}e^{-\frac{\epsilon}{kT}}, \tag{2.9}$$

where T is the absolute temperature and $k = 8.62 \times 10^{-5}\,\mathrm{eV/K}$ the Boltzmann's constant. The average thermal energy is:

$$\langle\epsilon\rangle = kT,$$

equal to 25 meV at normal conditions. The corresponding velocity ν distribution of a particle of mass m is:

$$f(\nu) = 4\pi\left(\frac{m}{2\pi kT}\right)^{\frac{3}{2}}\nu^2 e^{\frac{m\nu^2}{2kT}},$$

with an average velocity and a most probable value respectively:

$$\langle\nu\rangle = \sqrt{\frac{8kT}{\pi m}}, \quad \nu_{MP} = \sqrt{\frac{2kT}{m}}.$$

A Gaussian law predicts the spread of a localized distribution of particles:

$$\frac{dN}{N} = \frac{1}{\sqrt{4\pi Dt}} e^{-\frac{x^2}{4Dt}} dx, \tag{2.10}$$

where the first term indicates the fraction of particles encountered in the infinitesimal element dx at a distance x from the origin after a time t. D indicated the diffusion coefficient in m^2/s. The standard deviations of such distribution σ_x and σ_V, respectively for a linear and volume distribution are:

$$\sigma_x = \sqrt{2Dt}, \quad \sigma_V = \sqrt{6Dt}$$

It is possible to obtain a net movement of the charges if an electric field is applied. The ions are accelerated along the field lines but the collisions with the gas molecules limit their velocity. The maximum average velocity attained by ions is called drift velocity and it is much lower than the maximum instantaneous velocity between two consecutive collisions. The drift velocity increases with E. For this reason the ion mobility μ [m^2/Vs] is defined:

$$\mu = \frac{w^+}{E},$$

which is constant over a large electric field range at fixed gas temperature and pressure. For example, the CO_2^+ mobility in Ar/CO_2 (70/30) gas is $1.541\,cm^2V^{-1}s^{-1}$ at a pressure of 8 mmHg and room temperature or $1.6 \times 10^{-2}\,cm^2V^{-1}s^{-1}$ in standard conditions [54]. In literature, the ion mobility is frequently expressed in terms of the reduced mobility μ_0 that takes into account the variation due to gas number density N:

$$\mu_0 = \mu \frac{N}{N_0},$$

where N_0 is the Loschmidt number ($2.6867 \times 10^{25}\,m^{-3}$). The Nerst-Townsend formula relates the mobility and the diffusion constant:

$$\frac{D}{\mu} = \frac{kT}{e}. \tag{2.11}$$

When the ions have moved for a time t and a length x they diffuse following the distribution of Eq. 2.10. When combining the two previous expressions, the variance of such distribution along the drift direction can be written as:

$$\sigma_x = \sqrt{\frac{2kT}{e}\frac{x}{E}},$$

hence the spatial diffusion does not depend on the ion type and gas properties but only on the electric field. In gas mixtures the process of charge transfer between specimens removes all ions except the one with the lower

ionization potential. For example in Ar/CO_2 mixtures, Ar^+ ions tend to transfer the charge to CO_2 molecules due to their lower ionization potential:

$$Ar^+ + CO_2 \rightarrow Ar + CO_2^+.$$

Then, the charge transfer mechanism will leave only one ion species migrating after some thousand collisions i.e. after some hundreds of µm in standard conditions [35].

The diffusion theory is reliable also for the electrons; however, they acquire larger energy between collisions than ions. In a qualitative formulation [55] the electron velocity can be expressed as:

$$w^- = k\frac{eE}{m}\tau$$

where τ is the average time between two consecutive collisions and k a constant depending on the assumption on the electron energy distribution (see for example [56]). Values of the electron drift velocity in Ar/CO_2 (70/30) simulated with Magboltz [57] are shown in Fig. 2.9. Since electrons

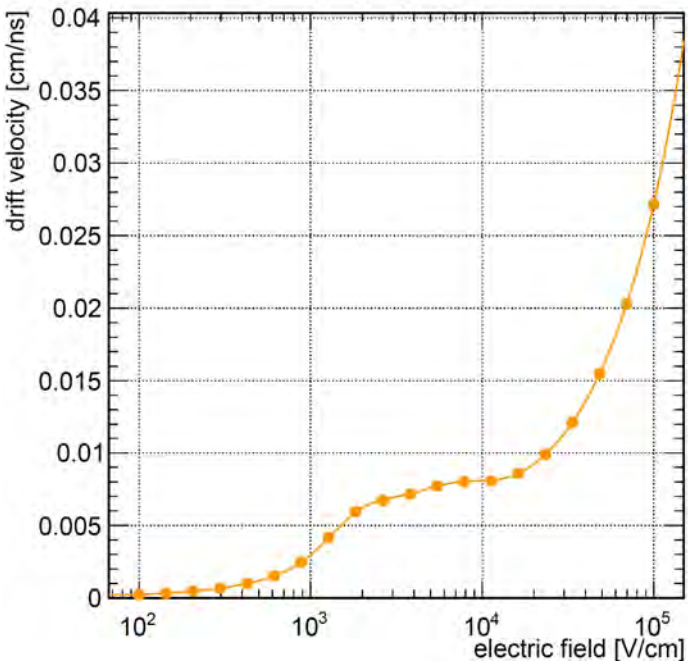

Figure 2.9: Simulated values of the electron drift velocity in Ar/CO_2 (70/30) as a function of the applied electric field. Output from Magboltz.

energies can overcome their thermal energy also at relatively low electric field, Eq. 2.11 is, in most cases, not valid. A reformulation can be done by introducing the phenomenological characteristic energy ϵ_k:

$$\frac{D}{\mu} = \frac{\epsilon_k}{e}.$$

Simulated values of the diffusion coefficient along the electron field direction D_L and along the transverse direction D_T are shown in Fig. 2.10. Values are output from Magboltz as a function of the applied electric field for Ar/CO_2 (70/30).

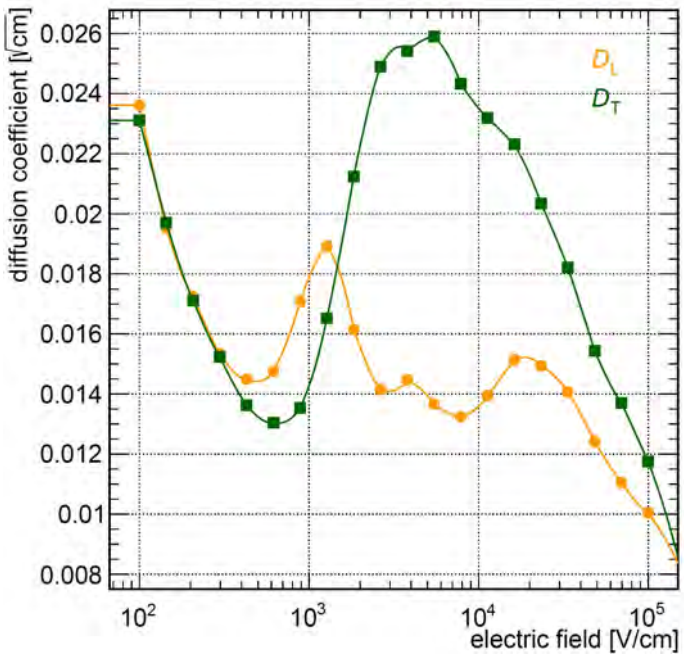

Figure 2.10: Simulated values of the transverse and longitudinal diffusion coefficient as a function of the electric field in Ar/CO_2 (70/30). Output from Magboltz.

The momentum transfer per each electron-atom collision is not a constant. Electrons with energies near the Ramsauer minimum, e.g. 0.23 eV in Argon (see Fig. 2.11), have long mean free paths and, as a consequence, can gain more energy before experiencing a collision with the surrounding gas. This effect can also be exploited to reduce the electron diffusion and make the electrons diffuse less and be faster. Indeed, if a molecule can cool down the electrons to energies near the Ramsauer minimum, a larger fraction of electrons can travel faster with a consequent reduction of the diffusion. Fig. 2.12 shows the simulated value of the drift velocity in Ar/CO_2 mixture for different CO_2 concentration with an electric field of 9 kV/cm at standard conditions.

Electrons are susceptible to recombination with ions and they can be captured by molecules with electronic affinity. While the recombination can be neglected if a sufficiently high electric field is present, the same cannot be said for the electron attachment. An electron interaction with an electronegative molecule may result in the creation of a negative ion

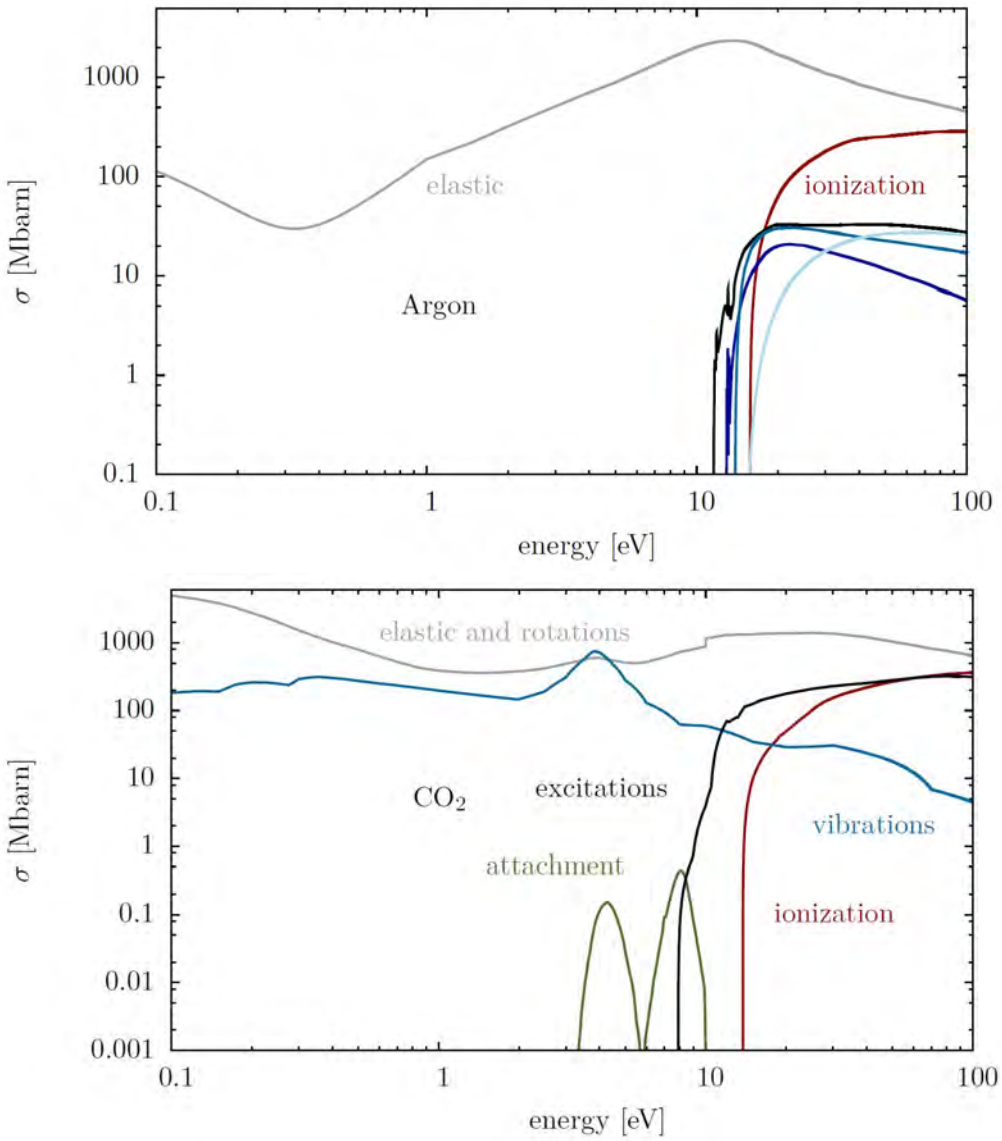

Figure 2.11: Cross-sections for scattering of electrons by Ar (top) and CO_2 (bottom) as implemented in Magboltz 8.9 [57]. For the sake of clarity, the above plots involve a few simplifications with respect to the actual cross-sections in the Magboltz database: (1) the 44 excitation cross-section levels for Ar are combined in four groups; (2) the rotation terms for CO_2 (inelastic energy loss $\leq 12\,\text{meV}$) are added to the elastic cross-section; (3) only the respective sums of the vibration, excitation and attachment cross-sections in CO2 are plotted. The cross-section data included in Magboltz extend beyond the energy range shown here [51].

and the loss of the initial electron. The electron attachment η is usually defined as the inverse of the mean capture length, it strongly depends on

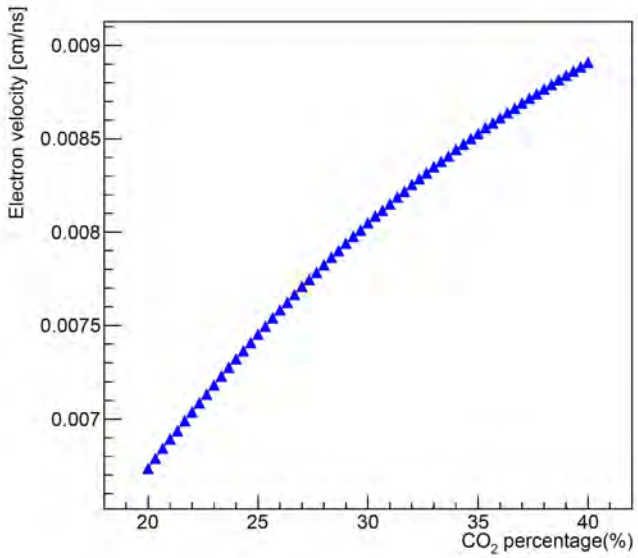

Figure 2.12: Simulated values of the electron drift velocity at $E = 9\,\mathrm{kV/cm}$ in Ar/CO_2 for different CO_2 concentrations and standard conditions. Output from Magboltz.

the molecule and the electric field. Fig. 2.13 shows simulated values of η as function of the electric field in a Ar/CO_2 (70/30) gas mixture.

2.2.2 Charge Multiplication

If the electric field is increased to values above few kV/cm, more and more electrons start to have enough energy to scatter inelastically with the gas via excitation and ionization processes. Molecules and atoms have many excitation modes, increasing in number and complexity with the atomic number and the molecule dimension. Noble gases usually de-excite through the emission of characteristic photons, while polyatomic molecules can return to ground state through non radiative processes like rotational or vibrational transitions. Therefore, the addition of polyatomic molecules in gas mixture as quencher is useful to dissipate part of the electron energy without the creation of photons or ions. This allows to reach high gain and operation stability in proportional counters. At higher fields, the excitation cross sections decreases in favour of the ionization one. The latter produces an electron-ion pair, creating a new electron that now move under the effect of the electric field. If the ionization interaction length is small with respect to the gas thickness, a chain reaction occurs where the new freed electrons extract even more electrons from the atoms. The creation of such electrons-ions avalanche is the basic mechanism of the signal am-

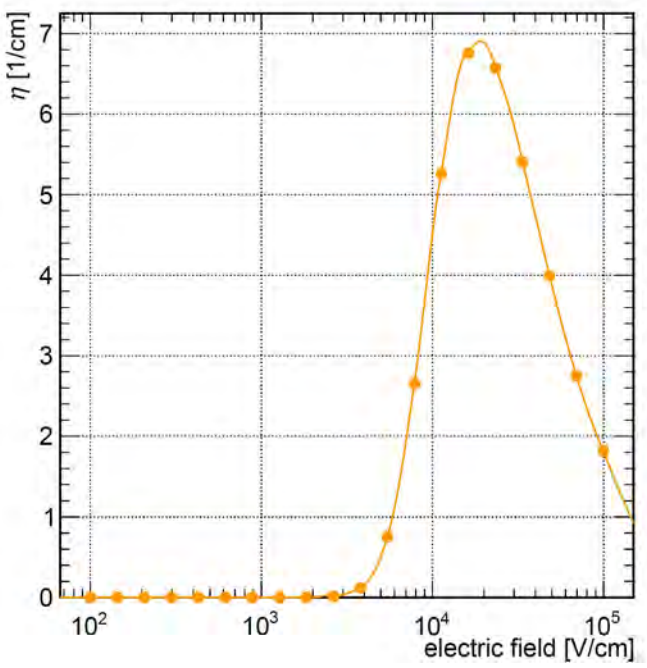

Figure 2.13: Simulated values of electron attachment as a function of the electric field in Ar/CO_2 (70/30). Output from Magboltz.

plification in proportional counters. Interaction cross sections for electron and molecules or atoms may be found in literature and they are usually implemented in the simulations tools, examples for Argon and CO_2 were given in the previous section in Fig. 2.11. Tab. 2.4 summarizes some of the processes that can occur after an inelastic collision and mostly affect gaseous detectors. Depending on the gases and fields, the probabilities of such processes may vary and some of them may not be energetically allowed. A detailed description of these processes can be found in [58, 59].

As already mentioned, the main mechanism behind the electron multiplication is the secondary ionization of atoms and molecules produced by primary electrons with sufficient energy. The ionization cross section rapidly increases above a threshold, usually some tens of eV, up to its maximum at around 100 eV (see for example Fig.2.11). The ionization mean free path λ_i can be defined as the average distance an electron have to travel to have an ionization scattering with a target atom or molecule. Its inverse $\alpha = 1/\lambda_i$ is the first Townsend coefficient, it represents the number of electrons-ions pairs created per unit path and can be written as:

$$\alpha = N\sigma_i,$$

where N is the number density of the gas and σ_i the ionization cross section. Some considerations about the α behaviour as a function of the ratio E/ρ

Process	Initial	Final
Excitation	A+e	A^*+e
Ionization	A+e	A^++e+e
De-excitation	A^*+e	A+e
Photo-excitation	A+hν	A^*
Photo-ionization	A+hν	A^++e
Photo-emission	A^*	A+hν
Electron capture	A+e	A^-
Radiative recombination	A^++e	A+hν
Excimers formation	A^*+A+A	A_2^*+A
Radiative excimer dissociation	A_2^*	A+A+hν
Collisional de-excitation	A^*+B	A+B^*
Charge exchange	A^++B	A+B^+
Penning effect	A^*+B	A+B^++e

Table 2.4: Major processes in electron and ion–molecule collisions; A and B designate two atoms (molecules), A^*, B^* their excited states and A^+, A^-, B^+ the corresponding ions [35].

or E/N will be given in Sec. 3.2.2. As an example, Fig. 2.14 shows the first Townsend coefficient simulated in Ar/CO_2 (70/30) at various electric fields and at standard conditions. If n is the number of electrons present at a certain position x, the infinitesimal number increase dn over a path dx can be written:

$$dn = \alpha(x) n dx.$$

By integration the multiplication factor, i.e. the gain, is obtained:

$$G = e^{\int_{x_{in}}^{x_{fin}} \alpha(x) dx}, \tag{2.12}$$

where x_{in} and x_{fin} are the spatial limits where the avalanche multiplication occurs. If the electric field and the gas density can be assumed constant in the range $[x_{in}, x_{fin}]$ the gain becomes simply:

$$G = e^{\alpha x},$$

with x the effective avalanche path. For GEM based detectors this assumption can be used to make qualitatively calculations.

2.2.2.1 Avalanche Statistics

In the previous part the average avalanche development was discussed following the definition of the α coefficient. However, dispersions around the

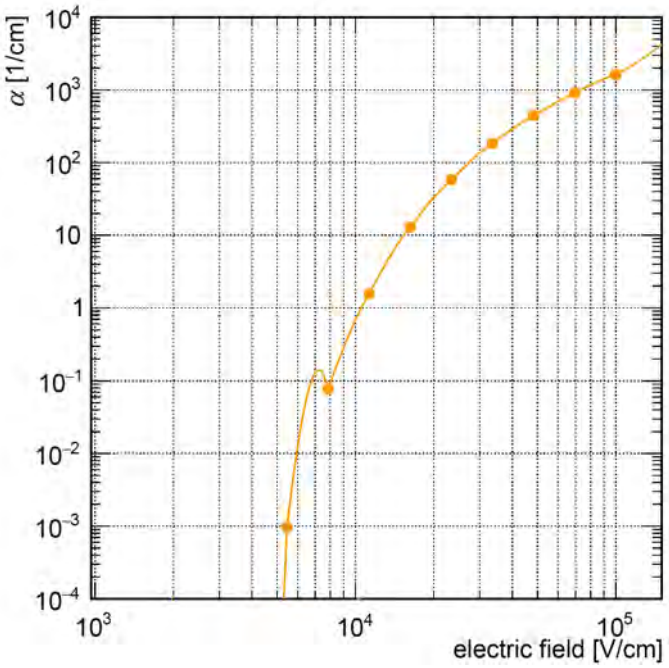

Figure 2.14: Simulated values of the first Townsend coefficient as a function of the electric field in Ar/CO_2 (70/30). Output from Magboltz.

average are generated because of the avalanche statistics. The probability of having n electron in the avalanche after a path s $P(n, S)$ can be estimated in the case of a uniform field (proper averaging is needed in more complex configurations [60]). If an avalanche is started by a single electron, its probability to not ionize any atom in the path s is:

$$P(1, s) = e^{-\alpha s}.$$

The probability that there is only one ionization in the same path is:

$$P(2, s) = e^{-\alpha s}\left(1 - e^{-\alpha s}\right).$$

Then, iterating, the probability to have n electrons is:

$$P(n, s) = e^{-\alpha s}\left(1 - e^{-\alpha s}\right)^{n-1}. \tag{2.13}$$

Since the avalanche is started by only one electron, the average number of electrons after a path s is $\bar{n} = e^{\alpha s}$ so the previous equation becomes:

$$P(n, s) = \frac{1}{\bar{n}}\left(1 - \frac{1}{\bar{n}}\right)^{n-1} \approx \frac{1}{\bar{n}} e^{-\frac{n}{\bar{n}}}, \tag{2.14}$$

The last approximation is valid for $\bar{n} \gg 1$ and it's usually referred to the Furry's law. Therefore, the distribution of avalanche size started by one

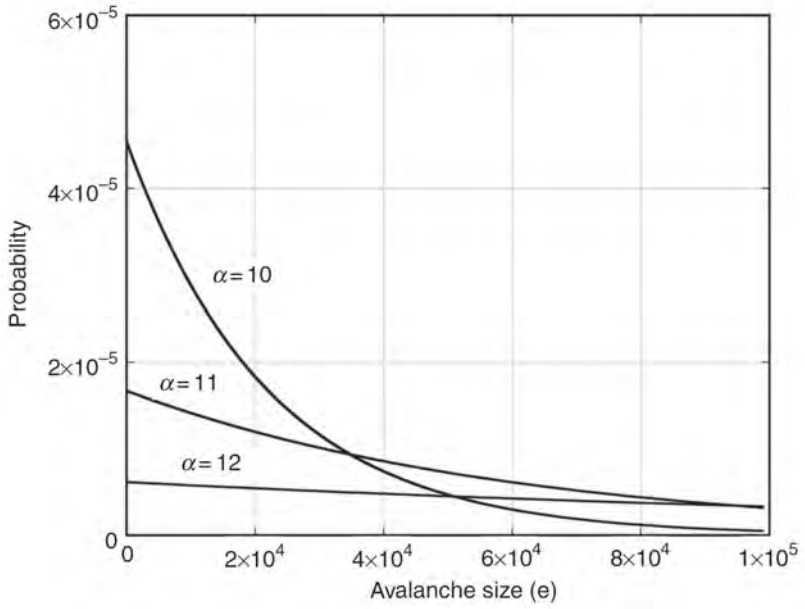

Figure 2.15: Avalanche size probability for several values of the Townsend coefficient [35].

electron is exponential having the maximum probability at not having any ionization at all. Fig. 2.15 shows the distributions for different values of the α coefficient in a unitary length. Such distribution has variance and mean equal to the avalanche size $\bar{n}$.

If the avalanche is started by N electrons, a convolution of N independent exponentials gives the distribution:

$$P()n, N) = \frac{1}{\bar{n}} \left(\frac{n}{\bar{n}}\right)^{N-1} \frac{e^{-n/\bar{n}}}{(N-1)!}, \tag{2.15}$$

where $\bar{n}$ is still the average avalanche size for one electron. The average is $N\bar{n}$ and the distribution is functionally equivalent to a Poisson in the variable $n/\bar{n}$. Fig. 2.16 shows the computed probability density at fixed gain for different primary electrons numbers. It is clear that if N is sufficiently large ($N \gtrsim 10 \div 20$), the distribution converges to a Gaussian with same mean and variance $\sqrt{\bar{n}N}$, as for Poisson distributions. Therefore, for this work purpose, supposing the avalanche size distributed as a Gaussian is a good approximation, since the number of primaries in CMS triple-GEMs is never below $\simeq$30.

2.2.2.2 Streamer Formation and Breakdown

The multiplication factor in a gaseous detector cannot be increased arbitrarily. The secondary ionization processes emit photons that may spread

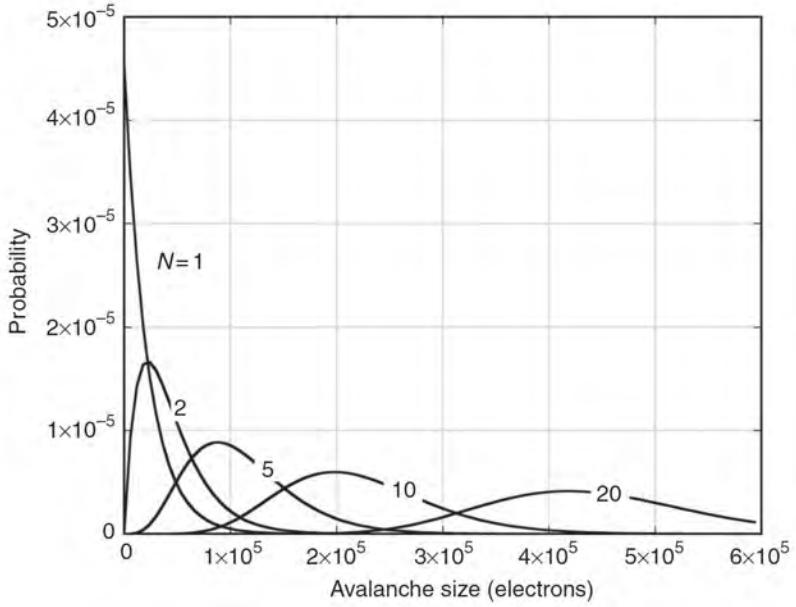

Figure 2.16: Avalanche size probability distributions for increasing values of the number of primary electrons [35].

the charge along the whole gas volume. The charge escalation, at a certain point, will distort the electric field in the neighbourhood of the avalanche, in particular in front and behind the charge cloud, leading the transition from an avalanche to a streamer or a spark. Fig. 2.17 is helpful to qualitatively understand the transition. The large charges developed during the

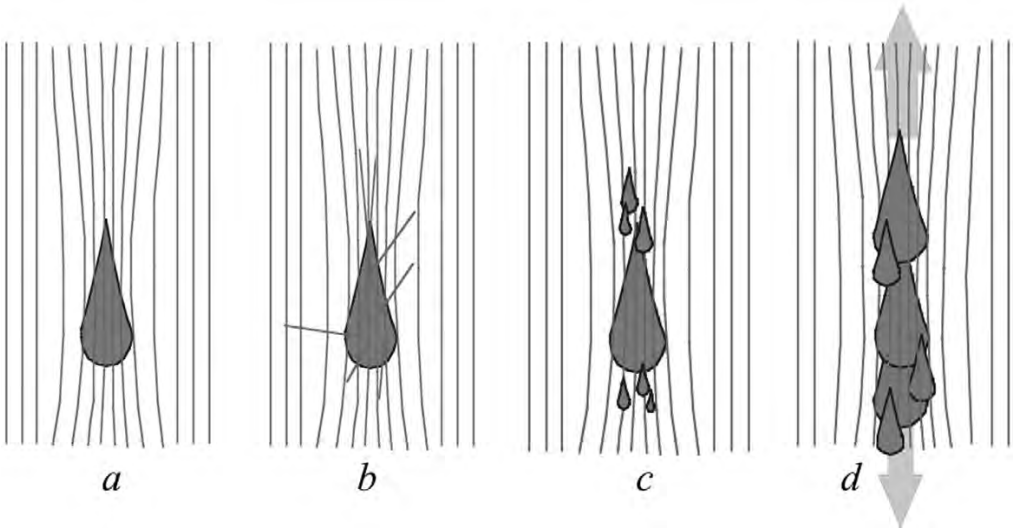

Figure 2.17: Schematic representation of the transition from avalanche to streamer [35].

avalanche lead to an increase of the electric field in front and behind it (a). De-excitation photons, that are emitted isotropically, generated secondary ionizations (b) that lead to other avalanches in the higher field regions (c). The process continues along the avalanche longitudinal direction (d). If not quenched, the streamer propagates through the entire detector volume leading to a spark breakdown because of the conducting path created between the electrodes. The Reather's limit gives an empiric value of the multiplication factor ($\alpha x < 20$) at which the transition starts to become not negligible [61].

2.3 Gaseous Detectors Technologies

This section will provide a semi-historical overview of some of the major detector technologies developed and used particularly for MIP detection. Also other aspects useful for this work purpose about detector physics will be given.

2.3.1 Parallel Plate Counters

Parallel plate counters consist of two spaced apart planar electrodes, filled with gas, where a voltage difference is applied. For moderate fields, the primary charge released by an incoming particle will drift through the electrodes following the field lines. Considering only a positive charge placed in the gap, it is clear that a charge density profile is induced on both the electrode. Fig. 2.18 shows an example of the charge profile induced by a positive ion in two different positions. If the ion approaches the cathode it

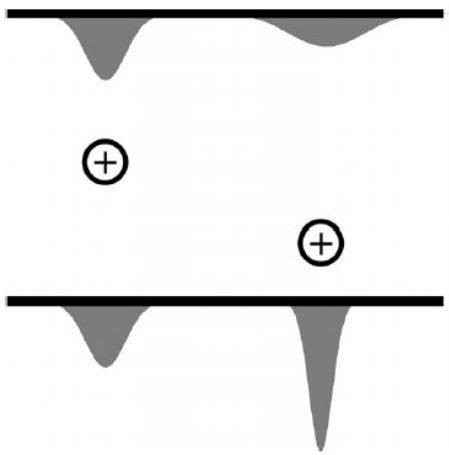

Figure 2.18: Profiles of charges induced on electrodes by a two charge in different positions. [35].

will move its surface charge resulting in a signal if readout on a load. In general a golden rule can be given: "A positive charge moving towards an electrode generates an induced positive signal; if it moves away from the electrode, the signal is negative and similarly for negative charges, with opposite sign" [35].

Ramo and Shockley [62, 63] developed a method to compute the induced signal for charges moving toward electrodes. The instantaneous current induced on an electrode by a single charge e moving at speed v can be written:

$$i = E_v e v, \tag{2.16}$$

where E_v is the so called weighting-field i.e. the electric field that would exist at the electron's position with that electron removed, the electrode raised to unit potential and all other electrodes grounded. Electrostatic theory can be used to calculate the induced signals expected in different geometries [64]. In general, for complex geometries, it is often more useful to solve the problem numerically [65].

For simple parallel electrode geometry, the induced signal functional form can be obtained from the energy conservation principle. Assuming, like before, a single charge in a gap with s_0 thickness, the work done by the field to move the charge Q by an infinitesimal path ds is equal to the change in the electrostatic energy stored in the system. The infinitesimal increase in the induced charge dq can be written [66]:

$$dq = Q\frac{dV}{V_0} = Q\frac{ds}{s_0}, \tag{2.17}$$

where s_0 is the position where the charge is created and V_0 the initial voltage difference. Being the charge drift velocity w, the induced current can be written:

$$i = \frac{dq}{dt} = \frac{Q}{ds}\frac{ds}{dt} = \frac{Q}{s_0}w.$$

The charge time dependency is then:

$$q(t) = \frac{Q}{s_0}wt, \tag{2.18}$$

the signal stops when the charge reaches the electrode. Then it's clear that the total induced charge on the electrode if the charge is created in position s is:

$$q = Q\frac{s}{s_0}, \tag{2.19}$$

that reduces to $q = Q$ if the charge drift through all the gap.

If two charges with opposite sign Q and $-Q$ drift along the field, e.g. in the case of a ionization in the gas, Eq. 2.18 can be written as:

$$q(t) = Q\frac{w^+ t}{s_0} + Q\frac{w^- t}{s_0}, \tag{2.20}$$

where w^+ and w^- are the drift velocities of the two charges. In this case the global charge induced after the whole drifting is $q = Q$, independent from the starting position. However, due to the large drift velocity difference between electrons and ions (three order of magnitude), the arrival time of the ions signal is way larger.

It is important to notice that usually the induced signal is readout on a load, hence a voltage $V(t) = q(t)/C$ is measured; then the lower the capacitance, the higher the induced voltage. For a parallel plate thickness of 1 mm and 100 cm^2 area filled with gas ($\epsilon_r \simeq 1$), a charge of some tens of electrons produces signals of the order of the µV. It is clear that, due to the intrinsic difficulty of detecting such small signals, an amplification is needed. Applying a sufficient electric field the charges starts to multiply in the gas, giving rise to an exponential increase of the charges drifting. Being n the number of electrons after an avalanche path s:

$$n = n_0 e^{\alpha s},$$

Eq. 2.17 can be rewritten:

$$dq^- = e n_0 e^{\alpha s} \frac{ds}{s}.$$

When integrated, it provides the induced charge after a path s:

$$q^-(s) = \frac{e n_0}{\alpha s_0} \left(e^{\alpha s} - 1\right) \simeq \frac{e n_0}{\alpha s_0} e^{\alpha s}. \tag{2.21}$$

Since the avalanche development is much faster than the ions collection time, the induced ion signal is very similar in shape, but not in amplitude.

It is clear that the response of a Parallel Plate Avalanche Counter (PPAC) depends on the primary ionization position of the impinging particle, this makes the avalanche size not proportional to the initial charge. However, for extended tracks, it can be demonstrated [35] that the collected charge maintains the proportionality with the initial charge.

The main limitation of PPACs is their tendency to discharge at high gain, that can irremediably damage the detector and the readout electronics, due to the very large amount of energy stored on the electrodes. An effective way to reduce this problem is the use of resistive electrodes, that dump the discharge thanks to the large current flowing through them. A structure capable of working at high gain while reducing the discharge propagation is often called spark counter. Many detectors were build with this principle reaching good energy resolution and timing performance [67–69].

Resistive Plate Chambers (RPCs) are the natural evolution of spark counters. Using phenolic polymer laminates as high-resistivity electrodes, large areas detectors can be build and operated to detect muons in high

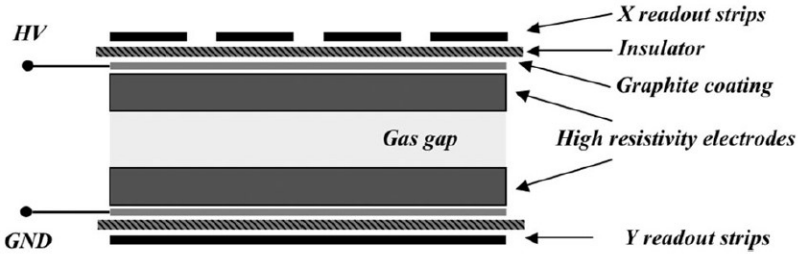

Figure 2.19: Schematic view of a resistive plate chamber.

energy physics experiments. Fig. 2.19 shows a schematic view of a typical single gap RPC. With gas thicknesses of order of mm operated with a quenched Argon gas mixture, RPCs can achieve full detection efficiency and time resolution of the order of ns [70, 71]. When an intense electric field is applied on the gap, the charge released by an impinging particle is multiplied due to the avalanche process. Because of the field geometry, the ionizations occurring near the cathode are the ones that give the larger amount of signal. When the number of electrons in the avalanche reaches $10^6 \div 10^7$ the exponential growth of the signal is stopped due to the large space charge within the avalanche, and this leads to the saturated avalanche regime. At even higher fields the avalanche transits to a streamer. In general the bigger limitation of RPCs is the rate capability, the local voltage drop due to the large induced current on the high resistivity electrode usually recovers in relatively long time. This effect is even more accentuated if an RPC is operated in streamer mode. Fig. 2.20 shows the muon detection efficiency of an RPC operated both in avalanche and streamer mode.

2.3.2 Wire Chambers

As already mentioned, the main limitation of the parallel plate technology is the non linearity between the deposited charge and the induced signal because of its dependency on the avalanche starting point. Furthermore, the Raether condition can be occasionally achieved because of the large fluctuation in the gain, leading to discharges. These limitations can be overcame if using a coaxial cylindrical geometry (it was used first in [73]). Using a conductive wire stretched along the axis of a metallic cylinder, a radial dependent electric field can be generated applying an opportune voltage difference. Using a wire with radius a ($V(a) = V_0$) inside a cylinder with radius b ($V(b) = 0$) the electric field developed inside the volume as a function of the distance from the wire can be written:

$$E(r) = \frac{CV_0}{2\pi\epsilon_0}\frac{1}{r}, \tag{2.22}$$

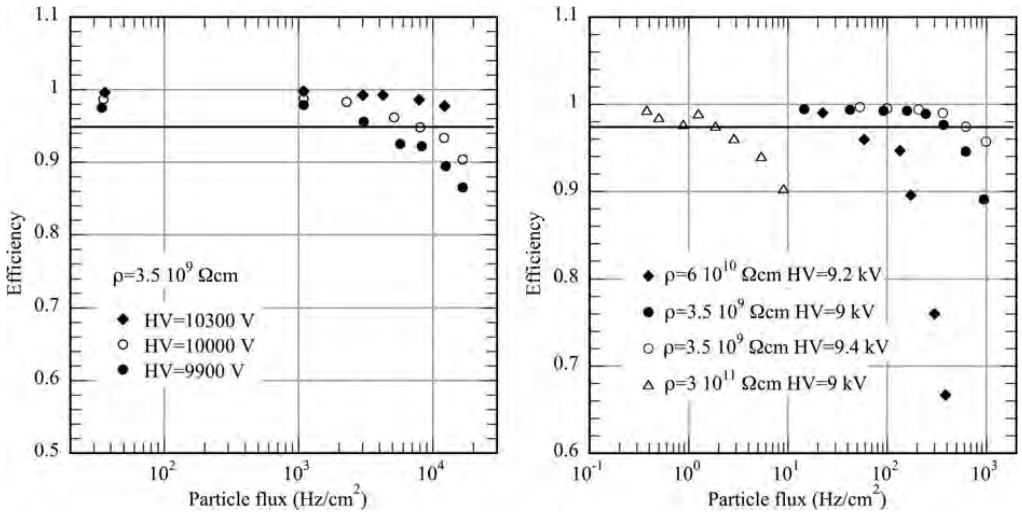

Figure 2.20: RPC efficiency as a function of particle flux and voltage in the avalanche (left) and streamer modes (right) for several values of bulk resistivity [72].

where C is the capacitance per unit length of the chamber:

$$C = \frac{2\pi\epsilon_0}{\ln b/a}.$$

Fig. 2.21 shows a transverse view of a cylindrical wire tube with the electric field dependency. The $1/r$ dependence of the field makes easy to distinguish

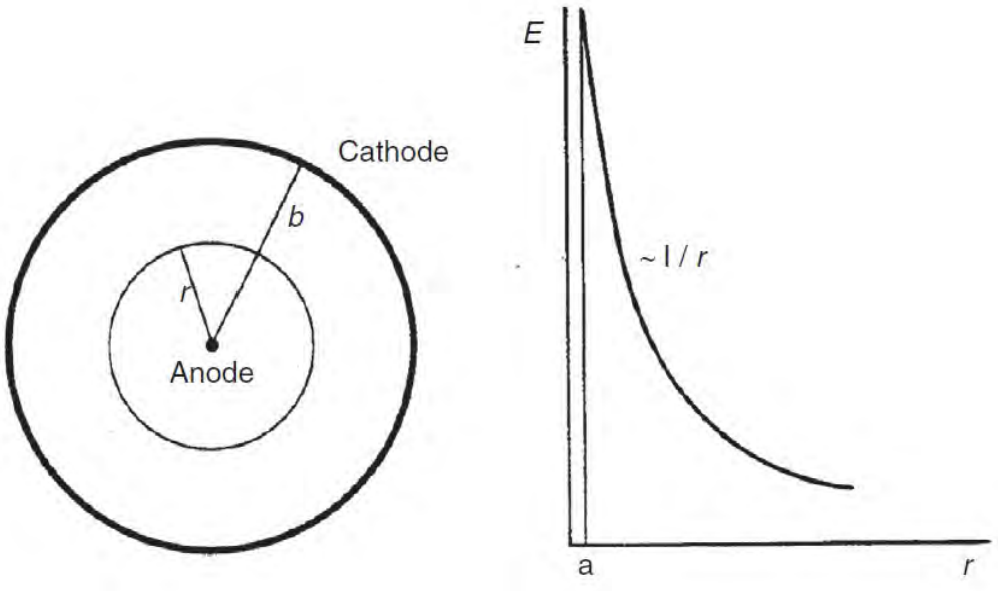

Figure 2.21: Schematics of a proportional counter and its field.

a region of low field, where the charges just drift in the gas and a region of high gain, near the anode. This region is where the amplification takes place and the signal is formed, usually it is around some wire radii near the anode. This removes the dependency of the signal on the ionization position since now the charges are collected and multiplied only near the anode. Fig. 2.22 shows an usual avalanche development in a cylindrical wire chamber near the anode. It can be demonstrated that, differently

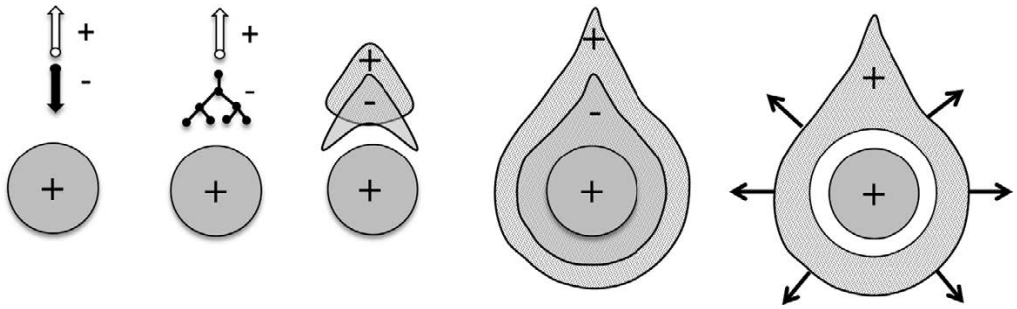

Figure 2.22: Avalanche growth around a thin wire.

from the parallel plate geometry, the signal induction is mainly due to ions drifting in the high electric field region [35, 41].

Fig. 2.23 shows the charge collected from a cylindrical tube as a function of the applied voltages for two different irradiating sources. If the voltage is too low, recombinations take place and no charge is collected. At higher electric fields the whole primary charge is efficiently drifted and the chamber is said to operate in ionization chamber mode. If the field is high enough to start the avalanche process, the charge is multiplied and the latter grows exponentially with the voltage. At very high voltage, formation of streamers appears. However, differently from the parallel plate geometry, the backward propagation of secondary ionization is disadvantaged due to the radial dependency of the field. In this region the signals lose proportionality with the deposited charge, giving always similar signals. Increasing again the field, and in case of poorly quenched gases and/or low pressure, a different mechanism is observed [75]. The huge number of photons created during the avalanche spreads along the whole detector volume and starts a chain reaction that fills the detector with charges until the effective field is extinguished below the multiplication threshold. This mechanism can lead to $10^9 \div 10^{10}$ electrons collected starting from a small primary ionization, obviously without any proportionality.

Single Wire Proportional Chambers (SWPC) are widely used for many application, but one of their limitation is the spatial resolution dictated by the detector size itself. A natural solution for this problem comes with the Multi Wire Proportional Chambers (MWPCs), a set of equally spaced anodic wires that share the same gas volume (see Fig. 2.24). Closing such

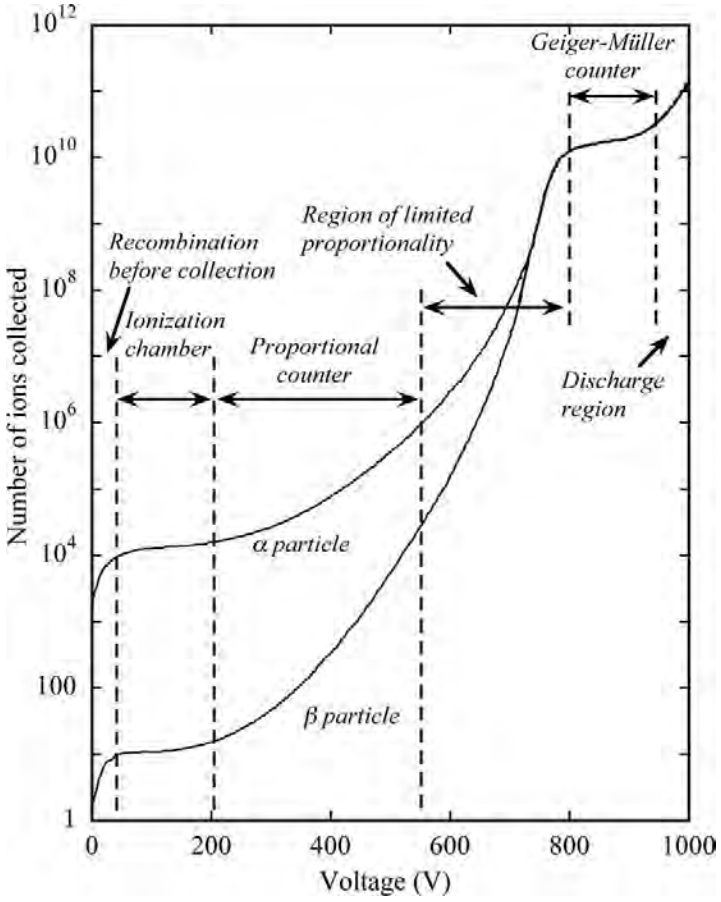

Figure 2.23: Voltage dependence of detected charge in a proportional counter [74].

wires between two cathode planes and applying the correct voltage the field will acquire a shape as displayed in Fig. 2.25, with a drift region near the cathode and an amplification region near the anode. Electric field functional form can be deducted form electrostatic theory [76–78], using the notations in Fig. 2.24:

$$E(x,y) = \frac{CV_0}{2\pi\epsilon_0}\left(1+\tan^2\frac{\pi x}{s}\tanh^2\frac{\pi y}{s}\right)^{1/2}\left(\tan^2\frac{\pi x}{s}\tanh^2\frac{\pi y}{s}\right)^{-1/2}, \tag{2.23}$$

where V_0 is the voltage difference between anode and cathode and C the capacitance per unit length:

$$C = \frac{2\pi\epsilon_0}{\frac{\pi l}{s} - \ln\frac{2\pi a}{s}}.$$

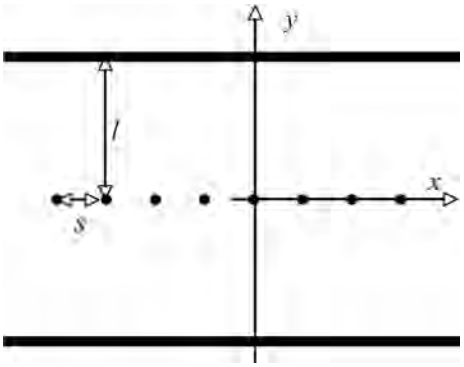

Figure 2.24: Schematics of a Multi Wire Proportional Chamber.

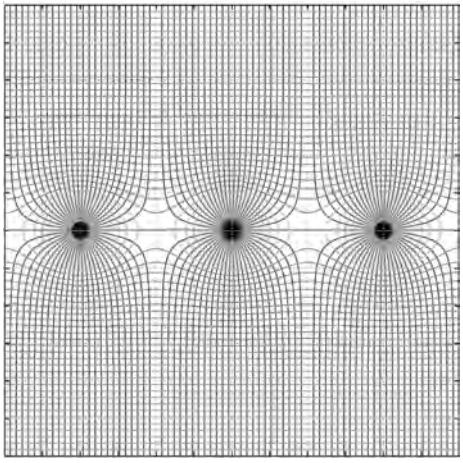

Figure 2.25: Field lines and equipotentials near the anode wires in the MWPC.

2.3.2.1 Space Charge Effects

The multiplication process near a wire creates a layer of ions slowly drifting through the cathode (see Fig. 2.22). Such ions lower the effective electric field until they are absorbed by the cathode, usually after some hundreds of µs. Generally, in proportional mode, the field lowering effect affects only the small amplification region near the anode. A lower field will produce a lower amplification factor, following the trend showed in Fig. 2.23. Fig. 2.26 shows an example of the gain behaviour under heavy irradiation for a wire based detector. It is possible to approximate the particle rate effect on the anodic potential V_0 [80]. Being R the rate of ionizations that create $n_0 Ge$ charges during the avalanche, the voltage drop can be written:

$$\Delta V = KGR \quad K = \frac{n_0 e T^+}{4\pi^2 \epsilon_0},$$

where T^+ is the global collection time for positive ions. Since the gain is exponential in the proportional region, its drop from the low rate value G_0 will be:

$$G = G_0 e^{\Delta V}.$$

Thus replacing:

$$\Delta V e^{\Delta V} = K G_0 R. \tag{2.24}$$

For small voltage variation the approximation is valid:

$$G = G_0 e^{-K G_0 R} \tag{2.25}$$

Other similar dissertations are found in [81–83]. For MWPC a modern mathematical formulation is presented in [84].

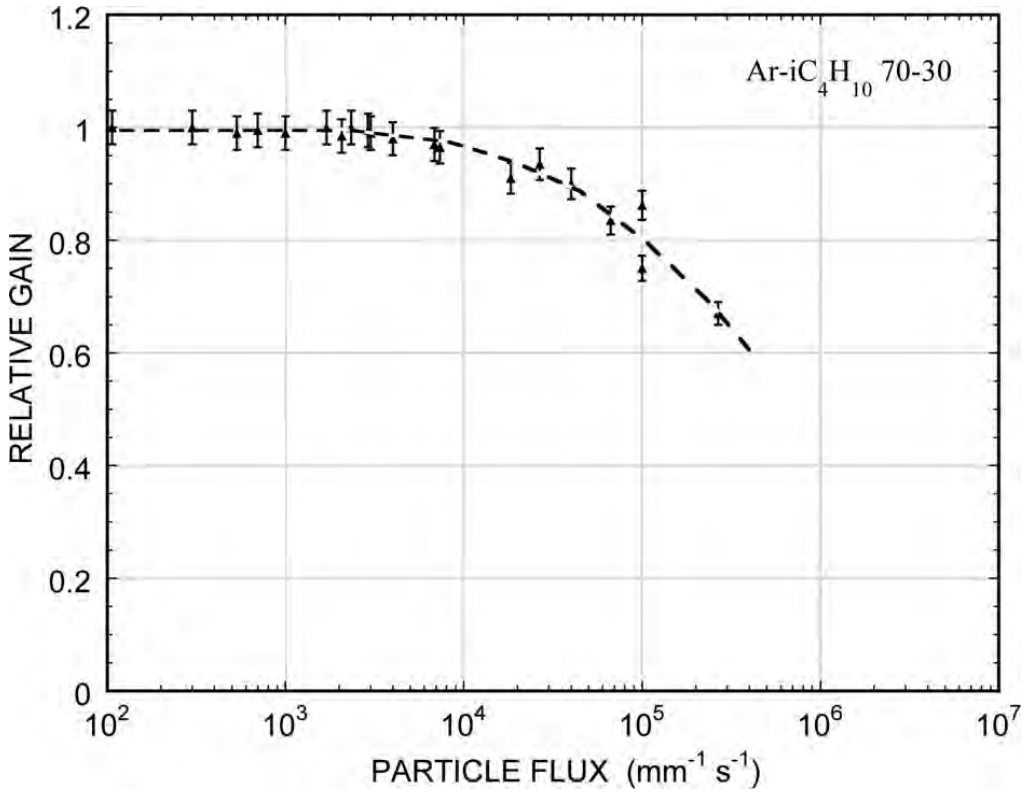

Figure 2.26: Relative gain as a function of rate measured with a drift chamber, normalized to the flux per unit wire length [79].

The space charge effect is still one of the main limitations in using wire based detectors for high rate applications. Because of the relatively long drift time of ions, only micro-pattern structures can efficiently and quickly remove the ions produced during the avalanche.

2.3.3 Micro Pattern Gaseous Detectors (MPGDs)

Micro Pattern Gaseous Detector (MPGD) is a family of detector technologies that exploits the novel techniques in miniaturization and photolithography to create small amplification structures (order of tens or hundreds of µm) to achieve high granularity and fast charge collection. A set of such technologies will be briefly described.

2.3.3.1 Micro Strips Gas Counter (MSGC)

The first attempt to overcome the large ions collection time in wire-based structure came from the Micro Strips Gas Counter (MSGC) [85]. It consists in a set of thin parallel metallic strips on a insulating substrate. The strips

are alternately narrow (tens of µm) and wide (hundreds of µm) respectively connected as anodes and cathodes (see Fig. 2.27). The detector is closed

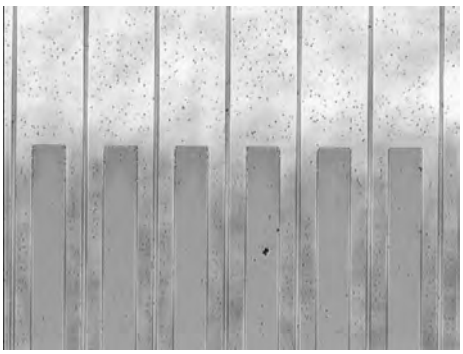

Figure 2.27: Close view of an MSGC plate, with narrow anodes alternating with wider cathode strips [85].

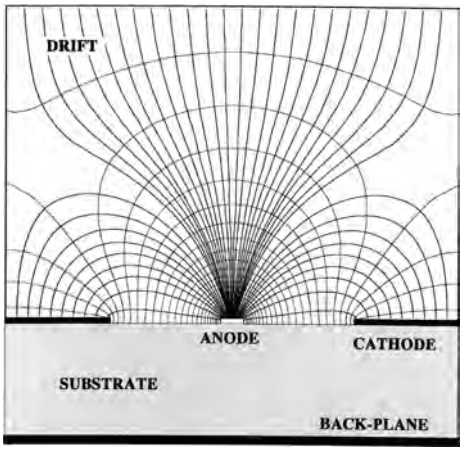

Figure 2.28: MSGC electric field in the vicinity of the strips.

with a cathode plane on the upper side. With this configuration, a drift region is defined far from the strips, with the field increasing in value near the anodic strips to let electrons multiply. All the field lines close on the anode allowing a good collection efficiency, during the multiplication the ions are rapidly collected on the nearby cathode strips, reducing their effect on the field distortion.

MSGCs are supposed to work nicely in high rate environment for the reasons explained before. However, a set of instabilities in operation make them challenging to use; a dedicated international collaboration was established to develop and engineer this technology [86]. First of all, the charging up and polarization of the substrate may cause electric field distortion. This effect is strongly dependent on the materials used and huge effort was made to have reliable substrate to operate MSGCs in high rate environments. Fig. 2.29 shows the gain of a MSGC as a function of the hit rate for different substrate materials. Moreover, the thin structure of the detectors made them exposed to discharges. It was observed that detectors operating well under high intensity X-rays beams experience instabilities and damages when irradiated with Heavy Ionizing Particles (HIPs) [88–90]. Discharges are caused by huge releases of primary charges that, when multiplied, can overcome the Reather limit; the relatively high amplification factor needed for MIPs detection provokes a higher probability to have the limit overtaken for larger energy deposit. Improvements were made by passivating the electrodes or depositing a thin resistive layer on them. The small dimensions and the high electric fields are also a problem from the aging points of view for MSGCs, the issue will be described in Sec. 5.1.

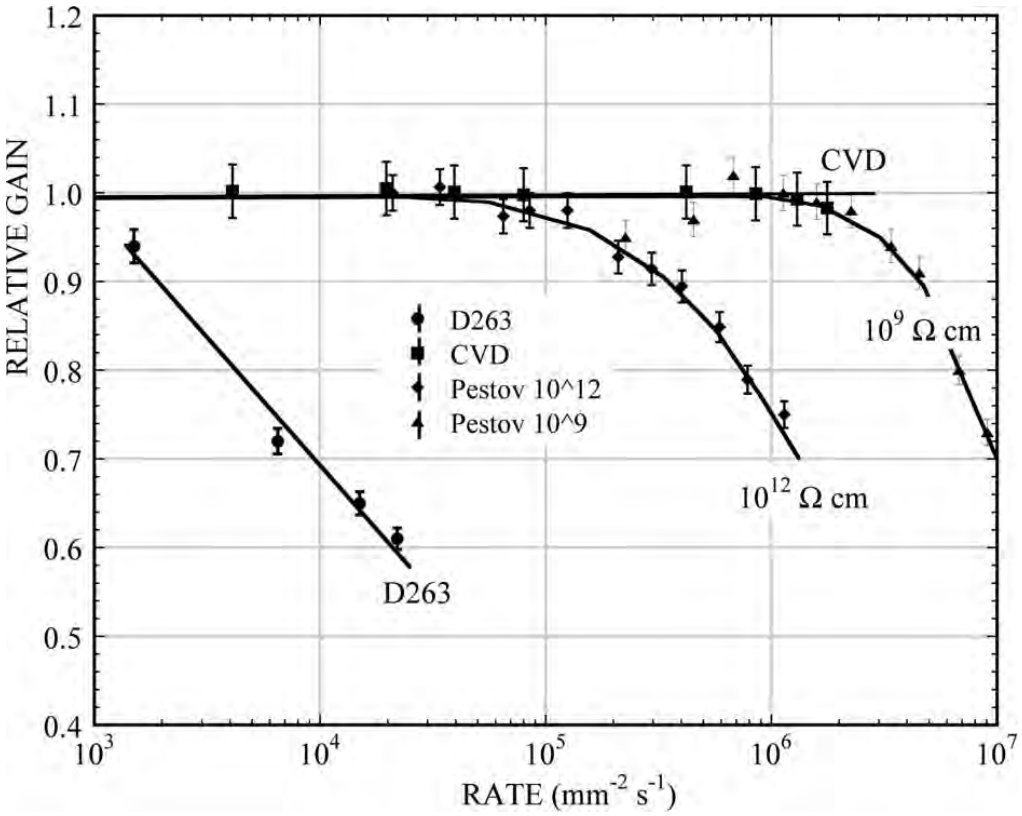

Figure 2.29: Rate dependence of normalized gain for different MSGC substrates [87].

These problems triggered in the community the will to develop alternative structures to overcome the limits of MSGCs. An overview of such technologies is given in [91]. Extended knowledge on the subject gave the opportunity to the rise of two main technologies: the Micromegas and the GEM.

2.3.3.2 MIcro MEsh GAseous Structures (MICROMEGAS)

In the previous sections, the limitation of the parallel plate geometry were discussed. However, Micromegas were firstly developed starting from the observation that, in sub-mm gaps, high gains can be achieved with small sensitivity on the gap variations and imperfections because of the saturation of the Townsend coefficient. The first concept of such detector was presented in [92] and it is shown in Fig. 2.30. In a parallel plate geometry, a micro-mesh structure separates the gap in two regions where different fields can be applied. Insulating pillars are often used to stabilize the distance between the mesh and the anode. In the upper, large regions (some mm) a relatively low electric field is applied to drift the primary ionization charge;

the thinner region is where the amplification happens with electric fields up to 100 kV/cm. Fig. 2.31 shows the electric fields lines in the proximity

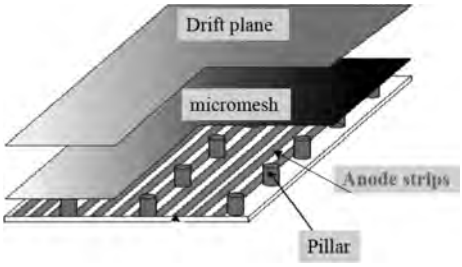

Figure 2.30: Schematics of the Micromegas construction, with insulating spacers across the multiplying gap [92].

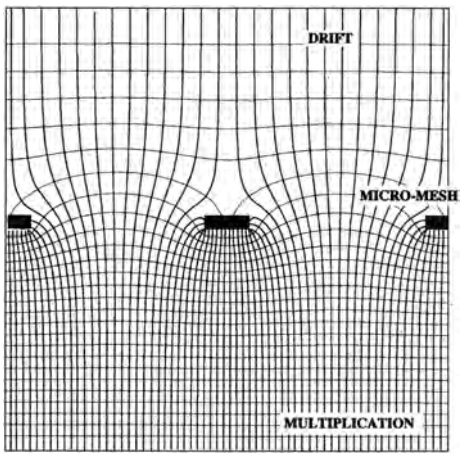

Figure 2.31: Electric field in the Micromegas [92].

of the mesh.

Because of the small gap and high electric field the electrons create a fast signal followed by a small ion tail. Example of a signal induced by soft X-rays is shown in Fig. 2.32. The positive charges are quickly collected on

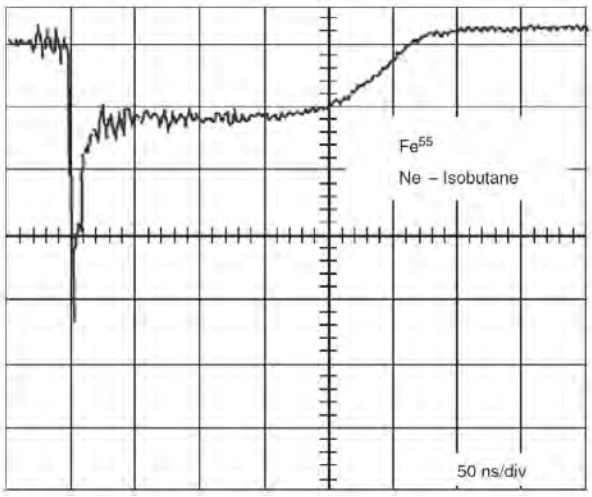

Figure 2.32: Fast signal detected on the anodes of Micromegas [93].

the mesh because of the large difference in drift and amplification fields, suppressing the ion backflow in the conversion gap. This leads Micromegas to maintain stable amplification factor also in high particles rate environments, Fig. 2.33 and 2.34 show the gain trend as a function of X-rays rate for different gas mixtures.

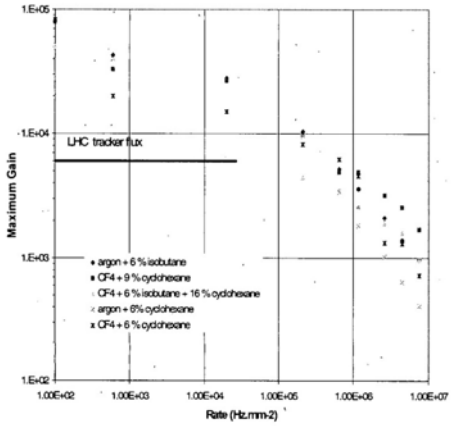

Figure 2.33: : Maximum of gain versus flux of X-rays (8 keV) for Argon and CF_4 based mixtures [94].

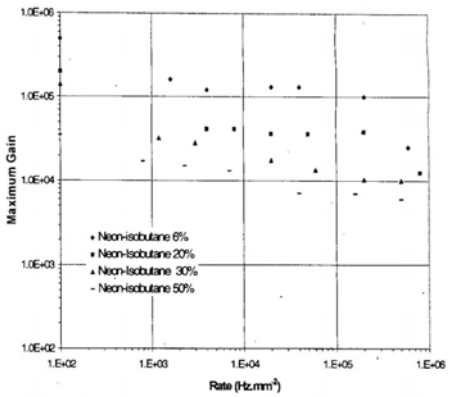

Figure 2.34: Maximum of gain versus flux of X-rays (8 keV) for Neon and Isobutane mixtures [94].

As all MPGDs, also MICOMEGAS are susceptible to discharges, and this issue is enhanced by the parallel geometry of the field. However, such detectors revealed to be relatively robust to the possible damages induced by sparks. The limitation factor is not any more the damage of the electrodes but the relatively long recovery time of the voltage after a discharge (order of ms) that introduces a large dead time in the operation. Studies were made to improve the gas mixture and geometry to reduce the discharge probability [93, 95] Another strategy is to deposit a resistive layer to insulate the anode from the amplification gap, as in the RPCs case. However, this procedure, as already discussed, may reduce the rate capability of such detectors [96].

2.3.3.3 Gas Electron Multiplier (GEM)

The Gas Electron Multiplier (GEM) is a thin polyimide foil (Kapton) Copper clad on both sides, chemically perforated with bi-conical holes (around $100\,\mathrm{mm}^{-2}$) [97]. Fig. 2.35 shows some details of typical GEM foils. GEMs are usually inserted in a parallel plate geometry with anode and cathode parallel to the foil. With an opportune tuning of the fields, the released charge in the upper drift region moves towards the GEM hole where it is multiplied. An extraction field drifts the multiplied electrons to the anode, where a signal is induced on an opportune anode pattern made by pads or strips. Fig. 2.36 shows field lines in a GEM detector.

It is clear that not all the primary electrons nor all the avalanche electrons proceed longitudinally. Indeed, because of some field lines closing on

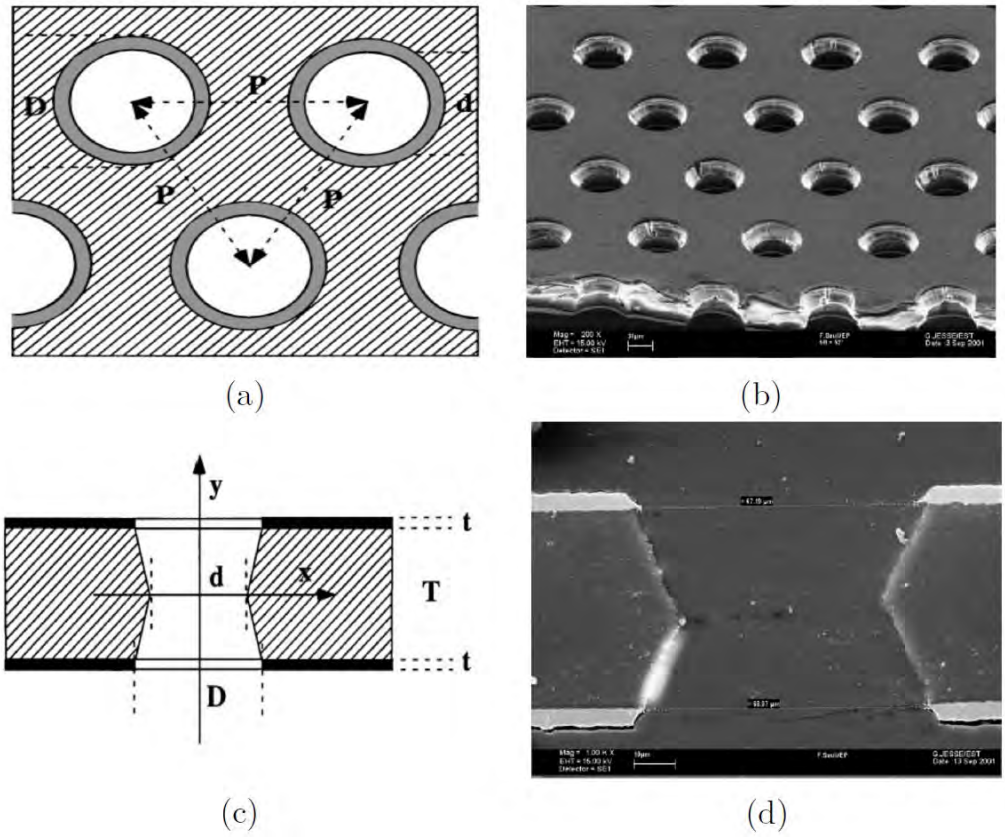

Figure 2.35: Schematic overview (a) and electron microscope picture (b) of a section of typical GEM electrode, $T = 50\,\mu m$ Kapton foil, clad on each side with a $t = 5\,\mu m$ Copper layer. The holes pitch is $P = 140\,\mu m$ and the external and internal diameter are $D = 70\,\mu m$ and $d = 50\,\mu m$, respectively. Schematic overview (c) and electron microscope picture (d) of the cross-section of a bi-conical hole of a GEM-foil [98].

the GEM sides, some charges are neutralized before or after taking part to the avalanche. It is useful to define the collection efficiency ϵ_{coll} as the number of electrons that enter the GEM holes divided by the number of primary electron; and the extraction efficiency ϵ_{extr}, i.e. the ratio between the avalanche size and the number of electrons proceeding through the anode. Therefore, the effective gas gain is lower than the intrinsic one due to the loss of a part of the charge. Being the ions mass much larger than the electrons one, it is clear that a large part of the positive charges produced in the multiplication are rapidly collected on the cathode GEM side. This fact guarantees low ion backflow and the possibility to operate the detector at very high fluxes without field distortion.

The manufacturing of a GEM takes advantage of the double-sided printed circuit technology. The metal clad polymer is engraved on both sides with

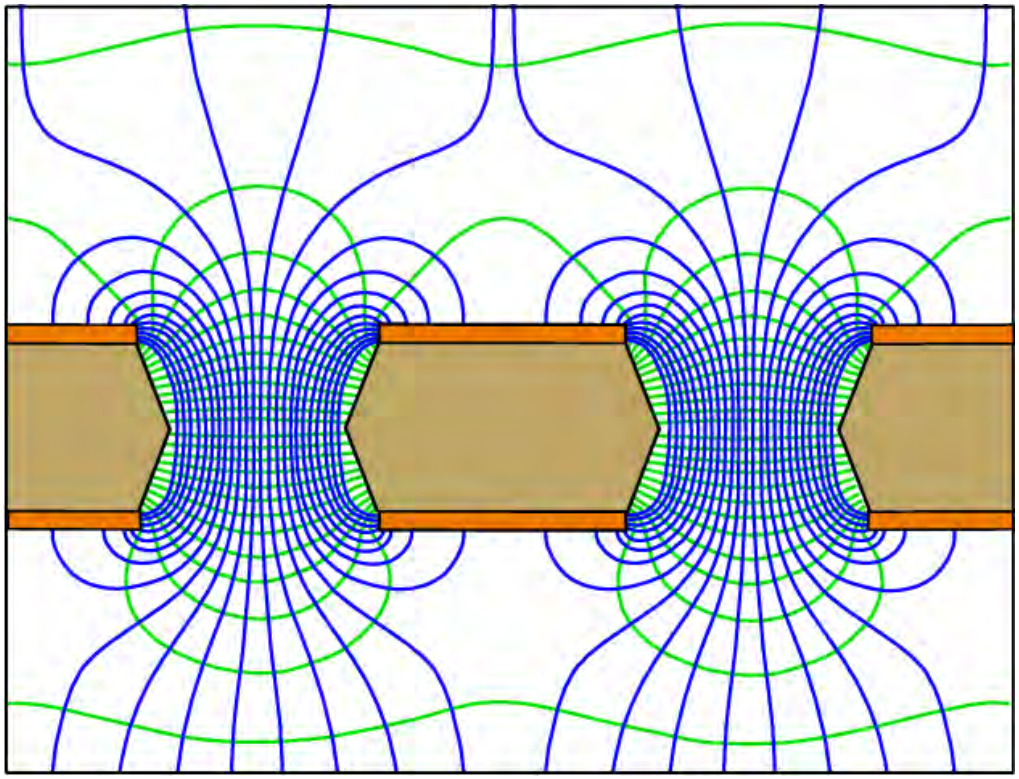

Figure 2.36: Typical electric field lines in a GEM detector.

opportune aligned masks and a chemical bath dissolves the excess Kapton leaving the desired holes. This technique is usually referred to as double-mask. However, for large area detectors, the masks' alignment can be tricky, so the so called single-mask technique reduces the defect due to misalignment. Fig. 2.37 shows the manufacturing steps of the two different procedure, a detailed description of the techniques is given in [99–101]. Single-mask technique usually produces foils with different holes diameters between the top and the bottom side. However, it was demonstrated that, if facing the smaller diameter holes toward the drift, no difference in operations are detected with respect to double-mask foils [102].

The intrinsic design of a GEM foil makes it suitable for stacked structures. Cascading multiple foils separated by low field transfer gaps, higher multiplication factors can be achieved with relatively low single GEM gains. In particular, the use of three GEM foils is a good compromise for efficient and safe detection of MIPs. Many studies were performed to optimize the triple-GEM structure [103–105]. From these studies results and from R&D performed within the CMS GEM group, the CMS triple-GEM will exploit a gap configuration of 3/1/2/1 mm with electric fields ratios as shown in Tab. 2.5. It is interesting to notice that the transfer gap between GEM2 and GEM3 is larger than the others to let the electron cloud diffuse more

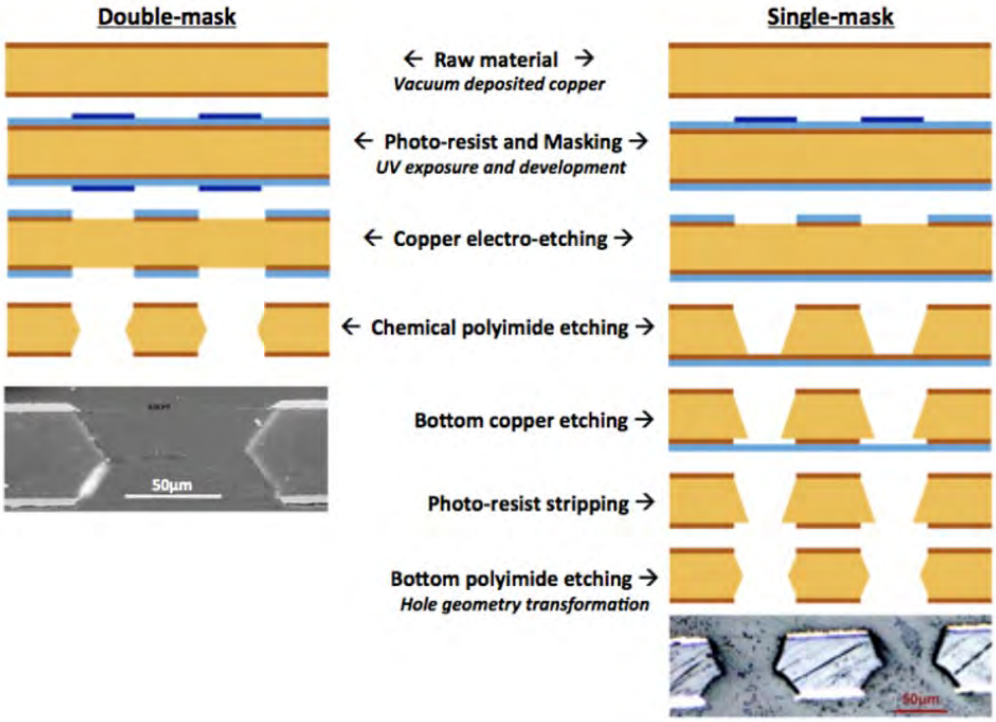

Figure 2.37: Schematic comparison of procedures for fabrication of a double-mask GEM foils (left) and a single-mask GEM foils (right) [99–101].

Gap	Relative Field Intensity
Drift	3.3×10^{-2}
GEM1	1
Transfer 1	3.9×10^{-2}
GEM2	0.98
Transfer 2	3.9×10^{-2}
GEM3	0.93
Induction	5.6×10^{-2}

Table 2.5: Normalized values (to the largest) of the electric field in the CMS GEM configuration.

before the final amplification steps. Indeed, a spreader cloud is less prone to overcome the Reather limit during multiplication. For the same reason, the electric fields across the three GEM foils are not the same, indeed the highest voltage is applied on the first foil and the field is reduced on GEM2 and GEM3. Extensive informations about the CMS GEM R&D campaign may be found in [46, 106–111].

Thanks to the absence of thin anodes, GEM detectors are rather insensitive to radiation damage induced by polymerization. Furthermore stacked GEMs structures share the global amplification reducing this effect as it will be discussed in Sec. 5.

Charging up The high resistivity of Kapton lowers the effective field inside the hole because of its polarization. This effect stabilizes itself after some time after the voltage is supplied, usually some RC time constant of the foils ($100 \div 1000$ s). When the detector is irradiated, some positive and negative charges attach on the inner hole Kapton surface because of its surface charge. This mechanism shields the effect of the Kapton polarization on the electric field increasing the latter. Fig. 2.38 shows the sketch of a GEM foil with the three contributions that play a role in the determination of the electric field in presence of charging up. An experi-

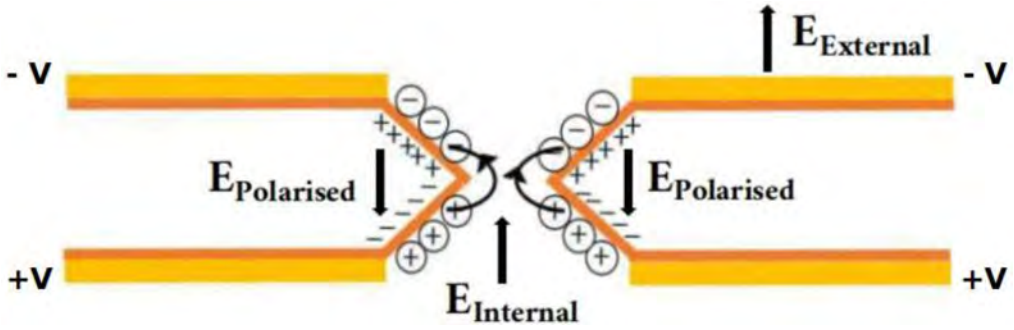

Figure 2.38: Schematic representation of the Charging up effect inside a GEM hole. $E_{polarised}$ indicates the electric field generated due to the dielectric polarisation. $E_{external}$ indicates the electric field generated due to the external high voltage and $E_{internal}$ indicates the electric field generated due to the accumulation of the charges on the Kapton wall [112].

mental work on the subject with some simulations attempts can be found in [112–114]. In general, when the HV and the irradiation are turned on at the same time, because of the charging up of the Kapton, a drop of the effective gain, that last only hundreds tens of s, is measured. When the Kapton is sufficiently charged, the attachment process on its surface takes over creating a local enhancement of the field and the gain. Fig. 2.39 shows an example of gain evolution of this type. After some irradiation time, the detector will stabilize to its nominal gain. The timing and the values of the gain variations may change a lot depending on the irradiated area, the hit rate, the working point etc.

Rate Capability A GEM proves to have a very high rate capability because of the fast ions collection near the production place on the top GEM

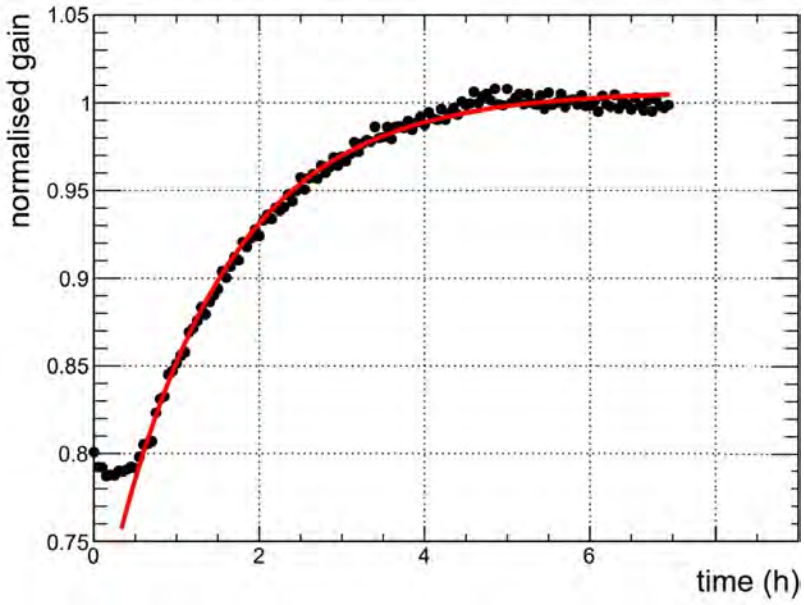

Figure 2.39: Variation of the normalised gain as a function of irradiation time with a 90 kHz X-rays beam impinging on a 28 mm^2 area. Data are fitted to obtain the rise time constant [112].

electrode. Fig. 2.40 shows a set of plots of the effective gain of a triple-GEM operating in Ar/CO_2 (70/30) at different nominal gains and gap configurations when irradiated with different X-rays fluxes. Despite some formal differences, the functional form of the gain behaviour is similar between the tests. In particular the gain remains stable up to $10^6 \div 10^7 Hz/cm^2$, then it starts to increase and at very high fluxes decreases. The fact that the gain increases with the flux is imputable to field distortions in the transfer regions between the drift cathode and the first GEM, and between the individual GEMs respectively. The electron collection and extraction efficiency of the GEMs, not being 100% under irradiation with low X-rays fluxes, are considerably increased at these fluxes [116]. At even higher fluxes the space-charge distorts the field inside the holes. This effect, along with the increased ion density on the top sides of the foils, reduces the effective gain.

These tests demonstrated the good behaviour of GEM detectors when used in high rate environments. However, it is important to notice that usually the high voltage is supplied with resistive chain and in general, for GEM stable operation, it is recommended to use additional protection resistor near the electrodes to quench discharges (see next section). This means that, irradiating a large detector, the non negligible currents induced on the electrodes can create a voltage drop across the resistors, hence reducing the effective voltage. In the next chapter the effect of large area

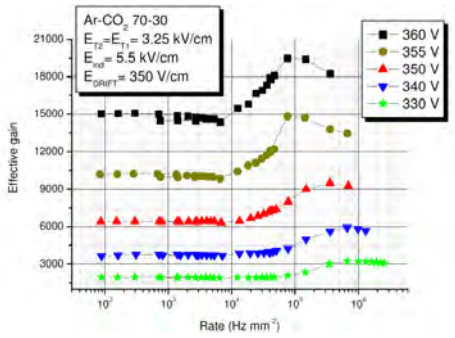

(a) Gap configuration 3/2/2/2 mm and different nominal gains [115].

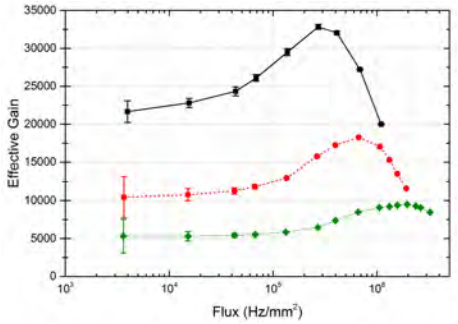

(b) Gap configuration 3/2/2/2 mm and different nominal gains [116].

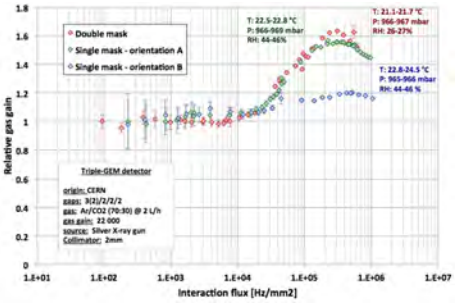

(c) Gap configuration 3/1/2/1 mm and different production methods and orientations [46].

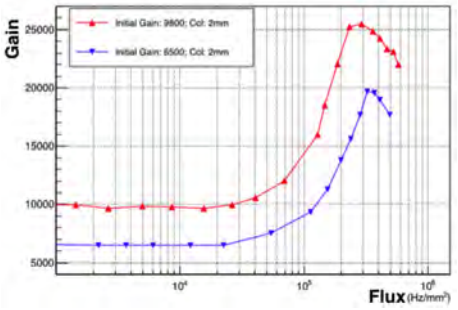

(d) Gap configuration 3/1/2/1 mm [117].

Figure 2.40: Triple-GEM gain evolution as a function of the X-rays flux in Ar/CO_2 (70/30).

irradiation, protection resistors, and filters will be analysed in detail.

Cathode Induced Signals Electrons travelling through the induction gap induce a signal both on the anode and on the GEM side they are leaving. Following the golden rule (Sec. 2.3.1), the signal induced on the GEM bottom electrode is positive and, if the capacitative coupling between GEM and anode is low, the appearance of induced signal happens far away from the electron cloud. This can occur only if the readout sectors face the same partition of the GEM bottom electrode and if the latter is small enough. In 10 cm × 10 cm detectors the effect is relatively small if the gain and the primary ionization are kept low. However, for high gains and/or an high energy deposit this effect causes large induced signals in non irradiated regions as it is described in Fig. 2.41.

A potential solution for this effect can be the introduction of resistive layer instead of Copper in the GEM manufacturing; this solution, however, can have impact on other detector parameters. A simpler mitigation strat-

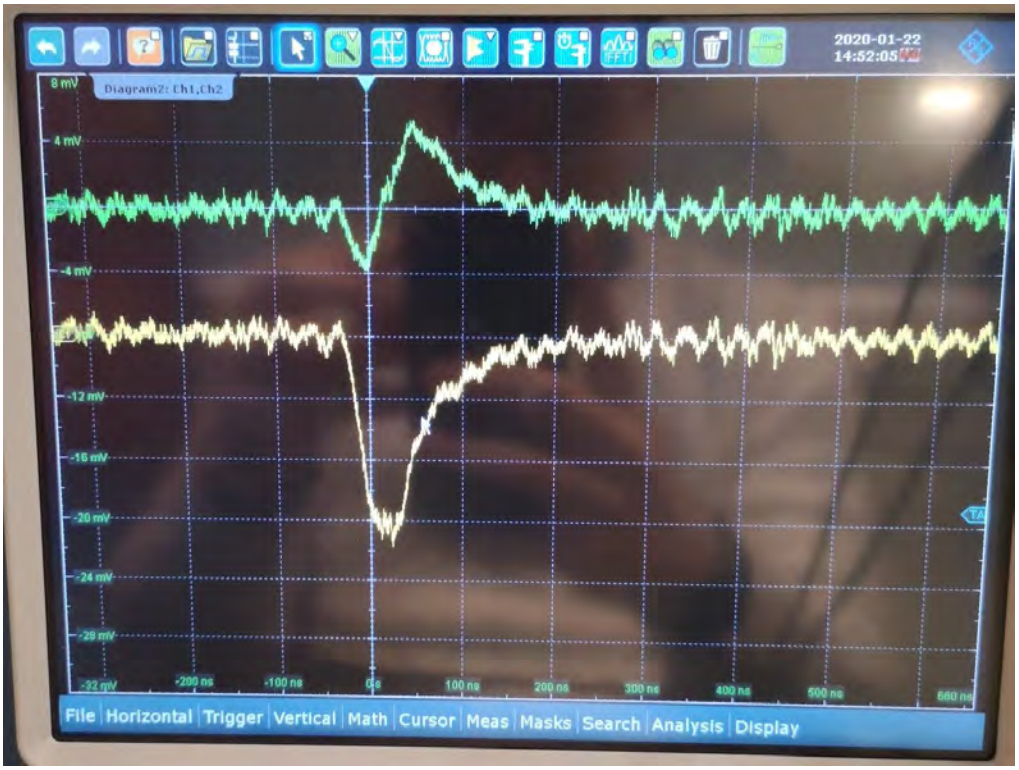

Figure 2.41: Signals induced on the anode of a 10 cm × 10 cm triple-GEM (gain 8×10^4) by a 5.6 MeV alpha particle with no amplification. The yellow signal is induced on the anodic strips facing the irradiated region, while the green one is induced on a sector not irradiated, but that shares the same GEM foil partition on top of it.

egy is to increase the capacitance by building larger foils or foil sectors or by placing a capacitor in parallel with the induction gap. However, as it will be discussed in the next section, the induction gap capacitance plays a leading role in discharge propagation through the anode, making convenient to lower the capacitance value to safely operate the detector. A GE1/1 detector with segmented and decoupled (with resistors) HV partitions on both sides was produced. The actual segmentation on the top side was mirrored on the bottom (see Fig. **??**). The discharge propagation probability was quenched by such design, but the cross-talk signals resulted in fake hits on the nearby sectors underlying the same HV partition [118]. For this reason, the next CMS GEM detectors will be build with the third GEM foil with a full Copper bottom side. The work done for the understanding of the discussed effect can be found in [118–120].

Discharges As mentioned in the previous sections, discharges limit the operative range of all MPGDs. Despite GEM detectors seem more promis-

ing than other technologies due to the possibility to share the gain between multiple foils, they are not immune to discharges. If the number of electrons in the avalanche overcomes the Reather limit (order of 10^7 electrons in the avalanche), a breakdown in the gas occurs. In GEM structures, usually, discharges develop in the last foil, that is the one that multiplies the larger charge. A spark in a GEM foil usually manifests as a fast drop of the voltage across the foil, with a small signal induced on the nearby electrodes. Fig. 2.42 shows one of the above mentioned behaviours. It is important to notice that the voltage recovery time is usually of the order of several ms, while the picture shows a faster recovery time because of signal derivation introduced by the readout circuit. It was early observed [104]

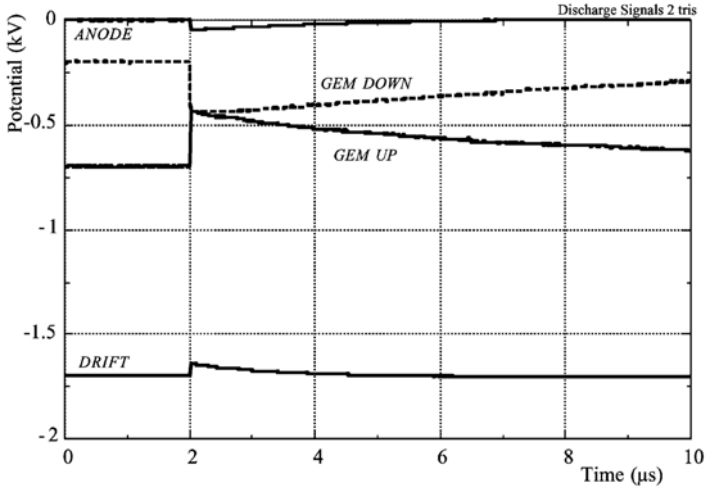

Figure 2.42: Non-propagating discharge in a single GEM detector: voltage levels and signals on all electrodes. No protection resistors were used [104].

that discharges can propagate through electrodes and also between GEM foils. This effect is probably due to photon mediated processes that extract charges from the gas or from the metallic electrodes. Another hypothesis is that the GEM hole Copper rim, heating up because of the discharge, may induce thermionic emission of electrons, creating a precursor current that propagates the discharge. The latter hypothesis was raised because of observations made on melted Copper near the GEM rim after multiple discharges [121–123]. However, it is important to notice that the propagations happen also in presence of a reverse electric field [104]. Fig. 2.43 shows a photo of an actual discharge occurring and then propagating to the anode.

Because of propagation, discharge patterns may vary from event to event. A useful way to reconstruct the topology of a discharge is the use of high voltages probes on the electrodes and inductively coupled antennas to trigger the events, since they give a signal every time a spark occurs. This

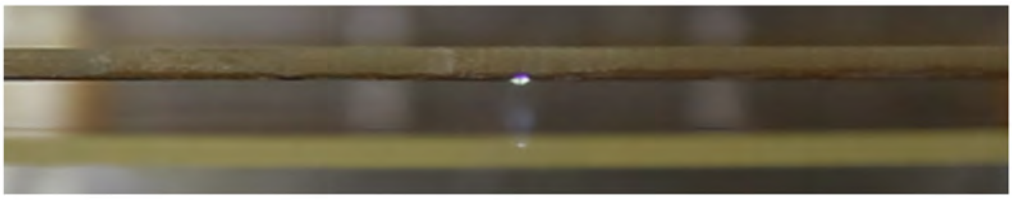

(a)

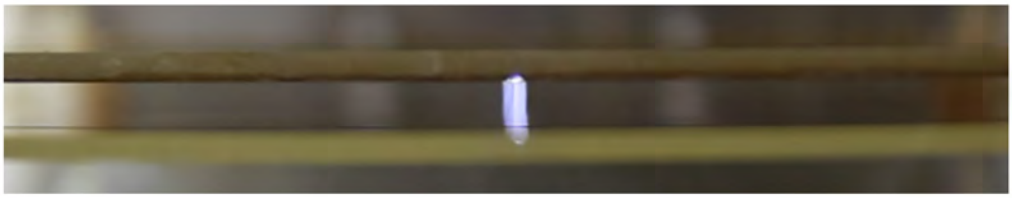

(b)

Figure 2.43: Side view on the induction gap. In both photographs the GEM (upper structure) and the readout anode (lower structure) are visible. Photo (a) shows a primary discharge while photo (b) shows a secondary discharge between GEM and readout anode [124].

technique procedure is well described in [125, 126]. Fig. 2.44 shows the voltages on the last GEM foil electrodes of a $10\,\text{cm} \times 10\,\text{cm}$ detector during a discharge event, the first antenna signal (tens of mV) arrives concurrently with the discharge, where the GEM voltage drops to zero (as shown in Fig. 2.42). After more than $10\,\mu\text{s}$, the discharge propagates through the readout with the consequent drop to zero of the two electrodes voltage, after a relatively brief time the process reignites, provoking another propagated discharge. In large area detectors that have huge induction gap capacitance, such GE1/1, the situation can be more dramatic. Fig. 2.45 shows a similar plot of voltages during a selected discharge event. In this case, the initial discharge is probably not across the last GEM foil due to the lack of voltage approaching on the monitored electrodes. However, seven propagation events are detected probably involving multiple electrodes. For a complete and refined reconstruction of discharge topology, the knowledge about the behaviour of all the electrodes and the help of antennas are required.

As already said, to reduce the intrinsic probability of discharges, a resistor can be placed in series between the power supply and the GEM electrode. This way, the intense precursor spark current reduces the field on the GEM, quenching the discharge production. This was clear since early measurement [104], so it has become a standard to use segmented top electrodes, each one protected and decoupled with a resistor ($1 \div 10\text{M}\Omega$). New interest on the issue rose in the last years [121, 122, 124, 127, 128], in par-

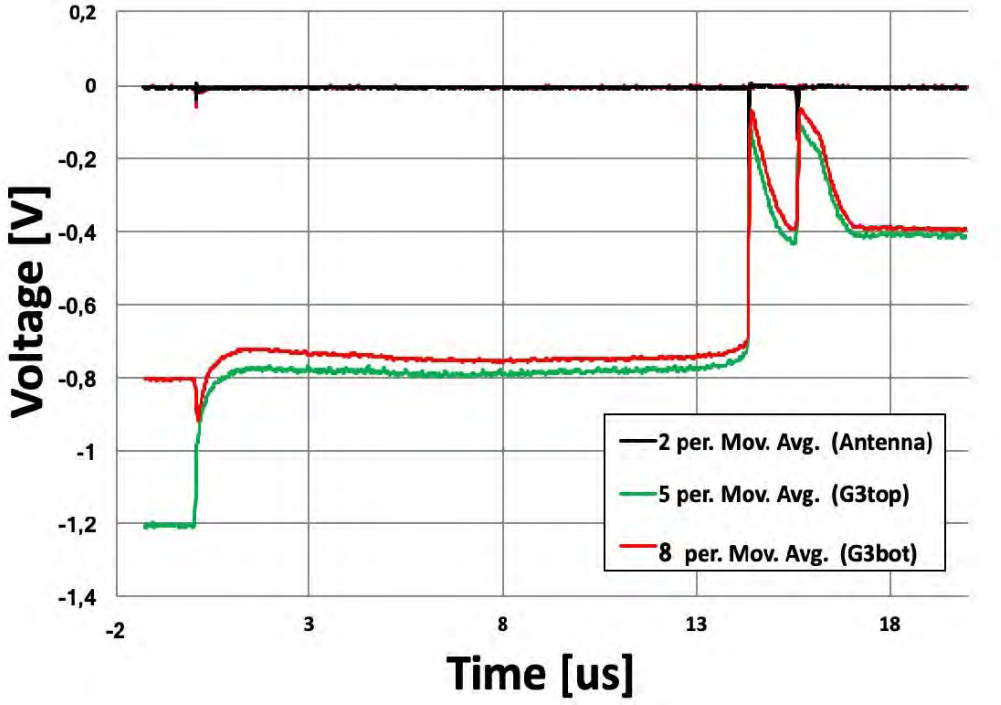

Figure 2.44: Discharge event recorded on a 10 cm × 10 cm detector by the voltage monitor of the two electrodes of the last GEM foil, namely G3top and G3bot. An antenna signal is used to trigger the acquisition [122].

ticular the CMS GEM group started an R&D campaign to investigate the electronic channel loss during the slice test [129], where discharges were found guilty of damaging the readout electronic channels. In particular, the effect of the induction gap capacitance and the bottom protection resistor on the discharge propagation probability was highlighted. Therefore, to build a large area detector it is recommended to segment GEM foils on both the sides with high granularity and decouple each segment with a high value resistor ($0.1 \div 10$ MΩ).

Since these effects were discovered after the whole GE1/1 mass production, the mitigation strategy on such single segmented detectors without resistors on the bottom sides could not involve these suggestions. However, the discharge resistance of the readout electronic was improved and the resistors values of the T-filter present between the electrodes and the power supply was increased. This resulted in an acceptable channel loss probability [123].

The observations made before will be implemented in GE2/1 and ME0 detectors. Such detectors will mount double segmented foils, except for the last one that needs to remain of one piece due to the cross-talk effect exposed in the previous section. GE2/1 electrodes will have protection re-

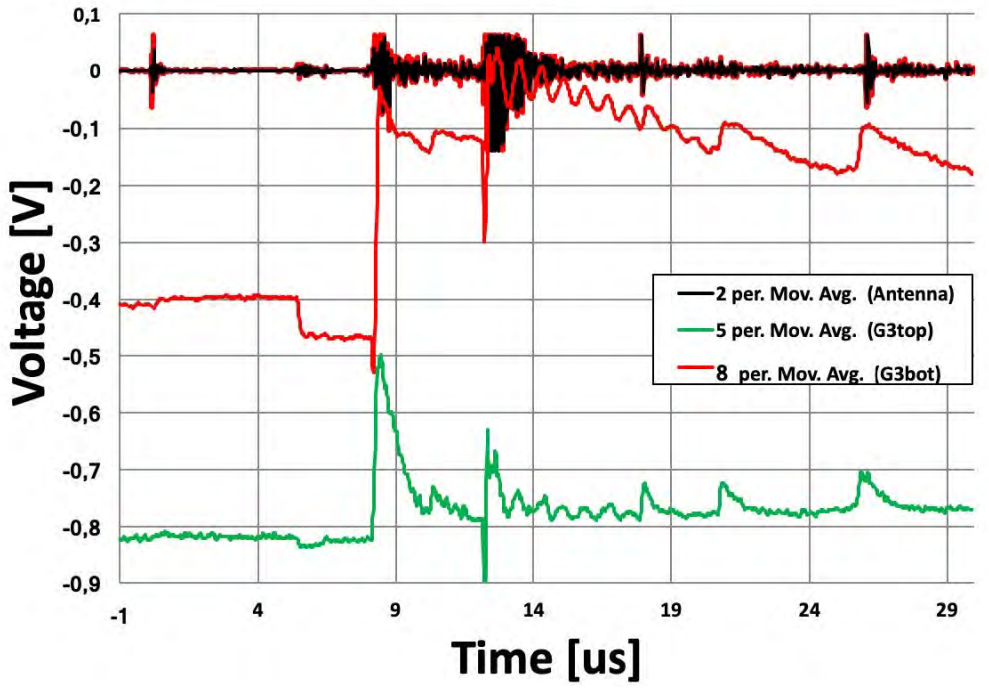

Figure 2.45: Discharge event recorded on a GE1/1 detector by the voltage monitor of the two electrodes of the last GEM foil, namely G3top and G3bot. An antenna signal is used to trigger the acquisition [122].

sistors of 10 MΩ on top and 100 kΩ on bottom while the T-filter will mount 220 kΩ, 20 kΩ resistors and a 2.2 nF capacitor. For ME0 the discussion on the resistors and filter is still under discussion, more information will be given in the Ch. 4.

CHAPTER 3

THE GAS MONITORING SYSTEM FOR THE CMS GEM SAFE OPERATION

LHC experiments exploit around 30 gas systems that deliver the correct gas mixture to the relative detector subsystems [130, 131]. These are huge and complex apparatus, extending over several hundreds of meters and satisfying stringent requirements on reliability and stability to ensure the quality of the gas mixture delivered to the detectors.

The CMS gas system, as the other infrastructures present at CERN, is always subjected to upgrades and optimization. The Gem gAS MONitoring system at P5 (GASMON@P5) will introduce a new setup to detect gas mixture failures in the CMS GEM gas system side by side with the current monitoring systems. After a brief introduction on the current CMS gas system, the influences of some parameters on the GEM detectors performances will be presented. Finally, the Gem gAS MONitoring system at P5 (GASMON@P5) will be introduced. The system aim is to test the gas mixture before sending the gas to the CMS GEM detectors in order to detect any variation of the Argon/CO_2 ratio, via the direct measurement of the effective gas gain of a small 10 cm $\times$ 10 cm triple-GEM detector. Pavia GEM Group had the full responsibility of the development of such monitoring module and I personally lead all the R&D work and follow the installation and commissioning activities.

3.1 The CMS gas system

All the LHC gas systems infrastructures follow a modular design, with every module fulfilling specific functions to satisfy the requirements and needs of the peculiar detector they are serving. The modularity and the standardization helps the construction of the systems and allow fast and easy maintenance with industrial standards. The software control is uniformed following the Programmable Logic Controller (PLC) logic [132]. The building block of a typical gas system infrastructure is distributed on three levels (see Figs. 3.1 and 3.2). The Surface room (SG) is where

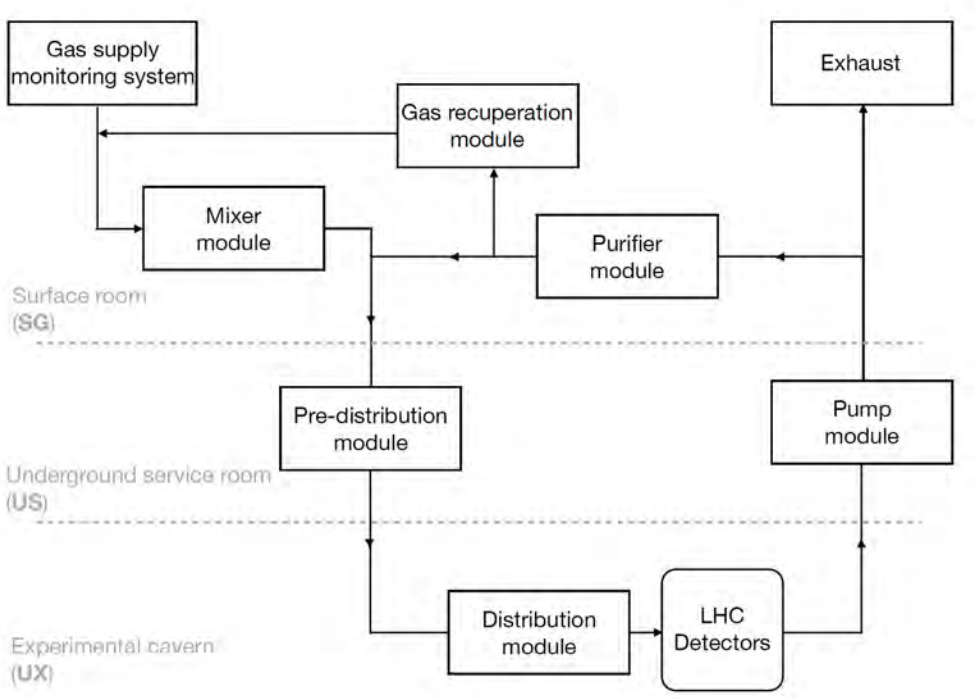

Figure 3.1: Schematic view of the main functional modules present in a typical LHC detector gas system [130].

most of the modules are placed, since it is the most accessible location also during beam operation. The main distribution line is supplied from here. The underground service room (US) is where the pre-distribution happens: the main supply line is divided into several lines. Finally, the experimental cavern (UX) is equipped with the final distribution module that separates the supply lines, with the desired granularity up to the detectors. Different modules may be differently equipped on the base of the detector requirement; a brief overview of the main components is given in the following.

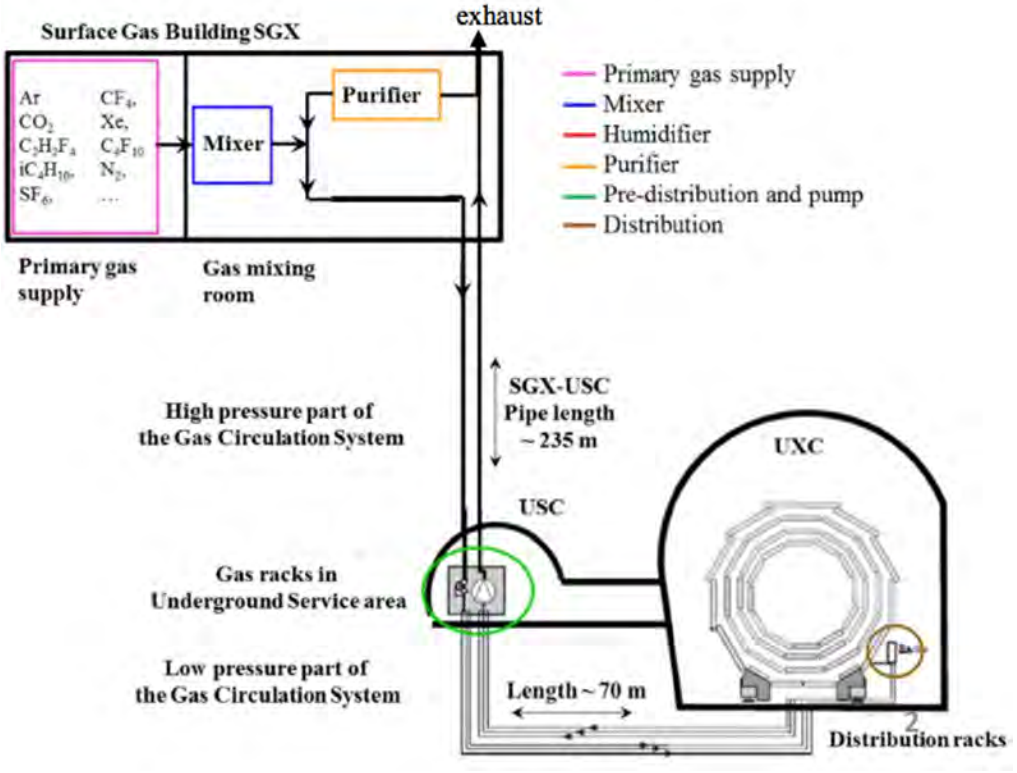

Figure 3.2: Schematic view of the CMS gas system.

Gas supply monitoring system For each gas, two different supply sources are available. The first one is usually in use while the second is a backup and starts automatically if the main one is empty. The monitoring system checks continuously the availability and quality of the gas before supplying it to the next system module. This way, contaminants are unlikely injected. Other measurements are made on the supply pressure, gas flows, and O_2 and H_2O concentrations.

Mixer module The aim of the mixer module is to supply the desired gas mixture. Up to four lines may be installed with Mass Flow Controllers (MFC) that control and measure the gas flux for every primary gas [133]. The MFCs are controlled via software to supply the correct gas ratios at the desired flux . Usually, two MFCs are present on each lines,for redundancy or, in some cases, because it is necessary to supply very high fluxes or different gases. The CMS GEM gas system is equipped with two lines of MFCs for Argon and carbon dioxide. Fig. 3.3 shows the scheme of the elements composing the gas mixer module. A CF_4 line was prepared at the beginning of the gas system commissioning due to the interest of the group in using such gas. However, as it will be explained in Sec. 5.1.2,

CF_4 was discarded from the gas mixture and Ar/CO_2 (70/30) mixture will be used for the CMS triple-GEM operations. Figs. 3.4 and 3.5 show the

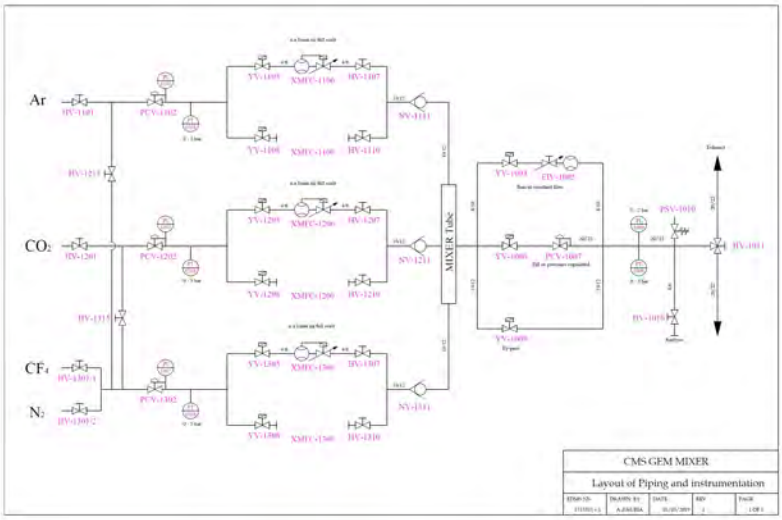

Figure 3.3: Schematics of the GEM gas mixer rack installed in the surface building [134].

distribution of the measured Argon and CO_2 percentages in the gas mixture supplied by the CMS GEM mixer module.

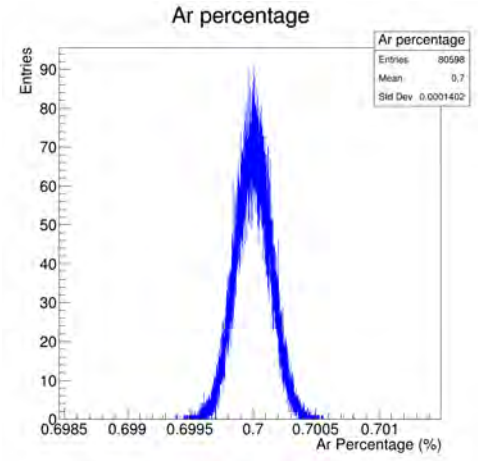

Figure 3.4: Supplied Argon percentage in the gas mixture supplied at the CMS GEM mixer module.

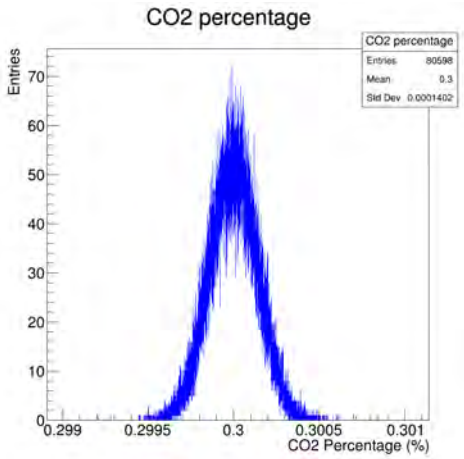

Figure 3.5: Supplied carbon dioxide percentage in the gas mixture supplied at the CMS GEM mixer module.

Gas distribution The distribution of the gas from the mixer to the detectors is performed in multiple steps. After the preparation of the gas mixture in the SG building, the gas is supplied to the pre-distributions modules in the US. The GEM system exploits four racks in the service cavern, one per each of the GEM stations: GE1/1, GE2/1 and ME0, plus one for controlling purposes. Every module manages both the supply and the return of the gas from the disk (see Figs. 3.6 and 3.7). Several

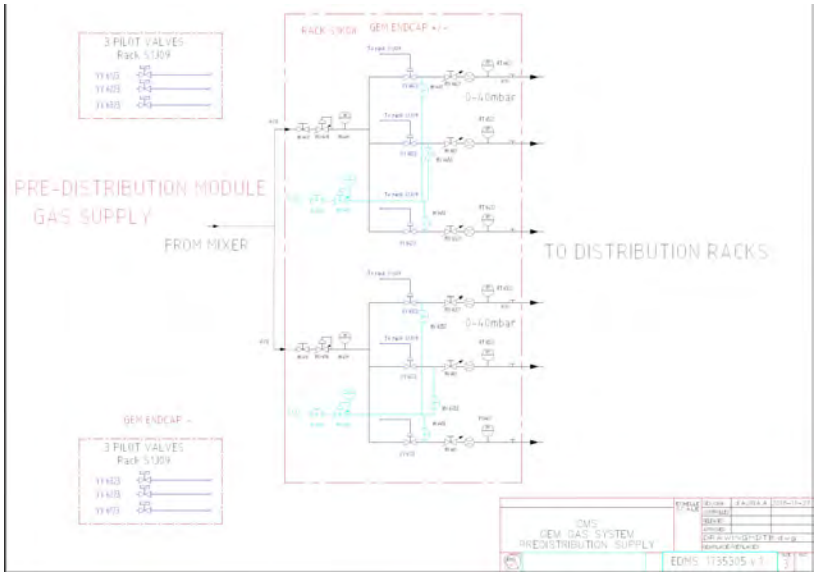

Figure 3.6: Schematics of the supply pre-distribution module [134].

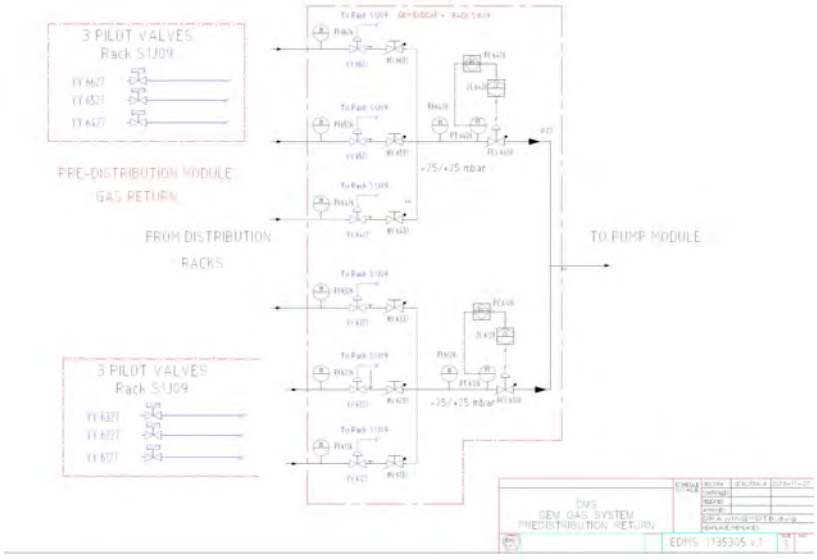

Figure 3.7: Schematics of the return pre-distribution module [134].

parameters (gas flow, pressures, etc.) may be changed and monitored also during beam time. Every pre-distribution rack supplies two distribution modules, one per end-cap, furnishing all the detector stations. For the GE1/1 system, which is the only one completely installed in CMS, the distribution rack has 12 output lines, each of them supplying 6 detector layers (3 Super Cambers) in series. The nominal gas flow for each line is 18 L/h, that corresponds roughly to one gas volume replacement every hour. The supply and return fluxes for every line are monitored by basic CERN-made flow-meters in order to spot leaks on the lines. A drawing of the whole GEM gas system scheme is shown in Fig. 3.8.

Many of the modules, such as the purifier and gas recirculation modules, (Fig. 3.1) were not discussed because they are usually present only in a closed loop gas system, i.e. the one that recuperates part of the used gas for further operation. The GEM gas system, on the other hand, is working in open loop mode, i.e. the return lines from the detectors are directly exhausted in the atmosphere. The GEM group chose this mode of operation for multiple reasons. First of all, the Ar/CO_2 (70/30) mixture is relatively cheap and the detector volumes are quite small compared to the other CMS gaseous detectors systems. Furthermore, the cost of the recirculating system would have been difficult to amortize during the GEM subsystem lifespan. Moreover, the mixture has a Global Warming Potential (GWP) of 0.3 [135], meaning a small impact on the overall CERN greenhouse emission.

3.2 GEM performance in Ar/CO_2

In order to develop a gas monitoring system based on the direct measurement of the effective gas gain of a test detector, it is fundamental to know the influence of other physical quantities on the gain itself. As discussed in Sec. 2.2.2 the gas gain, in proportional regime, is exponential with the supplied voltage. However, since the voltage is supposed to remain constant during the normal operation, this behaviour is not responsible for the gain fluctuations. Other parameters, that may change the detectors behaviour, have to be searched within the gas itself. Indeed, the three main factors influencing the gas gain are:

- Air pollutants with their electronegative molecules, that may reduce the avalanche propagation.

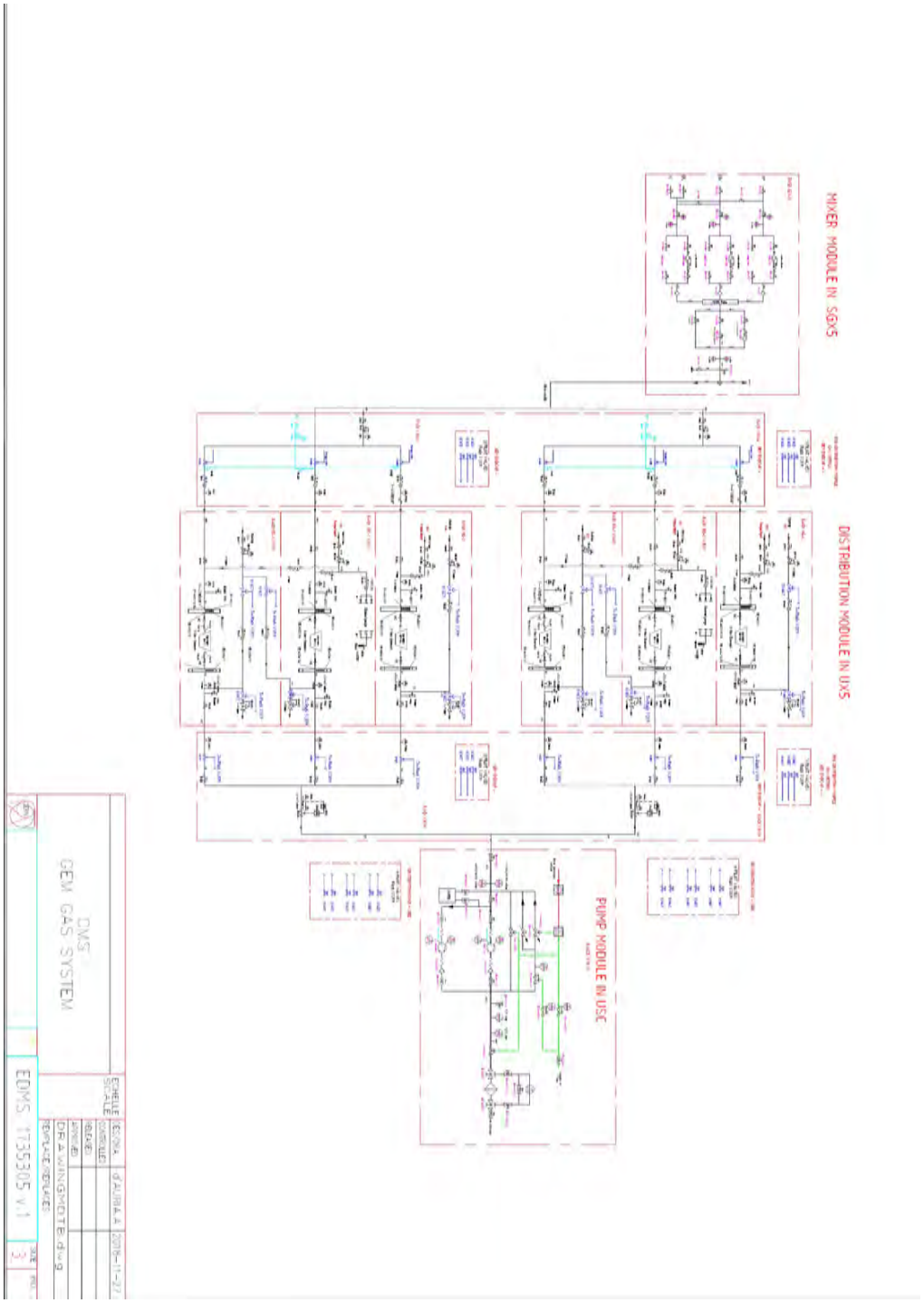

Figure 3.8: Schematic of the whole CMS GEM gas system [134].

- Environmental temperature and pressure, that change the density of the gas, hence the Townsend coefficient value of the mixture.

- The concentration ratio between Argon and CO_2 in the gas mixture; since CO_2 is used as a quencher, the gas gain will decrease if the percentage of such gas increases in the mixture.

The aim of the GASMON@P5 is to measure precisely the effective gas gain of a triple-GEM detector by removing the fluctuations not due to the intrinsic composition of the gas, i.e. the first two points of the previous list. This way, the gain carries the information about the gases percentages ratio in the mixture. Having an opportune calibration of such corrected gain and knowing the concentration of Argon and CO_2 will provide a system able to directly detect any variation of the relative composition of the gas mixture. In the following, the parameters influencing the gas gain will be described.

3.2.1 Influence of air contamination

Air contains multiple elements and molecules that may affect the operation of a gaseous detector. In particular, N_2, O_2 and H_2O (contained in relatively large fractions in the atmosphere [136]) influence on a $10\,\text{cm} \times 10\,\text{cm}$ triple-GEM were deeply studied in [137]. While Nitrogen alters the detector only in relatively high concentration ($\geq 1\%$), Oxygen and water influence appears at lower concentrations. Both O_2 and H_2O are electronegative molecules that tend to subtract electrons from the avalanche. O_2 levels start to affect the operations at concentrations ≥ 50 ppm, while H_2O has always some gain reduction effects that increase with its concentration.

These type of contamination can be found in large gas systems. Since such gases are used in other subsystems, the contamination is always possible. Another typical pollution comes directly from air. If leaks or loose connections are present, air can easily mix with the gas mixture, then particular attention has to be paid to develop gas tight detectors. CMS GEM were designed in order to have a good gas tightness and one of the steps of the production quality control, performed on every detector, was completely dedicated to this issue . Such quality control step, named QC3 [110], consists in inflating CO_2 in a detector up to an internal overpressure of around 25 mbar. The overpressure is monitored during time and data are fitted with an exponential function to get the pressure drop constant; the test is passed if the latter is lower than 0.12 mbar/min. Fig. 3.9 shows the QC3 result of a typical good GE1/1 detector, while Fig. 3.10 displays the same test performed on a typical $10\,\text{cm} \times 10\,\text{cm}$ detector. The comparison between the two plots indicates the evident non-gas tightness of the small detector. Since such detectors are usually used for R&D purposes, it's not dramatic that they exchange gas with the outside environment a lot. However, the exact knowledge of air infiltration influence is important for developing a system that want to measure only the gain dependency on

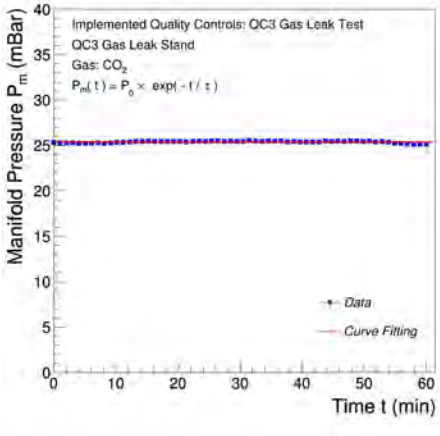

Figure 3.9: QC3 performed on a GE1/1 triple-GEM detector, an overpressure is created between the detector volume and the outside environment and its decrease is monitored during time.

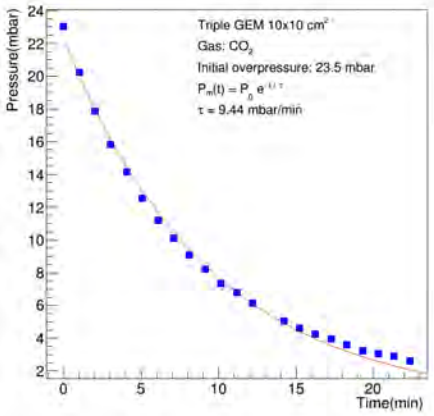

Figure 3.10: QC3 performed on a 10 cm × 10 cm triple-GEM detector, an overpressure is created between the detector volume and the outside environment and its decrease is monitored during time.

the gas mixture. In [137] it was demonstrated that increasing the gas flux, it is possible to reduce the concentration of water and Oxygen in the gas volume. A higher gas flux helps to eliminate the accumulated molecules of such contaminants and helps to inhibit their accumulation. Fig. 3.11 shows an example of gain and concentration of O_2 and H_2O in the gas volume as a function of the gas flux, confirming the previous affirmation. Fig. 3.12 shows a trial to reproduce part of the data of the previous one: the effective gas gain and the relative humidity in the detector volume as a function of the gas flow are illustrated. Humidity is measured on the detector used for the GASMON@P5 via the BME280 sensor [138]. The trend in the latter test confirmed the one presented in [137], the different gain plateau are attributable to the distinct voltage settings of the two setups. The previous plot highlights the non-gas tightness of small GEM detectors and the necessity to operate them at relatively high fluxes. Indeed, for a tight detector, a gas flow of some vol/h is usually enough for good operation (1 vol/h for the GE1/1 detectors). For such 10 cm × 10 cm detector a higher gas flux is required to completely exploit the potential of a gas mixture with low concentration of water and oxygen. The GASMON@P5 is operated at a constant flux of 3 L/h corresponding to 7.5 vol/h. This working point is near the edge of the gain plateau in Fig. 3.12. In general, having a constant gas flux is fundamental for such small detectors to remove the possibility to have air contamination influence on the effective gas gain. For this reason the GASMON@P5 setup exploits a MFC to regulate and measure the gas

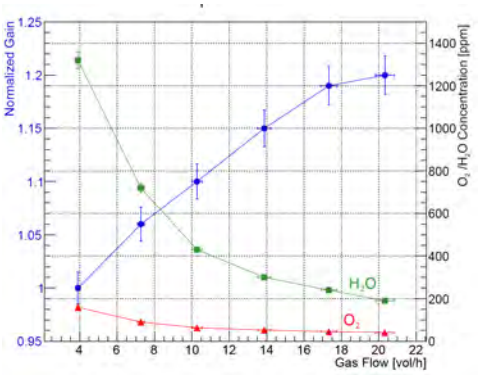

Figure 3.11: GEM gain at fixed HV and mixture impurities concentration (H_2O and O_2), with respect to the increase of input gas flow. Gain is normalized to the value at lowest flow rate [137].

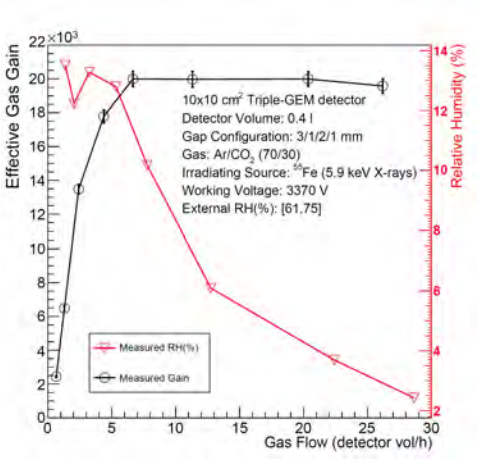

Figure 3.12: GeEM gain at fixed HV and relative humidity as function of the input gas flow.

flux entering the detector.

3.2.2 Influence of temperature and pressure

As pointed out in Sec. 2.2.2, the charge multiplication factor is given by the Townsend equation:

$$G = e^{\alpha x},$$

where x is the distance in the multiplication avalanche and α is the Townsend coefficient. Since α is defined as the inverse of the mean free path of electrons in the gas, it is possible to deduce that $\alpha = \nu_i / w^-$ where ν_i is the average ionizations per unit time and w^- is the electron drift velocity. It has been demonstrated that, upon other dependencies, the ratio between α and the electric field value E only depends on the ratio E/ρ with ρ the gas density [139, 140]. Then from the ideal gas law, it is possible to assume that:

$$\alpha \propto 1/\rho \propto T/P. \tag{3.1}$$

So, with this simple approach, the gain dependence on temperature and pressure is:

$$G(T/P) = Ae^{B\frac{T}{P}}, \tag{3.2}$$

with A and B parameters to be defined experimentally. This approach to remove the environmental fluctuation of gain has been used in [141].

From the experimental point of view many other types of empirical formulas were used to correct gain measurement from temperature and

pressure fluctuations. If environmental fluctuations are small, which is a valid approximation when operating a gaseous detector in controlled environments, a first order expansion of Eq. 3.2 gives good correction to the gain:

$$G(T/P) = A\frac{T}{P} + B.$$

This type of correction was used for example in [130]. A more suitable correction formula can be obtained modifying the previous one by adding different exponents to temperature and pressure variables:

$$G(T,P) = G(T_0,P_0)\left(\frac{T}{T_0}\right)^a\left(\frac{P_0}{P}\right)^b. \tag{3.3}$$

This power law dependency was used in [46, 110, 142] with good results and it will be used to correct gain data during the aging tests presented in Sec. 5.

Similar version of Eq. 3.2 was used to correct the gas gain of GE1/1 detectors during the mass production. Detectors produced in different places around the world need to be normalized to the same environmental condition in order to assure the same quality of production. The formula used to normalize the detector gas gain was, at the beginning:

$$G = Ae^{BV\frac{P_0}{P}\frac{T}{T_0}}, \tag{3.4}$$

where V is the working voltage, P_0 =964.4 mbar and T_0 =297.1 K the average pressure and temperature in the CMS experimental cavern. The correction is applied to the detectors during the last step of the quality control (QC8). The QC8 measures the cosmic muon efficiency of GE1/1 detectors with their final electronics. During this test the detector high voltage is set to have each chamber working at a gain of 2×10^4, exploiting Eq. 3.4. It was observed that some detectors did not reach full efficiency at the nominal gain, making guess that the environmental correction was overestimating the detector gain. Fig. 3.13 show the gain as a function of the equivalent divider current ($I_{divider} = R_{divider}V$) measured at the production site for two production chambers with codenames GE1/1-X-L-GHENT-0022 and GE1/1-X-L-CERN-0024. On the other hand, Fig. 3.14 shows the gain corrected with Eq. 3.4 for the same two detectors. While GE1/1-X-L-CERN-0024 chamber behaved nicely during the QC8, showing an average efficiency $> 97\%$ as required for passing this quality control step, GE1/1-X-L-GHENT-0022 showed an average efficiency of $\simeq 85\%$. The muon detection was improved by manually increase the supplied voltage that was relatively low because of the strong environmental correction. Multiple occurrences of such issues, triggered the CMS GEM collaboration

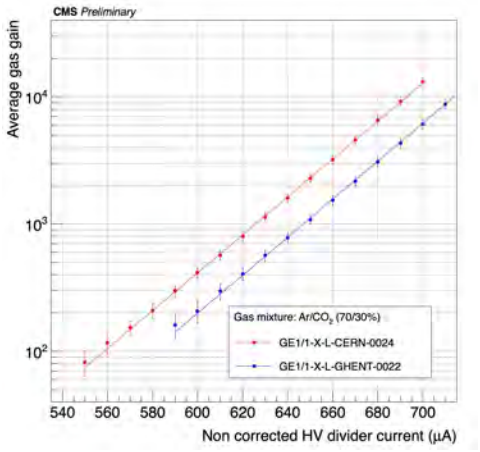

Figure 3.13: Non-corrected gas gain as function of the equivalent divider current for two production chambers: GE1/1-X-L-GHENT-0022 and GE1/1-X-L-CERN-0024.

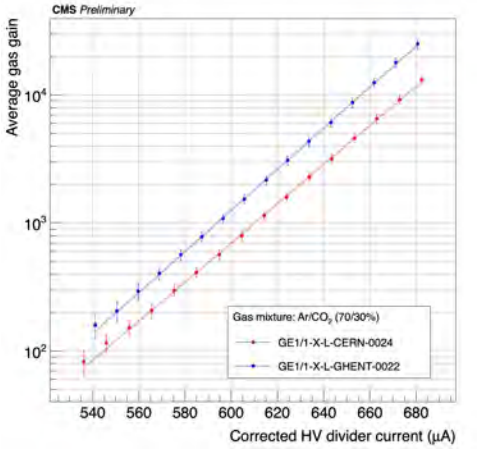

Figure 3.14: Gas gain corrected with Eq. 3.4 as function of the equivalent divider current for two production chambers: GE1/1-X-L-GHENT-0022 and GE1/1-X-L-CERN-0024.

to develop a better temperature and pressure correction for the GE1/1 detectors.

The assumption made in Eq. 3.1 was relaxed, adding a free exponent to the α and ρ proportionality:

$$\alpha \propto 1/(\rho)^k \propto (T/P)^k.$$

The presence of an exponent in Eq. 3.1 could have been guessed from the beginning if supposing that the multiplication process is not isotropic in space ($k = 1$ case). Assuming the avalanche propagation only in one direction, the parameter k should be equal to 1/3. However, fitting the gains of all the produced GE1/1 detectors with the function:

$$G = Ae^{BV\left(\frac{P_0}{P}\right)^a\left(\frac{T}{T_0}\right)^b}, \tag{3.5}$$

gives two different values of exponents, a=0.433 and b=0.537 [143, 144]. With these parameters, all the produced detector efficiency reached values $> 97\%$ at gain of 2×10^4. The CMS GEM collaboration carried out also a GARFIELD++ [65] simulation to find a and b values [145]. Result of these simulations gave a=0.432 and b=0.443.

It was demonstrated that using a=b=1 in triple-GEM detectors gain correction would overcompensate tit, since such values suppose an isotropic behaviour of the avalanche in space. However, the two values are greater

than 1/3, meaning that the multiplication process is not mono-directional but it has some spread perpendicular to the electric field direction.

It can be assumed that Eq. 3.5, with the experimental values of a and b, should work for every triple-GEM built and operated in the same way as the GE1/1 detectors. To confirm that hypothesis the 10 cm × 10 cm detector used for the GASMON@P5 was used to collect data and find a and b parameters. Such detector was irradiated with a ^{55}Fe for 1 month when operating at a gain of 2×10^4, recording every 30 s the effective gas gain, the temperature and the pressure, inside the gas volume. Such data points were fitted with Eq. 3.5, with only a and b as free parameters. A, B, P_0 and T_0 were derived from a gas gain scan, performed before the beginning of the test as a function of voltage . Fig. 3.15 shows the χ^2 test

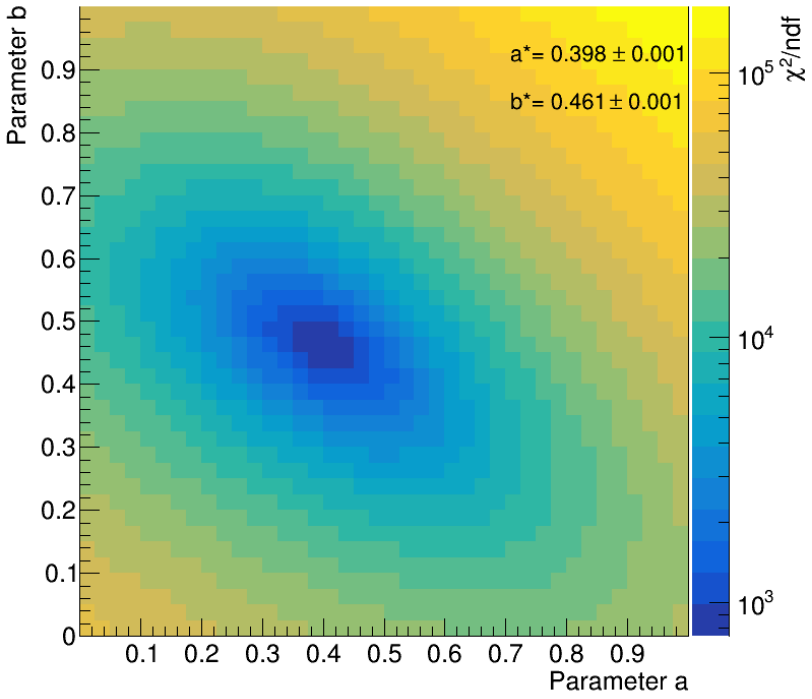

Figure 3.15: χ^2 test values on the acquired data tested with the model from Eq. 3.5 as function of the parameters values.

values computed as follows:

$$\chi^2(a,b) = \sum_i \frac{\left(G_i^{meas} - G^{model}(T_i, P_i, a, b)\right)^2}{\delta G_i},$$

where G_i^{meas} and δG_i are respectively the i-th measured gain and its error and $G^{model}(T_i, P_i, a, b)$ is the gain computed with Eq. 3.5. The values $a^* = 0.398$ and $b^* = 0.461$ minimize the χ^2 values, i.e. they are the ones that

better fit the data with the model. Using a^* and b^* values found during this run, it was possible to nicely correct the gain points as shown in Fig. 3.16 and Fig. 3.17. This was made using the inverse relation of Eq. 3.5:

$$G(T_0, P_0) = Ae^{BV} = \frac{G(T,P)^{\left(\frac{P_0}{P}\right)^{-a^*}\left(\frac{T}{T_0}\right)^{-b^*}}}{A^{\left(\left(\frac{P_0}{P}\right)^{-a^*}\left(\frac{T}{T_0}\right)^{-b^*}-1\right)}}$$

These parameters are very close to the ones found by the CMS GEM group,

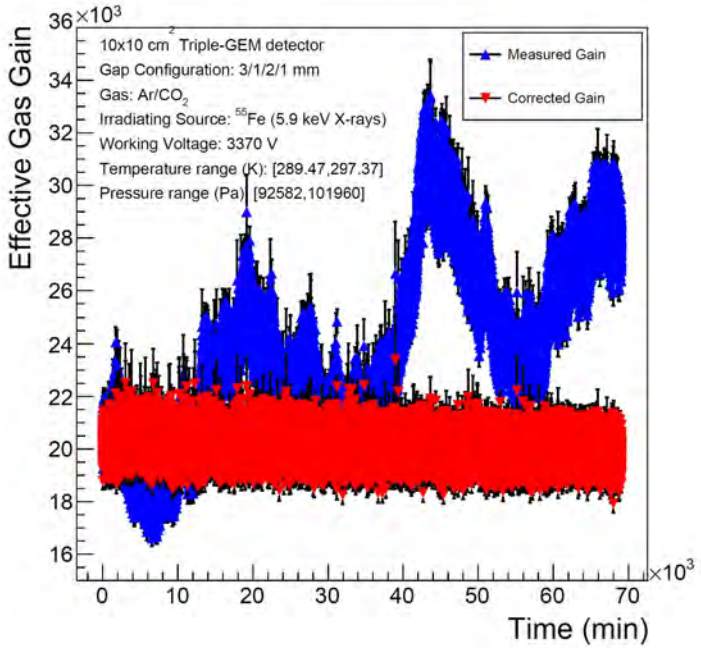

Figure 3.16: Effective gas gain as a function of the time before and after the correction.

however they are not fully compatible. This fact probably indicates that the model is not perfect and does not fully represent all the triple-GEM detectors. Still, the corrections made in this way nicely removed most of the fluctuations due to temperature and pressure variation. The standard deviation of the data passed from 3312.8, for non-corrected data, to 477.7 for the corrected ones, leading to a mean over sigma ratio μ/σ improvement of a factor 5.8.

The GASMON@P5 setup is exploiting Eq. 3.5 as correction formula to have a precise measurement of the gain normalized to a fixed pressure and temperature. Other runs were performed to check the reproducibility of the results and they confirmed values of a^* and b^* very close together. A

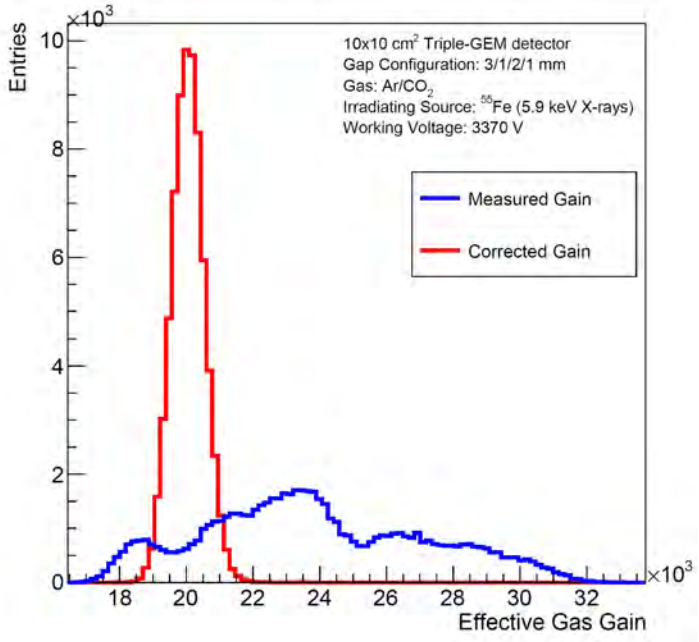

Figure 3.17: Histograms of the effective gas gain points before and after the correction.

new data taking run will be done after the installation of the system, and it will improve continuously as new data will be collected.

Other correction formulas for the gain are proposed in [146–152] but they were not considered because of their complexity, inefficiency or difficulty in exploit them.

3.2.3 Influence of Ar and CO_2 ratio

The aim of the GASMON@P5 system is to detect variation of the gas composition. Therefore, the precise knowledge of the effect on a triple-GEM gain of an higher or lower concentration of one of the two gases that compose the mixture is fundamental. To the writer knowledge, there is no analytical function that predicts the gain value in a triple-GEM as a function of the percentage concentration of gases in Ar/CO_2 mixture $G(\%_{CO_2})$. In general, the gain at fixed voltage, should increase with higher concentration of Argon and decrease with lower ones, because of the different concentration of quencher gas fraction. Fig. 3.18 shows the values of the simulated Townsend coefficient of a Ar/CO_2 mixture at fixed electric field (70 kV/cm) for various CO_2 concentrations. The simulation was done with Magboltz [57] and it clearly shows that, in the CO_2 percentage range [20,40], the Townsend coefficient grows more than linearly with an

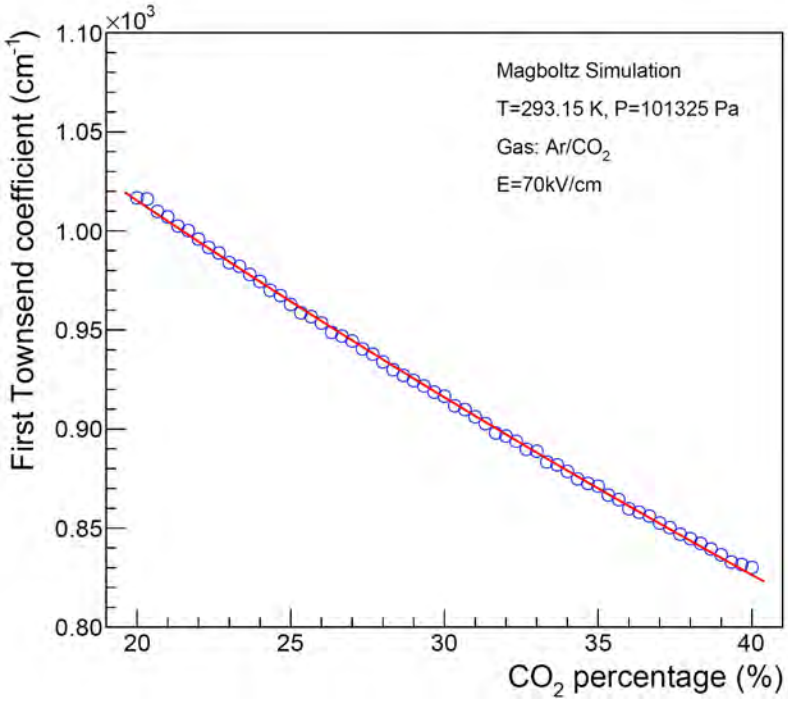

Figure 3.18: Townsend coefficient at fixed electric field, temperature and pressure for different concentration of gases in Ar/CO_2 gas mixture. Output from Magboltz [57]. An exponential curve is superimposed to guide the eye.

increasing quantity of Argon.

To quantify the effect of different gases concentration on the triple-GEM gain, the latter was measured precisely changing the gas mixture composition. The gas gain was measured, according to the procedure explained in App. A, on the GASMON@P5 10 cm × 10 cm detector. This was operated at a fixed voltage, equivalent to the one needed to have 2×10^4 gain with nominal Ar/CO_2 (70/30). The CO_2 percentage was then varied in the range [21.67, 40] with 0.33 steps; lower concentrations were not reached to avoid stressing the detector too much. The gas flux was maintained at the nominal values of 3 L/h. The mixture was prepared using Argon and CO_2 from bottles (N5.5). Gases flows were regulated with two calibrated MFCs from Bronkhorst®. After mixing them in a 1 L lung, the gas is sent to the detector. Fig. 3.19 and Fig. 3.20 show details of the mixer station used for this test.

Gain measurements were performed every 30 s during the percentage scan. The detector gas volume refreshing time was around 13.3 min at the selected flux. This means that, after changing the gas concentrations,

Figure 3.19: Mixer station used for the test. Green bottle is Argon while the grey one is carbon dioxide.

Figure 3.20: Detail of the Mass Flow Controllers used for the test.

some time has to pass to have the detector fully working with the new gas. Fig. 3.21 shows, as an example, the change of gain when the CO_2 percentage in the mixture is decreased from 30% to 29.67%. Experimentally, it was found that at least 20 min have to pass after the change of the gas to have stable gain. For this reason, the gain measurement started 30 min after the gas mixture changed, and collected data for one hour after that. The data were averaged over the acquisition time, the result of this scan is presented in Fig. 3.22. An exponential function was used to fit the data. The χ^2 test outputs a value of 0.171, a low value probably because of the very small errors on the gain measurement (because of the average of many data points). However, this suggests that a single exponential function $G(\%_{CO_2}) = Ae^{B\%_{CO_2}}$ can describe very well the gain behaviour when changing the CO_2 percentage. The inverse function:

$$\%_{CO_2} = \frac{1}{B} \log \frac{G_{meas}}{A}, \tag{3.6}$$

will be used in the GASMON@P5 system to directly measure the concentration of gases inside the gas mixture supplied to the CMS GEM detectors.

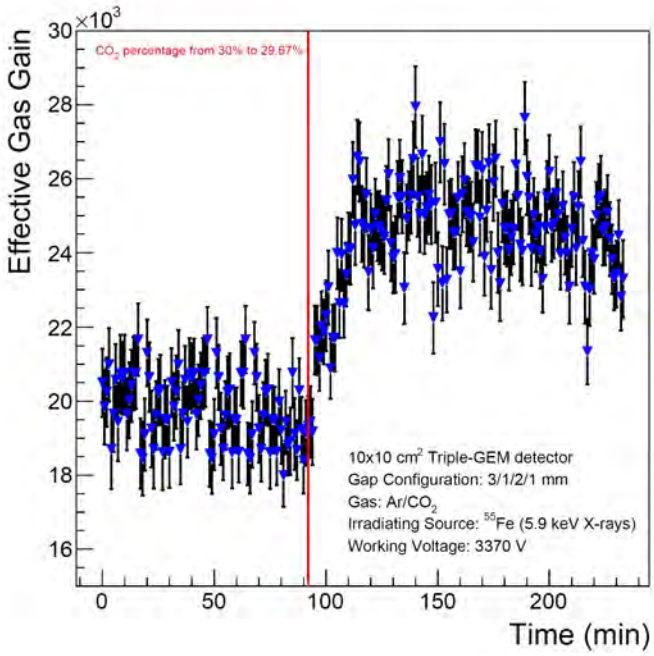

Figure 3.21: Gain change when decreasing the CO_2 percentage in the mixture from 30% to 29.67%. Data are corrected from temperature and pressure fluctuations.

3.3 The Gem gAS MONitoring system at P5 (GASMON@P5)

The Gem gAS MONitoring system at P5 has been developed to detect the Ar/CO_2 relative concentration inside the gas mixture that supplies the CMS GEM detectors installed in experimental cavern. In the previous sections it was discussed how to remove, from the measured gas gain, the known fluctuations in order to have a measurement that contains only informations about the gas mixture composition. In the following, the experimental setup and the software tools used to obtain a functional system will be described.

3.3.1 Experimental setup

Fig. 3.23 shows a sketch of the system setup. A derivation from the main GEM supply line was made to collect gas sample to analyse. The gas flux is regulated by a MFC controller, that can be bypassed in case of problems. Rotameters are placed before the MFC and after the detector for reading and controlling the flux if the MFC is bypassed. Fig. 3.24 and Fig. 3.25

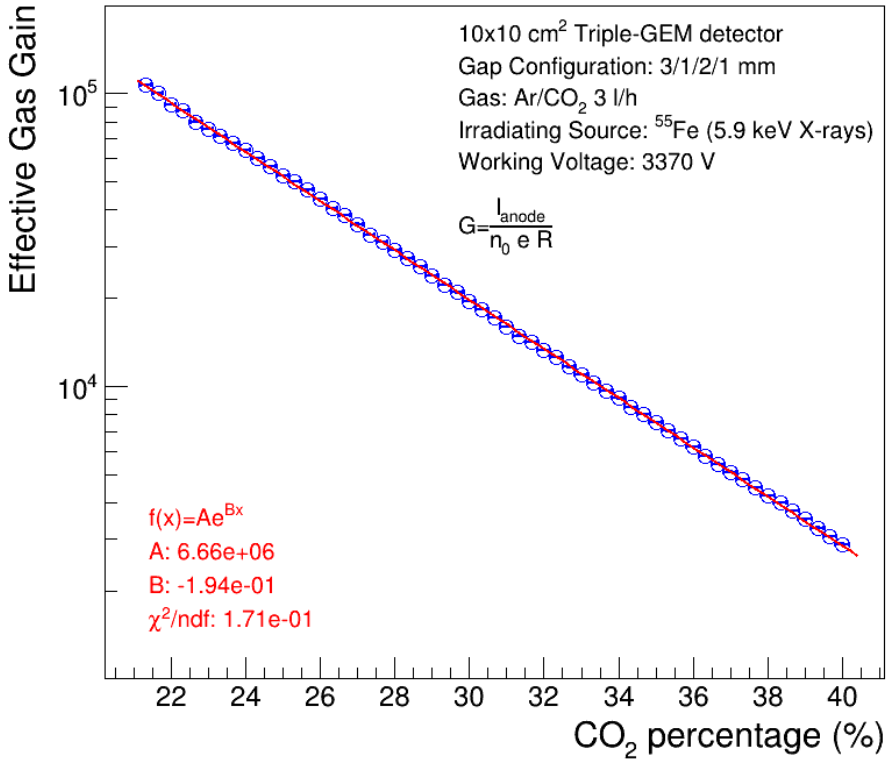

Figure 3.22: Triple-GEM effective gas gain measured as a function of the CO_2 concentration in the mixture. Data are corrected from environmental fluctuations and fitted with an exponential function.

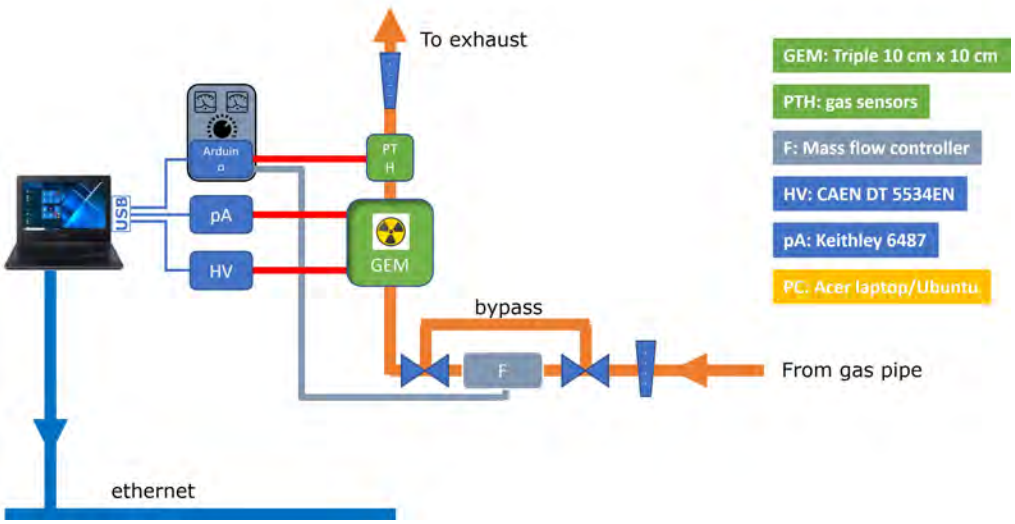

Figure 3.23: Experimental setup scheme of the GASMON@P5 system.

show details of the gas panel that contains the above mentioned accessories. The gas is then flushed inside the 10 cm × 10 cm triple-GEM detector. Such

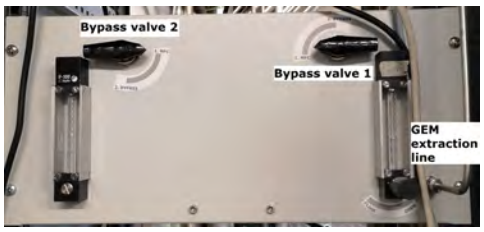

Figure 3.24: Front view of the gas panel.

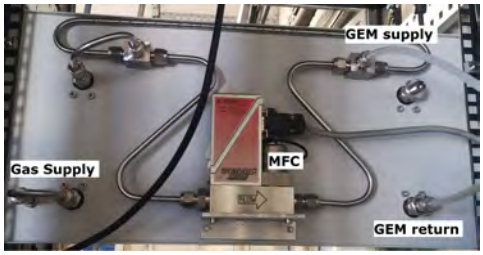

Figure 3.25: Back view of the gas panel.

chamber is a small area GEM with the same gaps configurations as the CMS GEM detectors: 3/1/2/1 mm. The anode is segmented in 128 strips readout in parallel to measure the whole current generated by the detector. The assembly kit (see Fig. 3.26) was produced at CERN and assembled in the clean room (ISO6 class 1000) available at the CMS-GEM QA/QC facility sited in building 904 at CERN. The assembled detector is presented in Fig. 3.27 irradiated with a ^{55}Fe source. The high voltage is supplied by a DT5534EN Desktop HV Power Supply Module [153] controlled by a Laptop via serial USB connection. Only one HV channel is required since the voltage is distributed with a voltage divider that ensures the correct biasing of all the electrodes. The detector was fully calibrated before the

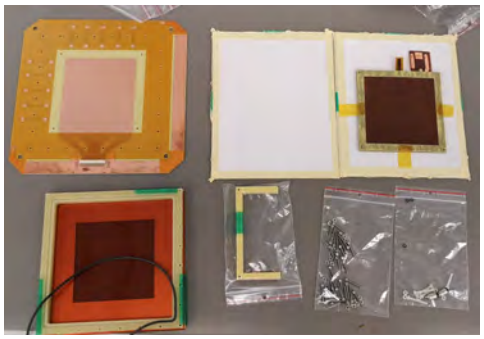

Figure 3.26: The pieces composing the kit to mount the triple-GEM used in the GASMON@P5 system. The readout board consists in 128 anodic strips.

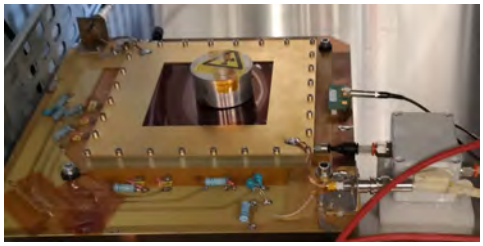

Figure 3.27: The assembled 10 cm × 10 cm GEM detector. The grey box contains the sensor to monitor the environmental parameters inside the gas mixture.

operation to fix the working point. A voltage scan was performed and the gain and the rate measured at different working points as shown in Figs. 3.28 and 3.29. The chosen working voltage was V_0 =3269.7 V that

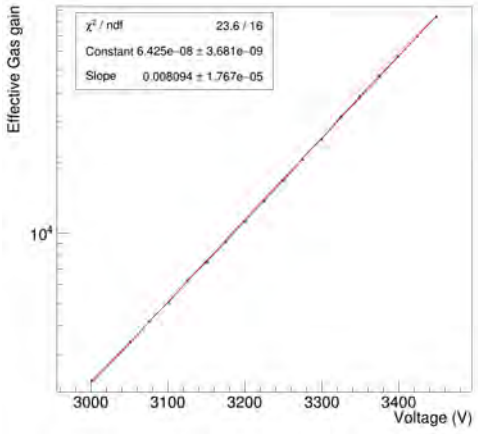

Figure 3.28: Measured effective gas gain as a function of applied voltage. Data are fitted with an exponential function.

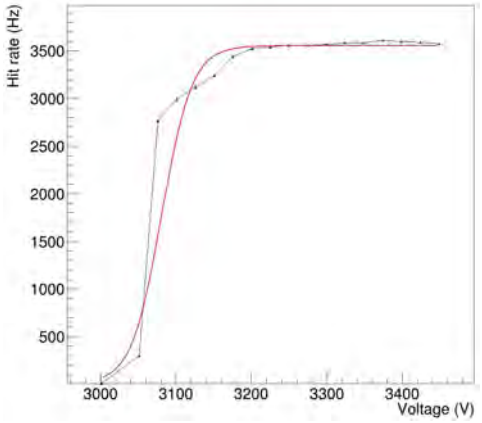

Figure 3.29: Measured hit rate as a function of the divider current. Data are fitted with a sigmoid function. The fit is not perfect due to the emission of Argon characteristic photons.

corresponds to a gain of:

$$G(T_0, P_0) = 2 \times 10^4,$$

where T_0 =296.02 K and P_0 =95 662 Pa.

The gas gain, during normal operation, is computed via Eq. A.2 by measuring the anodic current. The average hit rate during the calibration was: $R_0 = (3592.3 \pm 0.8)$ Hz. This value is fundamental for a precise gain measurement. However, it is not measured during the normal operation, but it is extrapolated via the decay equation:

$$R(t) = R_0 e^{-t/\tau},$$

where t is the time passed after the calibration and τ is the ^{55}Fe decay constant equal to 1.255×10^8 s [154, 155]. The anodic current is measured continuously for 30 s by a Keithley 6487 picoammeter [156], the average value is used to compute the effective gas gain and, after that, the measurement cycle restarts. In the same time window, the pressure, temperature and humidity of the gas mixture are measured by a BME280 sensor [138] placed inside a sealed box downstream the GEM gas output (see Fig. 3.27). The sensor is read by an Arduino via I^{2}C protocol. This is placed inside an aluminium box called controller box that contains the electronic for Arduino and the MFC powering (see Figs. 3.31 and 3.30). Indeed, the microcontroller also reads the values of the set and measured gas flux from the MFC. The latter can be shut down via a software command. The full

Figure 3.30: Front panel of the controller box. Displays show the set flux and the measured one, the potentiometer regulates the set flux. Connectors to the MFC, PC and the environmental sensor are shown at the bottom.

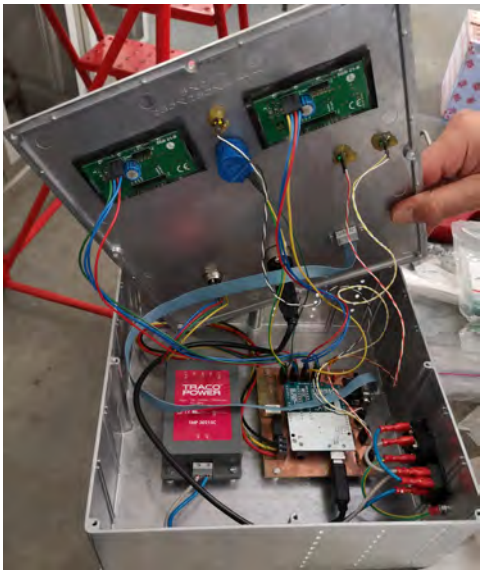

Figure 3.31: Internal view of the controller box.

electrical scheme of the controlled box is shown in Fig. 3.32. The flux has to be regulated with a potentiometer placed in front of the controller box, the readings of the set and measured flux are performed during the same 30 s time window as the other measurements.

3.3.2 Software and Data Flow

The scheme of the software infrastructure is presented in Fig. 3.33. It is composed by ywo main C/C++ programs (in blue): the first reads and controls the power supply parameters (voltage, divider current...), the second reads the GEM current from the picoammeter, the environmental parameters from the gas sensors, the gas fluxes, and the valve status from the MFC. The environmental correction on the gain measurement and the CO_2 concentration computation is done at this stage. It also takes synchronized values of voltage and current from the HV program via an intermediate file and it writes all the relevant data into a text log file. The reading frequency is set to 30 s. A scheduler automatically restarts the two programs every day at midnight. This technique has two advantages:

- it splits the data into small daily files;
- it minimizes the on-line interventions and reduces data losses, because

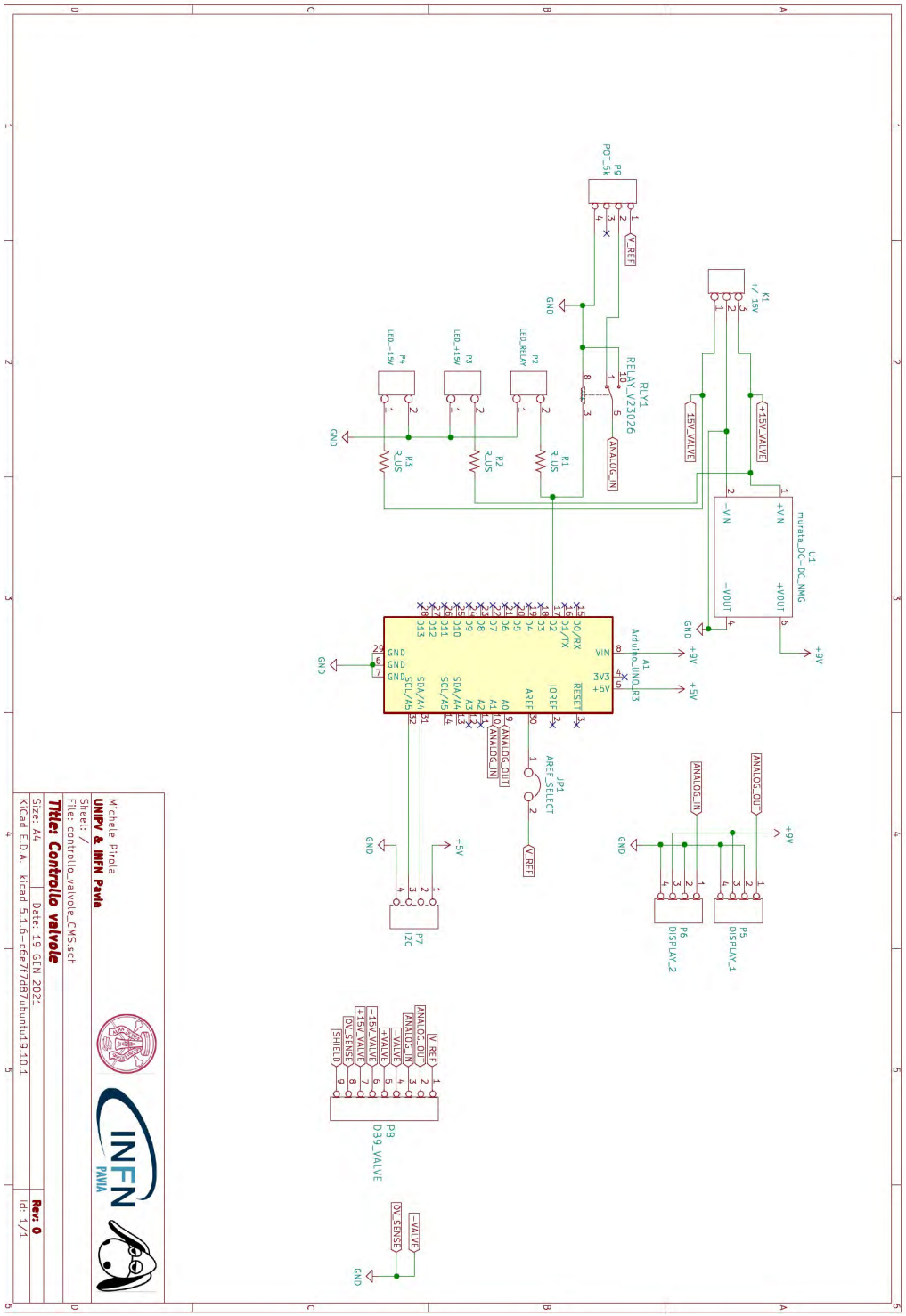

Figure 3.32: Electrical scheme of the controller box.

the program starts at midnight in any case, even if they previously were stopped by accident or if they died because of a power cut.

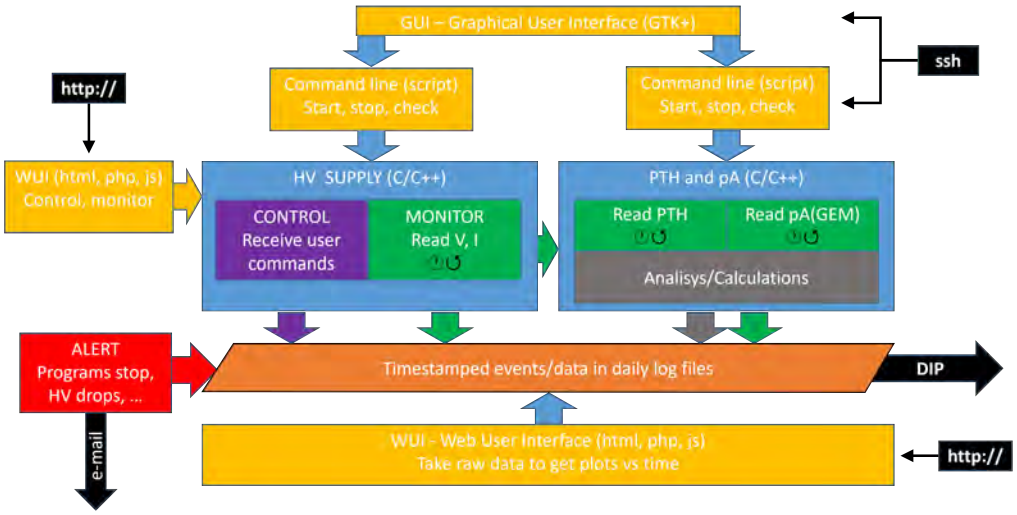

Figure 3.33: Schematics of the software tools develop for the measurements control and monitoring.

Some conditions were defined to detect a failure of the system. A program identifies these events and it records them in a text file with a sequence number. Usually these events require a human action to be solved, for example the possibility of restoring the HV after a trip. The program monitors the system and it records in the same file a message when the problem has been solved. It is possible to activate a notification of these events via email. A script allows to activate or deactivate the notification and to define addresses of the recipients. Email notification through the firewall is possible because the local mail server uses a public mail server as relay host. Graphics User Interface (GUI) and Web User Interface (WUI) were developed to let the user easily control and monitor the system parameters. The full system is accessible within the CERN network and with the outside network via ssh tunnel through the lxplus service [157]. Communication with the Detector Control System (DCS) [158] of CMS is carried out via an infrastructure developed at CERN called Data Interchange Protocol (DIP) [159, 160] that permits the exchange of small amounts of real-time data in a heterogeneous system.

3.3.3 Analysis Algorithm and Performance

In the previous sections the procedures to take a precise measurement of the CO_2 concentration inside the gas mixture were discussed. The goal of the GASMON@P5 is now to detect systematic fluctuations of the gas mixture quality and to trigger warnings and alarms to let the detector user intervene and solve the cause of that. Because of the exponential relation between

the gain and the quantity of CO_2 in the gas (Eq. 3.6), it is clear that a little variation in the gas concentration will create a large change of the gas gain. Therefore, an algorithm able to detect systematic gain fluctuations has to be developed to reach a high resolution in the gas composition detection.

Fig. **??** shows the distribution of the corrected gas gain data points acquired during one calibration run. The logarithm scale helps to identify a deviation from a pure Gaussian shape. Indeed such distribution presents a small right tail, probably a leftover from the intrinsic distribution trend of the gain values (see Sec. 2.2.2). However, such effect is very small because the number of primary charges in case of ^{55}Fe irradiation is 198 ± 4 (see Sec. 4.1) and the Central Limit Theorem [161] moves the distribution to a Gaussian. Furthermore, it was demonstrated that the following analysis behaves in the same way when supposing the gain distribution purely Gaussian. Fig. 3.35 shows the distribution of a set of gain data points Gaussian generated using a 256-bit Ziggurat method [162, 163] starting from the experimental mean and standard deviation of a calibration run.

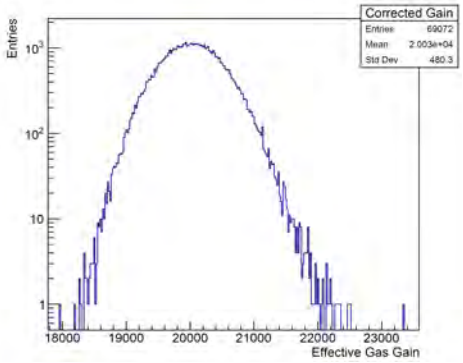

Figure 3.34: Distribution of a sample of the measured gas gain values, a small right tail makes the distribution not exactly Gaussian.

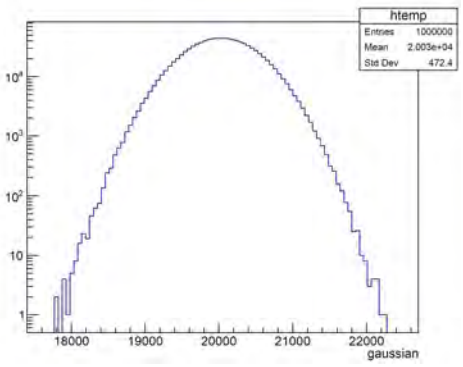

Figure 3.35: Distribution of gas gain values sampled in a Gaussian way using the experimental mean and variance of a real gain measurements.

The gain variation detection algorithm of the GASMON@P5 takes a moving average on the last 10 measured gain points and tests it against the mean and standard deviation of the ordinary distribution of the gain points in normal operation. Mean μ and standard deviation σ of corrected gain points during ordinary operation in Ar/CO_2 (70/30) are supposed to be the population ones. m and s will be the mean and standard deviation computed with the last 10 points measured, since a point is collected every 30 s a time window of 5 min is considered. The variable t is now computed

as:

$$t = \frac{|\mu - m|}{\sqrt{\sigma^2 + s^2}}. \tag{3.7}$$

Such variable quantifies the deviation of the sample from the population distribution. t values will distribute in a t-Student like way, however the distribution is not exactly a t-Student since s and σ are not normalized to the sample size. Fig. 3.36 shows 1 million gain points generated starting from the mean and variance of the measured gain data. Fig. 3.37 shows the distribution of all the computed t by moving through the previous dataset. A Gaussian fit is superimposed to highlight the distribution's longer tails, typical of a t-Student distribution. Such distribution is centred in zero

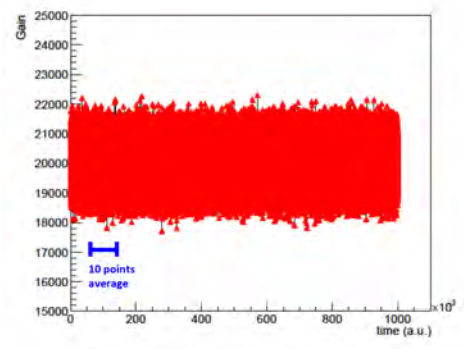

Figure 3.36: A set of simulated gain points. To get the variable t 10 points are considered.

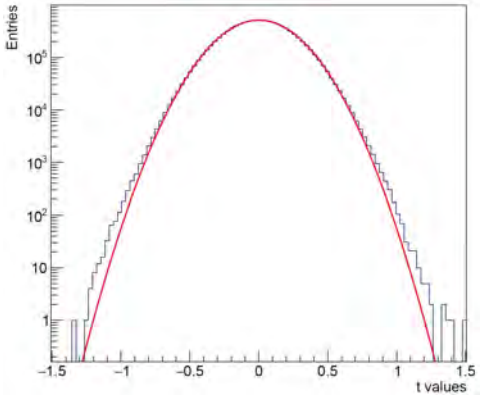

Figure 3.37: Distribution of the t values calculated from a set of gain points measured by the GASMON@P5 system.

and have a standard deviation of 0.23; with 1 million generated points the variable fluctuate in the range [-1.5,1.5].

In order to detect systematic fluctuations of the gain a threshold t^* has to be chosen. If the last measure gives $t > |t^*|$ a warning will be generated. The threshold has to be selected in order to have the highest gain deviation resolution and at the same time the lowest fake warning probability i.e. probability to detect a variation when it is just a statistical fluctuation. It may be guessed that these two requirements cannot be optimized independently, the higher the threshold the lower the fake warning probability and the lower the gain change resolution and vice-versa. First of all, a study on the fake warning probability has been carried out. A large sample of data (7×10^{10} events) have been generated and all the t values were computed. The number of occurrences of t values higher than a certain threshold t^* divided by the total number of generations gives the probability of having a fake warning. Fig. 3.38 shows such probability as

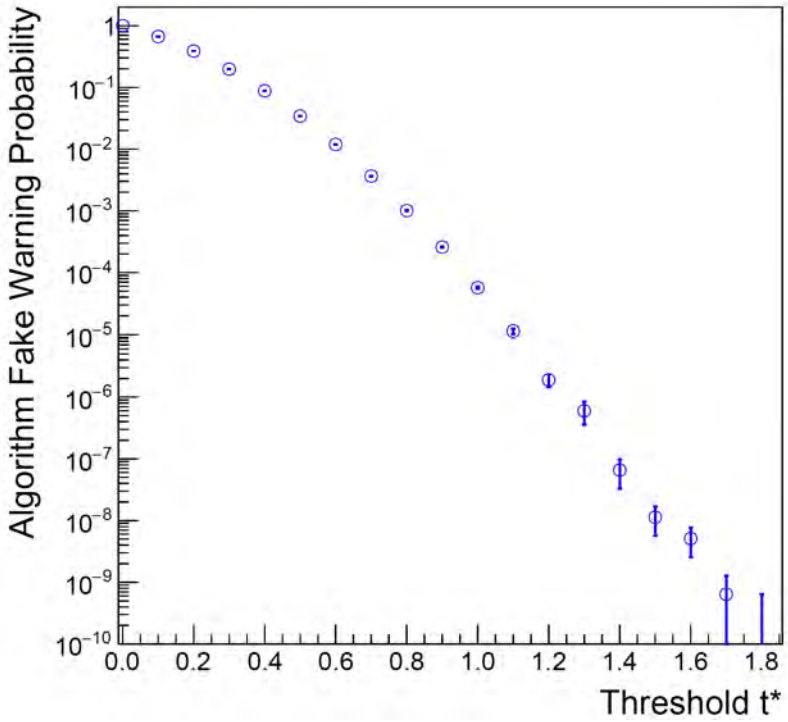

Figure 3.38: Fake warning probability as a function of the threshold on the t^* variable.

a function of the threshold t^*. The GASMON@P5 system is supposed to acquire around one million point every year and it is expected to work for at least 10 years. This means that choosing a t^* value of 1.4 will result, on average, in one fake warning every 15 years.

To test the algorithm performance in detecting systematic gain variations two dataset were analysed, one obtained from simulated data and the second directly measured by the GASMON@P5 system. The first set of data was generated starting from the mean and standard deviation of normal operation data (see Fig. 3.34). Ten thousands points are normally generated from the starting distribution. After that, the points are generated linearly increasing the generated mean, while the variance untouched. Fig. 3.39 shows the generated gain points, the right axis indicates the expected CO_2 concentration that may cause that gain increase, computed via Eq. 3.6. Despite the fact that the variance should decrease with the gain increase, this is a good test bench for the algorithm. Fig. 3.40 shows the computed t values during time; these values are lower than 1 for all the points generated following the normal operation conditions, while they start to increase with the growth of the average. In order to test the gain

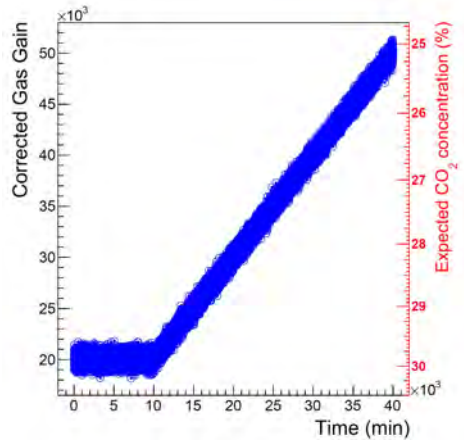

Figure 3.39: Simulated gain points and expected CO_2 concentration. After some stable points, the gain average is artificially increased.

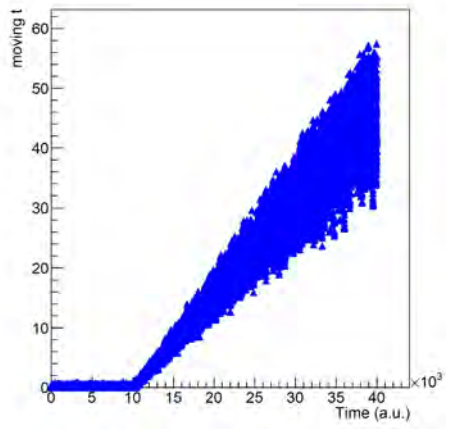

Figure 3.40: t values computed with the simulated gain data points.

change resolution, the first t value that overcomes the selected threshold t^* (the one that firstly triggers the warning) is searched. The corresponding average gain that generates the warning G_{war} is used to compute the percentage algorithm gain resolution:

$$R_G = 100\left(1 - \frac{G_{norm}}{G_{war}}\right),$$

where G_{norm} is the mean gain during normal operation (2×10^4). The percentage algorithm gain resolution as a function of the threshold t^* is shown in Fig.3.41. The CO_2 concentration resolution, computed in similar way as the gain one, is present on the right axis. With this simulation, the algorithm demonstrated that with $t^* = 1.4$ it is possible to detect systematic fluctuations of the gain of $(3.9 \pm 0.4)\,\%$ from the average measured gain and, in any case, $<6\,\%$ up to $t^* = 2$. This result confirm the high sensitivity to the CO_2 concentration in the gas mixture. Tab. 3.1 shows values of the resolutions for selected values of the threshold t^*. It is important to remind that the resolution values obtained here are overestimated since at higher multiplication factors the spread of the measured gain will reduce. On the other hand, if the gain will decrease, it is expected to have a worse algorithm resolution than the measured one.

In order to measure the upper limit of the algorithm resolution, it is important to test it with a measured set of gain points during a real event of Argon decrease in the gas mixture. This test will validate the results of the simulation with real data and with the real variance of the gas gain. To perform this test, the GASMON@P5 system was let run during the

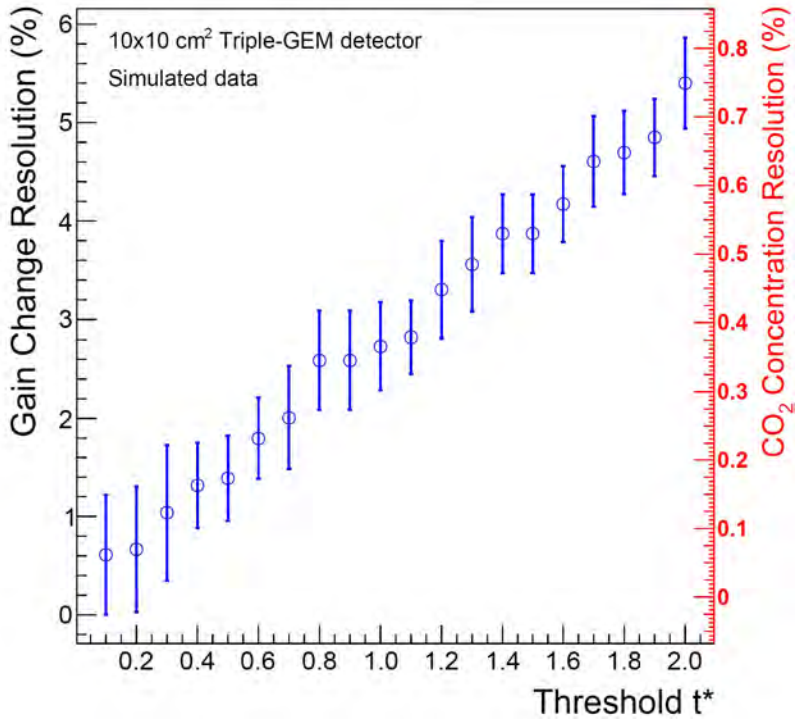

Figure 3.41: Gain change resolution as a function of the threshold on the t variable. Simulated gain points increasing in time were used to test the algorithm.

Threshold t^*	**Gain resolution** (%)	**Error** (%)	**CO_2 Resolution** (%)	**Error** (%)
1.4	3.87	0.40	0.48	0.09
1.6	4.17	0.39	0.53	0.09
1.8	4.70	0.42	0.62	0.08
2.0	5.40	0.46	0.73	0.08

Table 3.1: Gain and CO_2 percentage resolutions for selected values of t^*. Results come from the simulated dataset.

end of the Argon bottle that supplied the gas mixer. Fig. 3.42 shows the measured gain points during the depletion of the bottle with the expected CO_2 concentration in the mixture. Fig. 3.43 shows the computed values of the variable t during the same period of time. The same analysis performed on the simulated dataset was carried out also in this case. The gain and CO_2 concentration resolutions at different values of the threshold t^* are shown in Fig. 3.44. Moreover, Tab. 3.2 shows values of the resolutions for

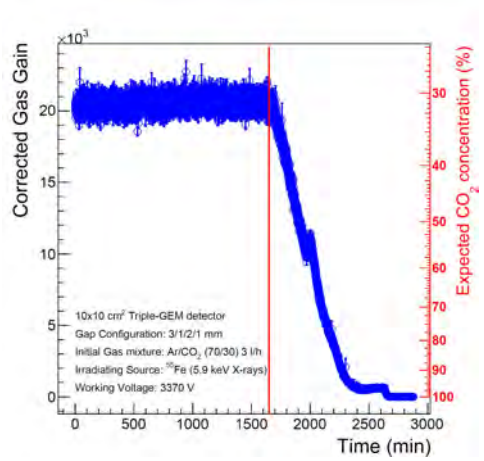

Figure 3.42: Gain points measured during the Argon bottle depletion. The Argon concentration in the mixture is progressively decreasing to zero.

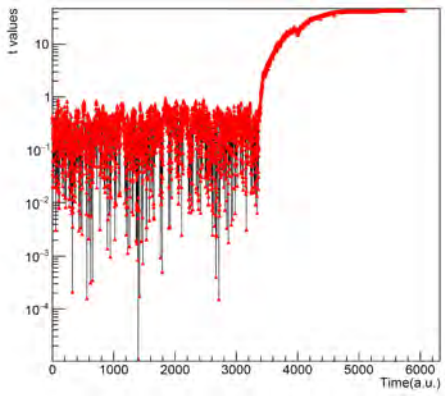

Figure 3.43: t values measured during the Argon bottle depletion.

selected values of th threshold t^*. It is evident that the resolutions measured

Threshold t^*	**Gain resolution** (%)	**Error** (%)	**CO_2 Resolution** (%)	**Error** (%)
1.4	4.56	0.40	0.60	0.09
1.6	5.52	0.61	0.75	0.05
1.8	5.52	0.61	0.75	0.05
2	6.68	0.68	0.94	0.04

Table 3.2: Gain and CO_2 percentage resolutions for selected values of t^*. Results come from the measured dataset.

during this experiment are slightly larger than the one from the simulated dataset. As already mentioned, this happens because of the higher spread of the gain when it is decreasing and because of the larger uncertainties due to the unknown behaviour of the bottle depleting.

Overall, it was demonstrated that the gain variation detection algorithm developed for the GASMON@P5 is able to detect systematic changes of the gain values with high resolution. With a choice of $t^* = 1.4$ it is possible to have a resolution lower than 4.6 % on the gain variation, meaning that it is possible to detect a CO_2 percentage change of the order of 0.6 % with a false positive probability of 6.57×10^{-8} (one false warning every 15 years). Furthermore, it is expected that the performance of the system will improve when a more intense irradiation source is used, since the intrinsic

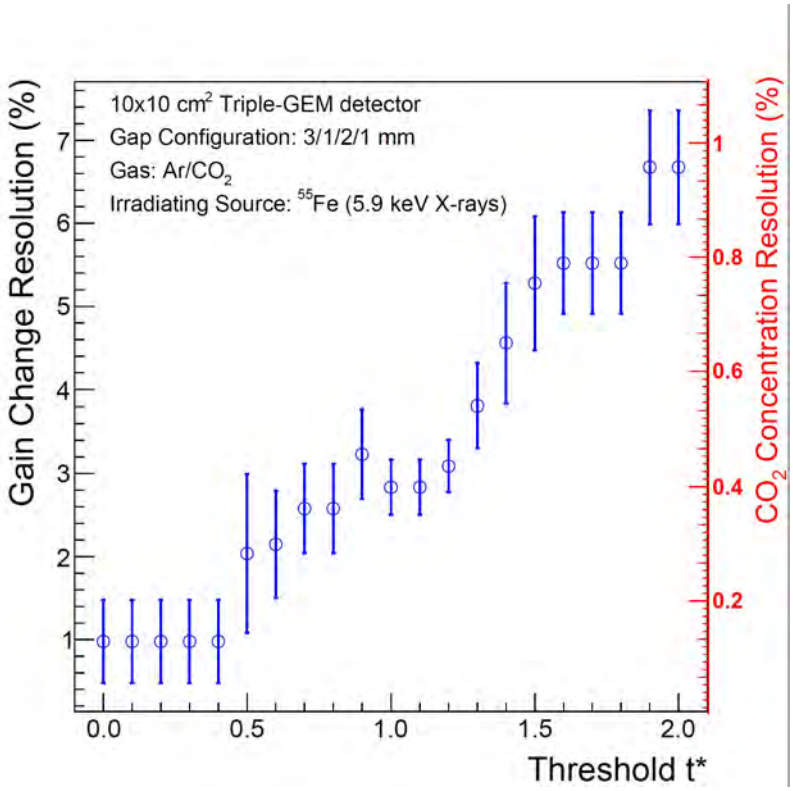

Figure 3.44: Gain and CO_2 concentration resolution as a function of the threshold on the t^* variable. Measured gain points were used to test the algorithm.

gain fluctuations will be reduced by the higher number of events averaged during the 30 s time window.

3.3.4 System commissioning

The GASMON@P5 system has been installed in the Surface Gas room (SGX5) of CMS. A dedicated rack was installed near the GEM mixer module in the room and all the the GAMON@P5 components were accommodated in it. Fig. 3.45 shows the disposition of the elements that compose it. The system is currently running, data are being collected to confirm the validity of the environmental correction parameters also at this site. After a calibration run the system will start to publish on the DIP server the warning status and the measured Argon and CO_2 percentage in the mixture. A dedicated DCS panel will be developed to send warnings to the central DCS in case of wrong gas mixture supply. No automatic intervention is scheduled if a warning is generated. Since the time between the detection of a wrong gas concentration comes hours before the same mixture flushes

in the detectors, the user will have all the time to take actions to correct the issue. In case the problem is not solved in a reasonable amount of time, the user will intervene on the detector HV to lower or increase the supply voltage accordingly to the situation.

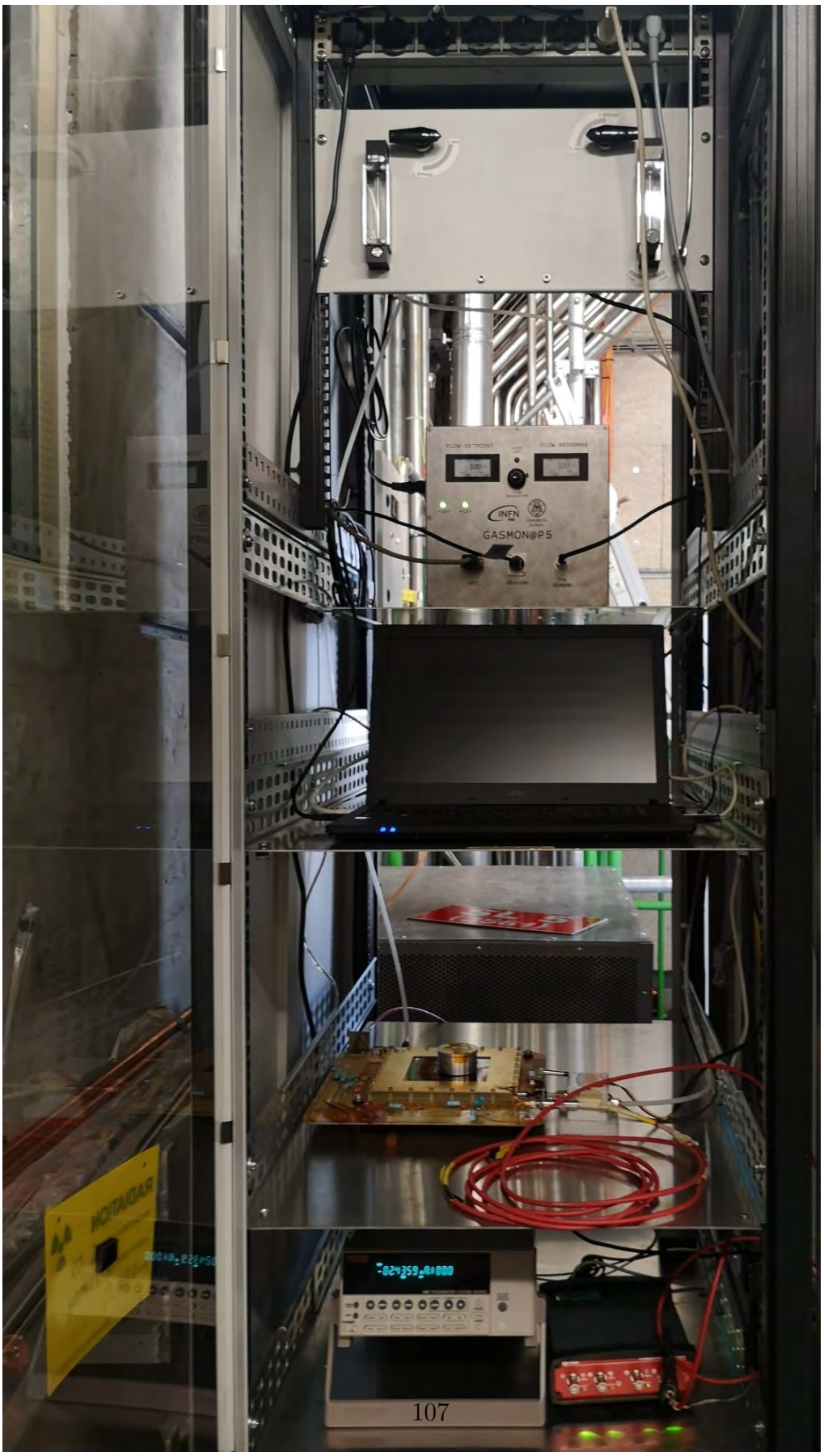

Figure 3.45: Picture of the GASMON@P5 rack.

CHAPTER 4

RATE CAPABILITY AND HV OPTIMIZATION FOR THE ME0 PROJECT

The rate capability is usually used to refer to the ability of a detector to sustain, without great performance loss, a certain particle flux. The intrinsic limitation in the rate capability of all non-resistive gaseous detector technologies lies in the space charge accumulation that distorts the amplification field or reduce the collection efficiency in the drift volume. In particular, MPGD structures behave better than wire-based ones from this point of view because of the fast ions collection that increases the operation range in high particle fluxes. Fig. 4.1 shows the different behaviour of a MWPC technology with respect to a micro-strips one in terms of rate capability.

As explained in Chapter 2 (see Sec. 2.3.3.3), GEM detectors have a unique behaviour in the gain dependency on the flux. The space charge, in the first instance, increases the electron extraction ϵ_{extr} and collection ϵ_{coll} efficiency causing a boost in the detector gain; while at even higher flux the expected gain loss appears. This effect limits the operation regime up to $10^6 \div 10^7$ Hz/cm^2 if a nominal gain is desired or up to $10^8 \div 10^9$ Hz/cm^2 if the increase of the gain is exploited. It is important to notice that these limits are the "metallic limit" i.e. the detector behaviour without any resistive chain for power supplying or protection. Measurements reported in the previous chapter (see Fig. 2.40) exploited such resistors for safe operation, however the metallic limit was measured by irradiating very small areas in order to have negligible currents flowing through such resistors.

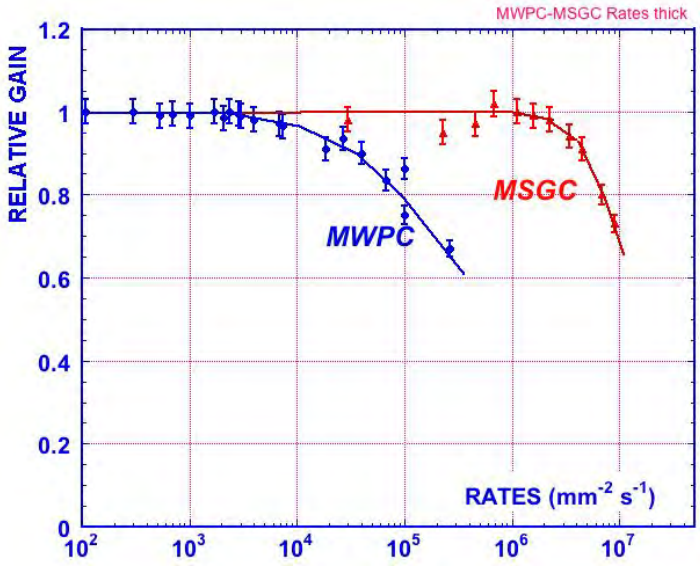

Figure 4.1: Measured gain as a function of the hit rate on the detector for a MWPC and a MSGC [164].

However, in real operation, where high fluxes are present on relatively large areas, the GEM electrodes currents may start to affect the fields at even lower fluxes. For example, in [117] (see Fig. 2.40d), the author irradiated a 10 cm × 10 cm detector on an area A_{irr} of 0.126 cm^2. If normalizing the hit rate on the whole HV sector (A_{sec} =100 cm^2) the scaling factor is around 10^{-3} meaning that the gain peak is reached at fluxes around 30 kHz/cm^2 instead of 30 MHz/cm^2. So depending on the normalization area different informations are given, the author is working at very high local flux (30 MHz/cm^2) to measure the field distortion effect of high charge densities by neglecting the effect of the electrodes currents that are small at low global fluxes (30 kHz/cm^2).

This chapter aims to study the behaviour of triple-GEM when irradiated with low local flux and high global flux, investigating in particular the effect of the protection and filter resistance in order to develop a reliable HV distribution scheme for the ME0 station. I took part actively in the R&D steps performed at CERN presented in this chapter. I had a leading role in the experimental, analysis and simulations tasks needed to reach the current status.

Fig. 4.2 shows the simulated background particle hit rate on the ME0 station expected for HL-LHC. It is also shows the expected average hit rate on each of the 100 cm^2 29 HV transverse sectors proposed for ME0 detectors, it goes from a minimum of 2 kHz/cm^2 to a maximum of 144 kHz/cm^2, i.e. 14 MHz of interacting particles on the hottest HV segment. For such rates no gain effect from space-charge effects is expected; however since

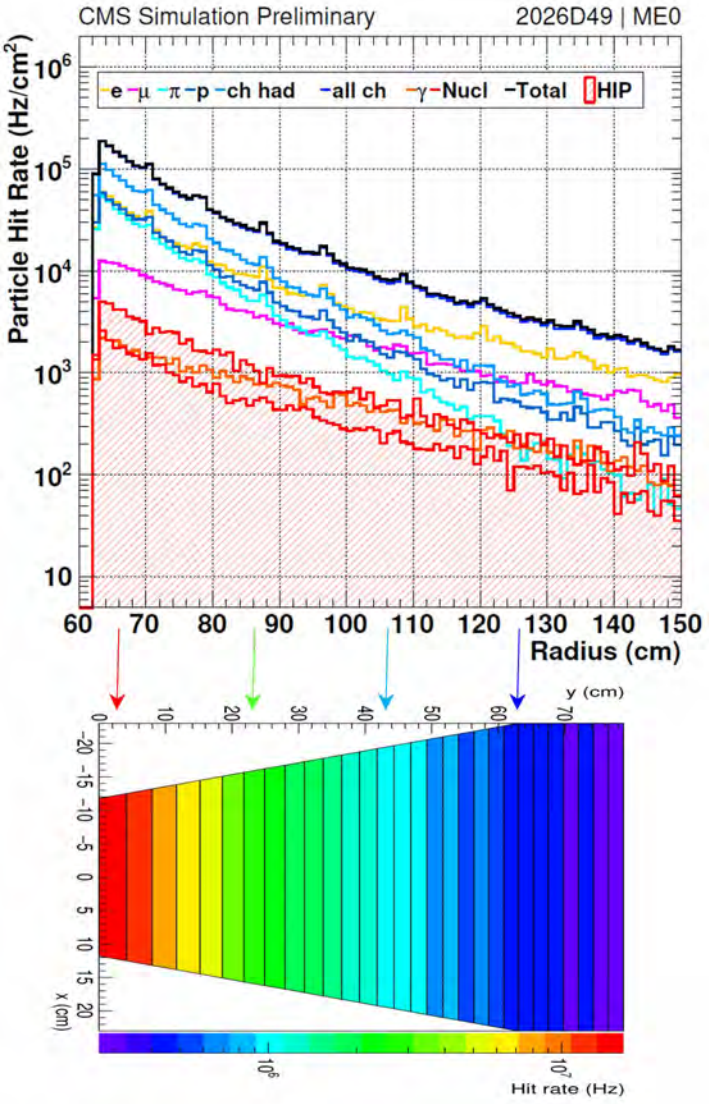

Figure 4.2: Simulated background particle rate in the ME0 region. The hit rate per unit area is given as a function of the distance from the beam pipe, the limits correspond to the ME0 station position [165]. ON the bottom the projected hit rate on the HV sectors of the proposed ME0 foil.

the large area involved the large currents induced on the GEM electrodes may vary the effective voltage present across the GEM foils and gaps. The simulations foresee an average energy deposition per hit of 5.8 keV (see Fig. 4.3), i.e. a number of primaries per hit of around 200, meaning that currents of the order of 10 µA are expected on the third GEM electrodes i.e. voltage drop of the order of tens of V on resistors of the order of MΩ. This drop may cause a huge change in the multiplication factor due to the exponential dependency of the gain on the applied voltage. The voltage

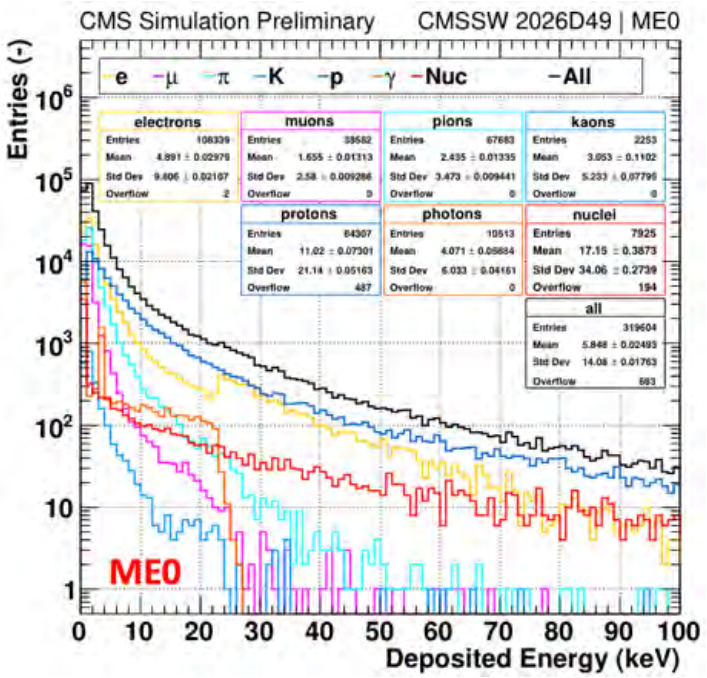

Figure 4.3: Simulated energy deposition of impinging particles in the ME0 detector sensible region [165].

drop ΔV dependencies are multiple:

$$\Delta V \propto R_{electrode} \times n_0 \times G \times \phi, \tag{4.1}$$

where $R_{electrode}$ is the resistor value between the power supply and the electrode, n_0 the average number of primaries charges per hit released by the beam, G the detector gain and ϕ the hit rate on the whole electrode area.

4.1 Measurement of X-rays sources primary charges

The measurements proposed in this chapter will exploit X-rays sources to irradiate triple-GEM detectors. Since the induced currents on the GEM electrodes depend also on the number of primary charges, it is important, to compare different measurements, to precisely know the average energy deposit of the used beams.

As discussed in Sec. 2.1.2.1 the average number of primaries (as referred in the following as n_0) can be estimated via Eq. 2.5:

$$n_0 = \frac{\Delta E}{W_I}$$

where ΔE is the average energy deposited by a particle and $W_I = 28.4\,\text{eV}$ the average energy needed to produce a pair in Ar/CO_2 (70/30). However, if the used X-rays beams are not monochromatic, the photons interact both via Compton and photoelectric effect or some energy is loss because of escaped photons, as in the case of Argon based mixture (see Sec. 2.1.2.1), the theoretical calculation of the ΔE can be difficult. In this section, an experimental measurement of the primaries released in a triple-GEM detector by some radioactive source and X-rays generators is given.

High intensity X-rays beams are usually obtained by X-rays tubes. Electrons are accelerated in the vacuum up to some tens of keV and impinged on a metallic anode target. The deceleration of electrons causes the emission of photons, their energy spectrum is a continuum from very low energies up to the electrons maximum energy ($E = qV$). If the energies involved allows the transitions, target material characteristic X-rays are also emitted. The X-rays tube used for these studies is an AMPTEK Mini-X2 X-rays Tube with a silver target [166]. Fig. 4.4 shows photons energy emission spectra of the aforementioned tube when powered at different voltages. Charac-

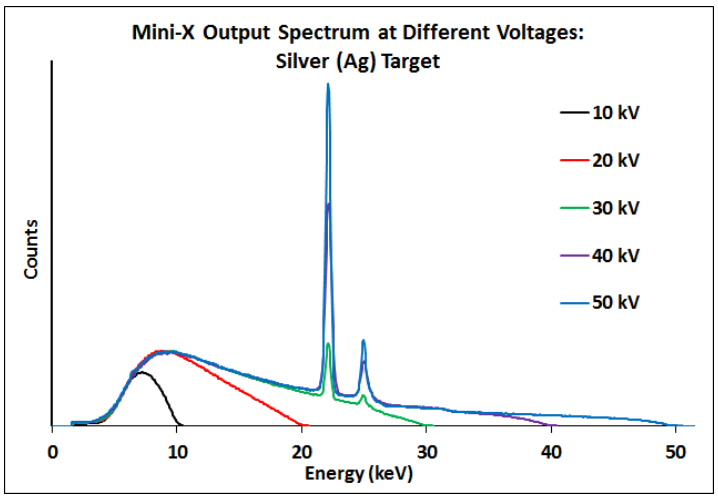

Figure 4.4: Mini-X2 Silver (Ag) Output Spectrum at 10, 20, 30, 40, 50 kV [166].

teristic photons are emitted for voltages higher than $\sim 22\,\text{kV}$ because of silver shells configuration. Tab. 4.1 shows the transition lines for silver, an averaged mean, weighted on the relative intensities, of the energies gives 22.371 keV. The maximum of the characteristic line yield is obtained when powering the tube around 40 kV. Since the photoelectric interaction probability for 22.371 keV photons in a 3 mm of Ar/CO_2 (70/30) is around 4% (see Sec. 2.1.2) such photons are hardly detected in triple-GEM detectors. A typical energy spectrum of the X-rays tube working at 40 kV measured with a CMS GEM like detector (see Fig. 4.5) highlight a peak around 8 keV,

Transition Line	**Relative Intensity**	**Energy** keV
Kα_1	100	22.162
Kα_2	53	21.990
Kβ_1	16	24.942

Table 4.1: Most energetic characteristic X-rays line energies for Silver. A relative intensity of 100 is given to the most probable transition. [49]

with the relative escape peak. Such peak is due to the Copper emission

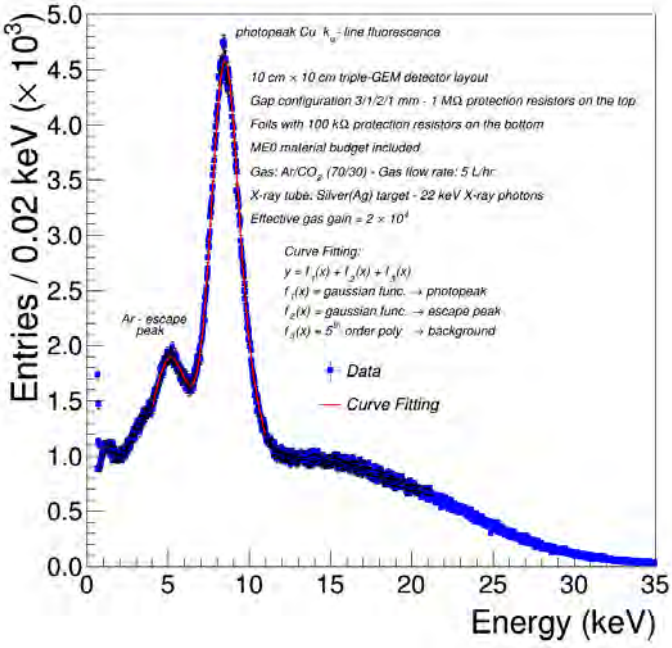

Figure 4.5: X-rays energy spectrum of the Mini-X2 generator at 40 kV when irradiating a 10 cm × 10 cm GEM with a ME0-like budget material.

lines, indeed both CMS and 10 cm × 10 cm GEMs are build with Copper drift electrodes and optional Copper layers in front of the drift gap. This fact allows the relatively high energy photons to excite the Copper electronics shells causing characteristic photons emission. Tab. 4.2 shows such transitions emissions with average 8.128 keV. ^{55}Fe [154] and ^{109}Cd [167] calibrations sources are also used for effective gas gain measurements and calibration. These sources decay by electron capture and emit the K electronic transition lines photons of the daughter isotope. ^{55}Fe decays in ^{55}Mn and the emitted photons are shown in Tab. 4.3, the average energy is 5.955 keV. ^{109}Cd decays in Silver and the emitted photons are the same presented in Tab. 4.1, an additional emission of around 88 keV photons

Transition Line	**Relative Intensity**	**Energy** keV
Kα_1	100	8.047
Kα_2	51	8.027
Kβ_1	17	8.905

Table 4.2: Most energetic characteristic X-rays line energies for Copper. A relative intensity of 100 is given to the most probable transition. [49]

Transition Line	**Relative Intensity**	**Energy** keV
Kα_1	100	5.898
Kα_2	50	5.887
Kβ_1	17	6.490

Table 4.3: Most energetic characteristic X-rays line energies for Manganese. A relative intensity of 100 is given to the most probable transition. [49]

is possible but it is neglected due to the low probability of emission and detection in gaseous detectors.

In the following the experimental setup and the data analysis for the number of primaries measurements is described. By calibrating the energy spectra scale with the help of calibrations sources, the average energy deposit of the sources can be estimated and with the help of Eq. 2.6 the average number of primaries.

4.1.1 Experimental Setup

The scheme of the experimental setup is shown in Fig. 4.6. The signals from the whole anode of a 10 cm × 10 cm GEM detector are readout by a single channel charge amplifier (Ortec 142PC [168]) and shaped (Ortec 474 [169]). The positive shaped signals are sent to a Multi-Channel Analyser (MCA-8000D [170]) that histograms the pulse heights in 8192 channels (corresponding to a range of [0,10] V). Since the pulse heights are proportionals to the induced charged and the whole chain is proportional to the deposited energy, this is the energy spectrum as seen from a GEM detector. Fig. 4.7 shows a typical energy spectrum of a 10 cm × 10 cm triple-GEM detector irradiated with a ^{55}Fe source.

The budget materials (ρx) in front of the 3 mm drift gaps changes a lot between a standard 10 cm × 10 cm (from now on referred as the "10 cm × 10 cm bare") is very different from a CMS GEM like ME0 (around a factor 20 lower). Since the aim of this measurements is to identify the average number of primaries released in a ME0-like detector to study its rate

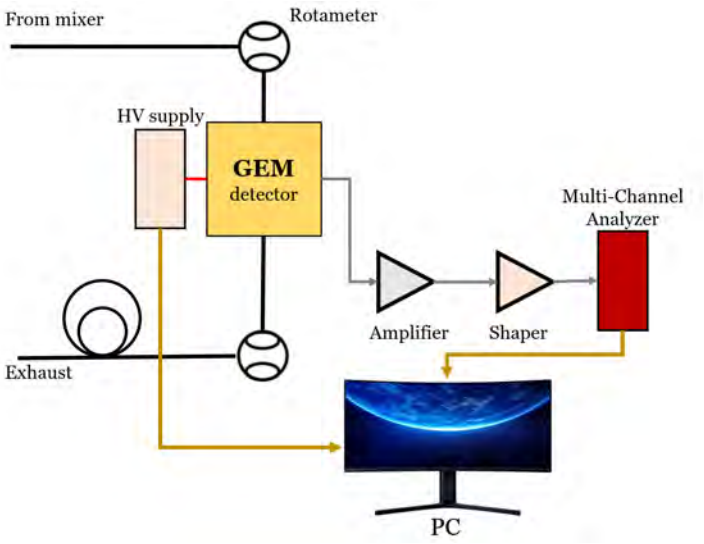

Figure 4.6: Data acquisition chain scheme for the spectra measurement.

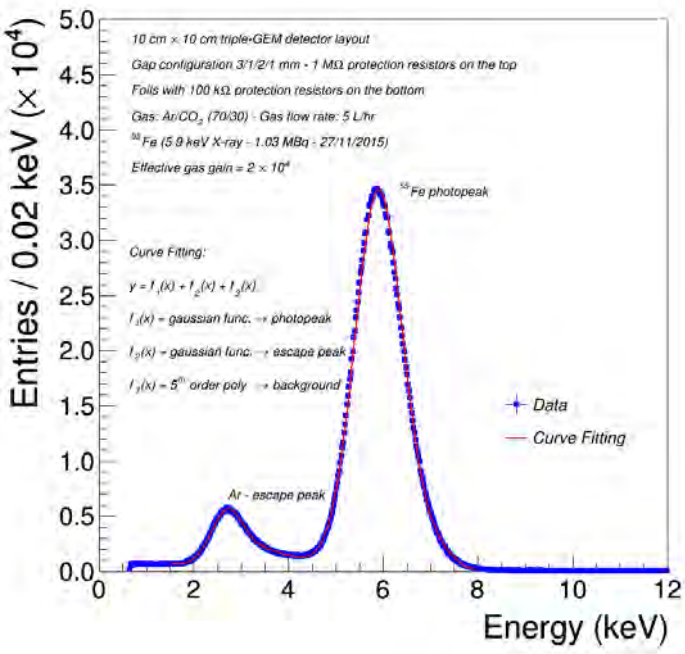

Figure 4.7: Energy spectrum of a ^{55}Fe source when irradiating a 10 cm × 10 cm bare GEM.

capability, it is important to use similar budget materials in front of the conversion gap. Because of the huge difference in budget material between the two detectors, if placing a piece of ME0 drift board in front of a bare 10 cm × 10 cm the difference in the ρx value is lower than 5% with respect

to a standard ME0 detector. This configuration from now on is referred as "10 cm × 10 cm ME0-like". Tab. 4.4 shows the budget materials (in g/cm^2) for the two different 10 cm × 10 cm configurations compared with the one of a real ME0 detector. The change caused in the energy spectra by the

Material	ρx (g/cm^2) 10 cm × 10 cm bare	ρx (g/cm^2) 10 cm × 10 cm ME0-like	ρx (g/cm^2) ME0
Copper	4.48×10^{-3}	6.72×10^{-2}	6.27×10^{-2}
Kapton	2.49×10^{-2}	2.49×10^{-2}	0
Ar/CO_2	5.15×10^{-4}	5.15×10^{-4}	0
FR4	0	5.55×10^{-1}	5.55×10^{-1}
Total:	2.98×10^{-2}	6.48×10^{-1}	6.18×10^{-1}

Table 4.4: Budget materials in front of the drift gap for different triple-GEM detectors.

difference in the budget material can be appreciated in Fig. 4.8 and Fig. 4.9 that show respectively the energy spectrum measured on a bare and on a ME0-like 10 cm × 10 cm detector. The general decrease in the intensity of

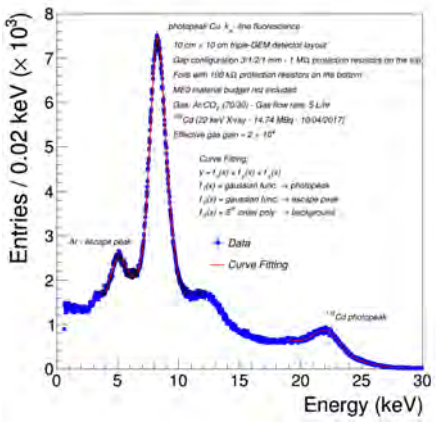

Figure 4.8: Energy spectrum of a ^{109}Cd source when irradiating a 10 cm × 10 cm bare GEM.

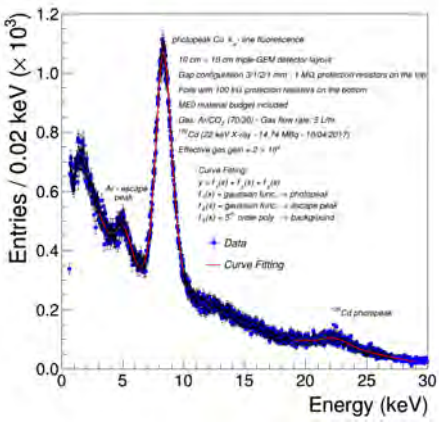

Figure 4.9: Energy spectrum of a ^{109}Cd source when irradiating a 10 cm × 10 cm ME0-like GEM.

the beam (the spectra acquisition times are the same) and the increase of the low energy part of the spectrum is evident.

The spectra presented in the previous are all expressed in energy. In order to have these, a calibration of the MCA Analog to Digital Converter (ADC) values is required. Spectra of the calibrations sources (^{55}Fe and ^{109}Cd) with bare 10 cm × 10 cm are acquired. The known peaks i.e. Silver photo-peak (22.371 keV), Copper photoelectric and escape peaks (8.128 keV

and 5.143 keV) and Manganese photoelectric and escape peaks (5.955 keV and 2.970 keV) are fitted with Gaussian functions and the background with a 5-th order polynomial. The known energies released associated to each peak are plotted against the average of the Gaussian in ADC counts and the data are fitted by a straight line ($f(x) = Ax+B$). Fig. 4.10 shows the result of a typical calibration. The linear parameters A and B can be used now to

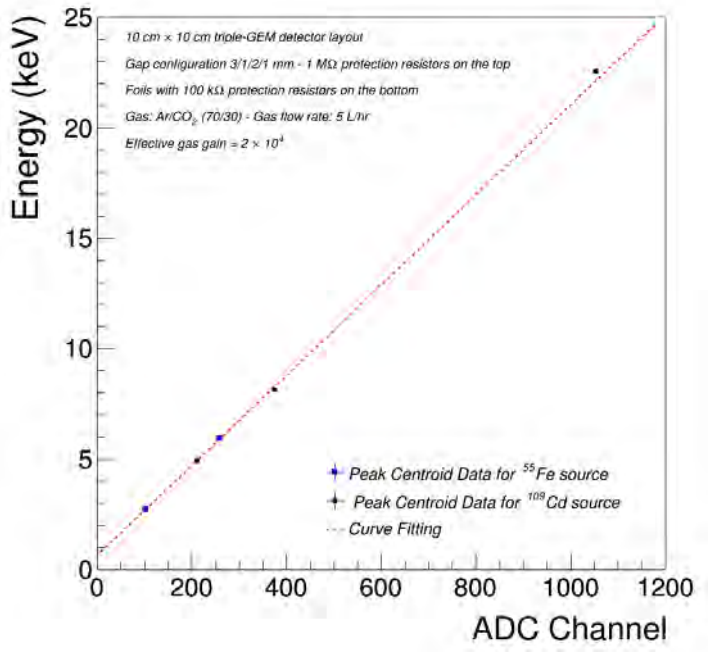

Figure 4.10: ADC value calibration with the centroid positions of the known peaks sources ^{55}Fe and ^{109}Cd.

calibrate the ADC channels of the MCA. After this procedure, the energy spectra relative to different sources with different GEMs budget materials are acquired for the number of primaries estimation. The detectors were operated at an effective gas gain of 2×10^4. However, the working point of the detector during calibration does not have to be the nominal one, the important thing is that all the spectra are acquired at the same gain. To minimize environmental fluctuations of gain and MCA response, all the spectra are measured during the same day. Only a 10 cm × 10 cm detector was used for such measurements, because of the impossibility of calibrating a ME0 detector with a ^{55}Fe source due to the too high budget material intrinsically present.

4.1.2 Data Analysis and Results

When the MCA is well calibrated in energy, the weighted average of the acquired spectra gives the average energy deposit, hence the number of primaries. However, before doing that, an experimental issue has to be solved. Indeed, the 8000-D MCA used for this work had the gating circuit damaged, this means that no trigger signal could be created to select only real signals to be acquired. This fact results in an increasing number of counts at low ADC channels since the MCA counts as signals the small baseline fluctuations of the voltage level due to the intrinsic noise. This background was modelled as an exponential and the signal as a constant, the fit function was:

$$f(x) = f_{noise}(x) + f_{signal}(x) = Ae^{-Bx} + C. \tag{4.2}$$

Fig. 4.11 shows a typical increase of counts in a spectrum fitted with the aforementioned function, parameters A, B and C are referred to "Constant", "Slope" and "Offset" respectively. After the fit, the $f_{noise}(x)$ was

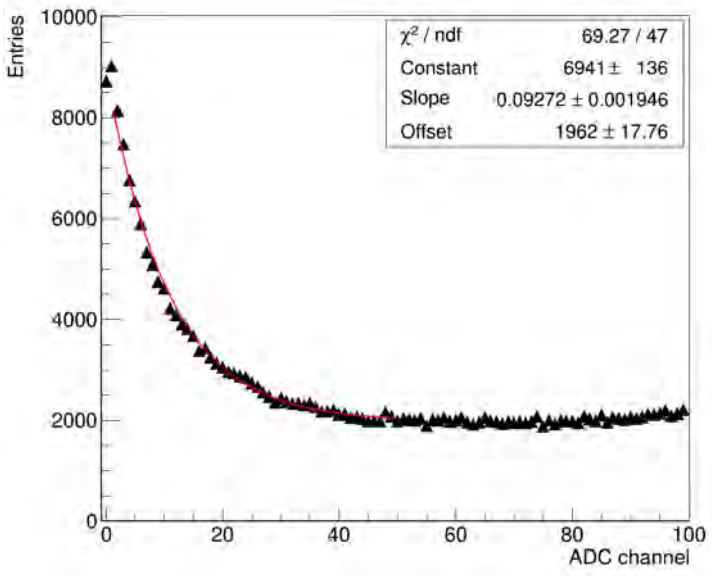

Figure 4.11: Example of a typical increase of counts in the low energy part of the spectra. An exponential fit with an offset is performed in this region to remove the non physical events.

subtracted to the spectrum. A cross check measurement of the number of ^{109}Cd source primaries in a bare 10 cm × 10 cm was performed with a gated MCA [171] and gave a compatible results with the noise suppressed method explained before.

The noise suppressed spectra energies E_i were then weighted averaged using the channel entries w_i as weights:

$$\bar{E} = \frac{\sum_{i=0}^{8191} w_i E_i}{\sum_{i=0}^{8191} w_i}, \tag{4.3}$$

where i runs over the energy calibrated MCA channels. The associated error of such mean is [172, 173]:

$$\bar{E} = \sqrt{\frac{Var(E_i)}{8192}}, \quad Var(E_i) = \left(\frac{\sum_{i=0}^{8191} w_i E_i^2}{\sum_{i=0}^{8191} w_i} - \bar{E}^2 \right) \frac{8192}{8191}. \tag{4.4}$$

The results of the measurements are shown in Tab. 4.5. The results

GEM configuration	**X-rays Source**	$\mathbf{n_0}$	**err** $\mathbf{n_0}$
Bare	^{55}Fe	198	4
Bare	^{109}Cd	365	7
Bare	X-rays tube 20 kV	310	10
Bare	X-rays tube 20 kV with 35 µm Copper attenuator	301	8
ME0-like	^{109}Cd	374	11
ME0-like	X-rays tube 30 kV	386	10
ME0-like	X-rays tube 40 kV	418	9
ME0-like	X-rays tube 50 kV	430	10

Table 4.5: Results of the average number of primaries measurements for different sources and configurations. GEM configurations are divided in bare and ME0, where bare refers to a standard 10 cm × 10 cm and ME0 to a 10 cm × 10 cm with a budget material similar to ME0 detectors.

are consistent between each other and follow the trend of higher number of primaries for higher photons beams energy. A HEED simulation [174] was carried out to test the energy deposit of ^{55}Fe photons in a 10 cm × 10 cm geometry and the result confirmed the measurements for this kind of source (see Fig. 4.12).

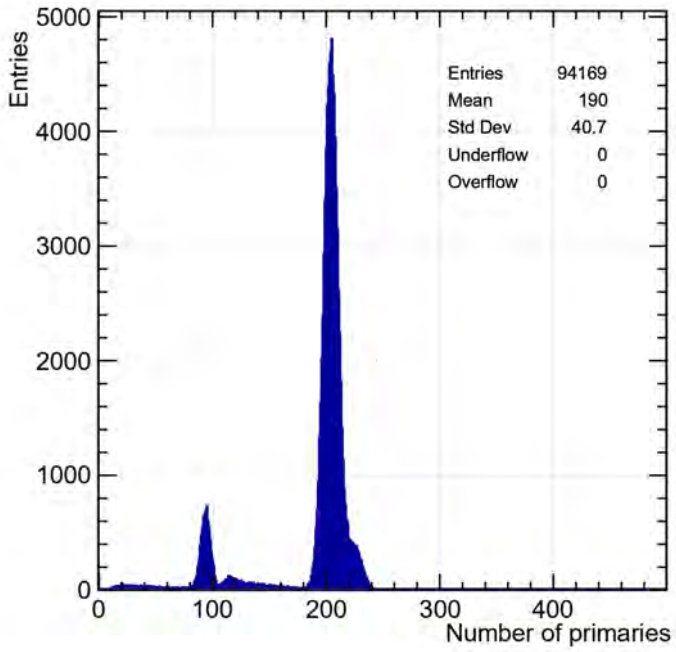

Figure 4.12: Simulated number of primaries distribution of ^{55}Fe photons in 3 mm of Ar/CO_2 (70/30) output by HEED [174].

4.2 Influence of the Protection Resistors and the Nominal Gain on the Rate Capability

In this section the influence of the working point and of the protection resistors on the triple-GEM rate capability is described. This section aims to understand the general trend between the gain drop and such quantities, developing, at the same time, an efficient method to extrapolate the effective gas gain and the hit rate without dedicated electronics.

Usually the effective gain G of a triple-GEM detector is computed by measuring the hit rate R due to a know source irradiating the detector and the anodic current I_{anode} via Eq. A.2:

$$G = \frac{I_{anode}}{en_0R}.$$

The number of primaries for various sources was measured in the previous section. As it will be clear in the following, the main experimental limitation for the gain measurement at high fluxes is the difficulty to take precise measurements of the hit rate because of electronics pile-up.

The procedure and results of this section measurements can be found

in [175].

4.2.1 Experimental Setup

In the following measurements, a bare 10 cm × 10 cm triple-GEM detector in the CMS configuration is irradiated uniformly with a X-rays tube working at 20 kV. The detector is powered with a single HV channel and the correct voltages are supplied to the electrodes with a resistive divider. The presence of the divider makes the measurement non compatible with the effective behaviour of the CMS GEM since they exploit a 7 channel floating power supply. However, the general influence trend of the resistor values and the nominal gain is conserved. Moreover, the work done in this section will be useful to define a reliable procedure to measure the hit rate in the following measurements. The uniform irradiation on the GEM surface helped to reach very high global fluxes with relatively low local rates. The X-rays tube working voltage (20 kV) was chosen to avoid the creation of relatively high-energy photons that may interact only partially in the drift gap and to exploit the highest possible source tube current (200 µA). Fig. 4.13 shows the angular response of the X-rays tube and the distance between the tube and the detector. Being the distance 15 cm and the subtended angle 16.5°, the irradiation uniformity on the detector is around 95%, i.e. the impinging flux in the detector centre is not higher than 5% than the one on the border. If only the voltage drop on the resistor is present and the

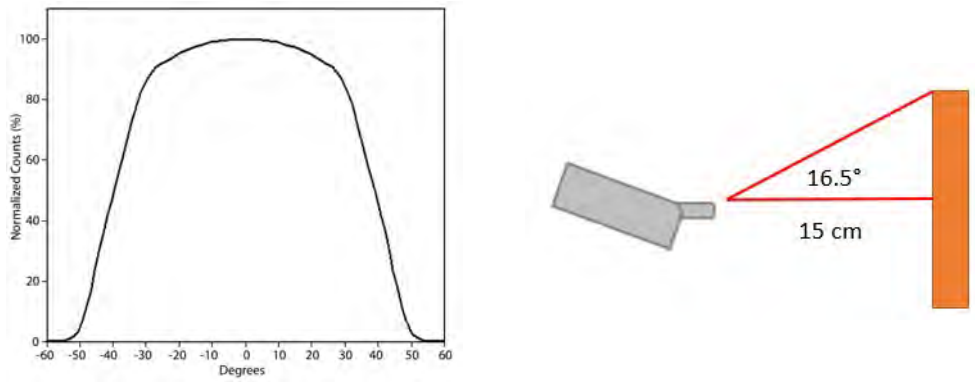

Figure 4.13: X-rays tube angular response (left) [166] and relative position of the triple-GEM detector and the tube (right). Placing the detector at 15 cm distance lead to a irradiation uniformity of 95% on all the detector.

space charge effects are negligible, the uniformity is not a strict requirement for such measurement. Indeed, the current flowing through the resistors is only due to the global hit rate on the HV electrodes and does not depend on its uniformity profile. However, to avoid space-charge effects to bias the

measurement because of a non-uniform irradiation the beam illuminates the detector with the same intensity on all the 100 cm^2 surface.

The detector was irradiated with the tube working always at the same voltage (20 kV), the electron beam current is varied within its range [0, 200]µA. An higher dynamic range in the irradiation flux is reached by shielding the source with attenuators: 1 to 7 35 µm thick Copper layers were placed in front of the X-rays gun. Since there is always a Copper layer in front of the tube, the number of primaries of 301 ± 8, measured in the previous section, is always supposed to be the corrected one for all the attenuations factors.

Both the anodic current and the hit rate were then measured during the irradiation, with a setup very similar to the one used for gain measurement (see Sec. A). The current is measured with a Keithley 6487 [156] that reads in OR all the anodic strips. The signals were pickup from the bottom of the third GEM foil channel and sent to a charge amplifier (Ortec 142PC [168]) and shaped (Ortec 474 [169]). The signal is fed to a discriminator [176] and its outputs are counted by a scaler module [177]. Fig. 4.14 shows the previous explained acquisition modules. The acquisition time for both

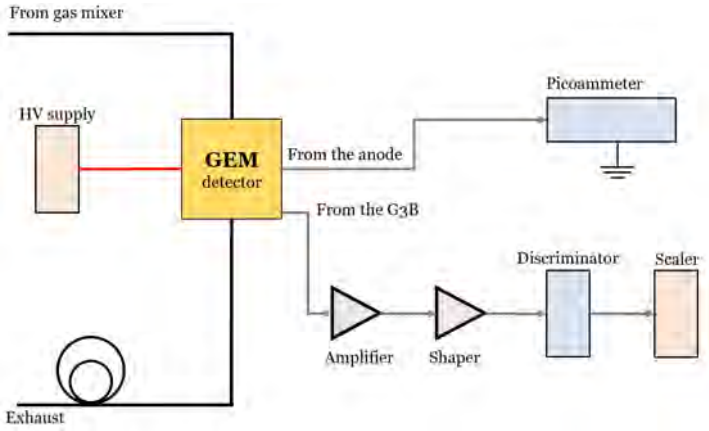

Figure 4.14: Schematics of the data acquisition blocks used for the rate capability measurements.

the rate and current measurements was 60 s.

After preliminary measurements to precisely detect the effective hit rate on the detector, measurement of the gain as a function of the particle interaction rate were performed. Different protection resistors were placed in series with the GEM electrodes and the detector was operated at 5 different nominal gains, the protections resistors values were the same for all the electrodes. Tab. 4.6 shows the selected protections resistor values and gains at which the detector was operated. The preliminary measurements to investigate the rate extrapolation procedure is performed with the detector

Studied gains with fixed resistor ($100\,\mathrm{k\Omega}$)	**Studied resistors at fixed gain** (2.29×10^4)
5.10×10^4	$100\,\mathrm{k\Omega}$
3.42×10^4	$1\,\mathrm{M\Omega}$
2.29×10^4	$10\,\mathrm{M\Omega}$
1.54×10^4	
1.05×10^4	

Table 4.6: Gains and resistors values under test during this section measurements.

working at a gain of 2.29×10^4 with $100\,\mathrm{k\Omega}$ protection resistors.

In the following, the hit rate on the detector will be computed starting from the measured rate and the measured current separately and the results will be discussed.

4.2.2 Hit Rate Extrapolation by Hit Rate Measurement

Fig. 4.15 shows the measured rates R_m as a function of the X-rays tube current I_X for different attenuating factors. Only rates measured with 3 to 7 attenuators are shown since for lower attenuation factors the rate does not carry any useful information due to its very high distortion. Despite this fact, the impinging flux is increasing linearly with the X-rays tube current while the measured rate is not. Because of the signals pile-up and the dead-time of the electronics the measured rate was deviating from linearity in a stronger way as the attenuations factor was reduced. In particular, Fig. 4.15a shows that increasing the flux, a maximum in the measured rate was reached and for higher fluxes the measured rate was reducing. This behaviour highlights the presence of extendable or paralyzable dead time in the acquisition chain.

Dead time τ is defined as the minimum time interval between two events to make the instrumental chain count them both. It can be due both to the detector itself and to the counting electronics, but in general the latter is the part that contributes the most. The pileup is the phenomenon whereby two events that come close enough to each other generate signals that are recognized as a single event. The difference between dead time and pile-up is that the former leads to a loss of the signal if the event that generates it is very close to the previous one, while the pile-up combines the two

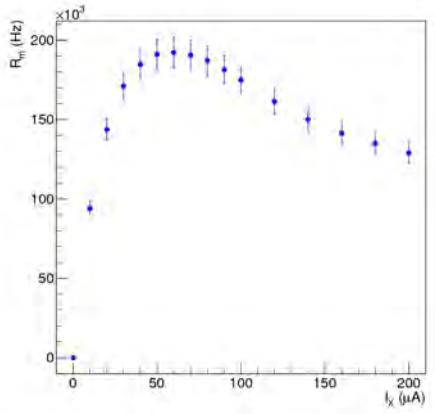

(a) *Measured rate with 3 attenuators*

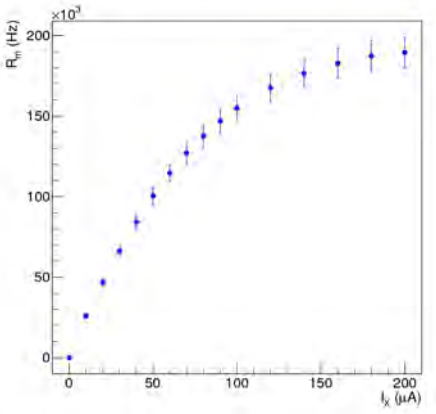

(b) *Measured rate with 4 attenuators*

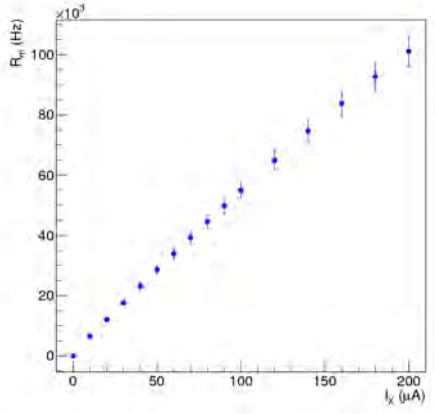

(c) *Measured rate with 5 attenuators*

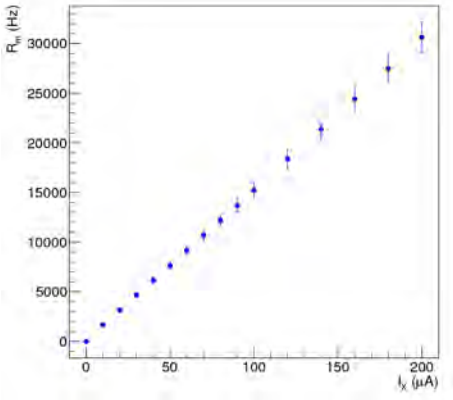

(d) *Measured rate with 6 attenuators*

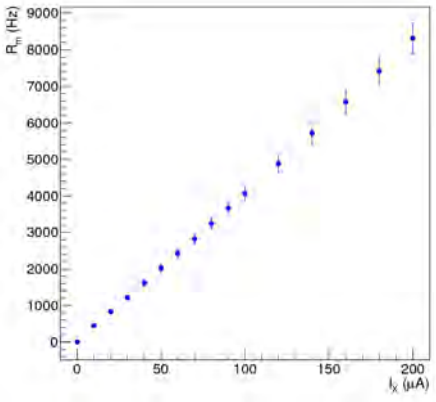

(e) *Measured rate with 7 attenuators*

Figure 4.15: Measured rate as a function of the X-rays tube current for different attenuation factors.

events, keeping track of the energy of both. In a counting experiment both phenomena can occur and their presence leads to a decrease in the number of events that are correctly detected. For such reasons, the measured rate R_m can be supposed to be a function of the effective rate R_e:

$$R_m = f(R_e).$$

Different parametrization can be done to model such effect, if no dead time or pile up is present then $R_m = R_e$. For the experiential counting chain, the resolution time τ can be defined as the minimum interval necessary to resolve two subsequent events. A system is said paralyzable if the arrival of a second event within a time τ leads to an increase in the dead time duration, having to wait an additional time τ before being able to detect a new signal. If the system is paralyzable, it is also possible to have the complete cancellation of the counts for sufficiently high rates, i.e. when there is always a intermediate time less than τ between events. A system is defined as non-paralyzable if the time that allows the detection of an event following the one just counted is set at τ. Therefore, in this case, the dead time is constant and does not depend on the hit rate. In [41, 178] formulas for dead time and pile-up parametrizations are derived. If the system is completely non-paralyzable the counts m in a time T give a measured rate of: $R_m = m/T$ and, on average, $R_e m\tau/T$ counts are lost. The relation can be written as:

$$R_e = R_m + R_e R_m \tau.$$

If inverting the relation the formula becomes:

$$R_m = \frac{R_e}{1 + R_e\tau}. \tag{4.5}$$

On the other hand, if the system is completely paralyzable a signals that are generated in a time smaller than τ from the previous event are not counted. If supposing that the signals arrival times follow a Poisson distribution, the time interval distribution between two events can be written as:

$$P(t) = R_e e^{-R_e t}.$$

Only events that arrive with a time interval larger than τ may be counted, hence the measured rate can be written as:

$$R_m = R_e P(t > \tau) = R_e \int_\tau^\infty R_e e^{-R_e t} dt = R_e e^{-R_e \tau} \tag{4.6}$$

Since experimental chains are usually made of many modules that affect both in a paralyzable or non-paralyzable way the dead time, the use of only one of the previous parametrizations can be limiting. In [178] two similar

empirical parametrization are proposed for taking into account both effects. The first hybrid parametrization proposes two different dead times: τ_p for the paralyzable part and τ_n for the non-paralyzable:

$$R_m = \frac{R_e e^{-R_e \tau_p}}{1 + R_e \tau_n}. \tag{4.7}$$

The second one supposes only one dead time τ but introduces the paralysis probability p:

$$R_m = \frac{R_e e^{-R_e \tau}}{1 + R_e \tau (1 - p)}. \tag{4.8}$$

Such parametrizations were used to fit the acquired data (see Fig. 4.15) to get the real hit rate on the detector. Since the effective rate R_e is linear with the X-rays tube current I_X the goal of this analysis is to find the parameters A and B that link such two quantities:

$$R_e(I_X) = AI_X + B. \tag{4.9}$$

Tab. 4.7 shows the functions used to fit the data shown in Fig. 4.15. Not

Function name:	**Functional form:**	**Number of parameters**
Linear	$AI_X + B$	2
Non-paralyzable	$\frac{AI_X+B}{1+(AI_X+B)\tau}$	3
Paralyzable	$(AI_X + B)e^{-(AI_X+B)\tau}$	3
Hybrid 1	$\frac{(AI_X+B)e^{-(AI_X+B)\tau_p}}{1+(AI_X+B)\tau_n}$	4
Hybrid 2	$\frac{(AI_X+B)e^{-(AI_X+B)\tau}}{1+(AI_X+B)\tau(1-p)}$	4

Table 4.7: Functions used to fit the measured rates R_m as a function of the X-rays tube current I_X to get the effective hit rate R_e.

all the functions are suitable to fit all the pieces of data. In particular, the Linear function is not able to fit non linear data so the fit is performed in the X-rays current subrange of [0,20]µA where the dead time can be neglected. Moreover, the Non-paralyzable function cannot fit the data acquired with 3 attenuators because this function does not foresee a stationary point. In general, some fine tuning of the fitting starting parameters and subranges have to be made to improve the quality of the fits.

The fit procedure revealed that the best χ^2 values are obtained when fitting the data with the Paralyzable function and with the two Hybrids. This fact clearly indicates that more complex functions with a larger number of degrees of freedom are necessary to model the dead time and pile up issue. A function is considered to fit correctly the data not only if the χ^2 gives reasonable values but two other requirements have to be satisfied. The B parameters have to be always compatible with zero within some standard deviation (not more than 3). Indeed, this parameter reflects the expected hit rate with the X-rays tube turned off which has been measured to be of the order of some Hz. Fig. 4.16 shows an example of the B parameter as a function of the number of attenuators when fitting with an Hybrid 1 function. Moreover, the parameter A has to increase exponentially with lower attenuation factors because of the Lambert-Beer law (see Eq. 2.7). The slope of the exponential has to be similar to the attenuation coefficient of Copper at around 10 keV i.e. $\simeq 50\,\mu m$. On average, all the fit functions provided similar results varying from 43.7 µm to 50.4 µm i.e. an average of 1.36 in attenuator unit. Fig. 4.17 shows an example of the A parameter as a function of the number of attenuators when exploiting an Hybrid 1 function, fitted with an exponential function.

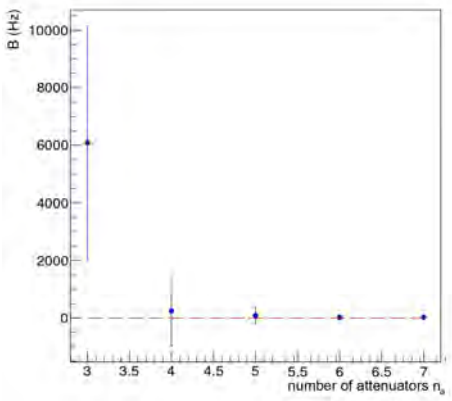

Figure 4.16: Example of B fit parameters as a function of the attenuators, this plot refers to the Hybrid 1 function.

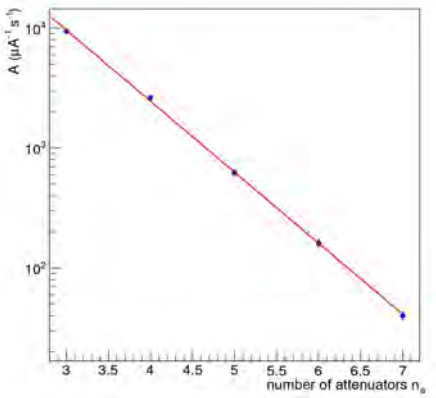

Figure 4.17: Example of the A fit parameters as a function of the attenuators, this plot refers to the Hybrid 1 function. Data are fitted with an exponential function

The exponential fit of the A parameters as a function of the number of attenuators is required to extrapolate the effective hit rate also at lower attenuations where the measurements where too distorted. Hence, the hit rate R_e is extrapolated for every attenuation factors using Eq. 4.9, where A and B are the outputs of the fit for attenuators 3 to 7 and, for the others

A is extrapolated exponentially and B is set to zero. Fig. 4.18 shows the extrapolated rates with the various fit functions for selected values of attenuators. From the plots it is clear that all the fit functions gave similar

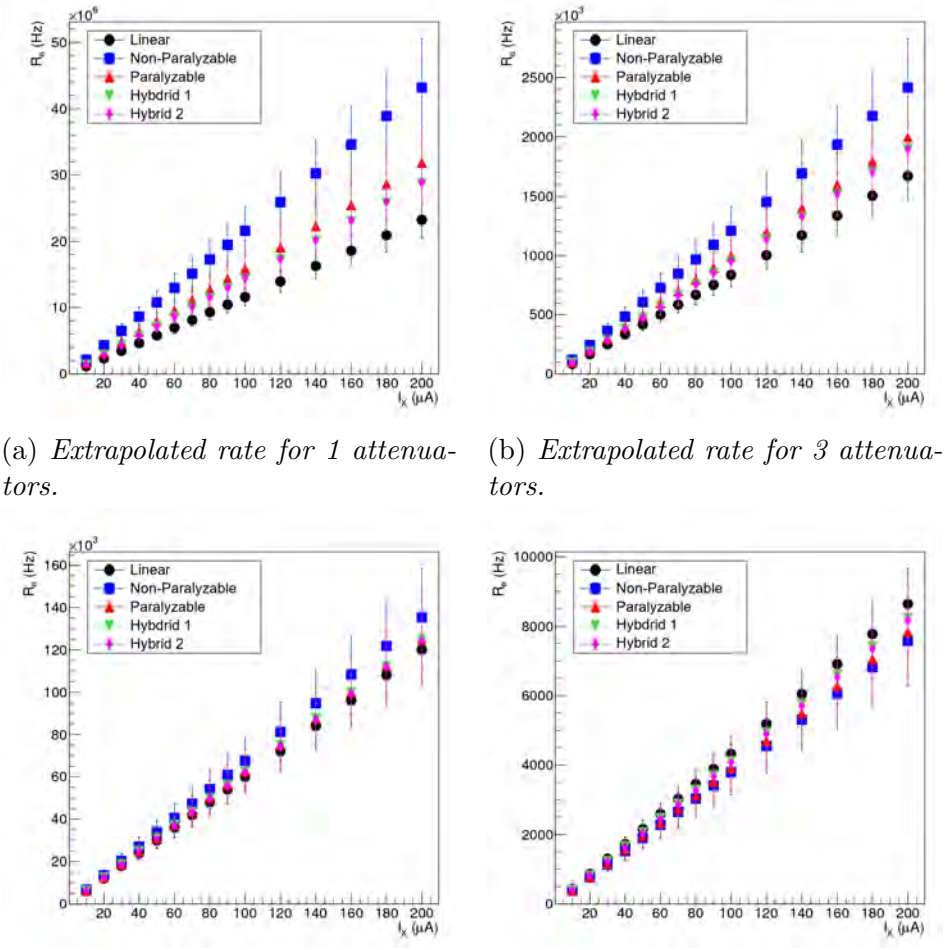

(a) *Extrapolated rate for 1 attenuators.*

(b) *Extrapolated rate for 3 attenuators.*

(c) *Extrapolated rate for 5 attenuators.*

(d) *Extrapolated rate for 7 attenuators.*

Figure 4.18: Extrapolated rates with the various fit functions for selected values of attenuators.

results between each other. However, the Non-paralyzable and the Linear functions progressively move away from the other ones. This fact suggests that the two aforementioned functions may not give reliable results for low attenuations factors. Indeed, a small systematic error in the definition of the A parameter can lead to very large variation in the extrapolated rate at small number of attenuators. The best extrapolated rates with this method is then calculated by the weighted mean of the rates obtained with only the Paralyzable, Hybrid 1 and Hybrid 2 functions. Fig. 4.19 shows the average

rate computed in such way.

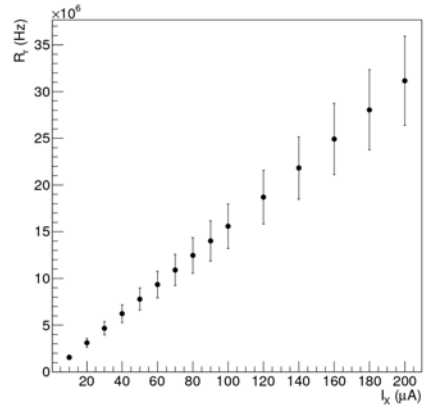

(a) *Average rate for 1 attenuators.*

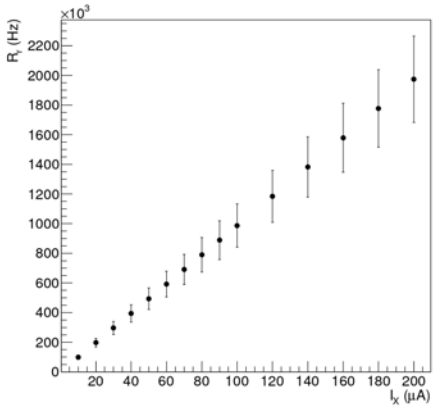

(b) *Average rate for 3 attenuators.*

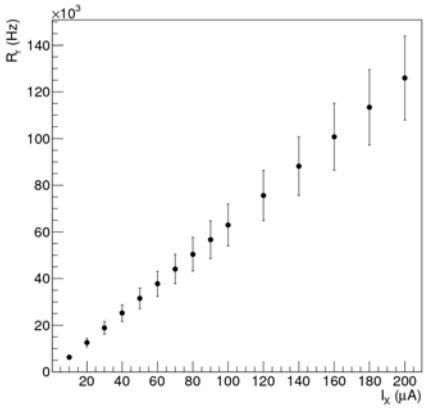

(c) *Average rate for 5 attenuators.*

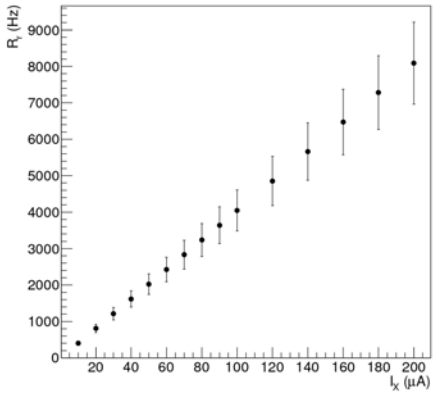

(d) *Average rate for 7 attenuators.*

Figure 4.19: Averaged rates obtained with the weighted average of the extrapolated rate from the Paralyzable, Hybrid 1 and Hybrid 2 functions.

4.2.3 Hit Rate Extrapolation by Anodic Current Measurements

To validate the previous method of measurement, a different procedure exploiting a different observable is needed. From Eq. A.2:

$$G = \frac{I_{anode}}{en_0R},$$

it is evident that, if the gain remains constant, the anodic current I_{anode} increases directly proportional with the hit rate. Fig. 4.20 shows the measured anodic current as a function of the X-rays tube current for different

number of attenuators. It is possible to notice that, for large attenuation

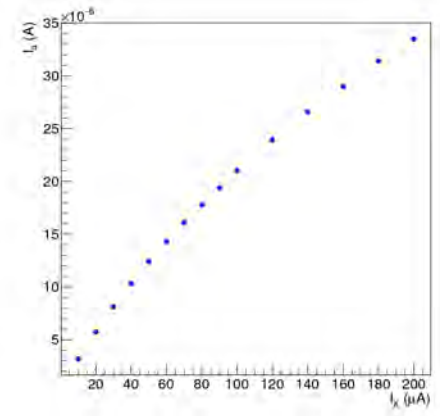

(a) *Measured current for 1 attenuators.*

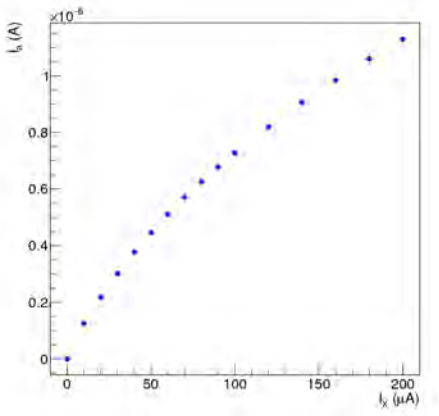

(b) *Measured current for 3 attenuators.*

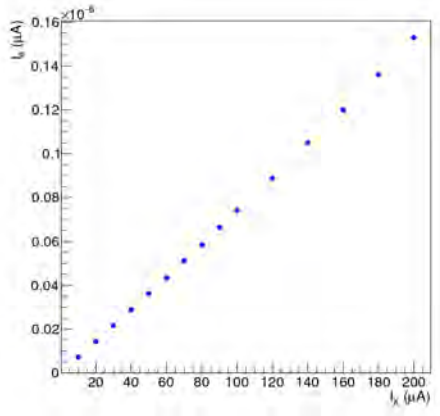

(c) *Measured current for 5 attenuators.*

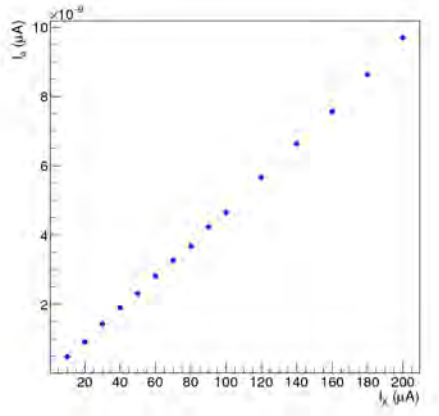

(d) *Measured current for 7 attenuators.*

Figure 4.20: Measured values of the anodic current as a function of the X-rays tube current for selected values of attenuation.

factors, the current is almost linear with the X-rays tube current, i.e. the impinging flux. On the other hand, for low attenuation, the current lose its linearity and the curve tend to bend at higher source currents. This fact is not imputable to any of the previsions issues such as pile up and dead time. Indeed, the anodic current is always representative of the detector behaviour and it is not dependent on the single event since it is measuring the average contribution of a large number of interactions. For this reason the current bending is only due to detector gain losses because of the voltage drops on the electrodes.

This rate extrapolation method was extensively used in literature for

rate capability measurement on detectors without dedicated electronics [46, 179–181]

The measured anodic current will be exploited in the next subsection to compute the gain. However, for the hit rate measurement purpose the anodic current has to be corrected for the gain drop. Indeed, to compute the effective hit rate, the current has to be linearized to get I_{lin}, i.e. the corrected current like no gain drop is present. If this is achieved the effective rate is:

$$R_e = \frac{I_{lin}}{en_0 G^*}, \tag{4.10}$$

where G^* is the gain at low irradiation fluxes. The linearization procedure can be carried on with the same strategy as the previous measurement. In this case two functions were used to fit the data and get the linearized current as a function of the X-rays tube current. The first function referred to as Linear can be written as:

$$I_{lin} = AI_X + B,$$

the fit has to be performed only in a I_X subrange were the gain loss is negligible. The second function, referred as Empiric can be written as:

$$I_{lin} = \frac{AI_X + B}{1 + k(AI_X + B)},$$

where k is a bending factor. The latter function is functionally the same as the Non-Paralyzable presented in the previous. However, in this case, the model behind the bending is not well know and this function is used just because it fits nicely the data.

Fig. 4.21 shows the extrapolated rate obtained by the linearized currents with both the proposed functions. It is evident that the two fit functions gave similar values of the rates. The slight differences are attributable to the small errors that are present in the measured currents. Indeed, because of the relatively long acquisition time the error on the single measurement is around 3 order of magnitude lower than the value itself.

In general, if the bending of the current is low or negligible a fit with the Linear function is preferable, while if the bending is more evident the Empiric fit is the one that gives better results.

4.2.4 Results

The weighted average of the hit rate extrapolated from the rate measurement (see Fig. 4.19) and the weighted average of the ones extrapolated from the anodic current linearisation are compared in Fig. 4.22. It is clear that

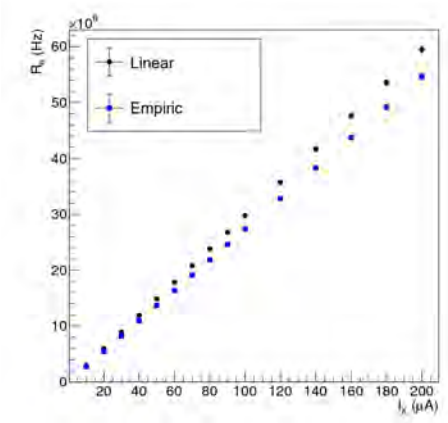

(a) *Extrapolated rate for 1 attenuator.*

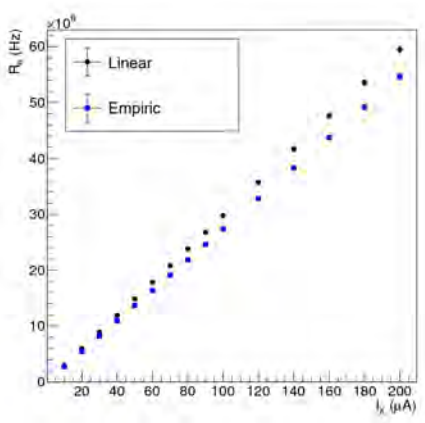

(b) *Extrapolated rate for 3 attenuator.*

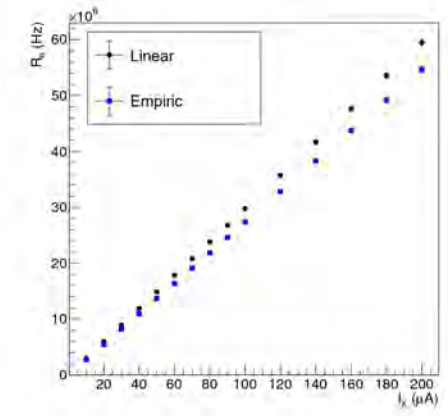

(c) *Extrapolated rate for 5 attenuator.*

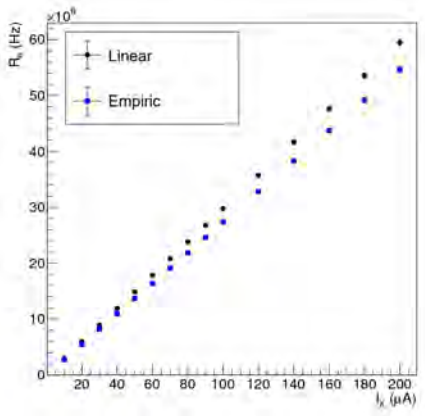

(d) *Extrapolated rate for 7 attenuator.*

Figure 4.21: Effective hit rates extrapolated from the anodic current linearization with the two different fit functions at different attenuation factors.

the extrapolated rates are compatible down to a number of attenuators of 3. For lower attenuation factors, the rate extrapolated from the rate measurements is systematically lower (up to a factor 2) than the one extrapolated from the current. This effect is related to the extrapolation at low attenuation factors, indeed a small bias in the the exponential interpolation may cause a large variation to the extrapolated data.

In conclusion, the extrapolation from the rate measurement is reliable only if the rate is directly measured and fitted, while the extrapolation at lower rates may fail due to its exponential dependency. In general it is recommended to use the current linearization method for precise rate

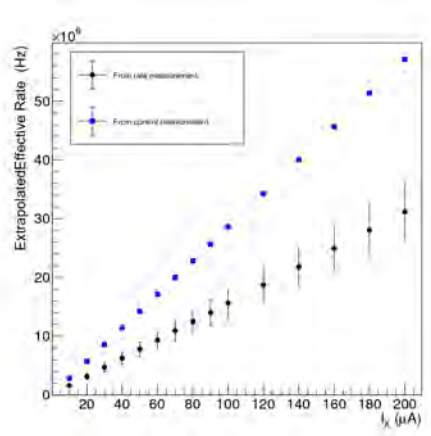

(a) *Extrapolated rate for 1 attenuator.*

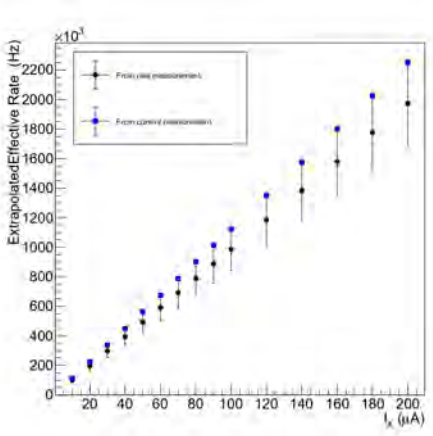

(b) *Extrapolated rate for 3 attenuator.*

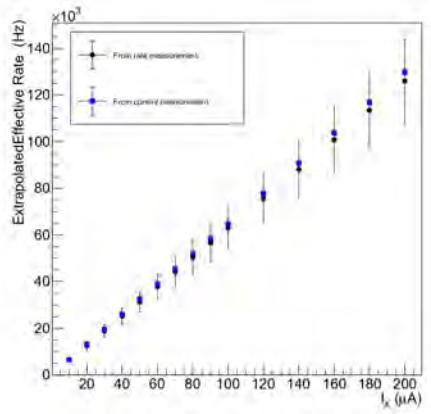

(c) *Extrapolated rate for 5 attenuator.*

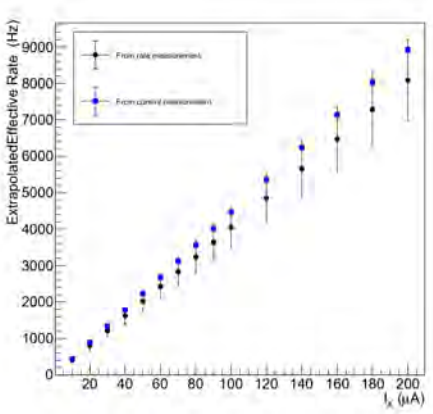

(d) *Extrapolated rate for 7 attenuator.*

Figure 4.22: Comparison of the effective hit rates extrapolated with the two methods at different attenuation factors.

measurement at high fluxes irradiation because it provides more reliable data also with smaller error bars. Indeed, for the following analysis, the rate from the linearized current method (blue dots in Fig. 4.22) is used and all the following measurements exploited such method for the rate estimation.

After having fixed the rate extrapolation method, the anodic currents at the various X-rays tube currents and attenuations factors are measured on the $10\,\text{cm} \times 10\,\text{cm}$ detector working at different nominal gain and protection resistors with the values presented in Tab. 4.6. Exploiting Eq. A.2 the effective gas gain is computed for all the data points. Fig. 4.23 shows the measured gains as a function of the hit rate for different values of

the nominal gain with fixed values of protection resistors (100 kΩ on all the electrodes). In particular, at higher gains the gain decreases with a larger slope at high effective rate. This behaviour is even more evident in Fig. 4.24, where the gains are normalized to their starting value. This

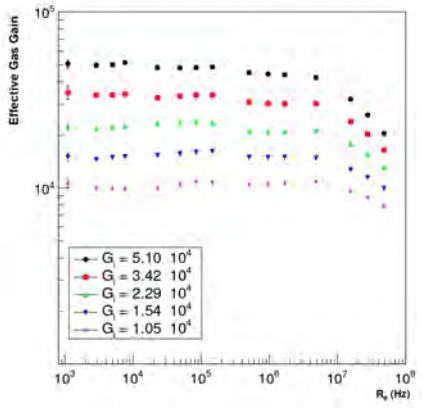

Figure 4.23: Effective gas gains as a function of the hit rate on the 10 cm × 10 cm for different values of the nominal gain.

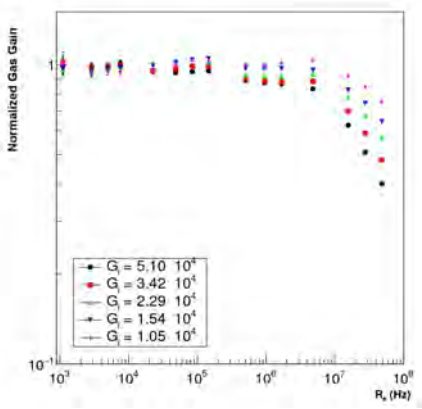

Figure 4.24: Normalized effective gas gains as a function of the hit rate on the 10 cm × 10 cm for different values of the nominal gain.

behaviour is expected since with higher multiplication factors the charge developed in the avalanche is larger as well as the current flowing on the electrodes. Despite the larger relative decrease in gain, in this range of R_e, the curve with the highest initial gain is still the one with the highest nominal value. This fact must be taken into consideration in order to optimize the detector's performance for its use in high rate environments. On the other hand, Fig. 4.25 shows the measured gains as a function of the hit rate for different values of the protection resistors at fixed gain (2.29×10^4). Fig. 4.26 shows also the same curves but normalized to the nominal gain. As expected, the higher the resistor the higher is the gain drop because of the larger voltage drop on the protection resistors.

In order to better understand the gain behaviour of a GEM detector as a function of the initial gain and protection resistors values, the percentage gain loss at fixed values of hit rate is plotted. Fig. 4.27 shows the maximum measured gain loss, i.e. when irradiating at 5.7×10^7 Hz, as a function of the initial gain. The trend is strongly non linear, however the exact trend is not precisely known. Nevertheless, the data are fitted with a logarithmic function that works fine enough, however nothing prevents the data to follow others trends. Fig. 4.28 shows the maximum gain loss at 5.7×10^7 Hz as a function of the protection resistor value. As for the previous plot the data are fitted with a logarithmic function and also in this case the

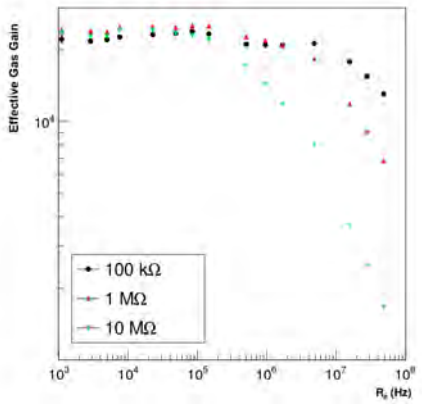

Figure 4.25: Effective gas gains as a function of the hit rate on the 10 cm × 10 cm for different values of the protection resistor.

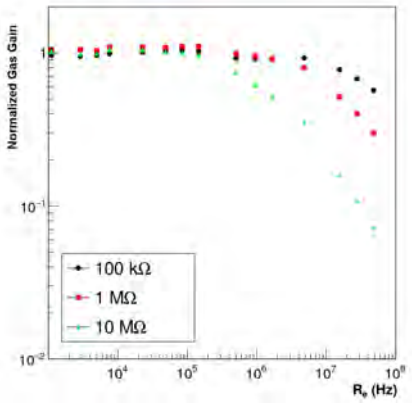

Figure 4.26: Normalized effective gas gains as a function of the hit rate on the 10 cm × 10 cm for different values of the protection resistor.

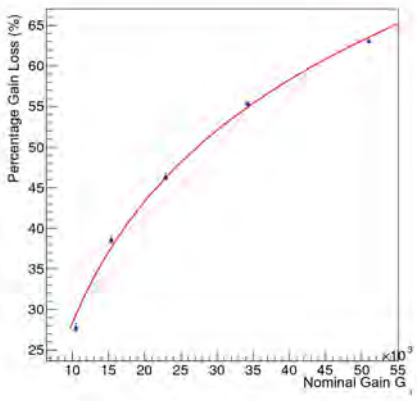

Figure 4.27: Percentage gain loss measured at 5.7×10^7 Hz for different values of the nominal gain. A logarithmic fit is superimposed to the data points to guide the eye.

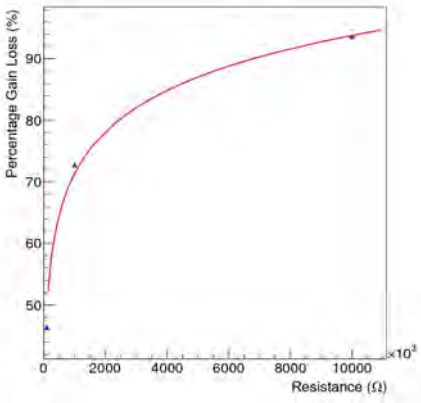

Figure 4.28: Percentage gain loss measured at 5.7×10^7 Hz for different values of the protection resistor. A logarithmic fit is superimposed to the data points to guide the eye.

procedure is good enough to fit nicely the data despite the presence of only three points.

This tests demonstrated the limit of extrapolating very high hit rate without the use of dedicated electronics. In particular using large pile up and dead time electronics may give good results only up to a certain

rate because the exponential interpolation is giving large systematic errors starting from small parameters bias. However, the interpolation with the anodic current linearization gave good results with relatively small statistical errors, giving a powerful experimental method to extrapolate the hit rate also in case of detector gain losses. The result of these tests confirmed the hypotheses that higher nominal gain and higher protection resistors increase the percentage gain loss at fixed hit rates. The trend is strongly non linear and can be modelled empirically with a logarithmic function. However this latter result has to be taken with a grain of salt in the CMS GEM framework since the detector used is not in the same configuration due to the use of a voltage divider for powering the electrodes.

4.3 Rate Capability Measurement on CMS-like detectors

After having defined the experiential procedures needed for rate capability measurements a set of tests on both small and large size prototypes were performed. A $10\,\text{cm} \times 10\,\text{cm}$ detector with the ME0-like materials in front of the drift gap was tested under heavy irradiation to have preliminary results for a following measurement with a ME0 prototype with transversal foils segmentation. Since both the detectors were powered with the A1515TG board [182],the board used for CMS operation, their behaviours is expected to be similar to the one during real ME0 operation. Since a single sector of the transversal segmented ME0 prototype is large around $100\,\text{cm}^2$ the behaviour of the small and large prototypes are supposed to be the same if the rate per HV sector is the same; however this is true only if there is no HV filter. Indeed, in presence of resistive HV filter, all the sectors currents will flow through the same filtering resistors causing a larger voltage drop. The detectors used mounted $1\,\text{M}\Omega$ protection resistor on the top side of the GEM foils and $100\,\text{k}\Omega$ on the bottom side. An additional $10\,\text{M}\Omega$ protection resistor was placed in series at the drift electrode.

4.3.1 Small Detector

The $10\,\text{cm} \times 10\,\text{cm}$ detector with ME0-like budget material was irradiated at the same time with two X-rays tubes working at $40\,\text{kV}$. The operating voltage of the X-rays generator was increased because of the larger budget material with respect to a bare $10\,\text{cm} \times 10\,\text{cm}$. Indeed, the X-rays generated with the tube working at $20\,\text{kV}$ were almost all absorbed before entering the gas gap. Increasing the working voltage provided more energetic X-rays and also the resonance creation of Silver characteristic X-rays

($\approx$ 22.4 keV). However, because of the limited power provided by the X-rays gun, at higher voltages the electron beam current dynamic range was limited to [0,100]µA. Therefore, in order to reach higher hit rates, two X-rays tubes were used to irradiated the detector. Fig. 4.29 shows a photo of the experimental setup.

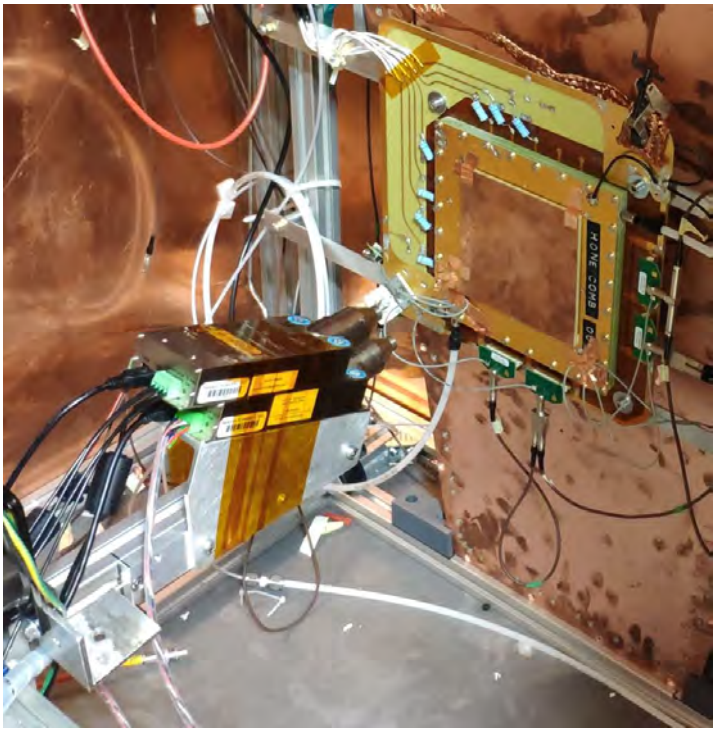

Figure 4.29: Photo of the setup during the 10 cm × 10 cm irradiation test.

During the test, the tube current of one X-rays generator is increased in step of 5 µA until the maximum. After that, the second generator is turned on and the current is increased in the same way maintaining the first tube at its maximum. For this reason the following plots will show X-rays current spanning from 0 to 200 µA. Two tests were performed with the detector working at two different gains: 2.0×10^4 and 3.1×10^4. No attenuation of the beam was applied but the distance from the tube and the detector was varied (110 cm, 30 cm and 15 cm). A dedicated LabVIEW code acquired the measured anodic current from Keithley 6487 pico-ammeter along with the power supply parameters such as the set voltages V_{set} and the currents on the electrodes I_{mondet}. The rate was extrapolated by linearizing the anodic current as explained in the previous section. Since the two X-rays tubes had slight different behaviours, better results were obtained by fitting the anodic current in the two separated sub-ranges corresponding to the use of only one or both the X-rays generators. An example of anodic current fit and rate extrapolations are shown respectively in Fig. 4.30 and

Fig. 4.31. The rates were extrapolated independently within the two tests,

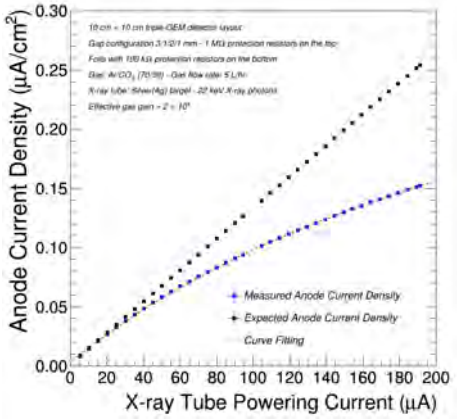

Figure 4.30: Example of anodic current measured with the 10 cm × 10 cm (in blue), with a fit with the Empiric function the linearized current is extrapolated (in black).

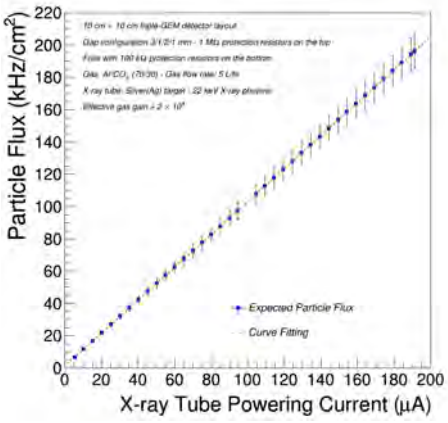

Figure 4.31: Example of extrapolated hit rate from the linearization procedure.

the obtained values at the various distances are compatible each other, confirming the robustness of the method.

With the estimated rate it was possible to normalize the electrodes currents on the number of events in case of no gain loss. The current per event on each electrode is depending on the extraction and collection efficiencies of the foils and on the number of primary charges released. Such values, for the eight GEM electrodes, are shown in Tab. 4.8. In particular the average current per event on the anode electrode is compatible with the one expected if a primary charge of 418 ± 9 is multiplied by a factor 2×10^4, confirming the result presented in Tab. 4.5.

In order to get the detector gain Eq. A.2 can be used:

$$G = \frac{I_{anode}}{n_0 e R}.$$

However, it is possible to notice that since the rate is extrapolated from the anodic current via Eq. 4.10:

$$R = \frac{I_{lin}}{n_0 e G^*},$$

if using the extrapolated rate and its error values to propagate the gain error the n_0 error is propagated two times. To avoid an overestimation of

Electrode	**Current per event (normalized)**	**Current per event (μA/event)**	**error (μA/event)**
Drift	32.2	6.85×10^{-13}	2.70×10^{-15}
G1T	6.1	1.31×10^{-13}	6.20×10^{-16}
G1B	1.5	3.87×10^{-14}	7.60×10^{-17}
G2T	9.2	1.95×10^{-13}	8.30×10^{-16}
G2B	-4.5	-9.54×10^{-14}	3.40×10^{-16}
G3T	100.0	2.13×10^{-12}	8.80×10^{-15}
G3B	-77.4	-1.65×10^{-12}	6.90×10^{-15}
Anode	-62.4	-1.33×10^{-12}	5.53×10^{-15}

Table 4.8: Average collected current per event measured for each electrode when a 10 cm × 10 cm with ME0 materials at 2×10^4 gain is irradiated with a X-rays tube working a 40 kV. The values are also normalized to the largest current, giving 100 to the G2T current.

the errors, the following equation, formally the same as Eq. A.2, was used for the gain and its error evaluation:

$$G = \frac{I_{anode}}{I_{lin}} G^* \tag{4.11}$$

The gain as a function of the hit rate for the two different initial gains is shown in Fig. 4.32 while Fig. 4.33 shows the same values but normalized to the initial detector gain. Since the average number of primary charges expected in ME0 (around 200) is a factor two smaller than the one used for this test, a correction is necessary. In first approximation it is possible to assume that the voltage drops (see Eq. 4.1) linearly with n_0. Therefore two beams named a and b that release on average $n_{0,a}$ and $n_{0,b}$ primaries, create the same gain loss if irradiating it with two different hit rates R_a and R_b:

$$R_a n_{0,a} = R_b n_b.$$

Fig. 4.34 and Fig. 4.35 show respectively the effective gas gain and the normalized one as a function of the corrected hit rate as the beam released on average the same amount of primaries as the one expected in ME0. It is important to notice that this approximation is corrected only at the first order. Indeed, the gain dependency on the voltage drop is not linear and the other quantities present in Eq. 4.1 showed non-linear dependency on the percentage gain variation (see previous section). Moreover, the local distortion of collection and extraction efficiencies with different avalanche sizes is not considered. Therefore, the gain drop of the detector when irradiated in this test configuration has to be considered an overestimation of the behaviour it would have with a lower number of primaries. A better,

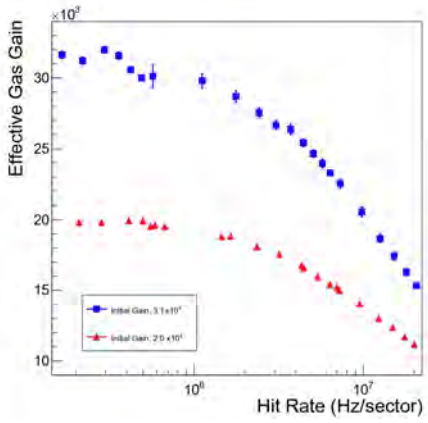

Figure 4.32: Effective gas gain measured as a function of the hit rate on the 10 cm × 10 cm detector working at two different gain values.

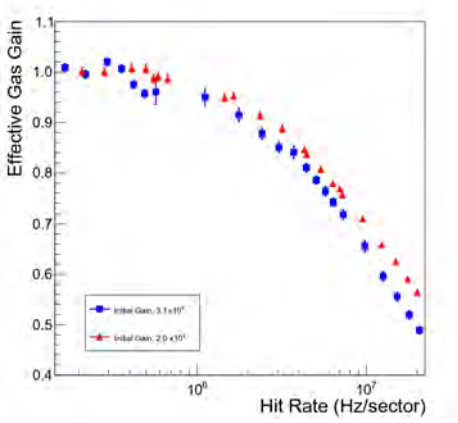

Figure 4.33: Effective gas gain normalized to the initial value as a function of the hit rate on the 10 cm × 10 cm detector working at two different gain values.

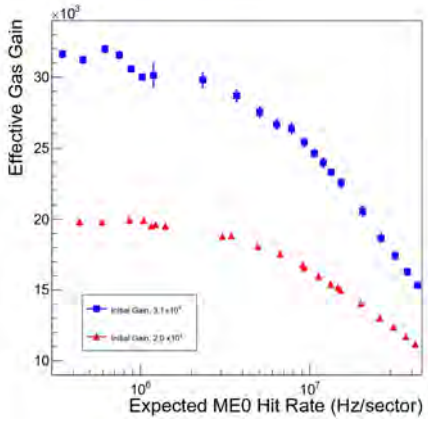

Figure 4.34: Effective gas gain as a function of the expected ME0 hit rate.

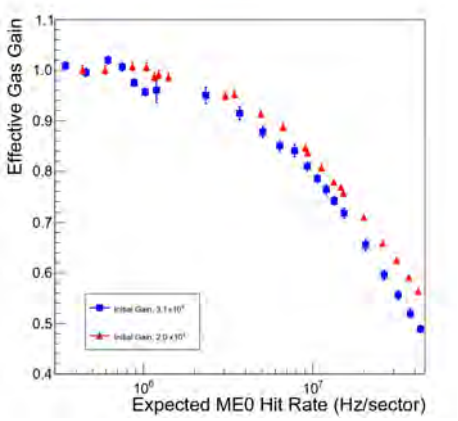

Figure 4.35: Normalized gain as a function of the expected ME0 hit rate.

but not perfect, estimation of a ME0 HV sector behaviour is given when correcting for the different number of primaries. In conclusion, a 10 cm × 10 cm detector, that is a good approximation of a double segmented ME0 sector, will lose around 20% of its nominal gain when irradiated with a ME0-like beam at 14 MHz/sector. If operating the detector at the nominal CMS gain (2×10^4) such gain drop may cause a muon detection efficiency loss on high η HV partitions [144] (at least the last two from Fig. 4.2) while the rest of the detector should operate normally. With an increased initial gain of 3.1×10^4, also in presence of gain loss, the detector will work

at full efficiency. However, operating a detector at relatively high gain in such harsh particle background may increase the discharge probability and negatively influence the operation stability.

To validate the fact that only the voltage drop causes the gain loss at such interacting fluxes, a further measure was performed. The same detector was irradiated at very low and constant X-rays flux while the voltages were set to the expected one during irradiation. Using the values of the currents monitored during the previous tests it was possible to compute the effective voltage at every irradiation flux. On the j-th electrode the effective voltage V^j_{eff} is:

$$V^j_{eff} = V^j_{set} - I^j_{mondet} R^j \tag{4.12}$$

where R^j and I^j_{mondet} are respectively the resistance value and the electrode current for the j-th electrode. It is important to notice that the voltages expressed here are the absolute voltage with respect to ground and not the voltage difference across the gap as the one treated by the power supply. Moreover, it is mandatory to use the electrode current I^j_{mondet} values and not the I^j_{mon} that measures the current flowing through one gap. Given this model, it is possible to simulate the voltage drop due to intense irradiation by setting the detector voltages equal to the effective one for various hit rate values. Fig. 4.36 shows the gain measured in the previous test (Real Irradiation) and the one measured by applying the effective voltages (Simulated Irradiation). Fig. 4.37 shows the same plot with the rate axis corrected for the ME0 background. It is possible to notice that the two gain

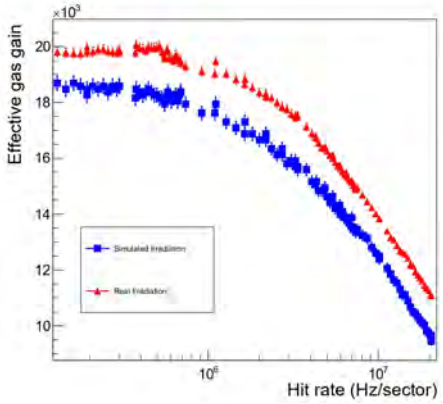

Figure 4.36: Effective gas gain measured under X-rays heavy irradiation (red dots) and measured while simulating the effective voltages (blue dots).

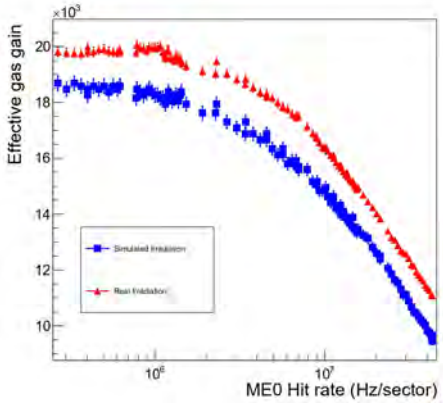

Figure 4.37: Effective gas gain measured as a function of the expected ME0 hit rate (red dots) and measured while simulating the effective voltages (blue dots.

curves are the same, the vertical shift is probably due to a change in the external weather that provoked a systematic decrease of the initial gain. Indeed, with a vertical shift of 7% of the Simulated curve, the two dataset completely overlap, as it is shown in Fig. 4.38. It was then demonstrated

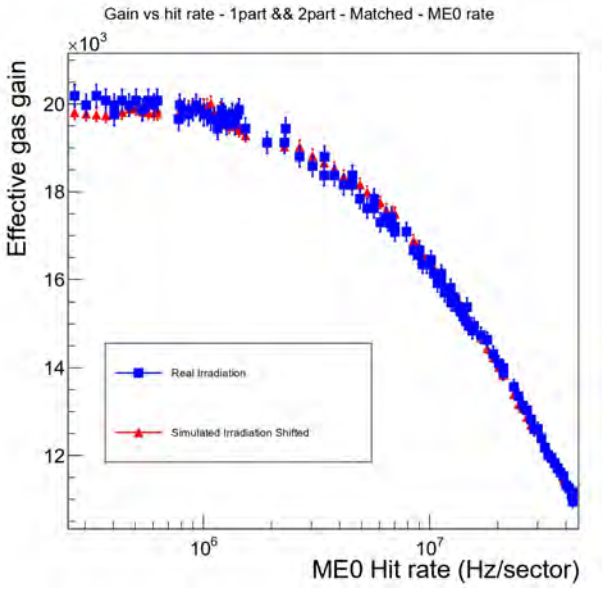

Figure 4.38: Effective gas gain measured under X-rays heavy irradiation (red dots) and measured while simulating the effective voltages (blue dots). The red curve gains were increased by a 7%.

that no space charge effects are present at these fluxes and the gain loss is only due to the voltage drop across the protection resistors.

4.3.2 ME0 Prototype with Transverse Segmentation

Previous preliminary results were expanded on a CMS size detector. The first ME0 prototype named ME0-I-CERN-0001 was produced with all the three GEM foils double segmented with the segmentation proposed in Figs. 4.2 and 4.40a. Since the segmentation was applied also on the bottom of the third GEM foil, such detector prototype suffers of cross-talk effect (see Sec. 2.3.3.3). However, this effect is not affecting the rate capability measurement presented in this section since only the currents are measured and they are not susceptible to this effect.

To characterize the prototype, usual quality control steps were performed (for details about the steps see [110]). Cross-talk effect was spotted during the gain uniformity test, QC5. Irradiating large part of the detector with an X-rays tube and measuring the gain in other places of the detectors, cathode induced signals were recorded invalidating the measurements. To

solve this problem a collimated ^{109}Cd source was used to irradiated locally the detector hence removing the cross-talk. Fig. 4.39 shows a 2D map of the gain measured avoiding the cross-talk [183]. However, for the quality

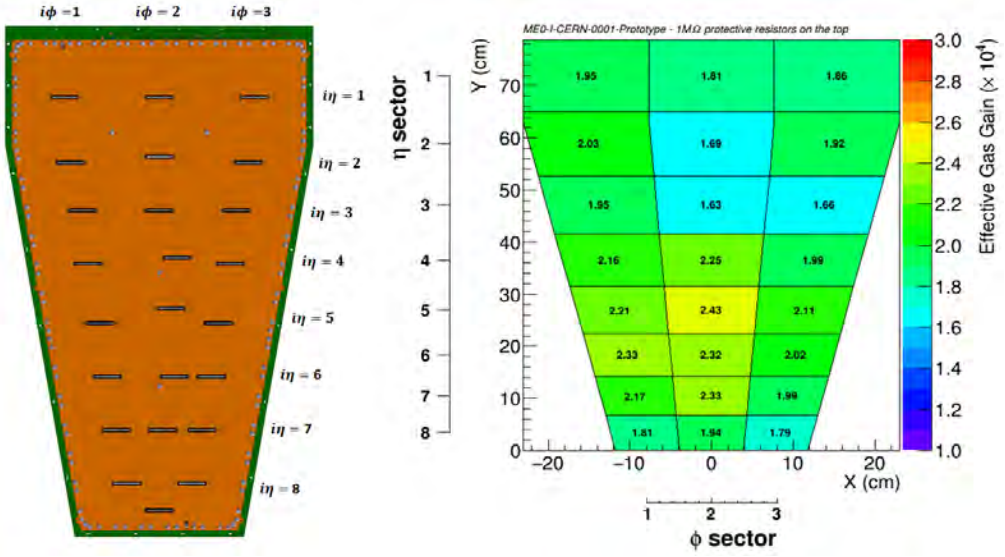

Figure 4.39: 2D mapping of the effective gas gain measurement of the first ME0 module prototype (ME0-I-CERN-0001) as a function of spatial location. These observations were taken at an ambient temperature of 22 °C, pressure of 975 hPa and relative humidity of 19%.

control of future detectors, the usual QC5 measurement will be possible since all the CMS GEM detectors will be produced with the bottom of third GEM foils non segmented to mitigate the cross-talk effect.

The rate capability measurement on such ME0 prototype requires simulations to estimate the fraction of the X-rays flux that every HV sector sees. From Fig. 4.13 it is clear that, to uniformly irradiate all the detector, the X-rays tube has to be placed at a distance > 100 cm, significantly reducing the hit rate per sector nevertheless a more powerful X-rays tube was used (maximum current at 40 kV is 200 µA). A strategy to irradiate the detector at high rates is to measure the anodic current from all the anode plane and, with a Montecarlo program, getting the weighting factor to estimate the fraction of such current that is under the selected HV sector. The X-rays generator is placed in position $z = 20$ cm and $y = 0$ cm with respect to the coordinates shown in Fig. 4.40a. The X-rays angular profile (see Fig. 4.13 and [166]) is used to randomly generate the photons directions that are hence propagated though the detector placed at different distances (10, 20, 30 and 110 cm). Each HV sector weight w_i is computed as the fraction of

the total generated photons N_{tot} hitting such sector N_{sector}:

$$w_i = \frac{N_{sector}}{N_{tot}}.$$

Fig. 4.40 shows the relative hit rate on the detector for different X-rays tube distances. Tab. 4.9 shows the simulated weights at the four different distances. The sector with the highest weight, i.e. the more irradiated, is the sector number 6 (from $z = 0\,\text{cm}$) that is the one directly in front of the X-rays generator. Such sector is the one taken into consideration for the rate capability measurements.

After this step, the measurement proceeded in a similar way as the ones already presented. The only difference is that the anodic current to linearize is not the global current measured on all the anode plane but only a fraction $w_6 I_{anode}$. The value of the nominal gain G^* is less precise in this case. Indeed, the detector was operated at a working voltage corresponding to an average detector gain of 2×10^4; then, since all the anode is readout, the nominal gain was $G^* = 2 \times 10^4$. However, the investigated sector is not representative of all the detector but only a part of it hence the gain is not exactly the average one. To take into account the gain non uniformity of the detector, the error on G^* is incremented of 2200, i.e. the 11% of 2×10^4 which is the measured gain uniformity along the detector. However, the measurement was corrected after the data taking since the detector gain was overestimated because of the use of a wrong number of primaries during the calibration. The nominal gain of the detector during the test was recalculated and it was 1.6×10^4. Fig. 4.41 shows the measured gain as a function of the expected ME0 rate, the ME0 data are displayed with the $10\,\text{cm} \times 10\,\text{cm}$ data for comparison. Fig. 4.42 shows the same points but normalized to the nominal gain. Despite the difference in the initial gain, the $10\,\text{cm} \times 10\,\text{cm}$ and the ME0 sector behaves in similar way. The gain drop is lower in the ME0 case due to the lower initial gain as expected. In general, there is no reason to assume that a $10\,\text{cm} \times 10\,\text{cm}$ and a $100\,\text{cm}^2$ ME0 sector behave differently. However, a very different behaviour is expected if a resistive HV filter will be mounted. Indeed, all the 29 sector currents will flow in the filter resistor causing a huge voltage drop along all the electrode also with relatively small resistor value. Another issue comes from having a transverse segmentation and a ME0 like background (see Fig. 4.2). In this case the voltage drop on each sector will be different because of the large difference in the hit rate (it varies within two orders of magnitude), causing a large gain non uniformity. A mitigation strategy could be to tune the HV sector sizes and/or their protection resistor values with the background profile to equalize the voltage drop on all the sectors. On the other hand, such modification will be made on simulations basis, if the simulated background radial profile will change for every reason, the

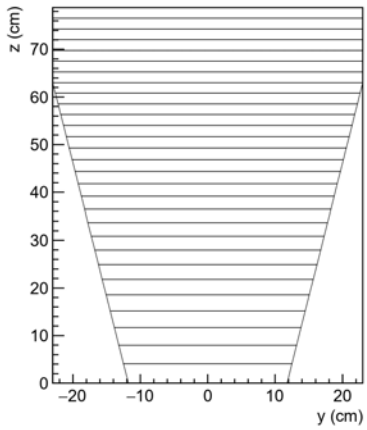

(a) *Transversal segmentation map of the ME0 prototype*

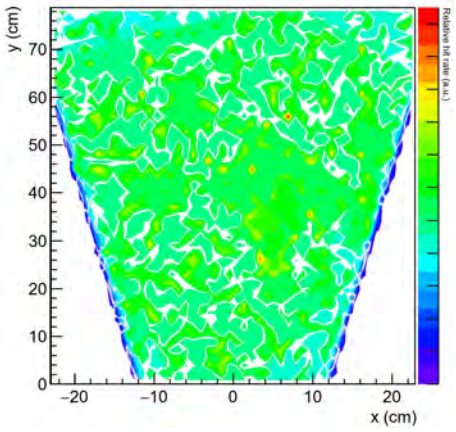

(b) *Hit rate map at* 110 cm

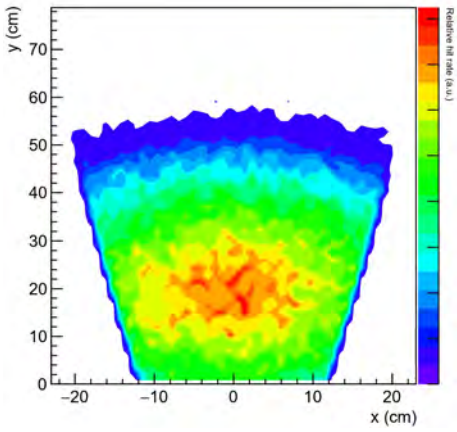

(c) *Hit rate map at* 30 cm

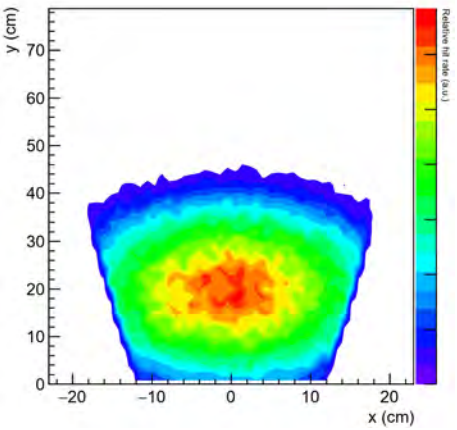

(d) *Hit rate map at* 20 cm

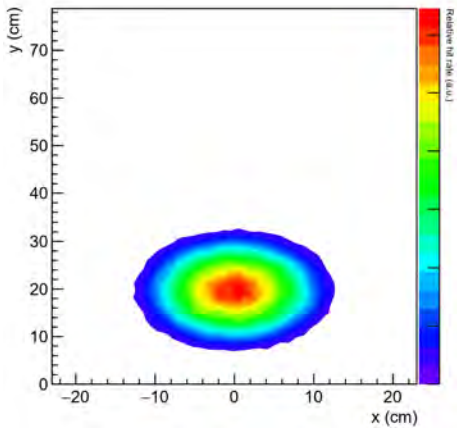

(e) *Hit rate map at* 10 cm

Figure 4.40: Simulated hit rates densities when irradiating the ME0 prototype with the X-rays tube at various distances.

Sector number (from z=0cm**)**	$\mathbf{w}_i$ **at 110**cm	$\mathbf{w}_i$ **at 30**cm	$\mathbf{w}_i$ **at 20**cm	$\mathbf{w}_i$ **at 10**cm
29	3.19×10^{-2}	0	0	0
28	3.18×10^{-2}	0	0	0
27	3.27×10^{-2}	0	0	0
26	3.43×10^{-2}	0	0	0
25	3.44×10^{-2}	0	0	0
24	3.45×10^{-2}	0	0	0
23	3.54×10^{-2}	0	0	0
22	3.36×10^{-2}	0	0	0
21	3.49×10^{-2}	0	0	0
20	3.46×10^{-2}	0	0	0
19	3.46×10^{-2}	4.73×10^{-3}	0	0
18	3.55×10^{-2}	1.64×10^{-2}	0	0
17	3.41×10^{-2}	2.44×10^{-2}	0	0
16	3.47×10^{-2}	3.10×10^{-2}	0	0
15	3.74×10^{-2}	3.50×10^{-2}	0	0
14	3.64×10^{-2}	3.90×10^{-2}	8.40×10^{-3}	0
13	3.65×10^{-2}	4.37×10^{-2}	2.63×10^{-2}	0
12	3.72×10^{-2}	4.95×10^{-2}	4.12×10^{-2}	0
11	3.63×10^{-2}	5.54×10^{-2}	5.56×10^{-2}	0
10	3.55×10^{-2}	6.19×10^{-2}	6.72×10^{-2}	5.36×10^{-3}
9	3.55×10^{-2}	6.77×10^{-2}	8.00×10^{-2}	5.98×10^{-2}
8	3.59×10^{-2}	7.32×10^{-2}	9.29×10^{-2}	1.17×10^{-1}
7	3.49×10^{-2}	7.63×10^{-2}	1.04×10^{-1}	1.78×10^{-1}
6	3.56×10^{-2}	8.00×10^{-2}	1.09×10^{-1}	2.18×10^{-1}
5	3.31×10^{-2}	7.91×10^{-2}	1.08×10^{-1}	2.05×10^{-1}
4	3.36×10^{-2}	7.60×10^{-2}	9.96×10^{-2}	1.46×10^{-1}
3	3.28×10^{-2}	7.02×10^{-2}	8.52×10^{-2}	7.02×10^{-2}
2	3.16×10^{-2}	6.22×10^{-2}	6.91×10^{-2}	6.52×10^{-4}
1	3.10×10^{-2}	5.42×10^{-2}	5.35×10^{-2}	0

Table 4.9: Simulated weights for each ME0 sector when it is irradiated with an X-rays generator in the position $z = 20\,\text{cm}$ and $y = 0\,\text{cm}$ at various distances.

voltage drops will be once again not equal. However, this solution has been discarded by the CMS GEM Group and other strategies will be described in the following sections.

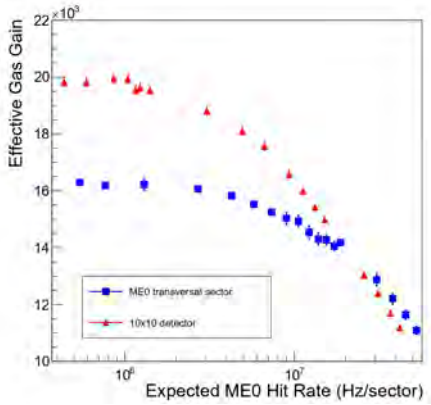

Figure 4.41: Effective gas gain measured on the most irradiated sector of the ME0 prototype as a function of the expected ME0 hit rate compared with the behaviour of a standard 10 cm × 10 cm.

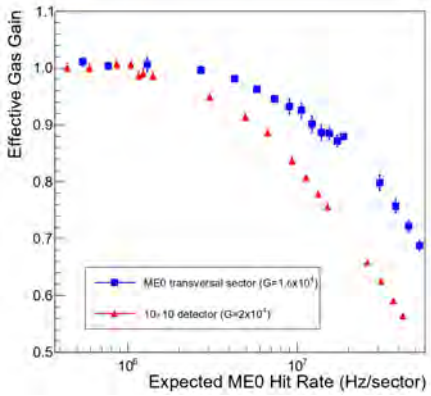

Figure 4.42: Normalize gain measured on the most irradiated sector of the ME0 prototype as a function of the expected ME0 hit rate compared with the behaviour of a standard 10 cm × 10 cm.

4.4 Gain Compensation Strategy

Compensation of the gain loss due to the voltage drop can be easily achieved by increasing the working voltage of the detector. In the previous sections it was demonstrated that working at high gain increases the percentage gain loss but can help to maintain the selected gain value. This procedure recovers the gain by increasing linearly the applied voltages to all the electrodes. This fact can be dangerous if a conspicuous gain increase is needed. Indeed, the GEM voltage drops are not the same within electrodes because of their different signs and values (see Tab. 4.8). In particular a compensation made in this way will aliment the induction field growth because of its large negative current, with side effects on the discharge propagation probability. Moreover, the gains of the first and second foils will be subjected to a large increase while the third will continue to work at low gain. Therefore, a compensation strategy that involves the voltage increases of all the electrodes without criteria is to avoid.

Since it was demonstrated in the previous sections that, at relatively low rates, no space charge effect is present and only the voltage drop causes the gain loss, it is possible to compensate electrode by electrode the voltage increase or decrease. From Eq. 4.12 it was possible to correctly estimate the voltage drop that caused the gain loss. Therefore, using the same formula for the j-th electrode:

$$V^j_{eff} = V^j_{set} - I^j_{mondet} R^j,$$

it is possible to obtain the nominal electrode voltage $V^j_{set}(I^j_{mondet} = 0)$ by progressively increase (or decrease in case of negative currents) the V^j_{set} until $V^j_{eff} = V^j_{set}(I^j_{mondet} = 0)$. It is clear that an increase in the V^j_{set} will cause an increase of I^j_{mondet} that moves away the compensating goal. However, it was demonstrated that, up to relatively high rates, this compensating strategy converges and works fine. Fig. 4.43 shows the results of such compensation procedure when operating a 10 cm × 10 cm detector. The gain

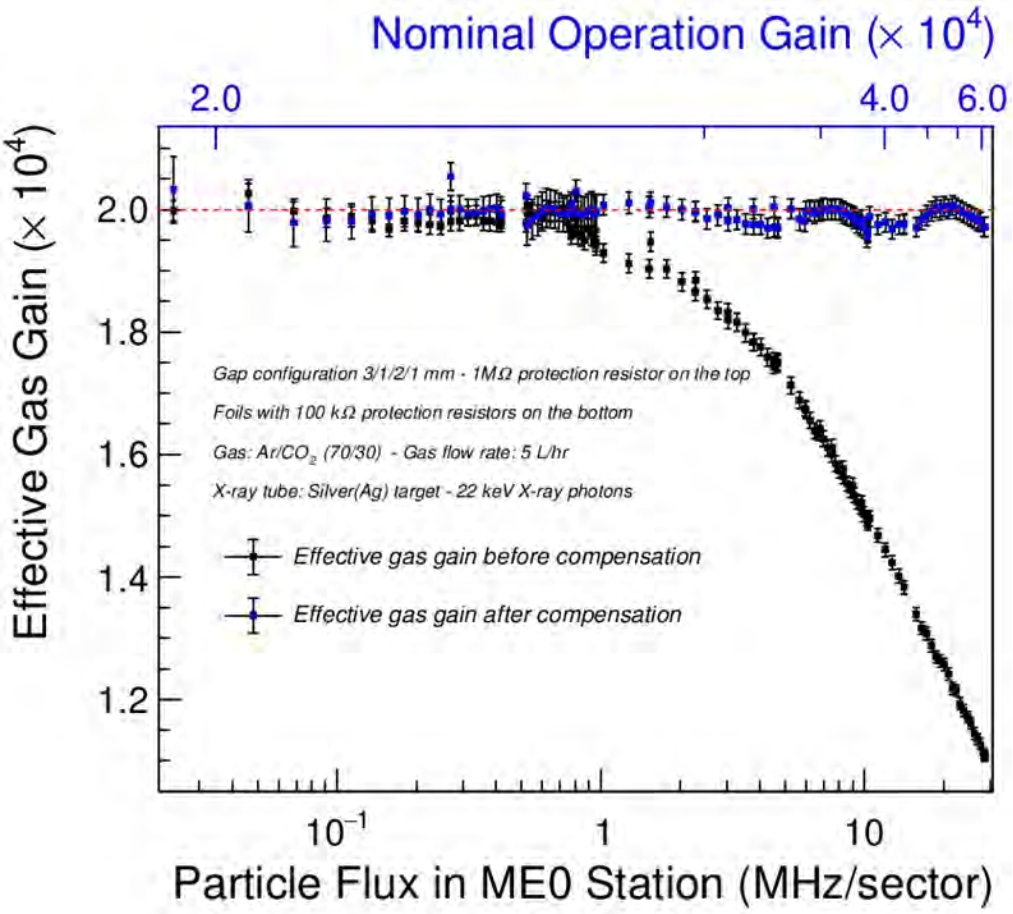

Figure 4.43: Effective gain of a 10 cm × 10 cm triple-GEM chamber operated at increasing values of the nominal gain as a function of the background particle rate per sector. The top axis shows the nominal gain at which the detector is operated to achieve full gain compensation.

drop curve (black dots) is very similar to the one presented in the previous sections because the similarity of the detector (1 MΩ protection resistor on the top side of the GEM foils and 100 kΩ on the bottom) and the irradiating medium. If compensating each electrode using the aforementioned approach the gain remain stable to its nominal gain up to 30 MHz/sector (blue dots). This procedure let the GEM fields untouched to their nominal

values because the effective voltages on the electrodes are the same of a non irradiated detector at the same gain.

This strategy is very promising since it can put together a strict discharge mitigation strategy (exploiting large resistors values) along with optimal operation in high rate environment. This strategy may have also some drawbacks. For example, if the particle beam is abruptly removed, the gain will rapidly increase because of the relatively low response time of the controlling system and the power supply (up to tens of ms) exposing the detector to instabilities due to the very high gap fields. Moreover, a large detector control system have to constantly monitor and tune the supplied voltages of many detectors each of them having 7 HV channels (a total of 504 HV channel are foreseen for the ME0 project). This is not an impossible goal to achieve, but it will require a fast and reliable system.

However, the compensation cannot work with a transverse electrode segmentation. Even if the sector sizes and/or resistor values will equalize the voltage drop at a fixed value, the compensating voltage will modify in a non uniform way the electrodes currents because of the large sector rates non uniformity. The only way to exploit such compensating strategy is to have hit rates and resistances on each HV sector equal between each other. This goal is hardly achievable with a transverse segmentation of the foils.

4.5 New ME0 foil design

As discussed before, the background profile along the orthogonal direction to the beam pipe (see Fig. 4.2) creates a non uniform gain drop across a transversal segmented GEM detector. A solution to this problem can be found by exploiting the symmetry along the ϕ direction of the CMS background. Indeed, if segmenting the GEM foils in the longitudinal direction it is evident that all the HV sectors intersect the same amount of particles independently from the background profile along the R direction. A longitudinal segmentation was proposed to overcome such limits and the first prototype was produced. Fig. 4.44 shows the first attempt to produce a radial segmented GEM foil. This configuration assure that the hit rate on each sector is exactly the same. With this sector arrangement, the HV connections and components are moved from the low η side of the foil. To make feasible to install correctly the components and reduce the foil production complexity, the design was slightly changed by verticalizing the low η part of the sectors as shown in Fig. 4.45. The number of sectors is a crucial quantity to determine. Indeed, having too small sector sizes (less than 5 mm) introduces some technical issue in the foil production and increases the dead-area (sectors are separated by 200 µm of non active area). On the other hand, too large sectors increase the gap capacitance hence

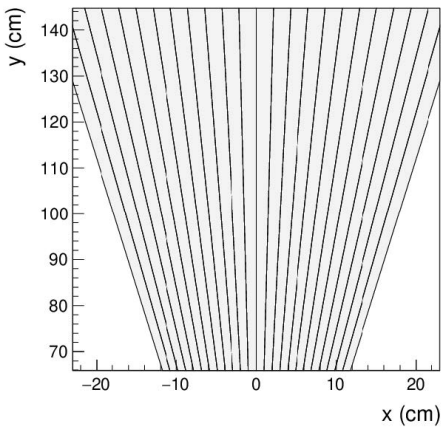

Figure 4.44: Radial segmentation along the whole GEM foils.

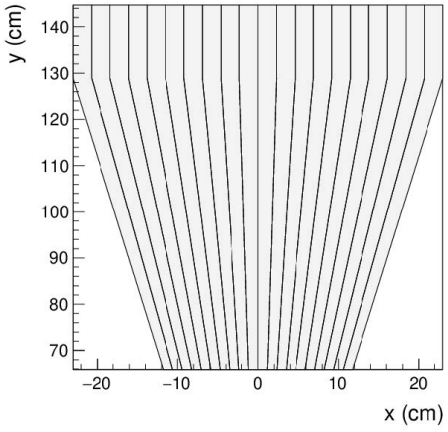

Figure 4.45: Proposed radial and vertical segmentation.

the discharge propagation probability. Fig. 4.46 shows the simulated hit rate per sector as a function of the number of sectors. A sector number

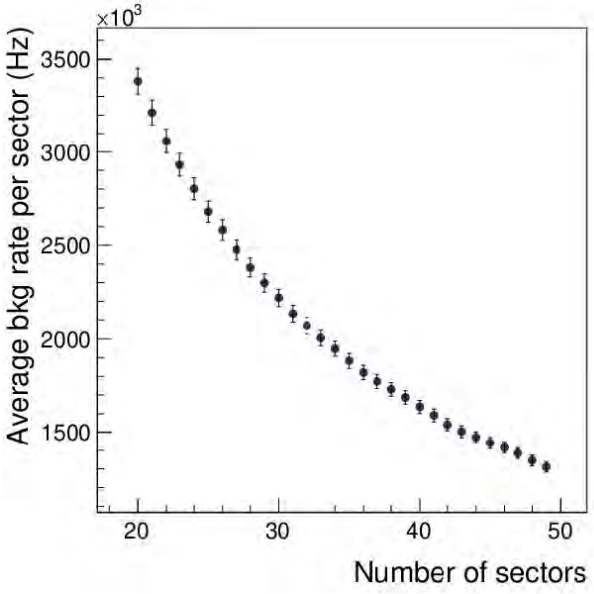

Figure 4.46: Simulated average hit rate per sector on longitudinally segmented foils as a function of the number of sectors, red coloured regions represent the non interesting parts.

of 40 was chosen (sector area $\approx 75\,\mathrm{cm}^2$), the final technical drawing of the GEM foil is presented in Fig. 4.47. The holes present in the drawing were made to accommodate spacers to assure a larger uniformity of the detector planarity. In particular, GE1/1 detectors suffered a systematic non uniformity of the drift board flatness that caused a relatively large gain non

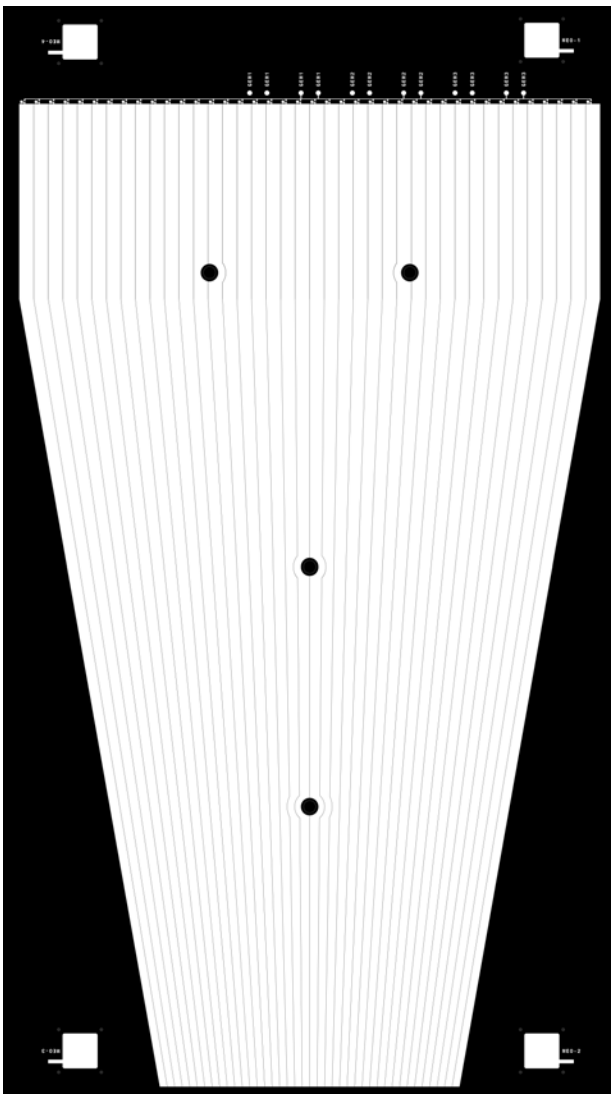

Figure 4.47: Technical drawings of the longitudinal segmented GEM foils for ME0, the segmentation is present on both sides for GEM1 and GEM2 and only on top in GEM3.

uniformity [144]. Baking the boards assured good uniformity for GE1/1 operation but it was decided to introduce spacing pillars to further improve it. The average gain uniformity along the detector of all the produced GE1/1 detectors was around 25% (μ/σ) [110], while the uniformity of the ME0 prototypes with pillars (longitudinal segmentation) is around 12%, that is clearly better than the design without the spacers [183]. This improvement was made at the expense of a small fraction of the active area ≈1.3%. With the selected design the hit rate will be around 1.6 MHz/sector with very small non uniformity between sectors (see Fig. 4.48).

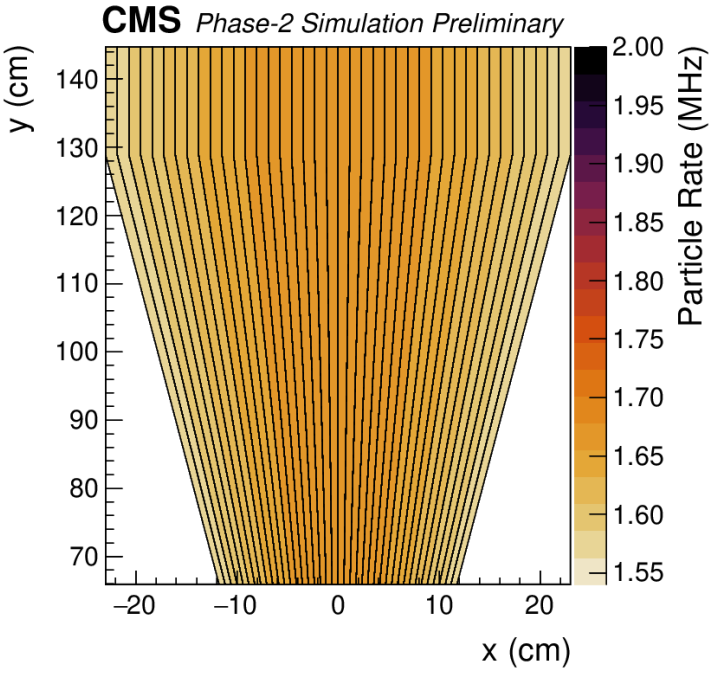

Figure 4.48: Simulated hit rate per sector map on a 40 sectors GEM foil.

A first prototype of the second generation longitudinal segmented ME0 detector was produced. Fig. 4.49 displays a photo of a GEM foil segmented longitudinally. Protections resistors values were chosen to be 2 MΩ on each sector of the top side of the foil and 100 kΩ on the bottom. An additional 100 kΩ is placed as a protection of the drift electrode which is not segmented. The top resistor value was increased with respect to previous design in order to allow operation also in cases of shorts. Each HV board (for ME0 it will be the CAEN A1515BTGHP), will supply three detector in parallel and its maximum supplied current is 300 µA per channel for a total maximum of 3 mA. Since during normal ME0 operation, the current flowing through the HV lines are not expected to be higher than 30 µA/channel, the power supply has no problem in manage all the three ME0 detectors. However if a short occurs in one of the GEM foils, a huge current will flow though the gap equal to the applied voltage divided by the sum of the resistance on top and bottom. If mounting 2 MΩ on top, the current drained by a short will be 400 V/2.1 MΩ ≈ 200 µA meaning that if one of the three detectors develop a short, the others can continue to work correctly, the same cannot happen if using 1 MΩ resistors. Therefore, with this resistors configuration each group of three ME0 chambers can work also if one chamber will have three simultaneous shorts, one on each GEM foil. the effective gas gain was measured on the novel produced prototype and the results are shown in Fig. 4.50.

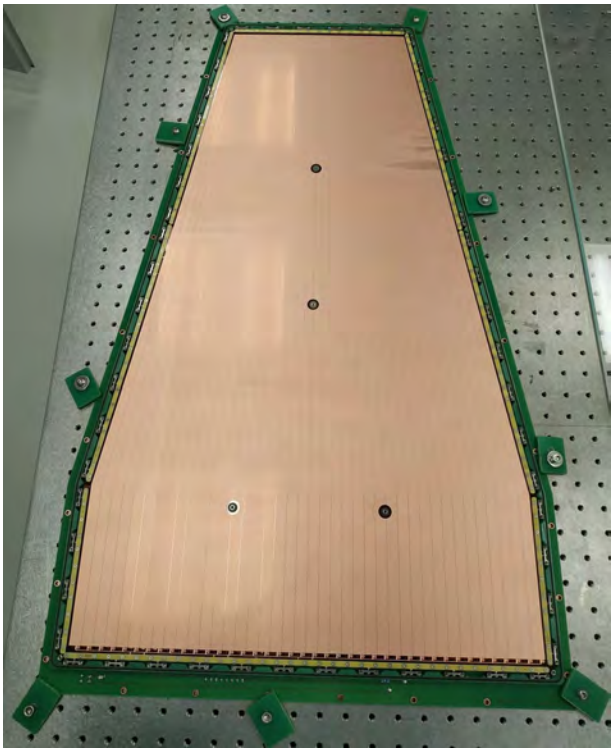

Figure 4.49: Photo of a longitudinal segmented GEM foil mounted on the first prototype of its kind.

Because of such change in the detector design a new set of measurements are required to understand the rate capability behaviour of such detector. The measurements are described in the following, future tests are foreseen to study the effect of the HV filter on the rate capability and the discharge behaviour.

4.5.1 Rate Capability Measurement

The ME0-II prototype was irradaited to test its rate capability behaviour and the uniformity of the gain loss along the HV sector. To do that, four HV sectors of only one eta partition ($\eta = 8$) of the detector were heavily irradaited. The rest of the detector was shielded with a 3 mm thick Copper plate. 1 mm diameter holes on the shield were made in the middle of the non irradaited η readout sectors to permit low local irradiation for the gain measurement. Fig. 4.51 shows a photo of such setup. An X-rays tube is used to irradiate the $\eta = 8$ partition. The flux is varied by changing the X-rays tube current, while the gain on the non irradaited partitions is measured with another tube working at a small current (10 µA) and pointing at the middle of each shield hole inducing an average rate of 1.4 kHz/sector.

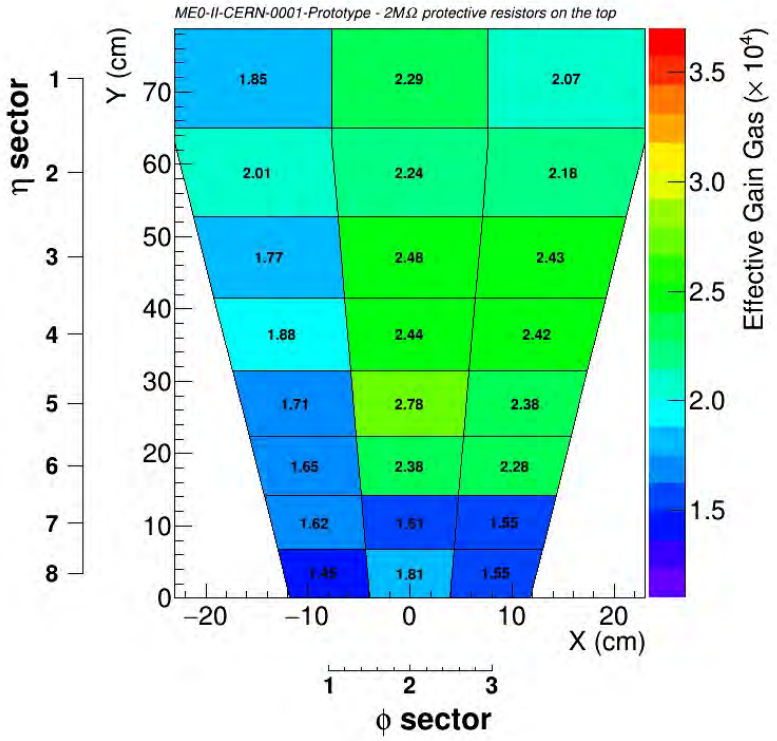

Figure 4.50: 2D mapping of the effective gas gain measurement of the longitudinal segmented ME0 module prototype (ME0-II-CERN-0001) as a function of spatial location.

Fig. 4.52 shows the gain curves of the investigated eta partitions (1 to 6) while Fig. 4.53 shows the same plot but with normalized gains. It is clear once again that the gain drop is only due to the voltage drop induced by currents flowing on the HV sector, hence the losses are equal on the whole partitions also if they are not directly irradaited. Fig. 4.54 shows the percentage gain losses of the six investigated eta sectors when they are irradaited with the expected ME0 hit rate. The drops are similar between each other because the closeness of their initial gains. With respect to the measurements made with prototypes that mounted 1 MΩ, the drops are higher but still not too large ($< 15\%$) to impose a mandatory gain compensation for ME0 operation.

The same measurement was repeated on the same prototype mounting a resistive filter with a 10 kΩ resistor per HV channel. Since only 4 HV sectors are irradaited the effect of a 10 kΩ filter is comparable to a 40 sectors irradiation with a 1 kΩ filter. Fig. 4.55 shows the gain curves of the investigated eta partitions (1 to 6) while Fig. 4.56 shows the same plot but with normalized gains. If comparing such results with the ones without

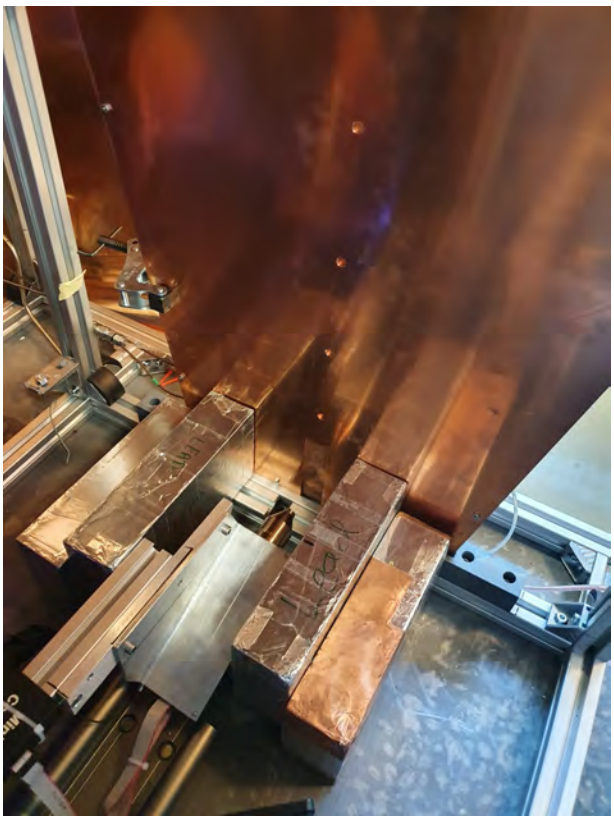

Figure 4.51: Photo of the setup for the irradiation test of the prototype. the X-rays tube is placed near the highest η partition and the whole detector is shielded with a Copper plate.

filter, it is clear that no large differences are detected. Indeed, if looking at Fig. 4.54, that shows the percentage gain losses of the six investigated eta sectors when irradaited with the expected ME0 hit rate, it is clear that the gain losses at the nominal ME0 hit rate are the same with or without filter.

Mounting a $1\,\mathrm{k}\Omega$ resistive filter will not introduce huge differences in the rate capability of the detector. However, dedicated noise studies with the final ME0 electronics have to be performed to check if such resistor is large enough to permit good detection of signals over the noise.

4.5.2 Future Plans

Despite the relative low gain drop ($< 15\%$) foreseen during ME0 operation both with or without resistive HV filter, the compensation algorithm tested in Sec. 4.4 has to be tested and validated. In particular, the algorithm has to be modified because the presence of the HV filter. The effective voltage

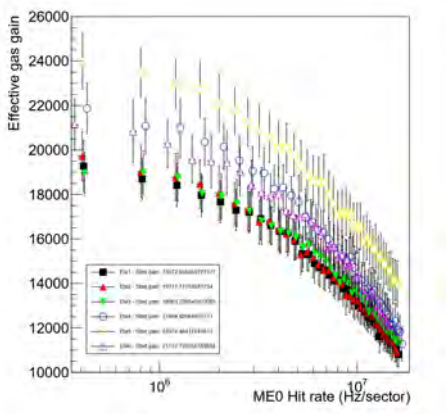

Figure 4.52: Effective gas gains measured on the non irradaited sectors of the ME0-II prototype as a function of the expected ME0 hit rate.

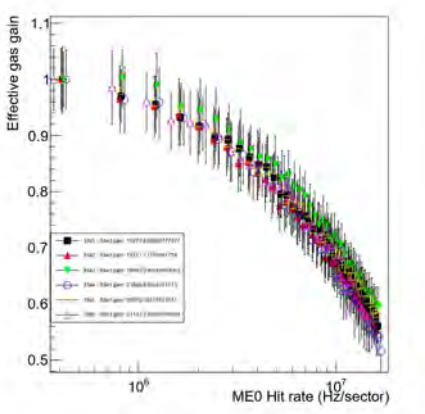

Figure 4.53: Normalized gains measured on the non irradaited sectors of the ME0-II prototype as a function of the expected ME0 hit rate.

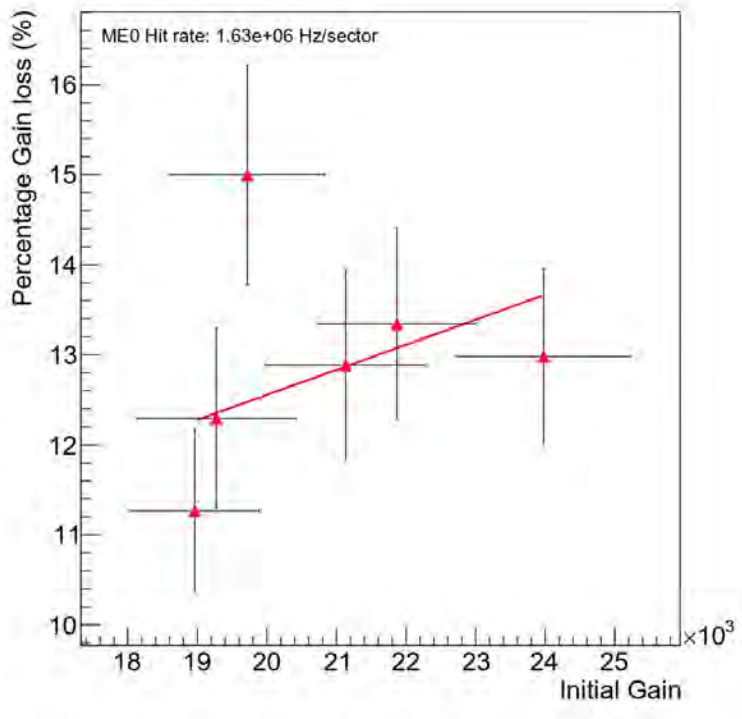

Figure 4.54: Percentage gain loss of the investigate eta sectors. A linear fit is superimposed to guide the eye.

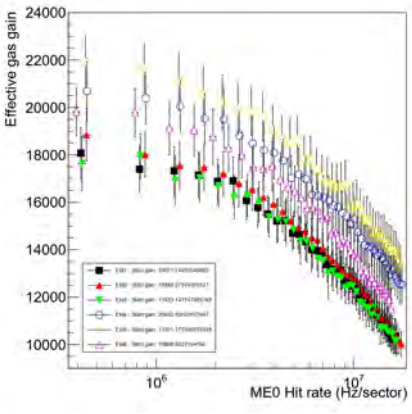

Figure 4.55: Effective gas gains measured on the non irradaited sectors of the ME0-II prototype with 10 kΩ filter as a function of the expected ME0 hit rate.

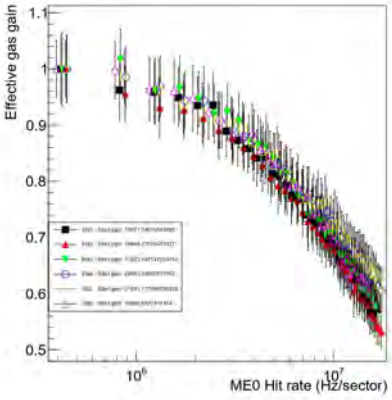

Figure 4.56: Normalized gains measured on the non irradaited sectors of the ME0-II prototype with 10 kΩ filter as a function of the expected ME0 hit rate.

on the j-th electrode V^j_{eff} when a ME0-like detector is irradaited uniformly in the ϕ direction will be (opportunely modifying the Eq. 4.12):

$$V^j_{eff} = V^j_{set} - \left(\frac{1}{40} I^j_{mondet} R^j_{protection} + I^j_{mondet} R^j_{filter}\right), \tag{4.13}$$

where $R^j_{protection}$ and R^j_{filter} are respectively the protection resistor and the filtering one on the j-th electrode. Tests will be carried out to test if the compensation works also in this case.

If the compensation will work, the presented ME0 configuration will be maintained. Discharge studies will be carried out to test if such configuration can cope with the discharge rate expected with the ME0 position particle environment. If the discharge behaviour will be unsatisfactory the resistors values will be increased, prioritizing the protection resistors over the filtering one. Further tests on the electronic noise induced by the power supply will confirm if the filter, as it works for rate capability and discharge point of view, requires a modification. All the tests needed to ME0 design validation will be carried out by the first quarter of 2022 for the final review.

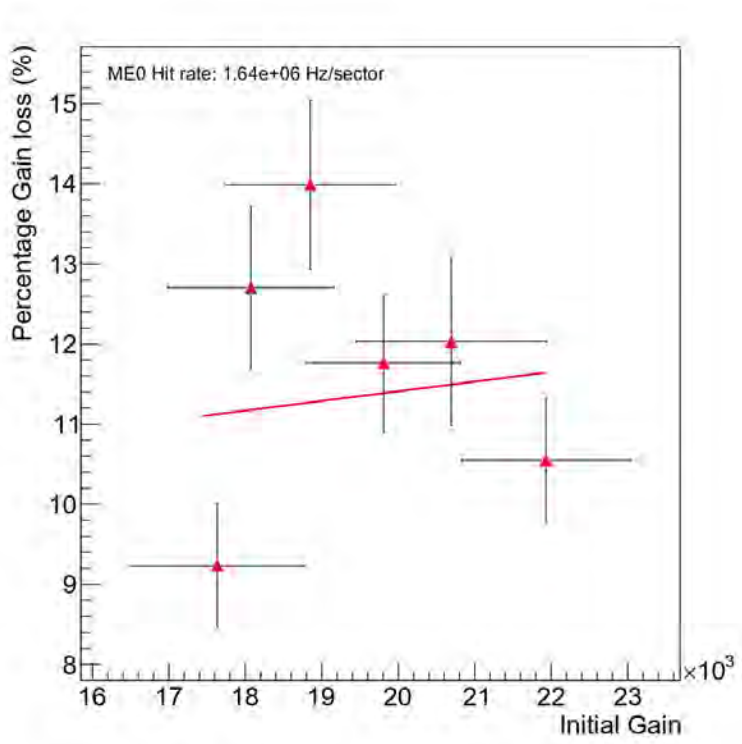

Figure 4.57: Percentage gain loss of the investigate eta sectors, the detector is mounting a 10 kΩ resistive filter. A linear fit is superimposed to guide the eye.

CHAPTER 5

ADVANCED AGING STUDIES ON TRIPLE-GEM AND WIRE CHAMBERS

Aging is one of the main limitations for the long term operation of gaseous detectors in High Energy Physics (HEP) experiments. Before entering the LHC era (started in 2010) the detector community reviewed the status of the technologies to fulfil the LHC detectors requirements. The last large aging review on gaseous detector was indeed held in 2001 [184], during this period. The discussions and developments examinated here and in all the R&D period, surely helped to deliver detectors and detector systems ready to face the LHC challenge. On the other hand, in the last two decades, with the development of MPGDs the scientific community had the chance to exploit detectors that are way more resilient to aging than more traditional technologies, channelling the scientific effort to other detectors aspects. This fact, with the general increased aging-purity of gaseous detectors, lead to a lower interest in the basic understanding of the aging processes. Nowadays, aging studies are performed to validate a partially developed detector for a certain experimental application [110, 185–188]. Irradiating with photons only, running at too high or low aging acceleration factors and using small and clean gas systems are just some of the reasons that could lead to promising results during the test but unexpected ones during the normal operation. In the near and far future the accelerators energies and luminosities will increase, for example HL-LHC will deliver a radiation dose to the CMS detector 10 times higher than today LHC [12]. Future proposed colliders such as High-Energy LHC and

Future Circular Collider will deliver a dose respectively 40 and 200 times more than at today LHC [189]. The new detector challenges proposed by the new accelerating machines have to be faced to correctly deliver detector systems capable to provide the highest discover potential.

Aging will be one of these challenges and this chapter will show the limits of some experimental procedure while investigating some variables playing a role in the aging issue. A brief introduction on the aging processes inside gaseous detectors is followed by a simple review of the status of the art of the issue. Afterwards, an aging test performed in the framework of the GEM technology validation for the CMS purpose is described with the experimental procedures and the original way to accelerate aging. Finally, the results of a R&D campaign aimed to understand the effects of the particle ionization power, hit rate and charge collection rate on different detector technologies are presented with some hints for future experiments. I personally followed and performed all the tests presented in this chapter.

5.1 Aging in gaseous detectors

Aging in gaseous detector is the temporary or permanent degradation of performance under sustained irradiation. This issue has been and it is still one of the main limitations of the long term use of such detectors in HEP experiments [190, 191]. The so called classical aging is the result of chemical reaction happening inside the gas volume during the electron multiplication, that leads to deposit formation on the detector's electrodes and sensitive surfaces [191, 192]. Ionizations processes, that sustain the multiplication, occur when electron energies are greater than 10 eV, while the breaking of molecular covalent bonds require energies of the order of 3 eV. This means that if an avalanche is occurring and molecules are present, the ions and electrons produced will be surrounded by molecular specimens with one or more unsatisfied covalent bonds also called free radicals. Because of their nature, free radicals are very chemically active. They may recombine forming the starting molecules or form new cross-linked molecular structures of increasing molecular weight i.e. monomers and polymers. The probability, the rate of polymers formation, and their composition are affected by several microscopic variables, such as electron and photon energy distributions, interaction cross section with the atoms and molecules, density of charge carriers and molecules, and many others. Plasma chemistry is the discipline that studies the chemicals processes occurring during the electron multiplication. Despite some general insights may be taken from this subject results, the huge differences in operating conditions with respect to gaseous detectors, limit the predictions in the latter field [192, 193].

5.1.1 Aging evidences in gaseous detectors technologies

Aging may appear in different forms. In wire chambers classical aging usually emerges when a polymeric deposit starts to appear either on the cathode or the anode. Anode deposition may reduce and distort the electric field near the wire resulting in the detector gain loss. On the other hand, cathode deposit may lead to the so called Malter effect [194]. An insulating film on the cathode can prevent the positive charge to neutralize, generating a strong electric field across the dielectric layer that may cause electron extraction from the cathode by field-emission [191, 192]. Usually Malter effect leads to an increase of noise rate and dark current and in the worst cases the emitted electrons may go into self-sustained current mode [195]. Sometimes the addition of water in the gas mixture may help to reduce Malter discharges by diminishing the layer resistivity; moreover the addition of Oxygen in the mixture and the operation at high ionization level cured a Malter damaged chamber [196]. Fig. 5.1 shows different example of wire deposit and Fig. 5.2 presents a comparison between a clean cathode surface and an aged one.

A Micro-Strip Gaseous Counter (MSGC) represents a detector technology that is intrinsically more susceptible to aging with respect to wire chambers. The filigree nature of these detectors may lead to several operation instabilities such as charging up of the substrate, polymer deposition on the thin surfaces and micro-discharges [199–201]. The main reason has to be searched in the small effective area used for charge multiplication that gives larger energy densities during the avalanche [191, 199]. Fig. 5.3 shows aged strips of a MSGC. The polymer depositions tend to distort the electric field increasing the probability to have micro-discharges. These increment the deformation and damage the electrodes shortening the detector's lifetime [199]. The RD28 collaboration [86] was carried on to develop the technology to be used in large experiments and aging was one of the main concerns. In optimal laboratory conditions MSGC were safely operated without any loss of performance when irradiated with soft X-rays [199, 202]. On the other hand, fast aging and increasing spark rate appeared when irradiating the detector with pion or proton beams, showing that high ionization densities and the induced micro-discharges are the major limitation of such technology [203, 204].

The first attempt to overcome the aging issue in MSGC was to introduce a pre-amplification stage between the drift volume and the strips. GEM foils were the natural solution, systems using GEM+MSGC overcame the limits of standard MSGC detectors. However, aging induced performance losses were not completely removed since the limitation was once again the

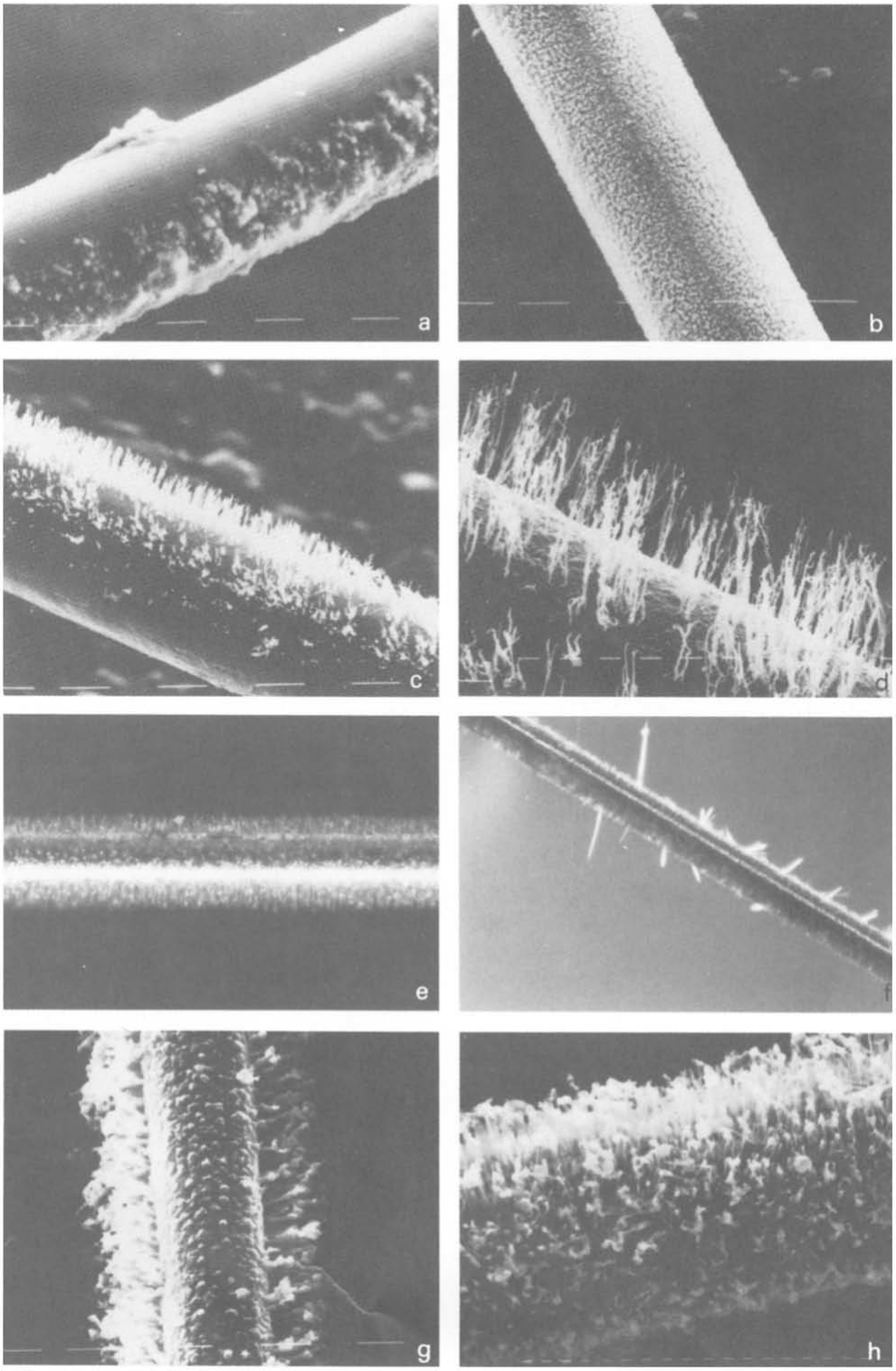

Figure 5.1: Examples of deposits on anode wires [197].

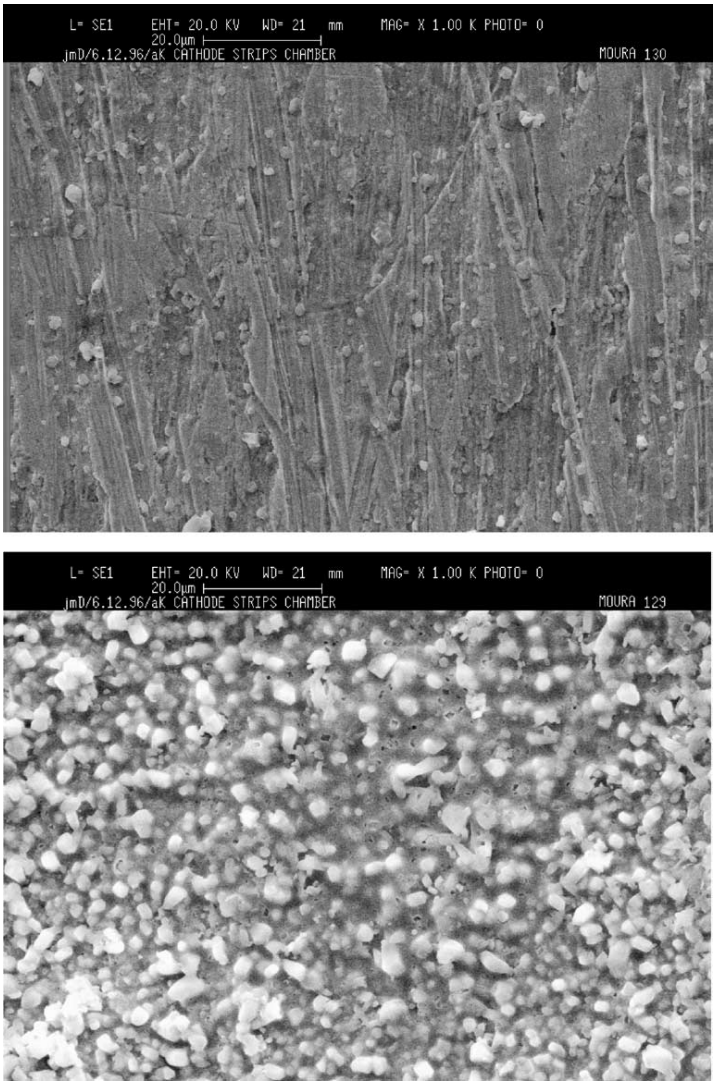

Figure 5.2: Scanning Electron Microscope micrograph of a clean cathode surface (top) and a cathode covered with silicon deposits (bottom) [198].

MSGC structure which is susceptible to micro-discharges and thin deposits on the strips [202, 203]

When using only GEM foils in cascade with no amplification near the electrode, aging seems not to manifest [46, 110, 205–207]. This is mostly due to two factors: firstly there is no amplification near the collection anode, which was the main limitation in using MSGC. This makes the polymers creation relatively far away from the delicate anodic strips. Then, GEMs structures share the global amplification between multiples stages, reducing the avalanche energy at the single stage level. However, on the last GEM foil, the avalanche density may be high enough to trigger discharges and to produce premature polymer deposition. To reduce the avalanche

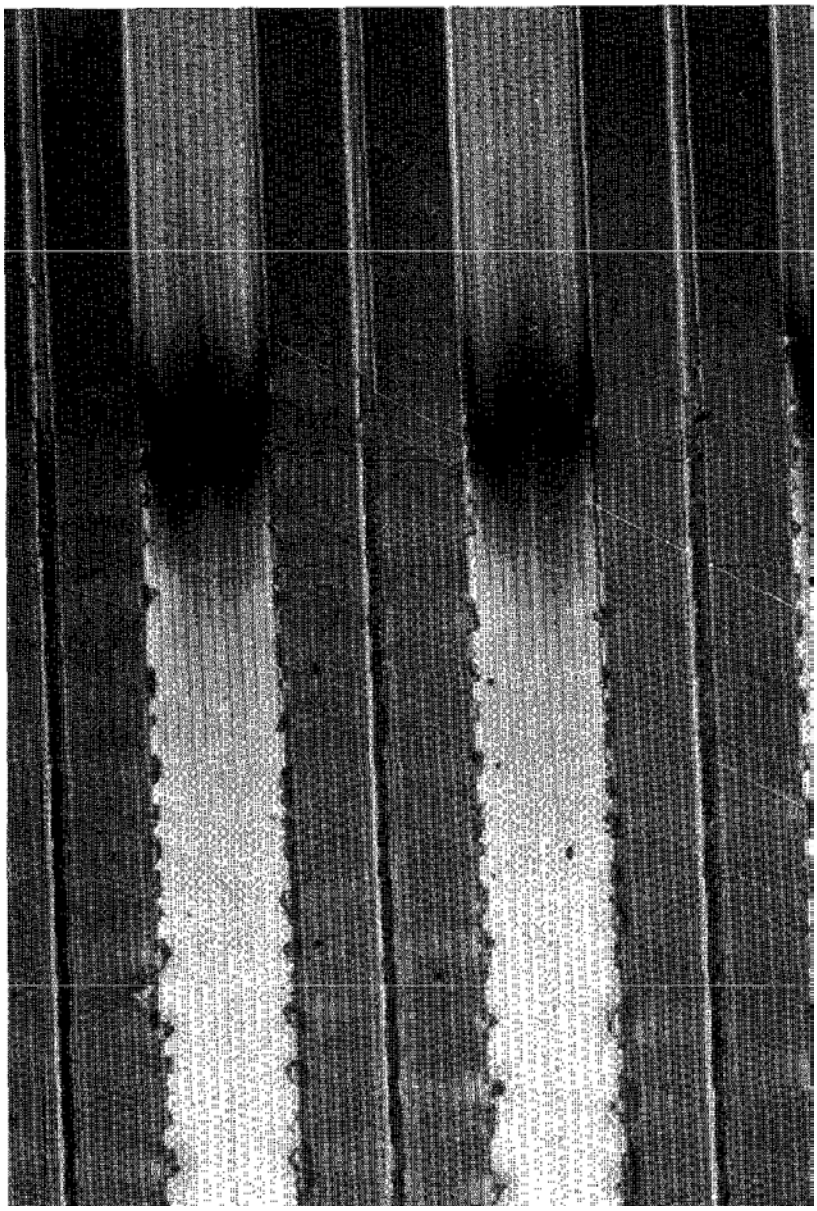

Figure 5.3: Close view of the strips in a MSGC damaged by long-term local heavy irradiation. A pattern of changing colours over the metal strips, typical of interference, indicates the presence of a thin polymer layer; the extended damages on the edges (mostly on cathodes) are probably a consequence of micro-discharges induced by the polymer formation. [199].

density on the last GEM foil it is possible to slightly reduce its gain with respect to the previous ones or increase the transfer gap between the last two foils to let the electron cloud diffuse on more GEM holes. Some operating issues were found when using triple-GEM with gas mixtures containing CF_4 and more details will be discussed in the next section.

Micromegas detectors demonstrated to be radiation hard [208, 209], but having a single amplification stage exposes the detector to a high risk of discharges. However, Micromegas operation in heavily ionizing particle beams showed no permanent performance loss after a large amount of discharges [93]. The radiation hardness of such detectors may be attributed to the collection of the electrons on the anodic grounded strips as in GEMs.

5.1.2 Aging evidences in different gaseous environments

As discussed before, classical aging is developing in gaseous detectors mainly because of the dissociation and recombination of molecules present in the gas volume. In the following, most of the gases and contaminants that may cause issues during detector operation will be analysed.

Hydrocarbon quenchers Hydrocarbons are usually used as quenchers in the gas mixture. Large and relatively complex molecules absorb electrons and photons from the avalanche dissipating the energy in nonradiative ways. There are many evidences about the dangerousness of using CH_4 and heavier hydrocarbons in the gas mixture [184, 191, 197, 210]. In particular, dissociation of such molecules may lead to creation of CH_2: radical that is a typical precursor of polyethylene, a good insulator [192, 211]. Moreover, CH_2: radical has a large dipole moment and tends to stick on the electrode surfaces. It was proved that adding molecules containing oxygen to the gas mixtures helps to eliminate CH_2: radicals by forming volatile products [192, 211]. However, it is not recommended to use hydrocarbons in gas mixtures for long term operation. Nevertheless, contaminations may came from sources different from the gas mixture: many materials are susceptible to outgassing, i.e. the release of molecules that are trapped inside the material itself. If these materials are in contact with the gas mixture, they may pollute it and start aging processes inside the detector.

Silicon contamination Silicon based molecules are not used in general as the active part of the gas mixture, however silicon contamination is periodically found in aged detectors and sometimes the exact source of the pollution is not clearly individuated [191, 197]. Silicon is present in many objects used in detector assembly and gas systems; many of them, such as lubricants adhesives and sealants, are known to be susceptible to outgassing. It is important to notice that, not always the manufacturer underlines the presence of silicon traces [210]. Silicon traces may be removed from the equipment by ultrasonic bath with isopropyl alcohol; the gas system itself can be cleaned from silicon pollution by flushing Di-Methyl Ether

(DME) through it [212]. In general, strict validation for all the assembly components has to be carried out to assure a contamination free gas environment. The RD10 collaboration [213, 214] was instituted to improve the radiation hardness of gaseous detectors; among other milestones, the collaboration classified many potentially dangerous materials and products that may shorten the detectors lifetime. In the framework of the CMS GEM upgrade, the materials selected for detector assembly were tested for outgassing and dangerousness for gaseous detectors with a wire chamber. These tests confirmed some of the previous results and helped to identify and remove a potentially dangerous element from the detector stack [46].

Usage of CF_4 CF_4 is commonly used in gas mixture because of its high electron drift velocity, low electron diffusion and high primary ionization. From the aging point of view, this gas seems to be a double-edged sword. On the one hand, it is demonstrated that CF_4 radicals are able to etch silicon polymers forming volatile SiF_4, although it is not so efficient in etching organic polymers. Furthermore, chemistry of CF_4 is shifted towards polymerization if hydrogenated species are added to the gas, while if oxygen is included some etching properties are restored [191–193]. It is noticeable how the CMS CSC system includes a small quantity of CF_4 in the gas mixture to prevent known silicon deposit on the anode [186, 198]. On the other hand, fluorine radicals may lead to the formation of hydrofluoric acid (HF) if water or hydrocarbon is present. HF is a good etching agent that may attack all non-gold electrodes, glasses, FR4 and also polyimide such as Kapton [215]. Fluorine radicals can also react with metals and create resistive layers of metallic fluorides directly on the electrode; noble metals react less readily with respect to other common electrodes materials (Copper, aluminium, chromium...). Fluorine radicals such as F^- and CF_3^- are elettronegative and long lived species; moreover CF_4 emits hard UV photons ($\lambda \simeq 160\,\text{nm}$, $E_\gamma \simeq 7.75\,\text{eV}$) that may trigger secondary electron emission near the electrodes. The last point seems to be less relevant for GEM detectors, since the confinement of the multiplication in the GEM holes suppresses the probability of emitting secondary electrons far away from the avalanche [191]. However, as already mentioned before, fluorine radicals can etch Copper and Kapton and this is very relevant for GEM operation with CF_4 based mixture. Indeed, it was demonstrated that operating a triple-GEM under heavy irradiation with a relatively low gas flux result in a premature gain loss [216]. In particular, bottom sides of the GEM foils (mainly the third one) were heavily etched by negative fluorine radicals, increasing the average diameters of the hole rim. Moreover, traces of fluorine on such electrodes indicates the presence of thin layer of resistive CuF. The highest impact on the gas gain was probably the etching of the Kapton region inside the hole. The reduction of this region diame-

ter combined with the enlargement of Copper rims, is know to reduce the multiplication factor inside the hole [98]. However, the test demonstrated that the gain loss can be avoided by increasing the gas flux thus removing fluorine radicals before they etch the sensible surfaces.

CO_2 and O_2 for clean gas mixtures As already mentioned, oxygen rich gas mixture may prevent the polymerization of hydrocarbons. CO_2 and O_2 with their potential reactions with CH_2: radicals tend to create volatile products that can be eliminated by a sufficient gas flux:
CH_2: + O_2 → CO_2 + H_2
CH_2: + O_2 → CO + H_2O
CH_2: + CO_2 → 2CO + H_2
Furthermore, oxygen-rich organic groups: -COOH, -CO-, -OCO-, -OH, -O-, -C=O are recalcitrant to polymerize in plasma environments [192, 193]. When dealing with silicon contamination, oxygen molecules are not effective against polymerization, since the equivalent molecule to CO_2 is SiO_2 which is not volatile.

The CMS GEM Group decided to use Ar/CO_2 (70/30) mixture for the triple-GEM operation. CF_4 was a potential candidate to further improve the time resolution of GEMs detectors. However, multiple reasons are behind the decision of removing such gas from the mixture. Indeed, CF_4 is still a controversial gas from the aging point of view. Moreover, the CMS requirements were satisfied also without the use of such a gas [34]. Finally, CF_4 has a very large Global Warming Potential (GWP), around 7000 [135]. This makes CF_4 quite expensive but, more importantly, very dangerous to the environment. Then Ar/CO_2 was the natural selection due to the lack of intrinsic polymerization mechanisms [191]; furthermore it may prevent the formation of hydrocarbon polymers. The silicon contamination was maintained under control by selecting non-outgassing materials for the assembly of detector and gas system [46].

5.1.3 Aging phenomena in extreme particle environment

LHC based experiments are using gaseous detectors not only for operation at high rate, but also in harsh particles environment, with background particles releasing primary charges order of magnitude higher than MIPs. In wire-based detectors, high rates are usually associated to gain losses due to the large amount of space charge development. This has a protective

impact on aging since it intrinsically reduces the energy available during the electron multiplication and the sparking rate. However, in MPGDs the small amplification structures help to remove the ion excess faster, making them more suitable to high rate operations. Still, the micro-pattern designs are intrinsically more susceptible to discharges due to the proximity of the electrodes. The fact that the gain remain untouched in high rate environments is not helping in discharge suppression. The detector users, in this case, may be tempted to decrease the intrinsic gain of the detector to reduce the sparking rate but if we take into consideration also the small integrating time required for some experiments (not higher than 25 ns in LHC), this may diminish the MIPs detection efficiency of the detector. Nevertheless, this issue seems not to be a huge problem for modern GEM and Micromegas detectors that can easily sustain the LHC induced particle environment [28, 34, 217].

Sparks, as explained before, are one of the main problems of MPGD. In heavily ionizing particles environments, the likelihood to have particles releasing large amounts of primary charges is not negligible. The higher the released charge, the higher the probability to have electron avalanches that overcome the Reather limit; these events create low resistivity channels between anode and cathode that, in some cases, may lead to sparks. Every spark is a potential hazard from the aging point of view, since it can prepare the electrode for polymer deposition or create imperfections that build-up the spark probability. In general heavily ionizing particles are more dangerous from the aging point of view than other types of particles, not only to discharges, but also for the possible different induced polymer chemistry. Indeed, avalanche energy and density may drastically change how the different polymers dissociate and recombine.

5.2 Status of the art of the aging studies

Aging studies are usually performed during the R&D phase that anticipate the usage of a certain gaseous detector technology in a certain experiment. Analysing some of the past aging campaigns performed by gaseous detector groups, it is possible to find some common procedures. Generally, an aging test involves a detector in its final version with the final geometry and materials. Then, such detector is irradiated with a beam to collect the same (or higher) charge expected in the real experiment. Usually, in order to achieve this goal in a reasonable time, the detector is operated at a higher gain or, more often, at a higher hit rate; even if this should be avoided, in most of the cases it can become mandatory. Furthermore, the detector is operated with a clean gas mixture with a gas system usually smaller than the one to be used in the experiment. This is not a dramatic issue if

the final gas system is perfectly clean as the tested one, but generally it is very difficult to create a completely clean gas system, and the cleanliness of course decreases as the time passes. Moreover, during the aging test, it is a common rule to irradiate with photons: X-rays or γ-rays. This is usually a necessity since photons are quite easy to produce and to shield in a very large quantity, and there is no activation after their use. Unfortunately, it is very improbable to have an experiment with only photons as background. Then, the main issue in these cases is to not well represent the particle environment impinging the detector, in particular in experiments operating at hadronic machines. A few examples of an aging test performed for gaseous detectors systems of large detectors can be found at [110, 185–188, 199, 205]. Having in mind the considerations made in the past sections, it is clear that the 'standard' way to perform an aging test may not represent exactly the detector behaviour in real operations.

5.3 Aging test on a triple-GEM in contaminated gas environment

In [28, 34] the maximum accumulated charge expected for the three GEM stations GE1/1, GE2/1 and ME0 is respectively $6\,\mathrm{mC/cm^2}$, $3\,\mathrm{mC/cm^2}$, $283\,\mathrm{mC/cm^2}$. This estimation was made in [46, 110] and derives from the assumption that all the particles expected to interact in the detector will behave as MIPs releasing an average of 30 pairs per hit (as described in Sec. 2.1.1). Because of this underestimation it was decided to validate the GEM detectors for the CMS muon system upgrade to a charge 3 times higher: $18\,\mathrm{mC/cm^2}$, $9\,\mathrm{mC/cm^2}$, $849\,\mathrm{mC/cm^2}$. However, simulations of the particle background with the new hadron calorimeter design (Sec. 4), show a dramatic change in the particle environment. For the ME0 station a particle rate 3 times higher than in [28, 34] is expected and it clearly indicates that the expected average number of primaries is around 200, a factor 7 higher than a MIP. The target charges are now $60\,\mathrm{mC/cm^2}$, $30\,\mathrm{mC/cm^2}$, $7900\,\mathrm{mC/cm^2}$ for GE1/1 GE2/1 and ME0 respectively.

The CMS GEM detectors have been validated irradiating a whole detector portion with X-rays up to $1550\,\mathrm{mC/cm^2}$ with no gain loss [218]. In front of the new simulation outcomes, this result is still encouraging GEMs for the operation in GE1/1 and GE2/1 station, while for the fully validation of the ME0 station the CMS GEM group has to continue the irradiation campaign to reach the $7900\,\mathrm{mC/cm^2}$ goal. Since the simulations are now more precise in quantifying the amount of irradiation, the safety factor is probably not required, however internal discussion is still ongoing.

An advanced aging test was proposed to test the GEM technology also

in limit situations. As discussed in the previous section, one of the limits of standard aging tests is the fact that they are performed in an accelerated way, exploiting a small and clean gas system that may hide small contaminations that may occur and build-up during a long period in large systems. The test presented here consists in the irradiation of a small 10 cm × 10 cm triple-GEM in the CMS configuration with 5.9 keV X-rays from a ^{55}Fe source. During this test the detector is flushed with the standard Ar/CO_2 (70/30) gas mixture polluted with some glues vapours containing both hydrocarbons and silicon based molecules (see Fig. 5.4 and Fig. 5.5). These contaminants are known to be dangerous for gaseous

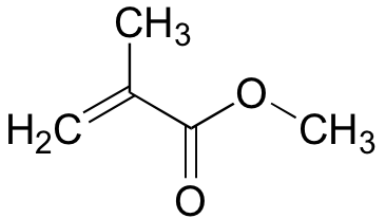

Figure 5.4: MethylMethacrylate molecule from 3140 RTV Coating®.

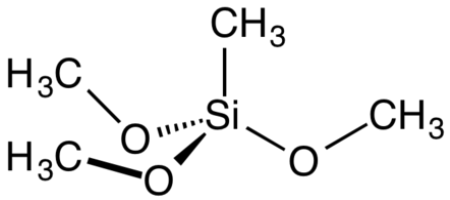

Figure 5.5: Methyltrimethoxysilane molecule from Acrifix 1R 0192®.

detector operations due to their tendency to polymerize during electron multiplication. The choice of these glues was made to cover a wide range of possible pollutants, in particular carbon and silicon structures. In the following, the experimental setup, the data analysis procedure along with the results are presented.

5.3.1 Experimental setup

The test was held at the CMS-GEM QA/QC facility sited in building 904 at CERN. A rack used for testing the outgassing properties of materials was cleaned and converted to accommodate the instrumentation to perform all the aging tests presented in this chapter (see Fig. 5.6). The gas supply is centralized and provides the standard CMS GEM gas mixture Ar/CO_2 (70/30) to all the four gas lines of the rack, which are made of stainless steel tubes except for the last detector connections pipes which are made of Rilsan®. The gas flow is controlled by valve rotameters, three of the four lines have a sealable cylinder (also referred as outgassing tube) used to insert materials that may release contaminants inside the gas volume before going to the detector. The outgassing tube can be heated up with a resistive tape, fixing the temperature by the supplied voltage. In this test little amounts (2 g each) of the two previously mentioned glues were placed

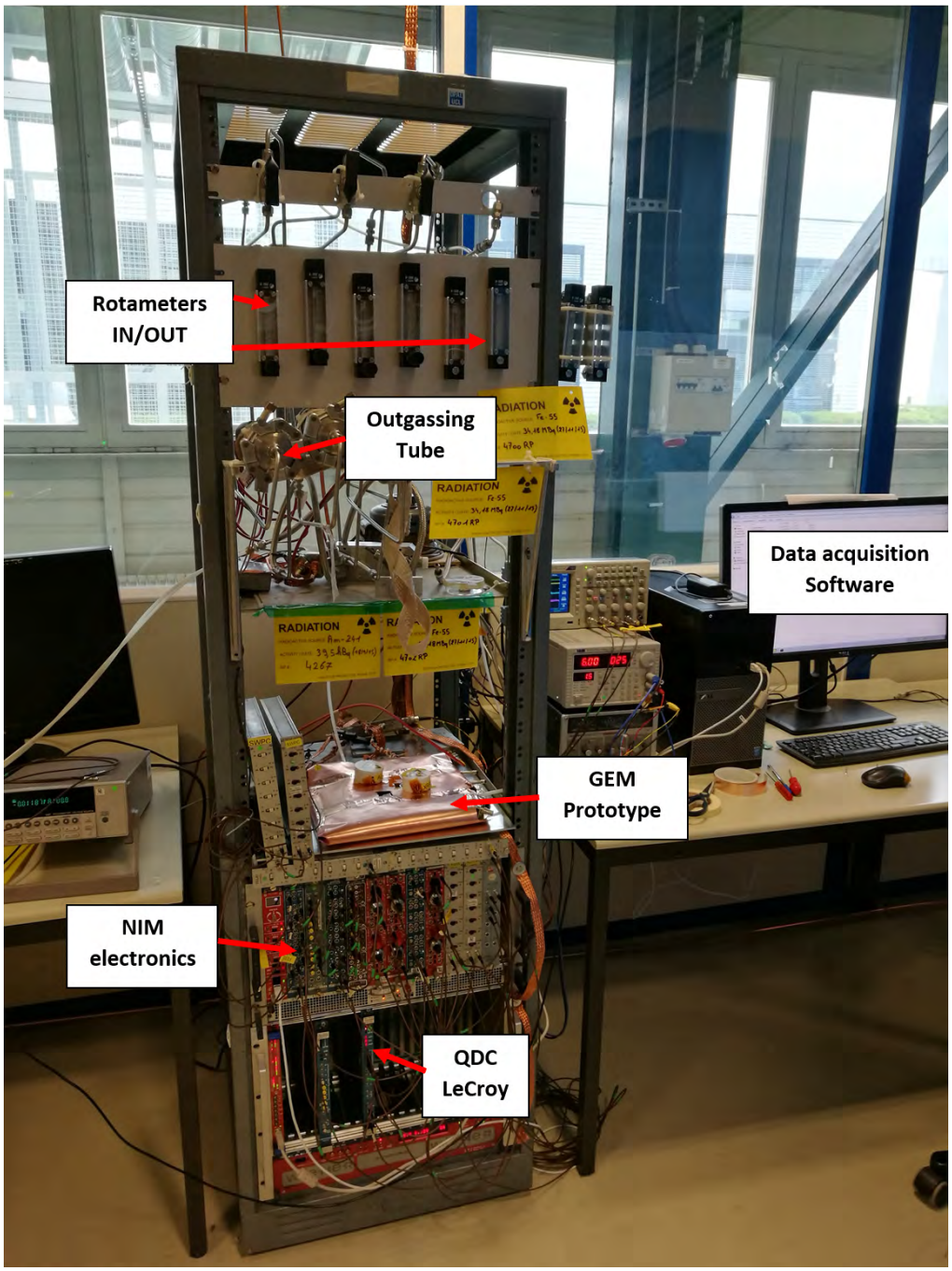

Figure 5.6: Photo of the aging setup, the rack can host multiple tests in parallel.

on a stainless steel plate dried for at least 24 hours and then inserted in the outgassing tube (Fig. 5.7). The contaminated gas is flushed through the GEM detector under test, a 10 cm × 10 cm stack of three GEM foils with 3/1/2/1 mm spacing between gaps (Fig. 5.8). The high voltage is supplied

Figure 5.7: Detail of the stainless steel plate where the glue is deposited; after being dried up the plate is placed inside the outgassing tube. The gas flushing here becomes contaminated before entering the detector.

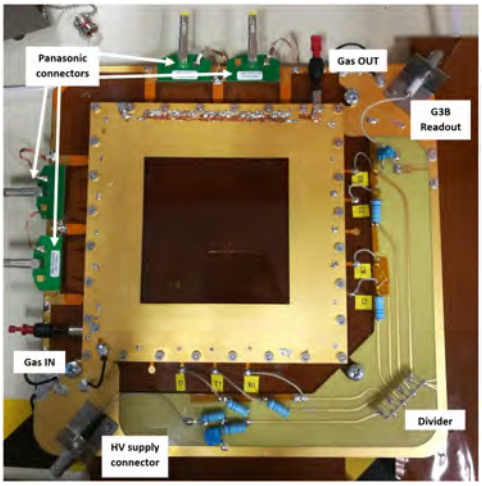

Figure 5.8: The GEM detector under test, the ^{55}Fe source is placed in the middle of the detector.

by one channel of a NIM HV module (CAEN N1470 [219]) and distributed to the electrodes through a voltage divider. Resistors (10 MΩ) are used as protection on the top electrodes and drift (Fig. 5.9). An additional T-filter (RCR: 100 kΩ, 2.2 nF and 100 kΩ) is used in series before the HV power supply to reduce the electromagnetic noise.

All the readout strips are read in OR by a single channel charge amplifier (Ortec 142PC [168]) and shaped (Ortec 474 [169]). The signal is duplicated by a Fan-in Fan-out module (Lecroy 428F [220]): one output produces a logic gate by feeding a discriminator (Ortec 935 [176]), while the other analogue output is attenuated, synchronized to the gate and sent as input to a 4096 channels VME charge analog to digital converter (QDC) module (Lecroy 1182 [221]). In addition a random trigger is generated using a dual timer module (CAEN N93B [177]) and summed to the discriminator output to sample both the signal and the baseline level. A further dual time module controls the length of the gate and is vetoed by the busy output of the QDC. QDC registers are readout and written by a PC via a LabView code that communicates with a VME bridge via USB (CAEN V1718 [222]); the PC controls the HV module too. A schematic view of the whole setup is shown in Fig. 5.10. To correct the effective gas gain from fluctuations due

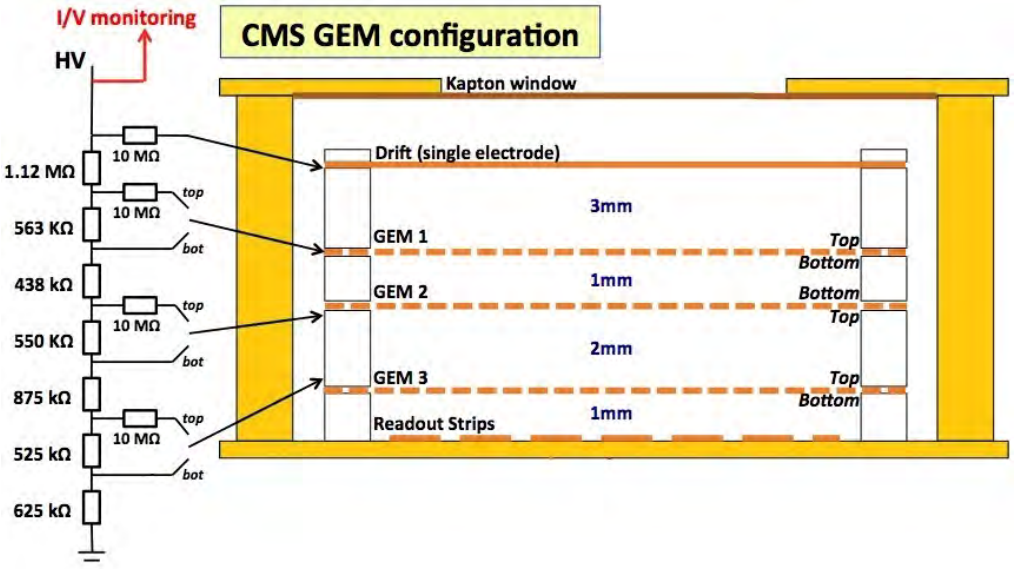

Figure 5.9: Schematic view of the triple-GEM used in this work showing the divider and the gap configuration.

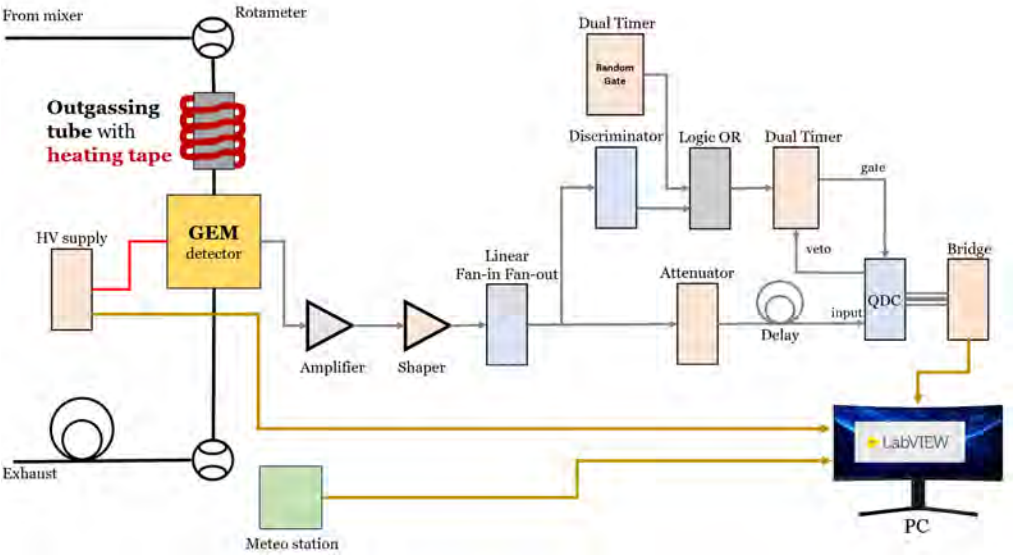

Figure 5.10: Data acquisition chain for the energy spectra measurement.

to change in environmental pressure and temperature, an Arduino-based meteo station is placed near the detector. Via a Python interface, measured values of temperature, pressure and humidity are saved every minute on a text file.

The $10\,\text{cm} \times 10\,\text{cm}$ detector has been calibrated before starting the data acquisition to assure its good behaviour and to find a reasonable working

point for the aging test. An effective gas gain scan was performed irradiating the detector with an attenuated ^{55}Fe source, according to the procedure explained in App. A. Fig. 5.11 shows the measured gain versus the applied voltage. The gain growths exponentially with the divider current, i.e. the current flowing in the voltage divider which is proportional to the applied voltage. Fig. 5.12 shows the measured hit rate on the detector, the selected threshold setting gives us full detection efficiency at divider currents higher than 640 µA. The working point has been set to 700 µA, corresponding to

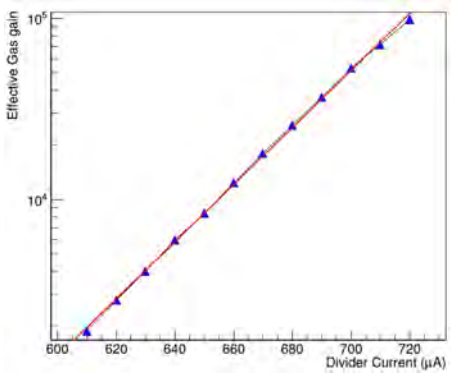

Figure 5.11: Measured effective gas gain as a function of the divider current. Data are fitted with an exponential function.

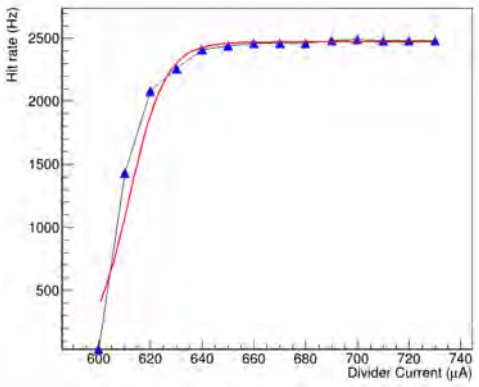

Figure 5.12: Measured hit rate as a function of the divider current. Data are fitted with a sigmoid function.

an effective gas gain of 6×10^4, 3 times higher than the nominal gas gain of CMS GEM detectors. This choice helps to further accelerate the possible aging processes and the charge integration rate. With the unattenuated ^{55}Fe source the measured hit rate is around 40 kHz, the current density on the irradiated area ($\approx 0.5\,\mathrm{cm}^2$) is around 130 nA/cm^2.

5.3.2 Data analysis and calibration

The data acquisition code collects signals for 30 minutes and saves the digitalized charge values on a text file for the offline analysis. Fig. 5.13 shows an example of a charge spectrum acquired by the system when irradiating the detector with 5.9 keV X-rays from a ^{55}Fe source. Every spectrum is fitted with three Gaussian functions: one for the pedestal and the others for the main photo-peak and the Argon escape peak. The gain information is extracted from the distance, in ADC value, of the signal peaks from the pedestal peak. In particular, the difference between the photo-peak mean and the pedestal mean ($\mu_{pp} - \mu_{pe}$) is used as gain variation indicator due to their mutual proportionality and the higher statistics of the photo-peak

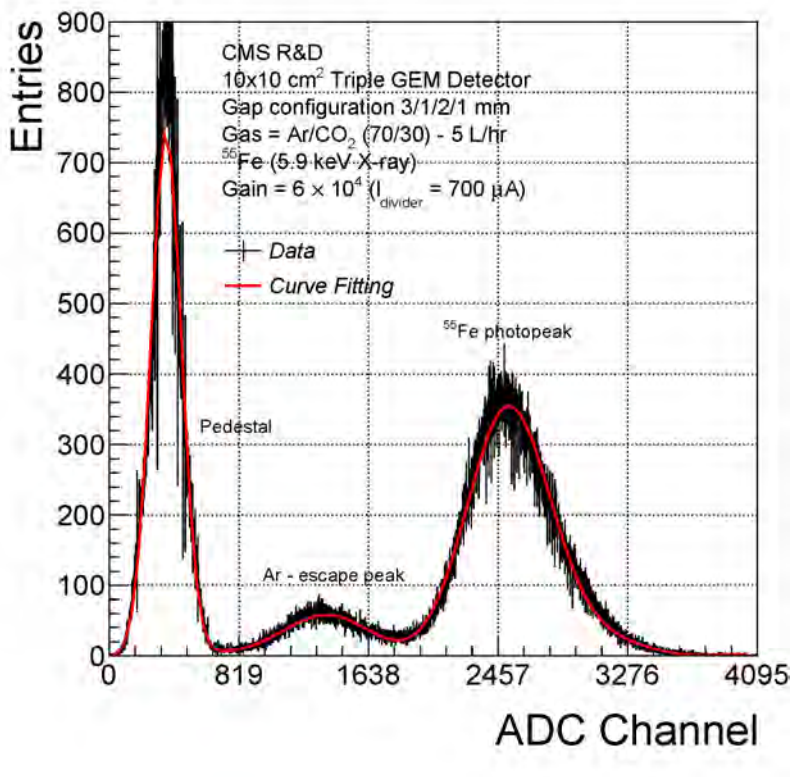

Figure 5.13: Example of a 30 minutes charge spectrum acquired from the detector under test.

with respect to the escape peak.

A calibration run is performed before starting the aging test. Spectra were acquired for one week flushing the detector in clean Ar/CO_2 (70/30) gas mixture at around $5\,L\,h^{-1}$. This is required for three reasons. First, this data taking run serves to have a reference measure of the $(\mu_{pp} - \mu_{pe})$ value to which the peak positions acquired during the aging test is normalized. The average value of all the peak distances, in ADC values, is used as reference to normalize all the following data. The calibration run also helps to calibrate the amount of charge collected during a spectrum acquisition. After the fit, at every spectrum channel value μ_{pe} is subtracted to have the 0-th channel to be centred at the position of the mean of the pedestal peak. The charge collected is proportional to the quantity:

$$q_{ADC} = \sum_{i=-\mu_{pe}}^{4095-\mu_{pe}} i \times h_i,$$

where the index i spans over the translated ADC channels and h_i is the number of entries in the i-th channel. The average value of the q_{ADC} during the calibration run $\tilde{q}_{ADC}$ is directly correlated to the average charge

collected in 30 minutes on the irradiated area: $234\,\mu C/cm^2$. The charge Q associated to every successive spectrum is then estimated by computing the q_{ADC} value and weighted with the reference values:

$$Q = \frac{q_{ADC}}{\tilde{q}_{ADC}} \times 234\,\mu C/cm^2.$$

Finally, the calibration run helps to find the correlations between the environmental temperature and pressure and the gain. Knowing these correlations and correcting the gain from them is essential to be sensitive to gain fluctuations only due to aging. Since the calibration runs are relatively short, not enough data are acquired to have a fine fit result with the procedure explained in Sec. 3.2.2. For this reason a more naive approach was used by parametrizing the gain dependency with a power law function where pressure and temperature are not correlated:

$$G_{uncorr}(T,P) = G_{corr}\left(\frac{T}{A}\right)^a\left(\frac{B}{P}\right)^b, \tag{5.1}$$

where A, B, a and b are parameters to be evaluated experimentally. The procedure to find these parameters consists in two steps: first, the correction of the pressure dependence and, then, the correction of the temperature dependence. During the first step the normalized gain points are fitted with the associated pressure values with a function (see Fig. 5.14a):

$$f(P) = \left(\frac{B}{P}\right)^b,$$

with the newly obtained B and b values, peak positions were corrected (see Fig. 5.14b):

$$G_{Pcorr}(T) = G_{uncorr}\left(\frac{B}{P}\right)^{-b}.$$

Last step is to fit the points with the temperature values, using this time the fit function (see Fig. 5.14c):

$$f(T) = \left(\frac{T}{A}\right)^a,$$

The peak positions can be now completely corrected (see Fig. 5.14d):

$$G_{corr} = G_{Pcorr}\left(\frac{T}{A}\right)^{-a}.$$

The steps of the correction parameters search are shown in Fig. 5.14. A and B were observed to converge to the pressure and temperature value in the

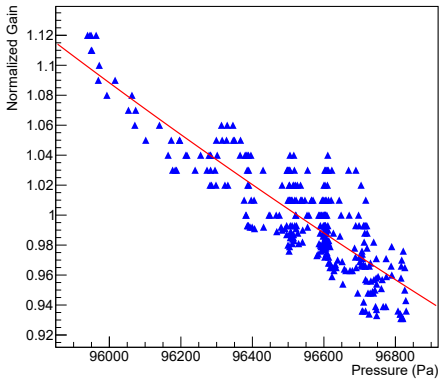

(a) Raw normalized gain as function of the environmental pressure, fitted with a power law.

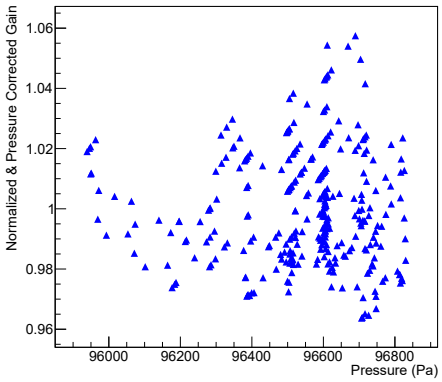

(b) Normalized gain corrected for the pressure dependency as a function of the environmental pressure.

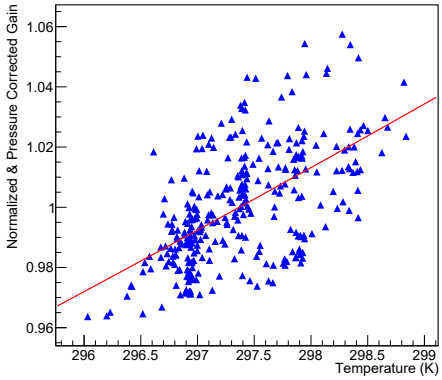

(c) Normalized gain corrected for the pressure dependency as a function of the environmental temperature, fitted with a power law.

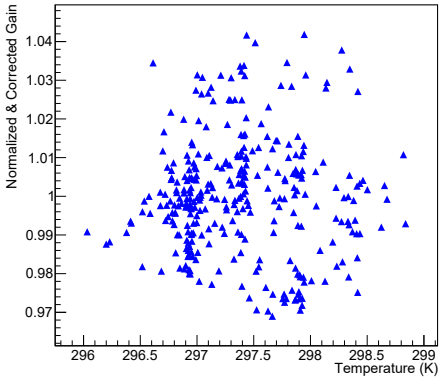

(d) Normalized gain corrected for both the pressure and temperature dependencies.

Figure 5.14: Steps of the simplified environment correction procedure

middle of the domain. Using the parameters found during this procedure, it is possible to correct the gas gain value referring it to a fixed temperature and pressure, namely A and B. The results of the correction is appreciable in Fig. 5.15 and Fig. 5.16, that show the comparison between corrected and non corrected gain respectively on a scatter plot against the time and on a histogram. In particular Fig. 5.16 shows a narrower peak for the corrected gains with respect to the non corrected ones. On the calibration dataset the ratio between gain mean and standard deviation μ/σ passes from 27.8 to 66.5 which is a good improvement (factor 2.4) that leads to a gain variation sensibility due to aging $> 5\%$.

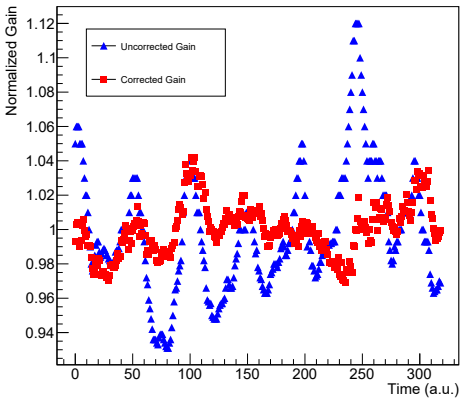

Figure 5.15: Gain evolution during the calibration run. In blue the raw measured gain points and in red the corrected ones.

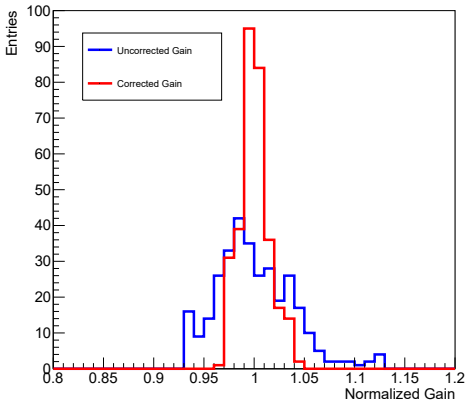

Figure 5.16: Histogram of the measured gains during the calibration run. In blue the raw measured gain points and in red the corrected ones.

5.3.3 Results

The detector working with the contaminated gas mixture was irradiated for about two months with a ^{55}Fe source, collecting a total charge of 500 mC/cm^2. After the collection of the first half of the charge the outgassing box was heated up to 50 °C to stimulate the contaminant emission. Despite the temperature increase in this section of the gas system, the gas gain seemed unchanged and the environmental correction continued to work well. This probably means that the 1 m stainless steel pipe between the outgassing tube and the detector is sufficient to bring the gas back to the environmental conditions. Fig. 5.17 shows the gain evolution as a function of the collected charge on the irradiated area. No gain loss was observed.

5.3.3.1 Scanning Electron Microscope analysis

Despite no macroscopic effects were noticed during the test, microscopic creation of polymers may have happened. To check for these effects, some pieces of all the three GEM foils were sampled and analysed using a Scanning Electron Microscope (SEM). SEM tests presented in this chapter have been performed by using similar instruments present both at CERN [223] and in Pavia [224]. Since the first and second GEM foil are undistinguishable from new ones, the following discussion refers only to the last GEM foil, the one that sees the higher charge density. The first step of the

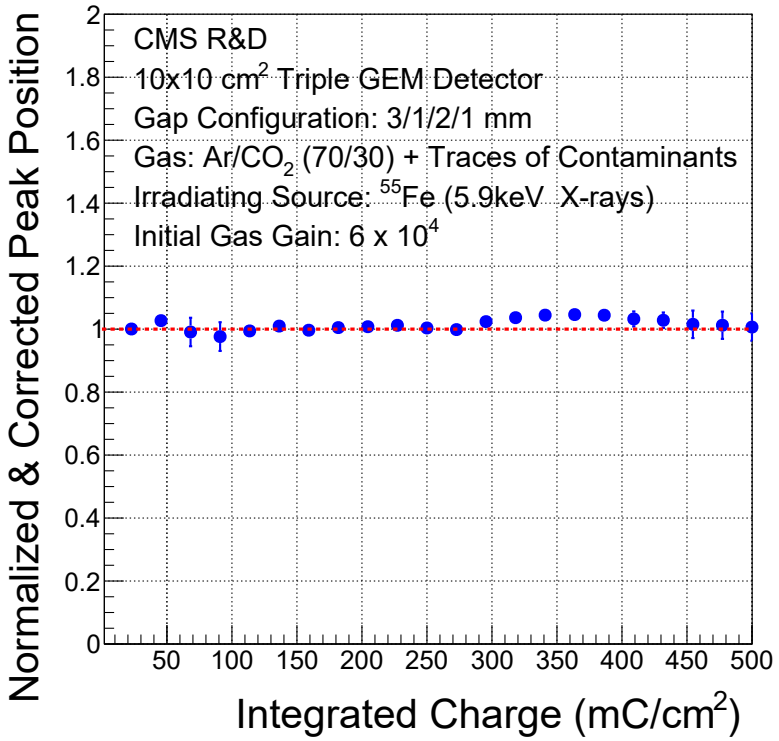

Figure 5.17: Peak position as a function of the integrated charge of the 10 cm × 10 cm GEM chamber. The peak position is normalized to the initial vale and corrected for the environmental fluctuations.

analysis is to look at the GEM holes to check for possible aging induced defects on the rims or changes in dimensions. Many holes were observed both with backscattered and secondary electrons. BackScattered Electrons (BSE) are high energy electrons that are reflected out of the irradiated surfaces due to multiple scattering. Since elements with high atomic number have a higher probability to backscatter electrons, looking for these electrons helps to detect different materials. Then pictures will present higher contrast between areas with different chemical compositions. On the other hand, Secondary Electrons (SE) are low energy electrons (<50 eV) that are freed from the specimen atoms by the incoming electron through inelastic scattering. When looking for SEs, steep surfaces and edges tend to be brighter than flat surfaces. This results in images with a well-defined, three-dimensional appearance [225]. Fig. 5.18 shows top and bottom images of the analysed holes (top and bottom do not correspond to the same hole). SE mode (Figs 5.18a and 5.18c) highlights the conical structure of the Kapton inside the hole, where possible defects or damages may be located. In particular Fig. 5.18a shows a narrow brighter region on the right part of

the Copper rim, suggesting that a polymer deposition may have took part here. Otherwise, in BSE mode (Figs 5.18b and 5.18d) the Copper is predominant on the other regions due to its high atomic number, Kapton is still visible and the high contrast is helping to detect irregularities on the interfaces and to measure the dimensions of the holes. A part from the

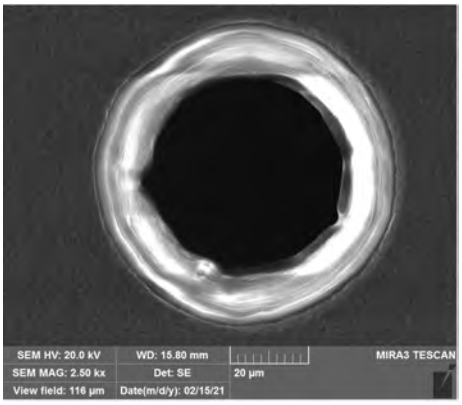

(a) Secondary electron analysis of the top side of a GEM hole.

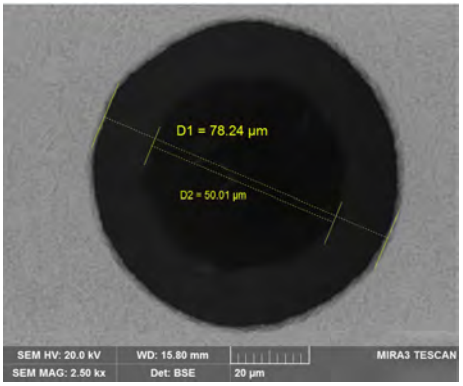

(b) Backscattered electron analysis of the top side of a GEM hole.

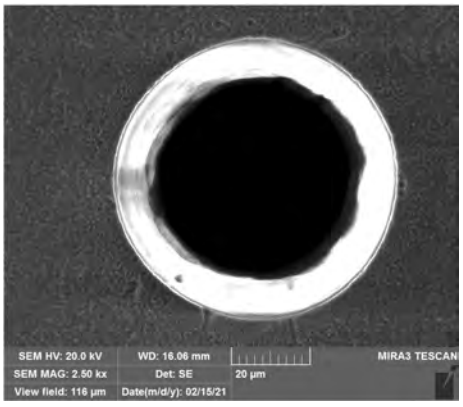

(c) Secondary electron analysis of the bottom side of a GEM hole.

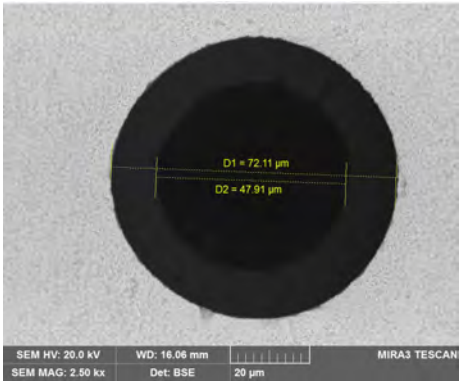

(d) Backscattered electron analysis of the bottom side of a GEM hole.

Figure 5.18: Scanning electron microscope images of top and bottom side of the third GEM foil holes with different imaging techniques.

bright shadow on the Copper rim of the top side of many GEM holes, in general they are very similar to non irradiated ones. No huge depositions, systematic damage or defects were observed in the samples. Furthermore, internal and external diameters of the holes are compatible with the non irradiated regions and with previous measurements on single-masks foils [102] (see Tab. 5.1).

	Digital microscopy		Cross section optical microscopy	
	Diameter (µm)	Error (µm)	Diameter (µm)	Error (µm)
Top	85.5	4.1	86.1	4.9
Middle	51.3	2.7	52.8	5.4
Bottom	73.8	3.3	71.0	2.1

Table 5.1: Measurements on GEM holes produced with the single mask technique. Top sides faces the cathode and bottom sides the anode. Data from [102].

5.3.3.2 Energy Dispersive X-ray Spectroscopy analysis

An additional semi-quantitative analysis may be performed on samples to look for polymer depositions. Energy-Dispersive X-ray Spectroscopy (EDS) is a well known technique that can be used with the same electron beam of the SEM. When beam's electrons excite the atom electrons they will emit characteristic X-ray lines and if detected they helps to identify the atomic compositions of the irradiated sample. Irradiating with 20 keV electrons the GEM samples, the interesting atomic specimens (Copper, oxygen and carbon) which are present also in a clean GEM and silicon, which is the signature of aging, can be excited hence detected [226]. All the elements except hydrogen and helium are, in principle, detectable with the EDS technique. However, EDS analyses presented in this chapter are not able to give quantitative measurement of the atomic concentrations but only semi-quantitative. Indeed, the elements concentration in the irradiated samples are normalized to the total quantity of detected X-rays, so the precise volumetric of superficial concentration is not measurable. Samples of the third GEM foils were analysed with this technique. In particular, square regions with sides of the order of 100 nm are investigated at various distances from the inner GEM rim. Fig. 5.19 shows the relative percentage concentration of the interesting atomic specimens (Copper, oxygen, carbon and silicon) as a function of the distance from the hole rim. The polymers that are expected to be created may contain oxygen, carbon and silicon. However, due to the EDS analysis limits and the fact that carbon and oxygen are also present in Kapton, only silicon will be treated as aging indicator. The starting position has to be taken with a grain of salt since the intrinsic defects of the Kapton holes may vary between samples, holes and inside the same GEM hole. The two plots are reflecting the GEM hole topology, indeed two regions are clearly distinguishable. At low distances (up to 13 µm for the top, Fig. 5.19a and up to 8 µm for the bottom, Fig. 5.19b) oxygen and carbon are dominant, highlighting the fact that we are looking at the Kapton rim inside the hole; Copper is detected at low

concentration, mostly because of the scattered electrons that excite also relatively far atoms, and silicon is present at concentrations lower than 1%, showing a very thin but diffused silicon polymers presence in this area. On the other hand, the second region (distances larger than 17 µm for the top, Fig. 5.19a and larger than 12 µm for the bottom, Fig. 5.19b) shows a clear dominance of the Copper cladding layer with some traces of oxygen and carbon that are present underneath the 5 µm Copper layer. Silicon is still present at relative concentrations lower than 1% but is very difficult to individuate it at distances larger than 25 µm to 30 µm. More interesting is the area between the two described regions. The interface between the Kapton and the Copper shows clearly a higher presence of silicon polymers, up to 5% on the top and 3% on the bottom, revealing that in this area, where the electric field is higher, the polymers tend to deposit (and probably to create).

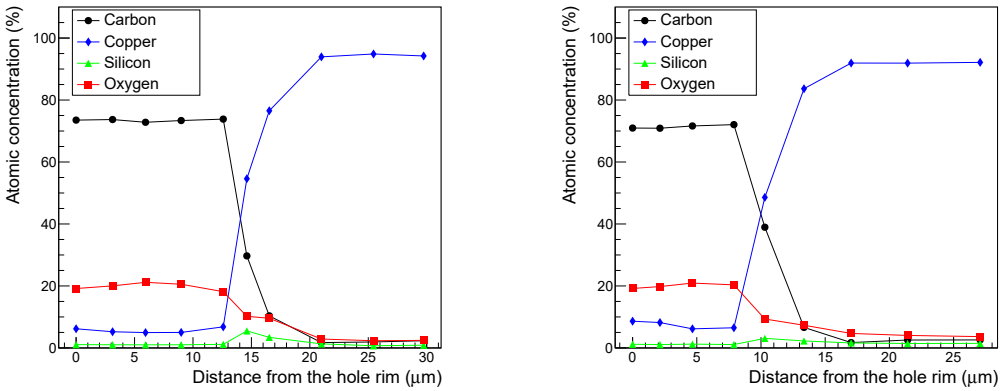

(a) Top side of the hole.

(b) Bottom side of the hole.

Figure 5.19: Atomic relative concentrations of selected elements as a function of the distance from the GEM hole rim. Measurements are made on a third GEM foil sample.

In light of the results of the test and the analysis some considerations may be drawn:

- GEM-based detectors are incredibly resistant to aging: a relatively long operation (500 mC/cm^2) of the detector under test in a polluted gas environment was carried out without any change in the macroscopic behaviour of the detector itself.
- SEM pictures didn't reveal any systematic damage or defects in the GEM holes structures, also polymers depositions are slightly visible on some GEM Copper rims showing only a light sediment.
- EDS scan in the GEM hole region shows a uniform but scarce silicon presence in all the investigated area. The peak concentration is on

the Copper edge where it reaches relative concentrations up to 5%, indeed this is the sector where the electric field is higher hence where the molecules dissociation and recombination take place with higher intensity.

This test, performed with the intention of validating the GEM technology for harsh gaseous environments, highlighted the radiation hardness of these detectors also in presence of silicon and hydrocarbon pollution. However, the accumulated charge of 500 $\mathrm{mC/cm^2}$ is equivalent to an extremely higher integrated charge than in a traditional aging test which exploits clean gas mixtures. The precise accelerating factor with respect to a classical aging test is not known because it is difficult to quantify the pollution or the probability of pollution in a clean gas system, moreover the polluting molecules may be different to the one used in this test. In conclusion, this aging test strengthen the idea in the community that the GEM detectors can be used also for the ME0 station in CMS. Nevertheless, a standard aging test of a ME0-like detector collecting up to 7900 $\mathrm{mC/cm^2}$ without any significant performance loss is required for the complete validation of the technology. The target charge (without safety factor) will be reached during two parallel test using two similar detectors at RTWH (Aachen) and ar Seoul university before the end of 2022.

5.4 Comparative aging studies on triple-GEM and wire chamber

As explained in Sec. 5.1 aging is still an open problem from the microscopic point of view mostly because of the different operating conditions between particles detectors physics and plasma chemistry. Without entering into details of other disciplines, it is possible to study the issue 'macroscopically' from the point of view of the detector. In this section a set of eight tests are presented, investigating the effects of particle ionization power, hit rate and charge collection rate on two different detector technology: a triple-GEM and a more traditional technology, a cylindrical proportional chamber. To study the effect of the particle ionization power, the detectors were irradiated with two different radioactive sources, alpha particles from ^{241}Am and soft X-ray from ^{55}Fe. For each of the technologies a series of four tests were performed: during the first two the detector was irradiated with the two different sources at similar interaction rate while in the other two with the sources giving the same amount of anodic current. The code names of the tests are: XRAY RATE and ALPHA RATE to identify the tests at the same rate with the 2 sources and XRAY CURRENT and ALPHA CURRENT for the tests at same anodic current. These pairs of tests

are carried out up to the same integrated charge or the same amount of percentage gain loss. Part of the work presented here can be found in [227–229].

The study presented in this section exploits the same setup and analysis procedure illustrated in Sec. 5.3.1. The Single Wire Proportional Chamber (SWPC) test is carried out by irradiating the detector with one source at the time; the detailed overview of the detector design is given in the following section. On the other hand 10 cm × 10 cm triple-GEM, similar to the one presented in the previous section, is irradiated in parallel with two sources placed in two opposite corners of the detector active area. This helps to accelerate the test outcome and to optimize the usage of GEM foils (the subsequent SEM and EDS analysis are disruptive). On the other hand, irradiating with two sources the same detector may introduce some uncertainties since polymers created in one region may deposit on other regions due to the gas flow. Moreover, particularly for the test performed with the two sources irradiating at similar hit rates, it may happen that polymers in alpha irradiated corner are removed by the gas flow due to the lack of irradiation. Indeed this latter test has to be performed intrinsically in 2 steps. Because of the same hit rate, the anodic current density is very different between the two region (alpha particles release way more primary charge than X-rays), hence the irradiation is started with both the sources but after a certain integrated charge on the alpha irradiated corner, the latter source is removed and only X-ray irradiation remains until the collected charge on the two region is reached. This issue is not present in the test performed at the same anodic current density because, by construction, the collected charge is reached more or less at the same time.

Because of the GEM design, 5.5 MeV alpha particles can not enter the drift gap since they are fully stopped by the external Kapton layer. A square windows of 0.3 mm^2 is manufactured on both the cover Kapton layer and the drift electrode to let these alpha particles enter the detector. The gas tightness is assured by a thin layer of polyethylene. The thickness of this layer may vary between 7 and 11 µm,depending on the stretching applied to the foil, Fig. 5.20 shows a sketch of the alpha irradiated corner modification. Precise knowledge of the thickness of the used foils is unavailable, but since the expected range of 5.5 MeV alpha particles in polyethylene is of the order of 40 µm [230], it is possible to say that particles enter the drift gap. Further investigation on the deposited energy of alpha particles will be given in Sec. 5.4.2. During these tests the aging was always accelerated exploiting the pollution of the gas from the glues vapours as explained in the previous section.

As discussed in Sec. 2.3.3.3, in GEMs, signals may be induced on non

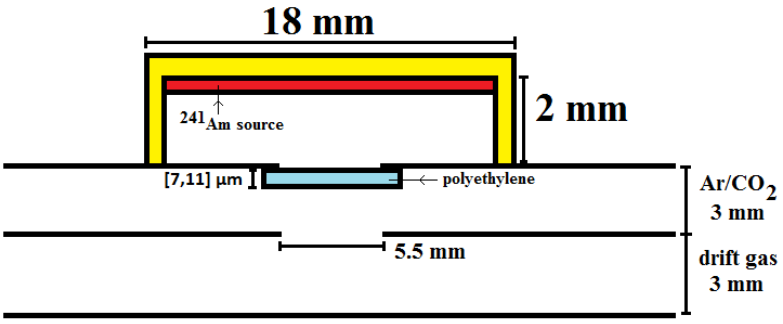

Figure 5.20: Schematic of the GEM corner modified to allows alpha particles to enter the drift gap.

irradiated sectors then, for example, the signals generated by the alpha particles can induce cross-talk ones in the X-ray irradiated region without any correlation. However, due to the large difference in the number of primaries explained in the following, the induced signals from one sector to the other are always way larger or way smaller than the considered ones. Therefore, if the dynamic range of the QDC is set for the optimal detection of a certain source spectrum, the cross-talk signals are always counted in the firsts or in the lasts channels.

5.4.1 The Single Wire Proportional Chamber

Usual cylindrical proportional counters don't meet all the requirements for conducting these tests. The requirements for a wire chamber to be used for these tests are:

- Gas tightness
- Good stability
- Easy to operate
- Fast and easy wire installation and removal
- Easy and efficient cleaning process
- Outgassing free materials (this point is not required for the presented tests but was necessary for other uses such as: checking cleanliness of a gas line, test outgassing of materials etc.)

The first effort to produce such a detector [46] was abandoned due to the instability of the gas gain. The new design of a Single Wire Proportional Chamber (SWPC) consists in a 26 cm long steel cylinder with a radius of 1.4 cm, moreover 4 mm holes are made on the surfaces to let particles enter the gas volume, see Fig. 5.21. Gas tightness is assured by stainless steel gaskets on the two end-caps that can be easily removed. The tension of the wire is maintained by two brass pieces screwed together that also assure the

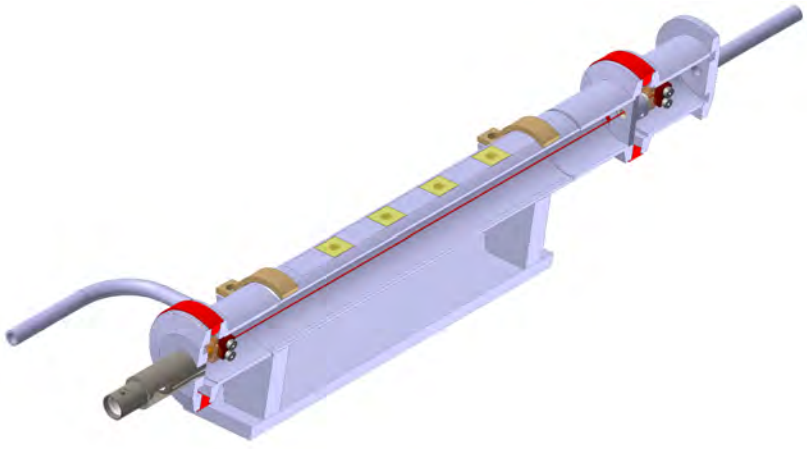

Figure 5.21: Section drawings of the designed SWPC.

high voltage connection, ceramic pieces separate the brass holders and the grounded cylinder. The detector build in such way satisfied all the previous requirements. Fig. 5.22 and 5.23 show a typical gain calibration and hit rate when irradiated with a ^{55}Fe source. The assembly procedure is easy and

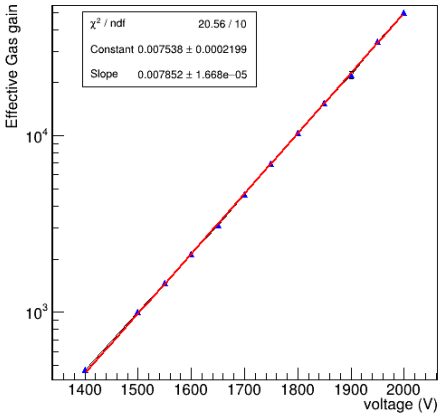

Figure 5.22: Measured effective gas gain as a function of the wire voltage. Data are fitted with an exponential function.

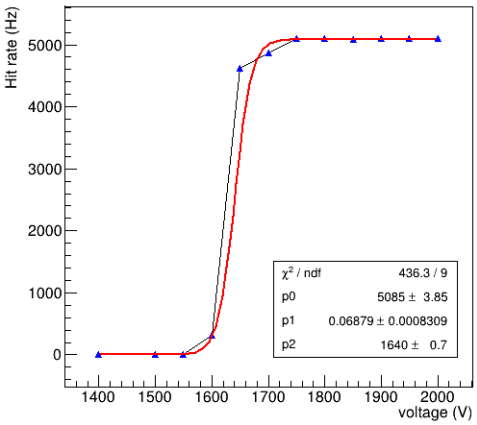

Figure 5.23: Measured hit rate as a function of the wire voltage. Data are fitted with a sigmoid function.

fast and after some practice the full dismantling, cleaning and assembly of a wire chamber take less than one hour. The cleaning process is performed by bathing with ultrasounds all the chamber pieces in a water and isopropyl alcohol solution (around 50% each). The wire is always tensioned using the same 84 g weight, see Fig. 5.25. Gas tightness is ensured by covering the holes in the cylinder with Kapton tape. In case of alpha irradiation, a setup similar to the one used for the GEM is exploited. A thin piece 7 µm to

11 µm of polyethylene is used to allow alphas entering the gas volume while conserving the gas tightness of the cylinder, see Fig. 5.24. Such detector

Figure 5.24: Close up of the wire chamber. The holes are made to let particles in, a thin polyethylene layer is placed to let alpha particles in and assure the gas tightness.

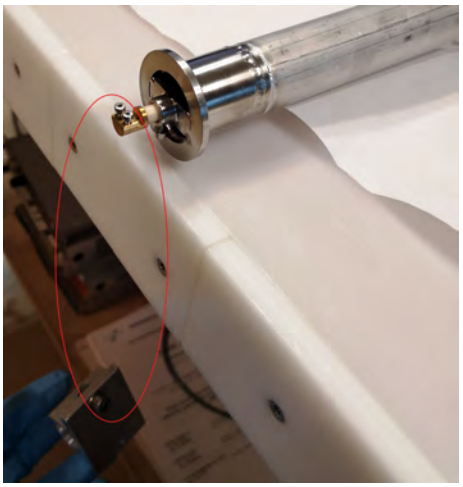

Figure 5.25: The wire is tensioned with a stainless weight (84 g). The brass holders are also visible with the ceramic piece to electrically separate the components.

has been used for the aging studies presented in this section showing, after complete cleaning, the same behaviour every time. The SWPC was also used to check cleanliness of the gas line in 904 laboratory and to tests outgassing properties of suspect glues and materials.

5.4.2 Estimation of the primary charge released by α particles

Measurements of the primary charge released by ^{55}Fe source were discussed in Sec. 4.1 and the results are still valid also in the case of the SWPC since the gas volume is way larger (GEM drift is 3 mm, SWPC internal diameter is 27 mm). In case of alpha irradiation, the deposited energy inside the gas volume is expected to be very different between detectors (around a factor 10). The primary charge is an important parameter for this test, since the different aging effects caused by this variable is under study. A direct measurement of the primary charge with the setup presented in Sec. 4.1 is not possible. Since the energy deposited by alpha particles in both detectors is expected to be $\sim$ 100/1000 times higher than 5.9 keV a calibration of a energy spectrum with X-rays source and a successive alpha energy spectrum are not compatible. Since the electronics (amplifiers and QCD) have not a sufficiently large dynamic range to acquire both sources

energy spectra a simulation were performed to have an estimation of the primary charge.

SRIM, The Stopping and Range of Ions in Matter [231], is a simulation tool that uses multiple programs to calculate the stopping power and range of ions into matter. In particular Transport of Ions in Matter (TRIM) is helpful for the primaries simulation because it will propagate the ion path and behaviour inside complex target of various material and dimensions. Fig. 5.26 shows simulated paths of 1000 5.5 MeV alpha particles emitted by the ^{241}Am source that imping on the GEM Kapton layer. No particles pass through this layer and the average range inside the Kapton, after 2 mm of air, is around 28 µm. To estimate the deposited energy, hence the average

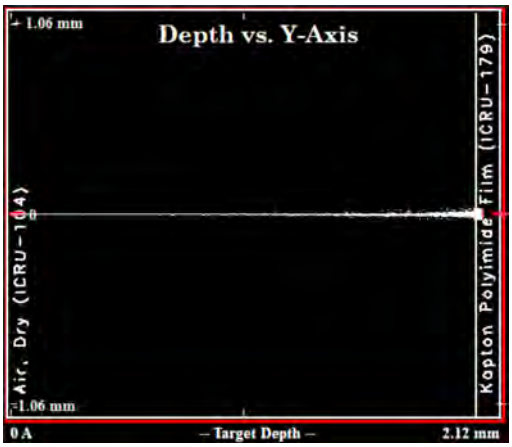

Figure 5.26: TRIM simulation of 5.5 MeV alphas entering a standard GEM. The 125 µm Kapton is enough to stop all the impinging particle.

primary charge, a simulation was performed to compute the average alpha energies when entering the drift volume and when leaving it. Layers were simulated according to Fig. 5.20 and they are shown in Tab. 5.2. The maximum entering angle for an alpha particle in the GEM configuration is calculated geometrically to be $\simeq 10°$. The energy of particles entering the drift was in the range [4.2, 4.7] MeV. When propagating the particles through the following 3 mm drift layer, the energy deposited in this gap was computed to be: (349 ± 38) keV corresponding to an average number of primaries of $(1.26 \pm 0.14) \times 10^4$, which is around 60 times higher than the primary charge released by a 5.9 keV X-ray.

A similar simulation was carried on also in the case of the SWPC. In this case the simulated materials are shown in Tab. 5.3, it is possible to note that the gas conversion layer is around a order of magnitude larger than the GEM one. However, the 27 mm gas volume is not enough to completely stop all the impinging alpha particles as shown in Fig. 5.27. Still, alphas are releasing in the gas volume a large amount of their energy: when averaging

Layer Material	Thickness (cm)	Density (g/cm^3)
Air, Dry (ICRU-104)	0.2	1.20 $\times 10^{-3}$
Polyethylene (ICRU-221)	[7,11] $\times 10^{-4}$	0.94
Ar/CO_2	0.3+0.3	1.72$\times 10^{-3}$

Table 5.2: Simulated layers of the GEM detector, polyethylene layer thickness is varied to obtain an average value of the deposited energy.

on the polyethylene layer and the impinging angle the deposited energy was simulated to be: (3846 ± 713) keV corresponding to an average number of primaries of $(1.39 \pm 0.26) \times 10^5$ a factor 700 higher than a 5.9 keV X-ray.

Layer Material	Thickness (cm)	Density (g/cm^3)
Ait, Dry (ICRU-104)	0.2	1.20 $\times 10^{-3}$
Polyethylene (ICRU-221)	[7,11] $\times 10^{-4}$	0.94
Ar/CO_2	2.7	1.72$\times 10^{-3}$

Table 5.3: Simulated layers of the SWPC detector, polyethylene layer thickness is varied to obtain an average value of the deposited energy.

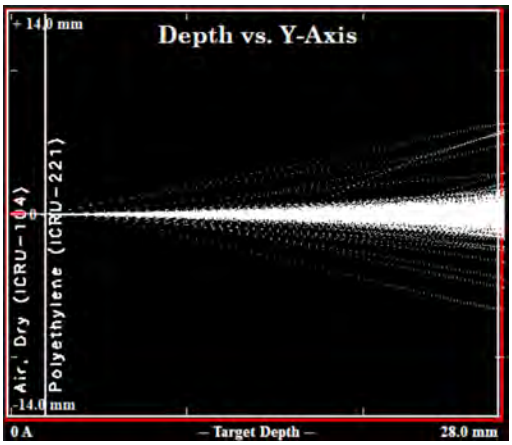

Figure 5.27: TRIM simulation of 5.5 MeV alphas passing across the SWPC materials.

5.4.3 SWPC tests results

Tab. 5.4 shows some of the crucial operating parameters of the SWPC during the performed tests. Fig. 5.28 shows the gain trend during all the 4 tests. The RATE tests present a relatively low integrated charge, 1.4 mC/cm due

	Same hit rate test		**Same anodic current test**	
	XRAY	ALPHA	XRAY	ALPHA
Operating Voltage (V)	1950	1950	1900	1900
Estimated Primaries	200	1.39×10^4	200	1.39×10^4
Irradiated Wire (cm)	0.4	0.4	0.4	0.4
Effective Gas Gain ($\times10^4$)	3.6	3.2	2.7	2.4
Hit rate (kHz)	0.11	0.08	41.0	0.08
Current density (nA/cm)	0.3	142.0	89.2	88.6
Integrated charge (mC/cm)	1.4	1.4	9.5	33.0

Table 5.4: Resume of some operating parameters of the SWPC tests.

to an experimental limitation. Since the rate has to be the same and there is a factor 700 between the primaries released by the two different particles, the duration of the two tests differs by the same factor, meaning that the XRAY RATE test duration may be too long to have results in a reasonable time. The RATE tests (Fig. 5.28a and 5.28b) do not present a large gain drop, it is estimated to be around 10% for both tests on average, showing no strong influence of the particle type up to this small integrated charge. CURRENT tests (Fig. 5.28c and 5.28d) do not have the same experimental constrain of the previous and in this case, since the gain drop is appreciable in both cases, the tests was stopped at the same gain drop ($50\% \div 60\%$). It is important to note that, during XRAY CURRENT test after around 18 mC/cm, the high voltage power supply of the detector tripped, leaving, for a whole weekend, the detector flushing without power. This seemed to have impacted on the further gain loss of the detector. Indeed, the gain loss trend was continuos up to that integrated charge, while after some days of flushing the trend stopped and it re-started only after further several mC/cm. This may suggest that flushing without high voltage an aged detector may help to prevent further aging, but probably it is not enough to fully restore the original performance of the detector. It can be observed, from the CURRENT tests, that the alpha particles are more effective in aging wire chambers, indeed the accumulated charge to reach around 50% gain loss is 2-3 times larger using X-rays than alpha particles.

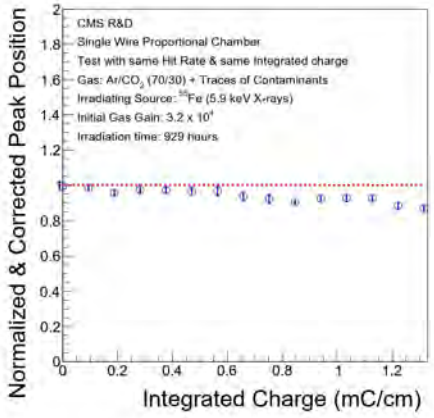

(a) Normalized and corrected gain of the SWPC during the XRAY RATE test.

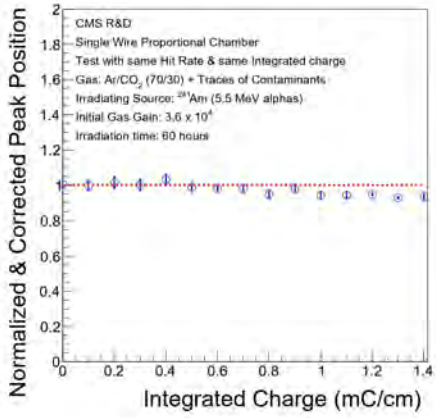

(b) Normalized and corrected gain of the SWPC during the ALPHA RATE test.

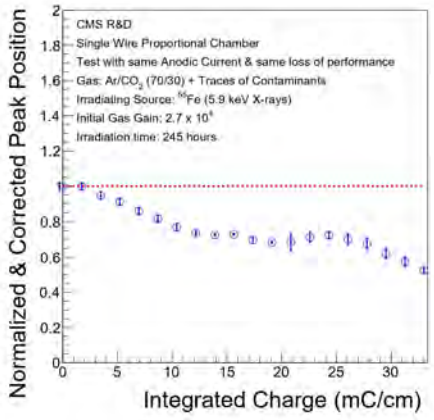

(c) Normalized and corrected gain of the SWPC during the XRAY CURRENT test.

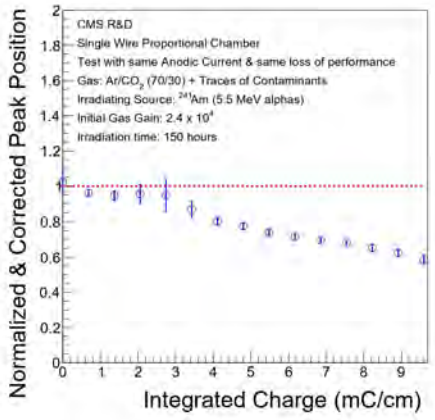

(d) Normalized and corrected gain of the SWPC during the ALPHA CURRENT test.

Figure 5.28: Gain trend plots during the SWPC tests.

5.4.3.1 Scanning Electron Microscope analysis

After the data acquisition period, the SWPC was dismantled in clean room and the wire was carefully collected. The wire was soldered on a 35×50 mm C-shaped aluminium piece to facilitate the analysis procedure, see Fig. 5.29. A Scanning Electron Microscope was used to look at the samples irradiated areas to find imperfections and deposition. Fig. 5.30 shows a portion of a non-irradiated wire, imperfections on the surface are natural due to the gold plating procedure. Fig. 5.31 shows the irradiated portions of the wires after the tests. It is important to note the absence of deposition on XRAY wires: Figs. 5.31a and 5.31c show no deposit. Despite the clear gain loss

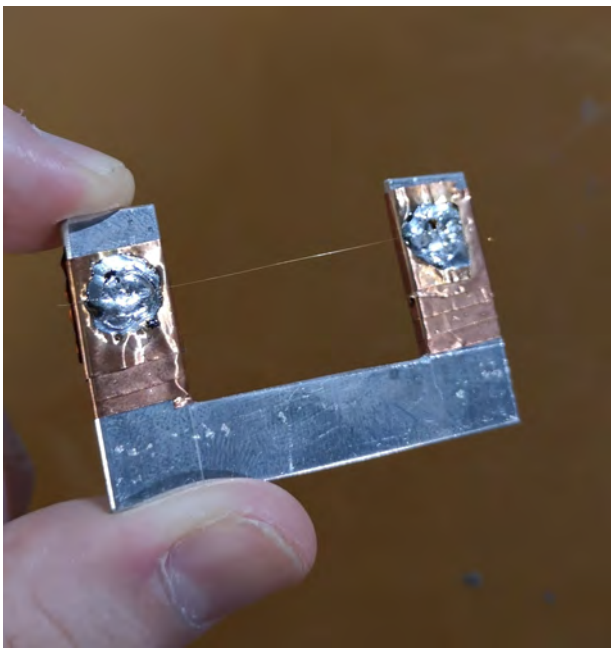

Figure 5.29: Wire sample soldered on its support to facilitate the analysis procedure.

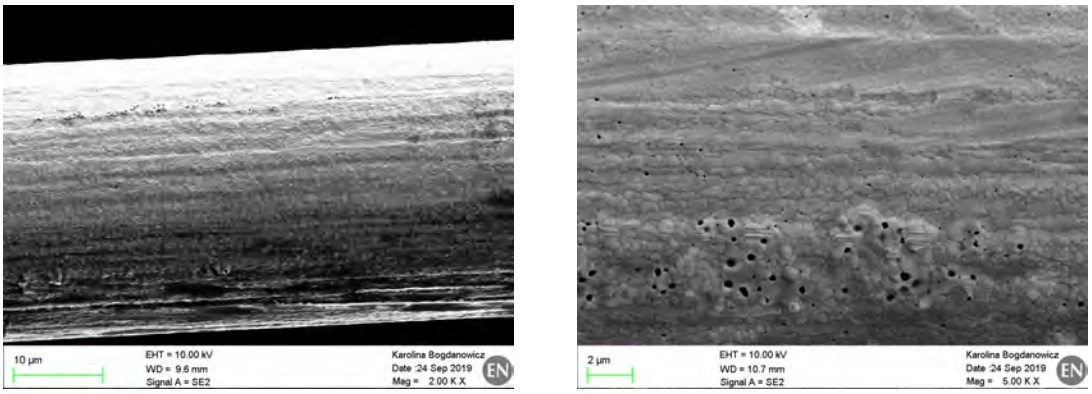

Figure 5.30: SEM pictures of a new wire portion before the irradiation.

of the detector in XRAY RATE and XRAY CURRENT, no polymers were found on the anode; while on the ALPHA irradiated wires, that reached a comparable gain loss with respect to the corresponding XRAY test, a clear and thick layer of polymers was present. There are multiple hypotheses to explain the lack of depositions: for example XRAY polymers on the anode were more fragile than ALPHA ones, which can be removed during the delicate sampling operation also if this wis made very carefully. If the sampling operation has no influence on the lack of polymers, it could be that the different chemical composition of the deposit lead to disruptive reaction with air only in the XRAY case. Lastly, it could be that the

deposit on XRAY was more prominent on the cathode, leaving no trace on the anode. Some hypotheses are less robust than others; e.g. since the sampling procedure is the same for all the wire, probably it is not affecting too much the presence of the polymers. Moreover, no indication of cathode deposit, such as increase of the dark count rate and current was individuated. On the other hand, the deposits are clearly visible in both the ALPHA tests. In ALPHA RATE (Fig. 5.31b) the deposit is 1.4 µm thick on the wire portion facing the source, while this thickness reduces to 0.6 µm on the opposite side. The deposit facing the source presents lumps structures suggesting a sort of footprints of the impinging particles that created the blobs. In ALPHA CURRENT wire (Fig. 5.31d) the deposit was thicker ($3 \div 4$ µm) and there is no clear distinction between the the side facing source and the opposite one. Therefore, it is possible to say that the

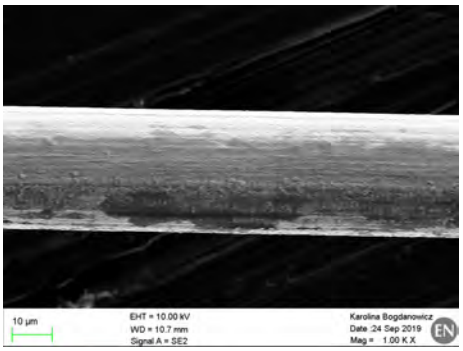

(a) Anode wire after the XRAY RATE test.

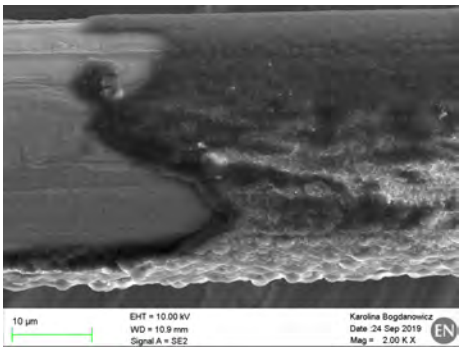

(b) Anode wire after the ALPHA RATE test.

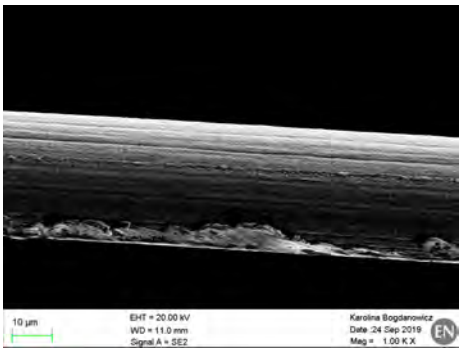

(c) Anode wire after the XRAY CURRENT test.

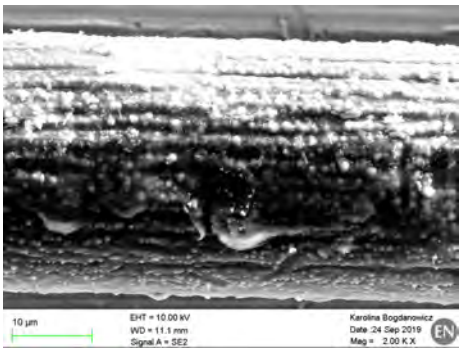

(d) Anode wire after the ALPHA CURRENT test.

Figure 5.31: SEM picture of the 4 irradiated wires.

ALPHA CURRENT deposit is $2 \div 3$ times thicker than the ALPHA RATE in front of the fact that the first collected around 6 times more charge than the latter.

5.4.3.2 Energy Dispersive X-ray Spectroscopy analysis

The semi-quantitative EDS analysis was performed on the irradiated areas of the wires under analysis. Fig. 5.32 shows a typical EDS spectrum of a non-irradiated wire. It is clear that EDS sees only gold if a clean wire is analysed; traces of aluminium are present because this is the material of the SEM anode where the samples stand. Since in a clean wire only

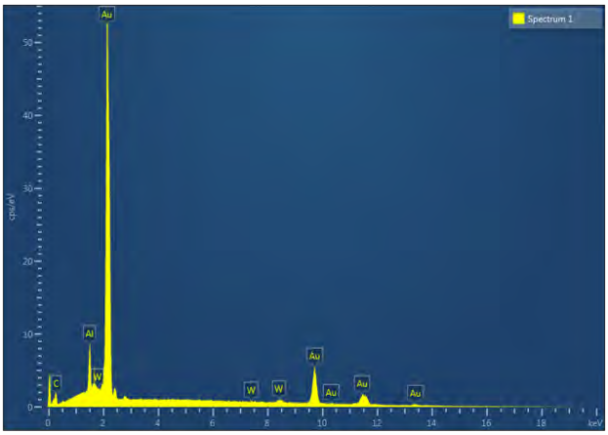

Figure 5.32: Typical EDS spectrum of a new, non-irradiated wire.

gold is expected to appear, it is possible to make EDS more quantitative on the irradiated wires by comparing, not the percentage concentration of the contaminants, but the concentration of a certain element normalized to the gold concentration. Indeed, in a clean wire this ratio is supposed to be near to zero, while it grows with the thickness of the layer depending on the atomic specimens. The elements found on the irradiated wires, and in general the aging markers, are: silicon, carbon, oxygen and sulphur. Fig. 5.33 shows the ratios of the concentration of the four elements with respect to gold. No contaminants were found on the XRAY wires, confirming that no polymers are present on such samples. On ALPHA wires, the largest presence of contaminants were detected on ALPHA CURRENT where all the concentrations seems to be double with respect to ALPHA RATE, confirming that the deposit thickness is around 2 times larger in ALPHA CURRENT. This result seems to be comparable with the one obtained by the HERA-B muon group [232], where they demonstrated that using a 100 MeV alpha beam, their drift chambers aged twice as fast as when they are irradiated with ^{55}Fe. Although the differences between the two tests are many (e.g. gas mixture contained CH_4 and CF_4, alphas energies are quite different and current densities were the same in the two tests but way higher: 700 nA/cm), the result seems to be compatible and attributable to the larger and denser charge released by heavily ionizing particles. The fact that the proportions between elements to gold ratios

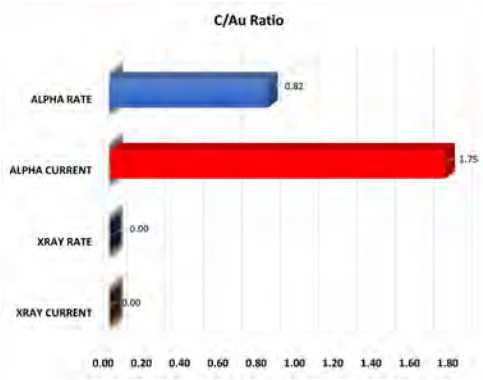

(a) Relative concentrations of carbon normalized to the gold one.

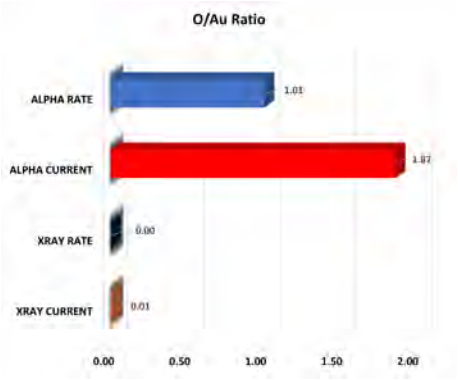

(b) Relative concentrations of oxygen normalized to the gold one.

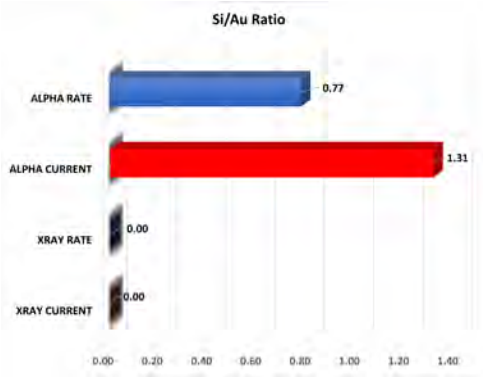

(c) Relative concentrations of silicon normalized to the gold one.

(d) Relative concentrations of sulphur normalized to the gold one.

Figure 5.33: Normalized concentrations of interesting atomic specimens on the irradiated wires areas normalized to the gold concentration.

remain similar between the two alpha tests may suggest that the polymers in the ALPHA tests are similar at least in chemical composition if not maybe also in the molecular structure. Finally, the sulphur presence was not expected at all. Its appearance is imputable to some materials used during the manufacturing processes of the glues.

5.4.4 GEM test results

Tab. 5.5 shows some of the crucial operating parameters of the GEM detectors during the tests performed. Fig. 5.34 shows the gain trend during the all 4 tests. The GEMs gain during all the tests was completely stable and no systematic variation of the performance was detected during all the irradiation period. The ALPHA CURRENT result by itself is highlighting the resistance to aging of GEMs detector with the astonishing result of

	Same hit rate test		**Same anodic current test**	
	XRAY	ALPHA	XRAY	ALPHA
Operating divider current (μA)	700	700	700	700
Estimated Primaries	200	1.26×10^4	200	1.26×10^4
Irradiated Area (cm^2)	0.5	0.3	0.5	0.3
Effective Gas Gain ($\times10^4$)	6.0	5.0	5.9	4.7
Hit rate (kHz)	1.4	0.6	48.3	0.6
Current density (nA/cm^2)	6.3	222.0	208.3	207.6
Integrated charge (mC/cm^2)	180	171	281	280

Table 5.5: Resume of some operating parameters of the GEM tests.

no performance loss up to 280 mC/cm^2 when irradiated with α-particles (releasing primary charge of the order of 10^4) in a strongly polluted gas environment.

5.4.4.1 Scanning Electron Microscope analysis

After the tests, samples of GEM foils were collected for SEM investigations and and analyses. For each detector, samples of two irradiated areas and one sample from a non-irradiated one were collected, see Fig. 5.35. Fig. 5.36 shows a pictures of the top sides of the third GEM foil after the irradiation. The third GEM foils is the one most subjected to aging since it is where the charge to amplify is the larger, indeed in all the analysed samples it is the one that present more sign of aging and concentration of polymers. The following considerations will regard the top side (the one facing the previous foil) since it is systematically more affected to aging than the bottom one. However, the atomic concentrations and effects found in the top side are not different in proportions with respect to on the bottom side, they only present a lower polymerization. Same thing is valid between the three GEM foils, the top of the third GEM foil is just the most affected by aging: there are no further information in other detector part that are not present here. XRAY foils (Figs. 5.36a and 5.36c) did not present any visible evidence of aging, while for ALPHA test the indication is more clear. Indeed, the ALPHA RATE (Fig. 5.36b) presents a dark halo around the hole rim, suggesting the presence of elements with lower atomic

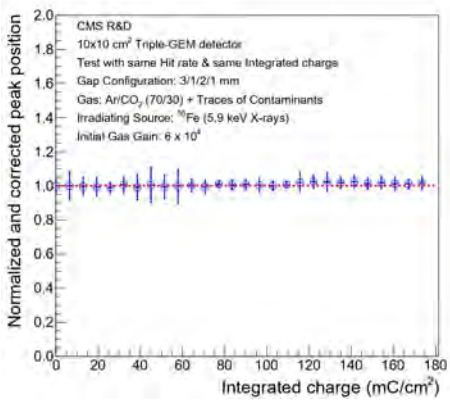

(a) Normalized and corrected gain of the GEM during the XRAY RATE test.

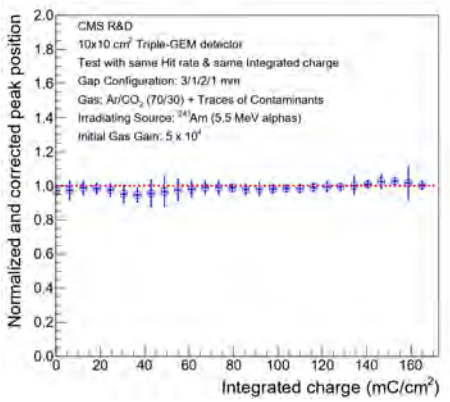

(b) Normalized and corrected gain of the GEM during the ALPHA RATE test.

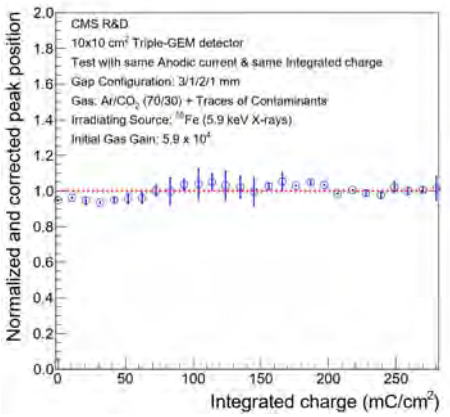

(c) Normalized and corrected gain of the GEM during the XRAY CURRENT test.

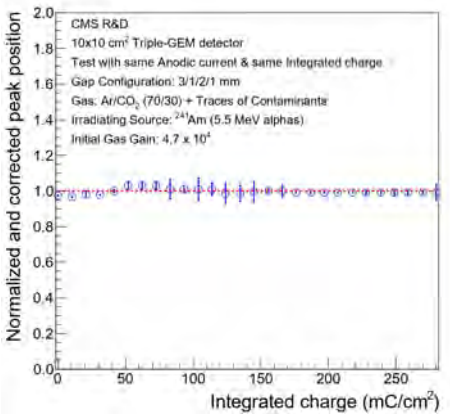

(d) Normalized and corrected gain of the GEM during the ALPHA CURRENT test.

Figure 5.34: Gain trend plots during the GEM tests.

number than Copper. Over this evidence the inner hole structure and the Copper rim did not present any systematic variation from a non-irradiated hole. ALPHA CURRENT (Fig. 5.36d) on the other hand seems radically different from a standard hole. The dark region around the rim extends on a wider region, the Copper rim is jagged and irregular and the inner Kapton hole is covered in polymeric bubbles, details in Fig. 5.37. It is clear that the latter hole is the one most affected by polymeric deposit both on the Kapton and the Copper and by spark that made the Copper electrode irregular. The main difference between the two alpha tests, apart the wider deposit on the Copper, is the fact that ALPHA RATE do not present evident polymeric structure inside the Kapton. The lower polymer deposit on

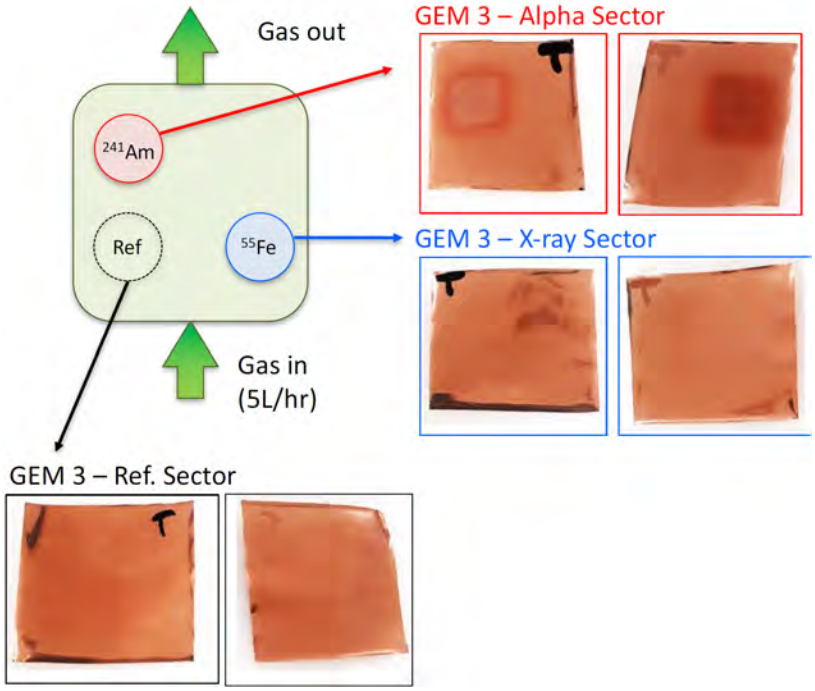

Figure 5.35: Samples are collected from the two irradiated corners and from a non-irradiated region for every foil. Samples photos are from RATE test.

both the Copper and Kapton may be attributed to the lower accumulated charge in ALPHA RATE, but the fact that the ALPHA RATE region was flushed with gas without irradiation for several time has to be taken into consideration for this comparison. It is important to remark that, despite the previously cited defects, the average dimensions of the irradiated holes have not systematically changed with respect to a non irradiated holes. The lack of macroscopic aging effects is probably imputable to this fact: the holes in some cases have deformed but in general the dimension are not changed that much to be macroscopically measurable.

5.4.4.2 Energy Dispersive X-ray Spectroscopy analysis

The EDS analysis of the GEM samples were analysed similarly as described in Sec. 5.3. The elements concentrations are measured as a function of the distance from the inner Kapton rim: Fig. 5.38 shows the results. Silicon is present in all the samples, in XRAY test (Figs. 5.38c and 5.38a) its concentration in below 1% on the Kapton region while it increases up to 3-4% around the Copper-Kapton interface before almost disappearing after 5 to 10 µm from that, in the same way observed in Sec. 5.3. In the ALPHA tests the situation is similar but the silicon is way more concentrated than

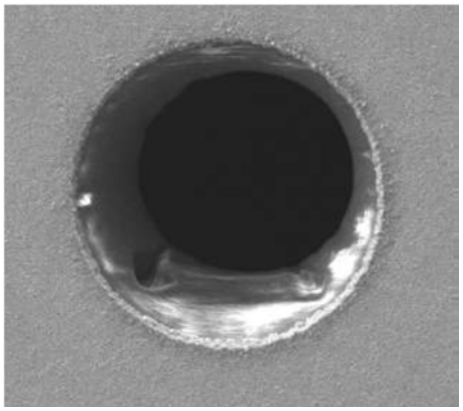

(a) Top side of a GEM hole from the XRAY RATE test.

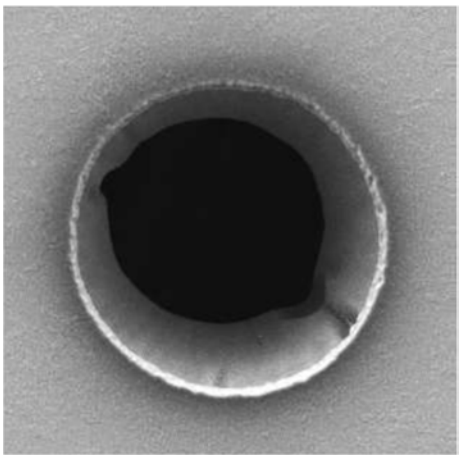

(b) Top side of a GEM hole from the ALPHA RATE test.

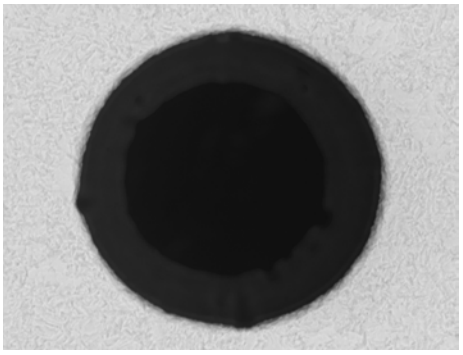

(c) Top side of a GEM hole from the XRAY CURRENT test.

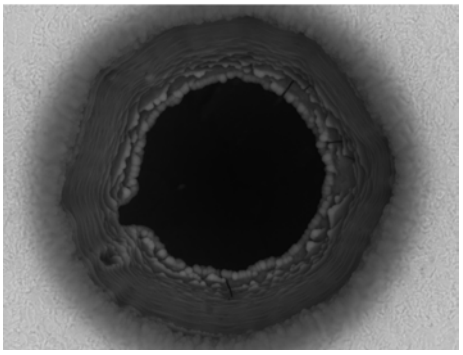

(d) Top side of a GEM hole from the ALPHA CURRENT test.

Figure 5.36: SEM pictures of top sides GEM hole from the tests performed.

in XRAYS. The maximum of the polymer concentration is found on the Copper-Kapton interface, while on the Kapton and the Copper, silicon is found constantly distributed everywhere on the irradiated region. In the Kapton region ALPHA CURRENT seems to have a larger quantity of oxygen with respect to ALPHA RATE, probably related to the visible polymeric deposit found in the first (Fig. 5.36d).

In order to better quantify the relative concentrations of the elements, a similar procedure to the one presented in the wire chamber tests has been performed. The concentrations of elements are normalized to the Copper concentration, this procedure has validity only if we consider EDS points on the Copper region. Indeed, only in this case we can assume that a clean foil shows more or less only Copper presence during an EDS. By the way, the normalization to Copper concentration was performed also inside the Kapton region. Here the concentrations ratio become less reliable because

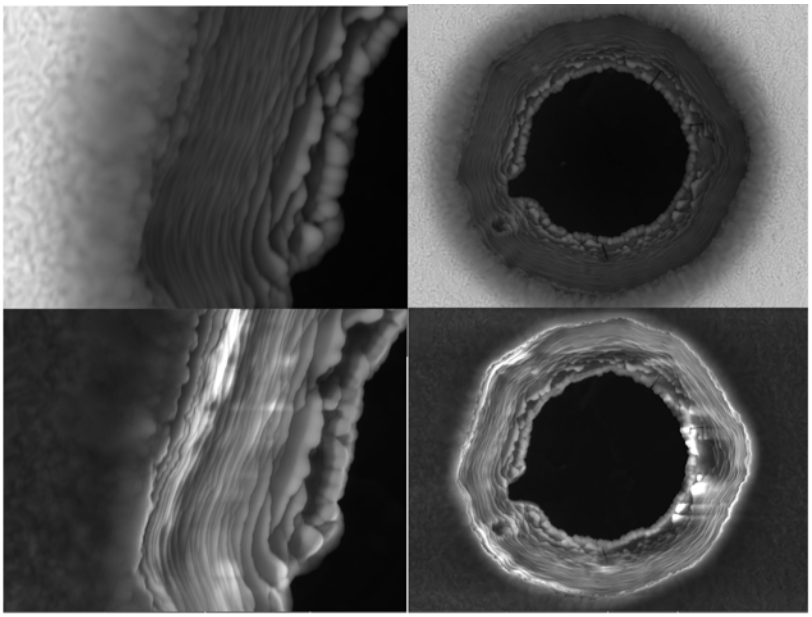

Figure 5.37: Detailed pictures of the top side of one GEM hole from the ALPHA CURRENT test.

the measured Copper concentration is only due to the scattered electrons hence it can vary locally and it may not be representative. Fig. 5.39 shows indicatively the two regions where the concentrations ratios are measured. Fig. 5.40 shows the measured ratios on the Copper region for carbon, oxygen and silicon for the four tests and for a non-irradiated hole. Carbon is probably not a good indicator of aging in this region for two reasons: firstly is always detected in all the samples due to its presence in Kapton structure. Moreover the concentrations in the specimens are small, suggesting that if polymerization occurred, it is probably not involving carbon based polymers. On the other hand oxygen and silicon present larger relative concentration and can be used to draw some conclusions. In XRAY tests, oxygen concentration do not seem systematically larger than the reference, while in ALPHA both the tests show similar and abundant presence of oxygen. The same is valid for silicon concentrations, where the ALPHA tests present large and similar amount while in XRAY only traces are found. This evidence suggests what already expressed in the previous section, alpha particles trigger more likely the polymerization than soft X-rays due to their higher ionization power. Noticeable is the fact that both ALPHA tests present similar concentration of polymers (made of oxygen and silicon) despite the larger accumulated charge in ALPHA CURRENT which is 50% larger than the ALPHA RATE one even though the latter have been flushed for a certain period without any irradiation. Fig. 5.41 shows the ratios measured on the inner Kapton rim of the GEM hole. As already

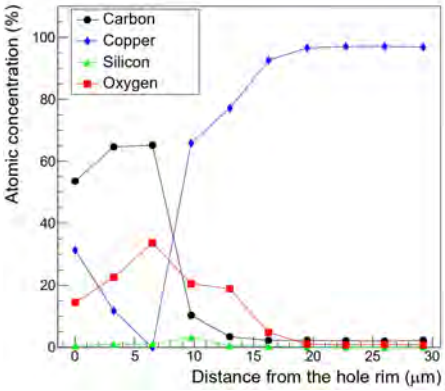

(a) Relative concentrations of selected elements as a function of the distance of the hole rim on a XRAY RATE hole.

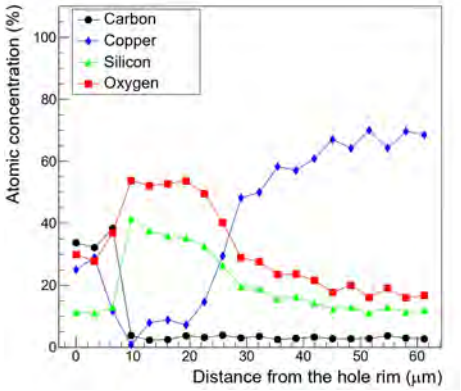

(b) Relative concentrations of selected elements as a function of the distance of the hole rim on a ALPHA RATE hole.

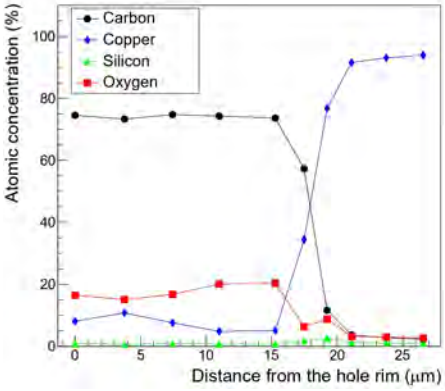

(c) Relative concentrations of selected elements as a function of the distance of the hole rim on a XRAY CURRENT hole.

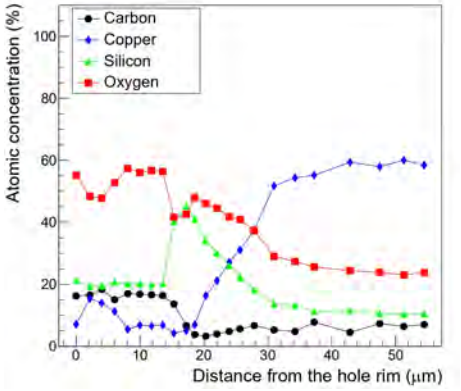

(d) Relative concentrations of selected elements as a function of the distance of the hole rim on a ALPHA CURRENT hole.

Figure 5.38: Atomic concentrations of selected elements as a function of the distance from the GEM hole rim. Measurements are made on the top side of the third GEM foil.

mentioned these results have to be taken with a grain of salt due to the non-Copper nature of the investigated region. It is clear how carbon and oxygen are not good indicator of aging in this region since are part of the Kapton molecular structure, fluctuations of their concentrations may be due local defects of the holes that leads to higher or lower concentration of Copper. However, the CURRENT tests present large concentration of oxygen with respect to the reference. If the ratio in the XRAY CURRENT case may

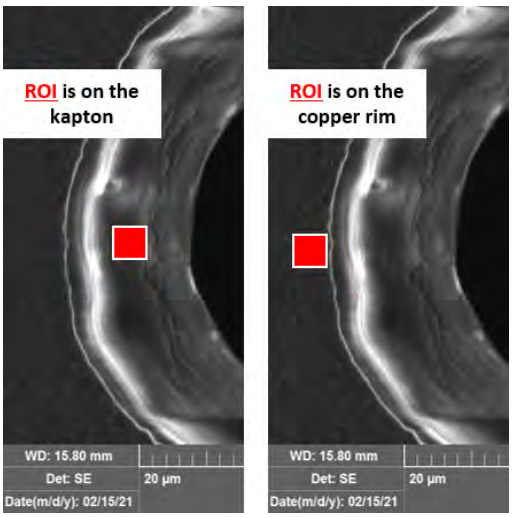

Figure 5.39: Indicative regions where the element to Copper concentrations ratios are measured.

be interpreted as a fluctuation, the ALPHA CURRENT one is an order of magnitude higher than all the other ratios. This fact was expected, the polymeric bubbles visible in Fig. 5.37 clearly indicate that during this test a huge quantity of polymer was deposited on the inner GEM rim. Similar information is given by the silicon concentration ratios, which are relatively low and similar on the XRAY tests as in the Copper region, and way higher in case of ALPHA tests. In particular in ALPHA CURRENT, differently from the Copper region analysis, the silicon ratio is double the ALPHA RATE one. Both the observations made on the differences of the two ALPHA tests explain the evident deposit on the Kapton region in ALPHA CURRENT suggesting that these polymers have a large concentration of oxygen (10 times than ALPHA RATE) and silicon (2 times than ALPHA RATE).

5.4.5 Comparative aging tests conclusion

The tests performed both on wire chamber and GEM detector gave some food for thought. However, due to the intrinsic nature of the aging processes the conclusions drawn here are not final since many tests in similar conditions are required to avoid punctual difference that may happen in stochastic processes.

Wire chamber tests showed that when alpha particles are used to irradiate, a gain loss appears between 2 and 3 times before than when using soft X-rays. ALPHA tests demonstrated that if the accumulated charge is 6 times higher the polymer thickness on the anode will be around $2 \div 3$ larger.

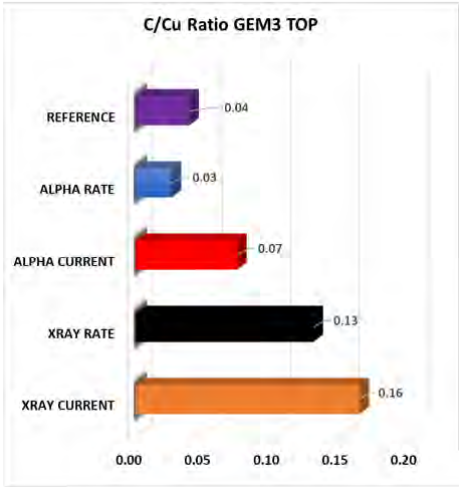

(a) Relative concentrations of carbon normalized to the Copper one.

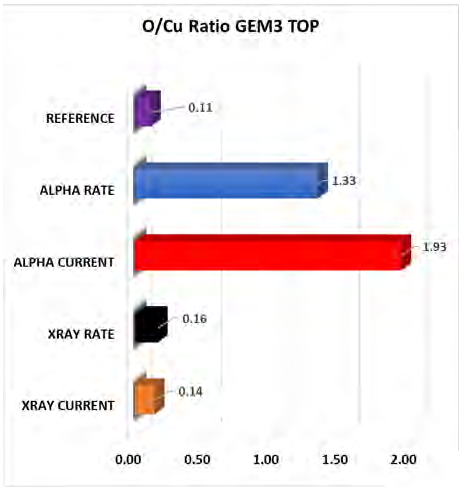

(b) Relative concentrations of oxygen normalized to the Copper one.

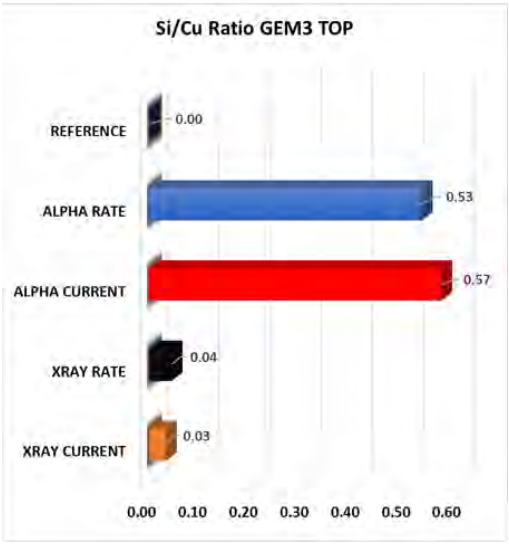

(c) Relative concentrations of silicon normalized to the Copper one.

Figure 5.40: Element to Copper concentration ratios on the Copper interface region.

Nevertheless, no polymers on XRAY wires were detected even though a gain loss was measured. This effect is clearly linked to the different nature of the polymers developed during the irradiation, the polymers may have formed on the cathode or they were removed by the gentle sampling operation or, again they may have reacted with the air, thus dissolved. Finally, an anomalous presence of sulphur was detected in wire ALPHA tests only, triggered by some traces present in glues. The fact that sulphur was not identified in GEM or wire XRAY tests may suggest that this kind

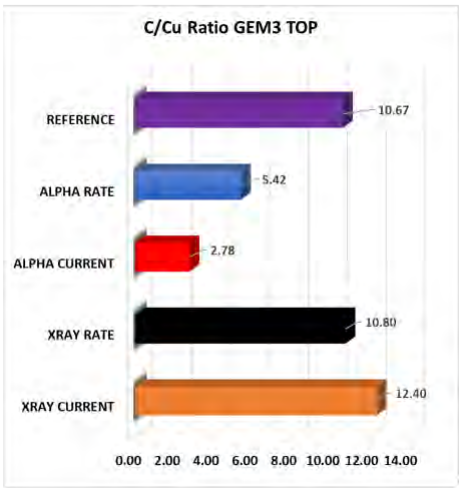

(a) Relative concentrations of carbon normalized to the Copper one.

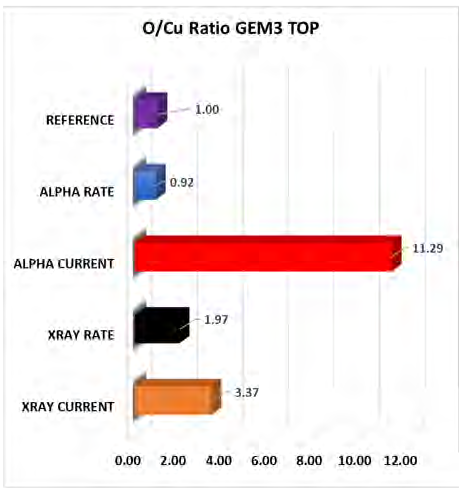

(b) Relative concentrations of oxygen normalized to the Copper one.

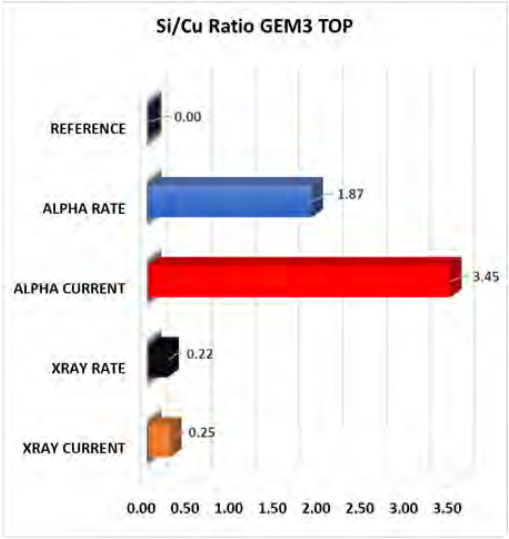

(c) Relative concentrations of silicon normalized to the Copper one.

Figure 5.41: Element to Copper concentration ratios on the inner Kapton region.

of pollution starts taking action in the polymerization process only if the released primary charge per hit is very high such as in the wire ALPHA tests (primaries of the order of 10^5).

GEM tests confirmed the incredibly high radiation hardness of GEM detectors and the higher dangerousness of alpha particles. Nevertheless, no gain loss was measured, 10 times more pollutants was detected on the GEM electrodes in ALPHA tests with respect to in XRAY showing the larger harmful potential of alpha particles. Despite the large difference

in accumulated charge between the two ALPHA tests and the fact that ALPHA RATE have been flushed without irradiation for a long time, the polymers concentration of the two are similar on the Copper-Kapton interface. Differently, in the Kapton region, ALPHA CURRENT showed a denser amount of polymers than ALPHA RATE, visible also from SEM pictures. The oxygen concentration in ALPHA CURRENT Kapton is 10 times larger than ALPHA RATE while silicon is almost the double. This evidence may suggest that polymers on Kapton are more fragile than the ones deposited on the Copper, indeed flushing the detector without irradiating it may be the cause of the lack of such large amount of polymers in ALPHA RATE. Finally, all the GEM tests revealed that top sides of the GEM electrodes are more susceptible to polymer deposit, but no chemical difference was found between the two sides. This is probably because monomers and polymers created during avalanches have more likely a positive charge rather than negative, letting them attaching in a easier way on the top; in a similar way negative fluorine radicals tends to adhere on the bottom side [187].

More general conclusions can be drawn in light of these tests:

- Polymerization in wire chambers affect the operation in very short time, while GEM, due to the fact that they have no amplification near the anode and the multiplication is shared between multiple stages, are more robust to this effect.
- Particle ionization power plays a leading role in aging more than other macroscopic variables, hence accumulated charge is not the perfect indicator to compare very different aging tests and effects.
- GEM are not immune to aging, the fact that they are astonishingly radiation hard does not mean that they can survive in every operation condition. A contaminated gas environment and heavily ionizing particles bombardment may lead to hole deformation and creation of insulating deposit on the GEM rims that may irreversibly undermine the GEM operation.

CONCLUSION

During this thesis work the CMS GEM Group successfully installed and started the final commissioning of the GE1/1 station. The production and operation of such detectors stimulated an intense R&D for the future GEM station to develop improved detectors, in particular to cope with the challenges imposed by the ME0 station.

For the safe operation of GE1/1 and the future stations, the GAS-MON@P5 system was developed and installed in the Surface Gas room (SGX5). The system aims to directly detect the relative concentration of CO_2 (or Ar) in the supplied gas mixture, nominally Ar/CO_2 (70/30). A dedicated algorithm is able to detect a CO_2 percentage change of the order of 0.6 % with a false positive probability of 6.57×10^{-8} (one false warning every 15 years). The system commissioning is currently ongoing and it will be fully operative for the first Run 3 LHC pilot beam.

Because of the expected challenging particle background environment, the ME0 detectors have followed a dedicated R&D phase to improve their design. A review of the high voltage distribution components was necessary to increase the nominal rate capability of the GE1/1 and GE2/1 detectors. A further change in the GEM foils partitions orientation was necessary to remove undesired gain non uniformity during the irradiation and it will permit to adopt a uniform gain compensation. Further studies to validate such design from the discharge point of view will be carried out in the future.

Aging can also be a issue for the harsh particle environment in the GEM stations positions. However, multiple tests demonstrated the incredibly high radiation hardness of GEM detectors also in presence of contaminants in the gas mixture. Despite such promising results, that will suggest a good operation of the GEM detectors in CMS, it is important to notice

that aging is always possible also in such detector technology and can have negative impact on the performance if it is not taken under control.

APPENDIX A

EFFECTIVE GAIN MEASUREMENT OF A GEM-BASED DETECTOR

In Sec. 2.2.2, the charge amplification factor, i.e. the gain G, of a gaseous detector has been defined as:

$$G = \frac{Q_T}{Q_0},$$

where Q_0 is the primary charge (of one sign) released by the particle when interacting and Q_T is the total charge created after the multiplication. For a given detector, usually, the measurement of the gain means to measure the effective gain, i.e. the ratio between the effective charge that is induced on the anode plane and the primary charge:

$$G_{eff} = \frac{Q_{eff}}{Q_0}. \tag{A.1}$$

Q_{eff} and Q_T are not necessary the same, they may be very similar in a proportional tube or very different in a GEM-based detector. Indeed, in the last case, it happens that not all the primary charges participate to the multiplication in the holes and not all the electrons produced during the avalanche may be efficiently drifted to the next electrode. This effect occurs because some the field lines end on the GEM electrodes, hence moving the charges through the GEM electrodes where they are collected. The difference between the real and effective gain was measured, for different hole sizes, in [98].

However, when exploiting GEM detectors for detection purpose, the effective gain is the one that determines the signal over noise ratio and the general behaviour of the detector. Hence, the effective gain is the most useful and easy to measure. Eq. A.1 keeps the same meaning when substituting the measured anodic current I_{an} and the measured primary current I_0 to the respective charges. This fact helps to rewrite the equation as:

$$G = \frac{I_{eff}}{I_0} = \frac{I_{anode}}{en_0R}, \tag{A.2}$$

where e is the electron charge (1.6×10^{-19} C), n_0 the average number of primaries released by one interaction and R the rate of interactions. Eq. A.2 shows that two quantities have to be measured to quantify the effective gas gain of a GEM detector: the anodic current I_{anode} and the hit rate R. In general the measurements of such quantities are made with a calibration source with known and relatively defined n_0 released into the detector under test. Usually, such radiative sources are soft X-rays emitters like ^{55}Fe [154] or ^{109}Cd [167] (see Sec. 4.1 for the primaries estimation for such sources).

Fig. A.1 shows the modules needed to measure the two quantities. Usu-

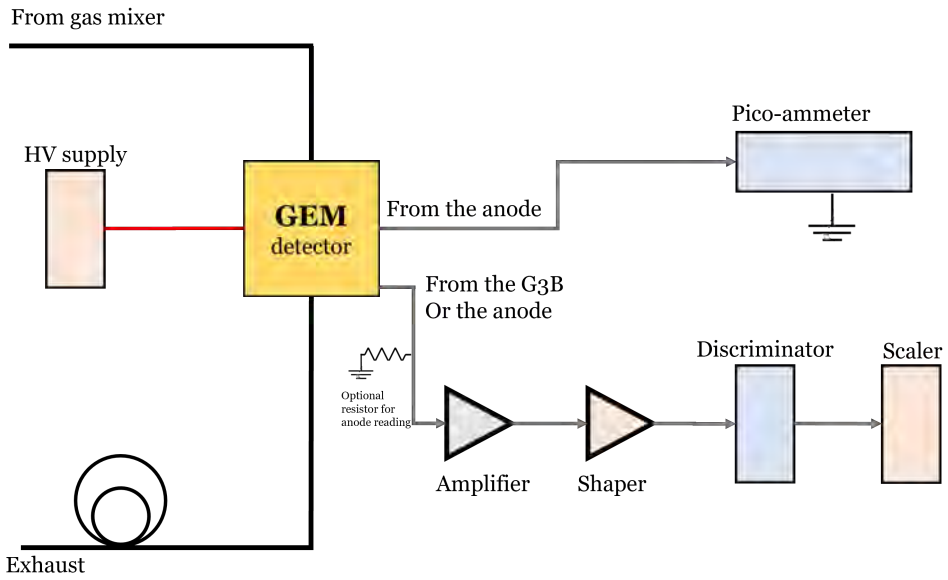

Figure A.1: Schematic view of the instrumentation needed for anodic current and rate measurement.

ally, the anodic current is measured by a precise picoammeter placed in series between the anodic plane (usually segmented in pads or strips) and the ground. The Keithley Model 6487 [156] is usually a good instrument to measure currents in the typical GEM ranges. For measuring the rate, a NIM-based set of modules is usually employed. A charge amplifier and a

shaper are used to amplify and shape the signal. The formed signal is discriminated and the number of events occurring in a certain amount of time is measured using a scaler or a similar counting device. In certain cases, the measurement of the current and the rate can be done simultaneously. Electric signals may be readout from the bottom side of the third GEM foil (the one that faces the anode). The signal induced on this electrode is very similar to the one induced in the anode. However, in some cases, the access to this electrode is not easy, or the presence of the protection resistors may distort the signals. In these cases separate measurements for the rate and the current have to be made to determine the two quantities. It is important to remember that, when reading signals from the anode, it may be mandatory to put a parallel resistor to ground between anode and charge amplifier. Indeed, many of them are AC coupled at the input; this may produce charging-up of the anode and the progressively quenching of the signals. To measure the gain it is important to remember that the hit rate

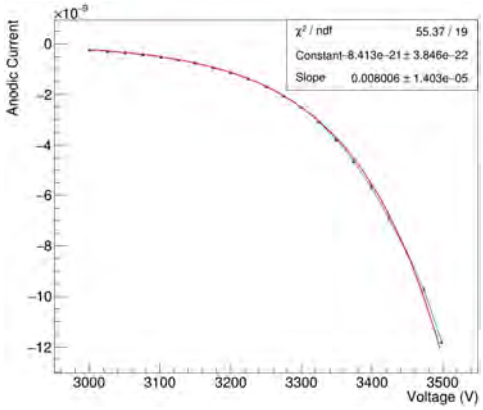

Figure A.2: Typical anodic current curve measured as a function of the working voltage. An exponential curve fits the data.

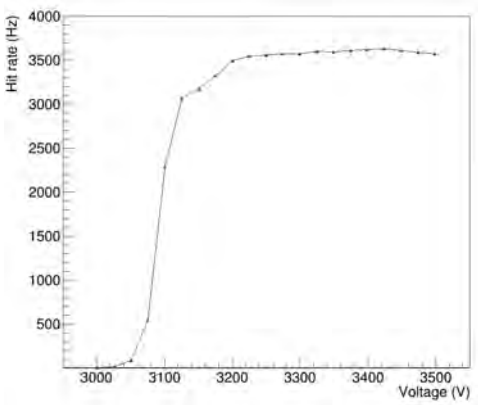

Figure A.3: Typical hit rate measured as a function of the working point.

measurement has to be taken with the detector at its maximum efficiency. Indeed, the use of a measured rate that is not at the plateau one may overestimate the measured gain. For this reason it is good practice to take current and rate measurements at different working points to individuate the correct value of the hit rate and also verify the usual trend. Fig. A.2 shows a typical anodic current curve as a function of the working point, the absolute value of the current growth exponentially. Fig. A.3 shows a typical hit rate measurement as a function of the voltage. The gain has to be computed with the rate at the plateau.

Another option to measure the effective gain consists in measuring the average charge collected on the anode per particle hit. Sampling the signal

from the anode (opportunely amplified and shaped) and measuring its pulse height (with a Multi Channel Analysed MCA) or its charge integral (using a Charge to Digital Converter QDC), a spectrum of the impulses is obtained. The whole detection chain has to be calibrated by injecting known charge pulses in order to have a well calibrated charge scale. If the irradiation source has a well defined particle energy that can be entirely released in the drift volume of the detector, a peak will appear in the spectrum. A typical charge spectrum of the signals induced by a ^{55}Fe source is shown in Fig. 5.13. Knowing the average primary charge emitted by a known peak ($Q_0 = n_0 e$) and measuring the Q_{eff} by fitting the peak gives the measure of the effective gas gain according to Eq. A.1.

One last procedure can be exploited to measure the effective gain. It consists in measuring the currents flowing through all the GEM electrodes to determine amplification factor. This method works fine in single-GEM detectors, while it gives problems in multi-stage detectors because of the difficulties in disentangling the various effects. Furthermore, this procedure requires the use of power supplies that measure precisely the supplied current or dedicated floating pico-ammeters. The procedure for a single GEM detector is explained in [233].

BIBLIOGRAPHY

[1] Lyndon Evans and Philip Bryant. "LHC machine". In: *Journal of instrumentation* 3.08 (2008), S08001.

[2] *CERN homepage*. URL: `https://home.cern/`.

[3] LHC Machine. *HL-LHC project*. 2020. URL: `https://project-hl-lhcindustry.web.cern.ch/content/project-schedule`.

[4] Georges Aad et al. "The ATLAS experiment at the CERN large hadron collider". In: *Journal of instrumentation* 3 (2008), S08003.

[5] CMS Collaboration et al. "The CMS experiment at the CERN LHC". In: *JInst* 3 (2008), S08004.

[6] A Augusto Alves Jr et al. "The LHCb detector at the LHC". In: *Journal of instrumentation* 3.08 (2008), S08005.

[7] Kenneth Aamodt et al. "The ALICE experiment at the CERN LHC". In: *Journal of Instrumentation* 3.08 (2008), S08002.

[8] Esma Mobs. *The CERN accelerator complex-2019*. Tech. rep. 2019.

[9] C Fluder et al. "The Development of the Control System for the Cryogenics in the LHC Tunnel". In: (2011).

[10] BJ Holzer. "Lattice design in high-energy particle accelerators". In: (2006).

[11] Jorg Wenninger. *Operation and Configuration of the LHC in Run 2*. Tech. rep. 2019.

[12] Giorgio Apollinari et al. *High-luminosity large hadron collider (HL-LHC): Preliminary design report*. Tech. rep. Fermi National Accelerator Lab.(FNAL), Batavia, IL (United States), 2015.

[13] S Lusin. "The CMS Detector Power System". In: (2008).

[14] The CMS Collaboration. *The CMS Detector Power System*. URL: https://cms.cern/news/cmsdetector-design.

[15] CMS collaboration et al. "Performance of the CMS drift tube chambers with cosmic rays". In: *Journal of Instrumentation* 5.03 (2010), T03015.

[16] Viktor Veszpremi. "Operation and performance of the CMS tracker". In: *Journal of Instrumentation* 9.03 (2014), p. C03005.

[17] Wolfgang Adam et al. "The CMS Phase-1 pixel detector upgrade". In: *Journal of Instrumentation* 16.02 (2021), P02027.

[18] Hans Hofer et al. *The electromagnetic calorimeter technical design report*. Tech. rep. Technical Report 4, CERN, 1997.

[19] The CMS Collaboration. *Energy Resolution of the Barrel of the CMS Electromagnetic Calorimeter*. Tech. rep. Geneva: CERN, 2006. DOI: 10.1088/1748-0221/2/04/P04004. URL: http://cds.cern.ch/record/1009081.

[20] J Man et al. *CMS technical design report for the phase 1 upgrade of the hadron calorimeter*. Tech. rep. Fermi National Accelerator Lab.(FNAL), Batavia, IL (United States), 2012.

[21] M Della Negra, E Radermacher, and A Hervé. "The Magnet Project Technical Design Report". In: (1997).

[22] CMS collaboration et al. "Precise mapping of the magnetic field in the CMS barrel yoke using cosmic rays". In: *Journal of Instrumentation* 5.03 (2010), T03021.

[23] CMS collaboration et al. "The performance of the CMS muon detector in proton-proton collisions at s= 7 TeV at the LHC". In: *Journal of Instrumentation* 8.11 (2013), P11002.

[24] Albert M Sirunyan, CMS Collaboration, et al. "Performance of the CMS muon detector and muon reconstruction with proton-proton collisions at s= 13 TeV". In: (2018).

[25] CMS Collaboration et al. "Performance of the CMS drift-tube chamber local trigger with cosmic rays". In: *Journal of Instrumentation* 5.03 (2010), T03003.

[26] D Acosta et al. "Large CMS cathode strip chambers: design and performance". In: *Nuclear Instruments and Methods in Physics Research Section A: Accelerators, Spectrometers, Detectors and Associated Equipment* 453.1-2 (2000), pp. 182–187.

[27] NP Ghanathe et al. "Software and firmware co-development using high-level synthesis". In: *Journal of Instrumentation* 12.01 (2017), p. C01083.

[28] *The Phase-2 Upgrade of the CMS Muon Detectors*. Tech. rep. CERN-LHCC-2017-012. CMS-TDR-016. Geneva: CERN, 2017. URL: https://cds.cern.ch/record/2283189.

[29] Pierluigi Paolucci et al. "CMS Resistive Plate Chamber overview, from the present system to the upgrade phase I". In: *Journal of Instrumentation* 8.04 (2013), P04005.

[30] Karol Bunkowski. "Optimization, Synchronization, Calibration and Diagnostic of the RPC PAC Muon Trigger System for the CMS detector". Presented on Jul 2009. 2009. URL: http://cds.cern.ch/record/1308715.

[31] Serguei Chatrchyan et al. "Commissioning of the CMS High-Level Trigger with cosmic rays". In: *Journal of Instrumentation* 5 (2010).

[32] CMS collaboration et al. "Performance of the CMS Level-1 trigger in proton-proton collisions at s=13 TeV". In: *arXiv preprint arXiv:2006.10165* (2020).

[33] CMS collaboration et al. "The CMS trigger system". In: *arXiv preprint arXiv:1609.02366* (2016).

[34] D Contardo et al. *Technical Proposal for the Phase-II Upgrade of the CMS Detector*. Tech. rep. Geneva, 2015. URL: https://cds.cern.ch/record/2020886.

[35] Fabio Sauli. *Gaseous radiation detectors: fundamentals and applications*. 36. Cambridge University Press, 2014.

[36] Fabio Sauli. *Micro-Pattern Gaseous Detectors: Principles of Operation and Applications*. World Scientific, 2020.

[37] Marcello Abbrescia, Vladimir Peskov, and Paulo Fonte. *Resistive gaseous detectors: designs, performance, and perspectives*. John Wiley & Sons, 2018.

[38] Walter Blum, Werner Riegler, and Luigi Rolandi. *Particle detection with drift chambers*. Springer Science & Business Media, 2008.

[39] Particle Data Group et al. "Review of particle physics". In: *Progress of Theoretical and Experimental Physics* 2020.8 (2020), p. 083C01.

[40] Glenn F Knoll. *Radiation detection and measurement*. John Wiley & Sons, 2010.

[41] William R Leo. *Techniques for nuclear and particle physics experiments: a how-to approach*. Springer Science & Business Media, 2012.

[42] RL Platzman. *Energy spectrum of primary activations in the action of ionizing radiation*. Tech. rep. Univ. of Chicago, 1968.

[43] U Fano. "Penetration of protons, alpha particles, and mesons". In: *Annual Review of Nuclear Science* 13.1 (1963), pp. 1–66.

[44] Lee C Northcliffe. "Passage of heavy ions through matter". In: *Annual Review of Nuclear Science* 13.1 (1963), pp. 67–102.

[45] Donald E Groom, Nikolai V Mokhov, and Sergei I Striganov. "Muon stopping power and range tables 10 MeV–100 TeV". In: *Atomic Data and Nuclear Data Tables* 78.2 (2001), pp. 183–356.

[46] Jeremie Merlin. "Study of long-term sustained operation of gaseous detectors for the high rate environment in CMS". PhD thesis. Université de Strasbourg, 2016.

[47] MJOK Berger. "XCOM: photon cross sections database". In: *http://www. nist. gov/pml/data/xcom/index. cfm* (2010).

[48] Ugo Amaldi. *Fisica delle radiazioni ad uso di radiologi, radiologi e protezionisti*. Boringhieri, 1971.

[49] A Thompson et al. "X-ray data booklet (2009)". In: *URL http://xdb. lbl. gov* (2009).

[50] Richard D Deslattes et al. "X-ray transition energies: new approach to a comprehensive evaluation". In: *Reviews of Modern Physics* 75.1 (2003), p. 35.

[51] Heinrich Schindler. "Microscopic simulation of particle detectors". PhD thesis. 2012.

[52] Charlotte Meaker Davisson and Robley D Evans. "Gamma-ray absorption coefficients". In: *Reviews of Modern Physics* 24.2 (1952), p. 79.

[53] Robley D Evans. "Compton effect". In: *Corpuscles and Radiation in Matter II/Korpuskeln und Strahlung in Materie II*. Springer, 1958, pp. 218–298.

[54] P M C C Encarnação et al. "Experimental ion mobility measurements in Ar-CO2mixtures". In: *Journal of Instrumentation* 10.01 (2015), P01010–P01010. DOI: 10.1088/1748-0221/10/01/p01010. URL: https://doi.org/10.1088/1748-0221/10/01/p01010.

[55] JS Townsend and VA Bailey. "XCVII. The motion of electrons in gases". In: *The London, Edinburgh, and Dublin Philosophical Magazine and Journal of Science* 42.252 (1921), pp. 873–891.

[56] Vittorio Palladino and Bernard Sadoulet. "Application of classical theory of electrons in gases to drift proportional chambers". In: *Nuclear Instruments and Methods* 128.2 (1975), pp. 323–335.

[57] Stephen Biagi. "Magboltz-transport of electrons in gas mixtures". In: *CERN program library* (2000).

[58] John M Meek and John Drummond Craggs. "Electrical breakdown of gases". In: (1978).

[59] Loucas G Christophorou, VE Anderson, and JB Birks. *Atomic and Molecular Radiation Physics.* Tech. rep. and others; Oak Ridge National Lab., Tenn., 1971.

[60] J Byrne. "Electron avalanches in inhomogeneous media". In: *Nuclear Instruments and Methods in Physics Research Section A: Accelerators, Spectrometers, Detectors and Associated Equipment* 491.1-2 (2002), pp. 122–125.

[61] Heinz Raether. *Electron avalanches and breakdown in gases*. 1964.

[62] Simon Ramo. "Currents induced by electron motion". In: *Proceedings of the IRE* 27.9 (1939), pp. 584–585.

[63] William Shockley. "Currents to conductors induced by a moving point charge". In: *Journal of applied physics* 9.10 (1938), pp. 635–636.

[64] Ernest Mathieson and Graham C Smith. "Charge distributions in parallel plate avalanche chambers". In: *Nuclear Instruments and Methods in Physics Research Section A: Accelerators, Spectrometers, Detectors and Associated Equipment* 273.2-3 (1988), pp. 518–521.

[65] H Schindler, R Veenhof, et al. *Garfield++-simulation of tracking detectors*. 2018.

[66] Wolfgang Franzen and LW Cochran. "Pulse ionization chambers and proportional counters". In: *Nuclear Instruments and their uses* 1 (1962), p. 3.

[67] Yu N Pestov. "Status and future developments of spark counters with a localized discharge". In: *Nuclear Instruments and Methods in Physics Research* 196.1 (1982), pp. 45–47.

[68] Yu N Pestov. "The status of spark counters with a localized discharge". In: *Nuclear Instruments and Methods in Physics Research Section A: Accelerators, Spectrometers, Detectors and Associated Equipment* 265.1-2 (1988), pp. 150–156.

[69] Yu N Pestov, Hans Rudolf Schmidt, and B Schreiber. "Timing performance of spark counters and photon feedback". In: *Nuclear Instruments and Methods in Physics Research Section A: Accelerators, Spectrometers, Detectors and Associated Equipment* 456.1-2 (2000), pp. 11–15.

[70] R Cardarelli et al. "Progress in resistive plate counters". In: *Nuclear Instruments and Methods in Physics Research Section A: Accelerators, Spectrometers, Detectors and Associated Equipment* 263.1 (1988), pp. 20–25.

[71] R Santonico and R Cardarelli. "Development of resistive plate counters". In: *Nuclear Instruments and Methods in physics research* 187.2-3 (1981), pp. 377–380.

[72] R Arnaldi et al. "Study of Resistive Plate Chambers for the Alice dimuon spectrometer". In: *Nuclear Physics B-Proceedings Supplements* 78.1-3 (1999), pp. 84–89.

[73] Ernest Rutherford and Hans Geiger. "An electrical method of counting the number of α-particles from radio-active substances". In: *Proceedings of the Royal Society of London. Series A, Containing Papers of a Mathematical and Physical Character* 81.546 (1908), pp. 141–161.

[74] CG Montgomery and DD Montgomery. "The discharge mechanism of Geiger-Mueller counters". In: *Physical Review* 57.11 (1940), p. 1030.

[75] Hans Geiger and Walther Müller. "Elektronenzählrohr zur messung schwächster aktivitäten". In: *Naturwissenschaften* 16.31 (1928), pp. 617–618.

[76] Philip M Morse and Herman Feshbach. "Methods of theoretical physics". In: *American Journal of Physics* 22.6 (1954), pp. 410–413.

[77] George A Erskine. "Charges and current induced by moving ions in multiwire chambers". In: *Nuclear Instruments and Methods in Physics Research* 198.2-3 (1982), pp. 325–336.

[78] Georges Charpak, D Rahm, and H Steiner. "Some developments in the operation of multiwire proportional chambers". In: *Nuclear Instruments and Methods* 80.1 (1970), pp. 13–34.

[79] Amos Breskin et al. "Recent observations and measurements with high-accuracy drift chambers". In: *Nuclear Instruments and Methods* 124.1 (1975), pp. 189–214.

[80] Robert W Hendricks. "Space charge effects in proportional counters". In: *Review of Scientific Instruments* 40.9 (1969), pp. 1216–1223.

[81] Heikki Sipilä, Vesa Vanha-Honko, and Jukka Bergqvist. "Mathematical treatment of space charge effects in proportional counters". In: *Nuclear Instruments and Methods* 176.1-2 (1980), pp. 381–387.

[82] E Mathieson. "Dependence of gain on count rate, due to space charge, in coaxial and multiwire proportional chambers". In: *Nuclear Instruments and Methods in Physics Research Section A: Accelerators, Spectrometers, Detectors and Associated Equipment* 249.2-3 (1986), pp. 413–420.

[83] Kosuke Kageyama et al. “Space charge effects in a thin rectangular proportional counter”. In: *Nuclear Instruments and Methods in Physics Research Section A: Accelerators, Spectrometers, Detectors and Associated Equipment* 369.1 (1996), pp. 151–156.

[84] Werner Riegler, C Lippmann, and Bernhard Schnizer. “Gas gain reduction due to space charge in wire chambers”. In: *Nuclear Instruments and Methods in Physics Research Section A: Accelerators, Spectrometers, Detectors and Associated Equipment* 582.2 (2007), pp. 469–473.

[85] A Oed. “Position-sensitive detector with microstrip anode for electron multiplication with gases”. In: *Nuclear Instruments and Methods in Physics Research Section A: Accelerators, Spectrometers, Detectors and Associated Equipment* 263.2-3 (1988), pp. 351–359.

[86] “Development of Gas Micro-Strip Chambers for Radiation Detection and Tracking at High Rates”. 1992. URL: `https://cds.cern.ch/record/5464`.

[87] Roger Bouclier et al. “Development of micro-strip gas chambers for high rate operation”. In: *Nuclear Instruments and Methods in Physics Research Section A: Accelerators, Spectrometers, Detectors and Associated Equipment* 367.1-3 (1995), pp. 168–172.

[88] Roger Bouclier et al. “On some factors affecting discharge conditions in micro-strip gas chambers”. In: *Nuclear Instruments and Methods in Physics Research Section A: Accelerators, Spectrometers, Detectors and Associated Equipment* 365.1 (1995), pp. 65–69.

[89] Bernhard Schmidt. “Microstrip gas chambers: Recent developments, radiation damage and long-term behavior”. In: *Nuclear Instruments and Methods in Physics Research Section A: Accelerators, Spectrometers, Detectors and Associated Equipment* 419.2-3 (1998), pp. 230–238.

[90] A Barr et al. “Construction, test and operation in a high intensity beam of a small system of micro-strip gas chambers”. In: *Nuclear Instruments and Methods in Physics Research Section A: Accelerators, Spectrometers, Detectors and Associated Equipment* 403.1 (1998), pp. 31–56.

[91] Fabio Sauli and Archana Sharma. “Micropattern gaseous detectors”. In: *Annual Review of Nuclear and Particle Science* 49.1 (1999), pp. 341–388.

[92] Yannis Giomataris et al. "MICROMEGAS: a high-granularity position-sensitive gaseous detector for high particle-flux environments". In: *Nuclear Instruments and Methods in Physics Research Section A: Accelerators, Spectrometers, Detectors and Associated Equipment* 376.1 (1996), pp. 29–35.

[93] A Bay et al. "Study of sparking in Micromegas chambers". In: *Nuclear Instruments and Methods in Physics Research Section A: Accelerators, Spectrometers, Detectors and Associated Equipment* 488.1-2 (2002), pp. 162–174.

[94] G Puill et al. "MICROMEGAS: high rate and radiation hardness results". In: *IEEE Transactions on Nuclear Science* 46.6 (1999), pp. 1894–1897.

[95] A Delbart, T2K/Tpc Collaboration, et al. "Production and calibration of 9 m2 of bulk-micromegas detectors for the readout of the ND280/TPCs of the T2K experiment". In: *Nuclear Instruments and Methods in Physics Research Section A: Accelerators, Spectrometers, Detectors and Associated Equipment* 623.1 (2010), pp. 105–107.

[96] T Alexopoulos et al. "A spark-resistant bulk-micromegas chamber for high-rate applications". In: *Nuclear Instruments and Methods in Physics Research Section A: Accelerators, Spectrometers, Detectors and Associated Equipment* 640.1 (2011), pp. 110–118.

[97] Fabio Sauli. "GEM: A new concept for electron amplification in gas detectors". In: *Nuclear Instruments and Methods in Physics Research Section A: Accelerators, Spectrometers, Detectors and Associated Equipment* 386.2-3 (1997), pp. 531–534.

[98] Fabio Sauli. "The gas electron multiplier (GEM): Operating principles and applications". In: *Nuclear Instruments and Methods in Physics Research Section A: Accelerators, Spectrometers, Detectors and Associated Equipment* 805 (2016), pp. 2–24.

[99] Serge Duarte Pinto et al. "A large area GEM detector". In: *2008 IEEE Nuclear Science Symposium Conference Record*. IEEE. 2008, pp. 1426–1432.

[100] S Duarte Pinto and R De Oliveira. "A method of manufacturing a gas electron multiplier". In: *Patent Wipo WO/2009127220* ().

[101] Marco Villa et al. "Progress on large area GEMs". In: *Nuclear Instruments and Methods in Physics Research Section A: Accelerators, Spectrometers, Detectors and Associated Equipment* 628.1 (2011), pp. 182–186.

[102] Jeremie A Merlin. "GEM single-mask characterization and influence of GEM foil orientation". In: *5th International Conference on Micro-Pattern Gas Detectors (MPGD2017)*. 2017, pp. 22–26.

[103] S Bachmann et al. "Charge amplification and transfer processes in the gas electron multiplier". In: *Nuclear Instruments and Methods in Physics Research Section A: Accelerators, Spectrometers, Detectors and Associated Equipment* 438.2-3 (1999), pp. 376–408.

[104] S Bachmann et al. "Discharge studies and prevention in the gas electron multiplier (GEM)". In: *Nuclear Instruments and Methods in Physics Research Section A: Accelerators, Spectrometers, Detectors and Associated Equipment* 479.2-3 (2002), pp. 294–308.

[105] G Bencivenni et al. "A triple GEM detector with pad readout for high rate charged particle triggering". In: *Nuclear Instruments and Methods in Physics Research Section A: Accelerators, Spectrometers, Detectors and Associated Equipment* 488.3 (2002), pp. 493–502.

[106] Duccio Abbaneo et al. "Performance of a large-area GEM detector prototype for the upgrade of the CMS muon endcap system". In: *2014 IEEE Nuclear Science Symposium and Medical Imaging Conference (NSS/MIC)*. IEEE. 2014, pp. 1–8.

[107] Ilaria Vai, CMS GEM Collaboration, et al. "Test beam and irradiation test results of Triple-GEM detector prototypes for the upgrade of the muon system of the CMS experiment". In: *Nuclear Instruments and Methods in Physics Research Section A: Accelerators, Spectrometers, Detectors and Associated Equipment* 824 (2016), pp. 586–588.

[108] Ilaria Vai. "Development and performance of Micropattern Gaseous Detectors for the CMS muon system upgrade". PhD thesis. Pavia U, 2017.

[109] Martina Ressegotti. "Micropattern Gas Detectors for the CMS Experiment's Muon System Upgrade: Performance Studies and Commissioning of the first GEM Detectors". PhD thesis. Università degli Studi di Pavia.

[110] Francesco Fallavollita. "Triple-Gas Electron Multiplier technology for future upgrades of the CMS experiment: construction and certification of the CMS GE1/1 detector and longevity studies". PhD thesis. Ph. D. thesis CERN-THESIS-2018-349 Pavia University Pavia Italy, 2018.

[111] D Abbaneo et al. "Test beam results of the GE1/1 prototype for a future upgrade of the CMS high-η muon system". In: *2011 IEEE Nuclear Science Symposium Conference Record*. IEEE. 2011, pp. 1806–1810.

[112] S Chatterjee et al. "Study of charging up effect in a triple GEM detector". In: *Journal of Instrumentation* 15.09 (2020), T09011.

[113] B Azmoun et al. "A study of gain stability and charging effects in GEM foils". In: *2006 IEEE Nuclear Science Symposium Conference Record*. Vol. 6. IEEE. 2006, pp. 3847–3851.

[114] M Alfonsi et al. "Simulation of the dielectric charging-up effect in a GEM detector". In: *Nuclear Instruments and Methods in Physics Research Section A: Accelerators, Spectrometers, Detectors and Associated Equipment* 671 (2012), pp. 6–9.

[115] Pieter Everaerts. "Rate capability and ion feedback in GEM detectors". PhD thesis. Gent U., 2006.

[116] Patrik Thuiner. "Ion space-charge effects in multi-GEM detectors: challenges and possible solutions for future applications". PhD thesis. Wien, 2016.

[117] Mohit Gola et al. "Stability tests performed on the triple GEM detector built using commercially manufactured GEM foils in India". In: *Journal of Instrumentation* 14.08 (2019), P08004.

[118] J Merlin. "GEM stack optimization for GE21 and ME0 (cross-talk studies, discharge mitigation)". In: *RD51 Collaboration Meeting (Virtual)*. 2020.

[119] Marcus Hohlmann. "A Model for Crosstalk in Micropattern Gas Detectors". In: *arXiv preprint arXiv:2012.11596* (2020).

[120] Stephen D Butalla and Marcus Hohlmann. "Investigation and Mitigation of Crosstalk in the Prototype ME0 GEM Detector for the Phase-2 Muon System Upgrade of the CMS Experiment: On behalf of the CMS Muon Group". In: *2020 IEEE Nuclear Science Symposium and Medical Imaging Conference (NSS/MIC)*. IEEE, pp. 1–6.

[121] J A Merlin. *Single-hole discharges in GEMs*. URL: https://indico.cern.ch/event/709670/contributions/3008626/attachments/1672294/2683230/JMERLIN_RD51ColMeeting_GEM_DischargeEffects_24052018.pdf.

[122] J A Merlin. *Discharge propagation study and foil double segmentation.* Internal comunication. URL: https://indico.cern.ch/event/801581/contributions/3331709/attachments/1802038/2939582/JMerlin_PhaseII_Discharge_Propagation_26022019.pdf.

[123] D Fiorina. *GEM Spark Protection Studies*. Muon Upgrade Workshop 7-9 Oct 2019. URL: https://indico.cern.ch/event/850576/contributions/3580313/attachments/1921830/3179456/Muon_Upgrade_Workshop_DFiorina_GEMSparkProtectionStudies.pdf.

[124] A Deisting et al. "Secondary discharge studies in single-and multi-GEM structures". In: *Nuclear Instruments and Methods in Physics Research Section A: Accelerators, Spectrometers, Detectors and Associated Equipment* 937 (2019), pp. 168–180.

[125] P Thuiner. *Inductivily coupled antennas as a versatile tool for discharge studies*. URL: https://indico.cern.ch/event/709670/contributions/3008627/attachments/1672068/2682762/20180621rd51cm_thuiner.pdf.

[126] Roman Zoechling. "Discharge studies on a Triple-GEM detector. GEM = Gaseous Electron Multiplier". In: (2016). URL: https://cds.cern.ch/record/2218017.

[127] A Utrobicic et al. "Studies of the delayed discharge propagation in the Gas Electron Multiplier (GEM)". In: *Nuclear Instruments and Methods in Physics Research Section A: Accelerators, Spectrometers, Detectors and Associated Equipment* 940 (2019), pp. 262–273.

[128] Lukas Lautner et al. "High voltage scheme optimization for secondary discharge mitigation in GEM-based detectors". In: *Journal of Instrumentation* 14.08 (2019), P08024.

[129] Santiago de Compostela-Spain. "Electronics System of the CMS GE1/1 Muon Upgrade and Lessons Learned From the Slice Test During the 2017-2018 LHC Runs". In: *Topical Workshop on Electronics for Particle Physics TWEPP2019*. Vol. 2. 2019, p. 6.

[130] Beatrice Mandelli. "Detector and system developments for LHC detector upgrades". In: (2015).

[131] R Guida et al. "The gas systems for the LHC experiments". In: *2013 IEEE Nuclear Science Symposium and Medical Imaging Conference (2013 NSS/MIC)*. IEEE. 2013, pp. 1–7.

[132] Stephen P Tubbs. *Programmable Logic Controller (PLC) Tutorial, Siemens Simatic S7-200*. 2007.

[133] LD Hinkle and C Fl Mariano. "Toward understanding the fundamental mechanisms and properties of the thermal mass flow controller". In: *Journal of Vacuum Science & Technology A: Vacuum, Surfaces, and Films* 9.3 (1991), pp. 2043–2047.

[134] A d'Auria. *CMS GEM gas system, 1735305 v.1*. Technical drawnings. URL: https://edms.cern.ch/nav/D:1735305:V1/D:1735305:V1.

[135] G. Myhre et al. "Anthropogenic and natural radiative forcing". In: *Climate Change 2013: The Physical Science Basis. Contribution of Working Group I to the Fifth Assessment Report of the Intergovernmental Panel on Climate Change*. Ed. by T. F. Stocker et al. Cambridge, UK: Cambridge University Press, 2013, pp. 659–740. DOI: 10.1017/CBO9781107415324.018.

[136] David R Lide. *CRC handbook of chemistry and physics*. Vol. 85. CRC press, 2004.

[137] R Guida, B Mandelli, and M Corbetta. "Effects of gas mixture quality on GEM detectors operation". In: *J. Phys.: Conf. Ser.* 1498 (2020), 012036. 7 p. DOI: 10.1088/1742-6596/1498/1/012036. URL: https://cds.cern.ch/record/2727129.

[138] *BME280 Combined humidity and rpessure sensor*. BOSCH. URL: https://www.bosch-sensortec.com/media/boschsensortec/downloads/datasheets/bst-bme280-ds002.pdf.

[139] VM Atrazhev, IT Iakubov, and VI Roldughin. "The Townsend coefficient of ionization in dense gases and fluids". In: *Journal of Physics D: Applied Physics* 9.12 (1976), p. 1735.

[140] A Sharma and Fabio Sauli. "First Townsend coefficient measured in argon based mixtures at high fields". In: *Nuclear Instruments and Methods in Physics Research Section A: Accelerators, Spectrometers, Detectors and Associated Equipment* 334.2-3 (1993), pp. 420–424.

[141] Mara Corbetta. "Studies on Gas Mixture and Gas Recirculation Effects on GEM Detectors Operation at the CERN GIF++ Facility". PhD thesis. Milan Bicocca U., 2018.

[142] M Capeans. "Study of the ageing of gaseous detectors and solution for use of MSGCs in HIGH rate experiments". PhD thesis. Santiago de Compostela U., 1995.

[143] G Mocellin. *Pressure and temperature correction across the world for performance comparison*. Internal comunication. URL: https://indico.cern.ch/event/976162/contributions/4111127/attachments/2144472/3614473/pTexponents-GM-P2_GEM.pdf.

[144] G Mocellin. "Performance of the GE1/1 detectors for the upgrade of the CMS Muon Forward system". PhD thesis. RWTH Aachen, 2021. URL: https://publications.rwth-aachen.de/record/822893.

[145] F Ivone. *Triple-GEM Gain dependence on temperature and pressure: Institute-wide measurement proposal*. Internal comunication. URL: https://indico.cern.ch/event/1007169/contributions/4227740/attachments/2187852/3697016/FIvone10022021.pdf.

[146] Takahiko Aoyama. "Generalized gas gain formula for proportional counters". In: *Nuclear Instruments and Methods in Physics Research Section A: Accelerators, Spectrometers, Detectors and Associated Equipment* 234.1 (1985), pp. 125–131.

[147] Tadeusz Z Kowalski. "On the generalized gas gain formula for proportional counters". In: *Nuclear Instruments and Methods in Physics Research Section A: Accelerators, Spectrometers, Detectors and Associated Equipment* 244.3 (1986), pp. 533–536.

[148] ME Rose and SA Korff. "An investigation of the properties of proportional counters. I". In: *Physical Review* 59.11 (1941), p. 850.

[149] W Diethorn. "US Atomic Energy Commission Report". In: *NYO-6628* (1956).

[150] A Williams and RI Sara. "Parameters affecting the resolution of a proportional counter". In: *The International Journal of Applied Radiation and Isotopes* 13.5 (1962), pp. 229–238.

[151] A Zastawny. "Gas amplification in a proportional counter with carbon dioxide". In: *Journal of Scientific Instruments* 43.3 (1966), p. 179.

[152] MW Charles. "Gas gain measurements in proportional counters". In: *Journal of Physics E: Scientific Instruments* 5.1 (1972), p. 95.

[153] *CAEN DT 5534EN module maual*. CAEN. URL: https://www.caen.it/products/dt5534e/.

[154] *Iron 55 decay scheme*. Laboratoire National Henri Becquerel. URL: http://www.nucleide.org/DDEP_WG/Nuclides/Fe-55_tables.pdf.

[155] S. Pommé, H. Stroh, and R. Van Ammel. "The 55Fe half-life measured with a pressurised proportional counter". In: *Applied Radiation and Isotopes* 148 (2019), pp. 27–34. ISSN: 0969-8043. DOI: https://doi.org/10.1016/j.apradiso.2019.01.008. URL: https://www.sciencedirect.com/science/article/pii/S0969804318310121.

[156] *Keithley 6487 manual*. Tektronix. URL: https://download.tek.com/manual/6487-901-01(B-Mar2011)(Ref).pdf.

[157] *The LXPLUS Service*. CERN. URL: https://lxplusdoc.web.cern.ch/.

[158] Gerry Bauer et al. "Status of the CMS Detector Control System". In: *Journal of Physics: Conference Series* 396.1 (2012), p. 012023. DOI: 10.1088/1742-6596/396/1/012023. URL: https://doi.org/10.1088/1742-6596/396/1/012023.

[159] W Salter. *DIP Description*. URL: https://cern.ch/dip/.

[160] Brice Copy et al. “Monitoring of CERN’s Data Interchange Protocol (DIP) system”. In: (2018), THPHA162. 4 p. DOI: 10.18429/JACoW-ICALEPCS2017-THPHA162. URL: https://cds.cern.ch/record/2305320.

[161] Alberto Rotondi, Paolo Pedroni, and Antonio Pievatolo. *Probabilità statistica e simulazione: programmi applicativi scritti con Scilab*. Springer, 2006.

[162] George Marsaglia and Wai Wan Tsang. “The ziggurat method for generating random variables”. In: *Journal of statistical software* 5.1 (2000), pp. 1–7.

[163] *Random sampling (numpy.random)*. URL: https://numpy.org/doc/stable/reference/random/index.html.

[164] Maxim Titov. “Gaseous Detectors: recent developments and applications”. In: *arXiv preprint arXiv:1008.3736* (2010).

[165] P Verwilligen. *ME0 Background Simulation*. Internal comunication. URL: https://indico.cern.ch/event/918611/contributions/3864586/attachments/2041443/3419415/20200519_Ph2Workshop_ME0Bkg.pdf.

[166] *AMPTEK Mini-X2 X-Ray Tube*. AMPTEK. URL: https://www.amptek.com/products/mini-x2-x-ray-tube.

[167] *Cadmium 109 decay scheme*. Laboratoire National Henri Becquerel. URL: http://www.nucleide.org/DDEP_WG/Nuclides/Cd-109_tables.pdf.

[168] *Ortec 142PC preamplifier maual*. ORTEC. URL: https://www.ortec-online.com/-/media/ametekortec/manuals/142pc-mnl.pdf?la=en&revision=a701ac9f-ee01-440b-bd23-7f1e4d7390f6.

[169] *Ortec 474 module maual*. ORTEC. URL: https://www.ortec-online.com/-/media/ametekortec/manuals/474-mnl.pdf?la=en&revision=c329d63d-8295-48df-864e-bcc8f79dfffc.

[170] *AMPTEK MCA-8000D Digital Multichannel Analyzer*. AMPTEK. URL: https://www.amptek.com/products/multichannel-analyzers/mca-8000d-digital-multichannel-analyzer.

[171] *ORTEC ASPEC-927 Dual Input MCB*. ORTEC. URL: https://www.ortec-online.com/products/electronics/multichannel-analyzers-mca/basic-analog/aspec-927.

[172] J W Kirchner. *Data Analysis Toolkits*. URL: https://seismo.berkeley.edu/~kirchner/toolkits.html.

[173] Philip R Bevington et al. "Data reduction and error analysis for the physical sciences". In: *Computers in Physics* 7.4 (1993), pp. 415–416.

[174] Igor B Smirnov. "Modeling of ionization produced by fast charged particles in gases". In: *Nuclear Instruments and Methods in Physics Research Section A: Accelerators, Spectrometers, Detectors and Associated Equipment* 554.1-3 (2005), pp. 474–493.

[175] M Brunoldi. "Studio del guadagno di un rivelatore tripla GEMsottoposto a intensi flussi di raggi X". PhD thesis. Universitá di Pavia, 2021.

[176] *Ortec 935 module maual*. ORTEC. URL: `https://www.ortec-online.com/-/media/ametekortec/manuals/935-mnl.pdf?la=en&revision=17ce85d8-c1d8-4cb5-812b-b601d1cf6cd2`.

[177] *CAEN N93B module maual*. CAEN. URL: `https://www.caen.it/products/n93b/`.

[178] Shoaib Usman and Amol Patil. "Radiation detector deadtime and pile up: A review of the status of science". In: *Nuclear Engineering and Technology* 50.7 (2018), pp. 1006–1016.

[179] G Bencivenni et al. "The micro-Resistive WELL detector: a compact spark-protected single amplification-stage MPGD". In: *Journal of Instrumentation* 10.02 (2015), P02008.

[180] A Andronic et al. "A comprehensive study of rate capability in Multi-Wire Proportional Chambers". In: *Journal of Instrumentation* 4.10 (2009), P10014.

[181] Pieter Everaerts. "Rate capability and ion feedback in GEM detectors". MA thesis. Gent U., 2006.

[182] *CAEN A1515TG board maual*. CAEN. URL: `https://www.caen.it/products/a1515b/`.

[183] Davide Fiorina. "Novel Triple-GEM Mechanical Design for the CMS-ME0 Detector, Preliminary Performance and R&D Results". In: *2020 IEEE Nuclear Science Symposium and Medical Imaging Conference (NSS/MIC)*. IEEE, pp. 1–5.

[184] M Hohlmann et al. *Proceedings of the International Workshop on Aging Phenomena in Gaseous Detectors DESY, Hamburg, Germany October 2-5, 2001*. 2003.

[185] M Abbrescia et al. "Study of long-term performance of CMS RPC under irradiation at the CERN GIF". In: *Nuclear Instruments and Methods in Physics Research Section A: Accelerators, Spectrometers, Detectors and Associated Equipment* 533.1-2 (2004), pp. 102–106.

[186] D Acosta et al. “Aging tests of full-scale CMS muon cathode strip chambers”. In: *Nuclear Instruments and Methods in Physics Research Section A: Accelerators, Spectrometers, Detectors and Associated Equipment* 515.1-2 (2003), pp. 226–233.

[187] M Alfonsi et al. “Aging measurements on triple-GEM detectors operated with CF4-based gas mixtures”. In: *Nuclear Physics B-Proceedings Supplements* 150 (2006), pp. 159–163.

[188] T Akesson et al. “Aging studies for the ATLAS transition radiation tracker (TRT)”. In: *Nuclear Instruments and Methods in Physics Research Section A: Accelerators, Spectrometers, Detectors and Associated Equipment* 515.1-2 (2003), pp. 166–179.

[189] Michael Benedikt and Frank Zimmermann. “Future circular colliders”. In: *Proceedings of Science, Lepton Photon 2015* 52 (2015).

[190] Georges Charpak et al. “Time degeneracy of multiwire proportional chambers”. In: *Nuclear Instruments and Methods* 99.2 (1972), pp. 279–284.

[191] M Titov. “Radiation damage and long-term aging in gas detectors”. In: *Innovative Detectors for Supercolliders*. World Scientific, 2004, pp. 199–226.

[192] Jaroslav Va’vra. “Physics and chemistry of aging–early developments”. In: *Nuclear Instruments and Methods in Physics Research Section A: Accelerators, Spectrometers, Detectors and Associated Equipment* 515.1-2 (2003), pp. 1–14.

[193] Hirotsugu Yasuda. “New insights into aging phenomena from plasma chemistry”. In: *Nuclear Instruments and Methods in Physics Research Section A: Accelerators, Spectrometers, Detectors and Associated Equipment* 515.1-2 (2003), pp. 15–30.

[194] Louis Malter. “Thin Film Field Emission”. In: *Phys. Rev.* 50 (1 1936), pp. 48–58. DOI: 10.1103/PhysRev.50.48. URL: https://link.aps.org/doi/10.1103/PhysRev.50.48.

[195] J. Va’vra. “Can TMAE photocathode be used for high rate applications?” In: *Nucl. Instrum. Meth. A* 367 (1995). Ed. by W. Bartl et al., pp. 353–357. DOI: 10.1016/0168-9002(95)00536-6.

[196] A. M. Boyarski. “Additives that prevent or reverse cathode aging in drift chambers with helium isobutane gas”. In: *Nucl. Instrum. Meth. A* 515 (2003), pp. 190–195. DOI: 10.1016/j.nima.2003.08.148. arXiv: hep-ex/0111090.

[197] John A Kadyk. “Wire chamber aging”. In: *Nuclear Instruments and Methods in Physics Research Section A: Accelerators, Spectrometers, Detectors and Associated Equipment* 300.3 (1991), pp. 436–479.

[198] T Ferguson et al. "Aging studies of CMS muon chamber prototypes". In: *Nuclear Instruments and Methods in Physics Research Section A: Accelerators, Spectrometers, Detectors and Associated Equipment* 488.1-2 (2002), pp. 240–257.

[199] R. Bouclier et al. "Aging of microstrip gas chambers: Problems and solutions". In: *Nucl. Instrum. Meth. A* 381 (1996), pp. 289–319. DOI: 10.1016/S0168-9002(96)00268-9.

[200] A. Barr et al. "Construction, test and operation in a high intensity beam of a small system of microstrip gas chambers". In: *Nucl. Instrum. Meth. A* 403 (1998), pp. 31–56. DOI: 10.1016/S0168-9002(97)01095-4.

[201] A. Bressan et al. "High rate behavior and discharge limits in micropattern detectors". In: *Nucl. Instrum. Meth. A* 424 (1999), pp. 321–342. DOI: 10.1016/S0168-9002(98)01317-5.

[202] J Miyamoto and IPJ Shipsey. "An aging study of semiconductive microstrip gas chambers and a gas electron multiplier". In: *Nuclear Physics B-Proceedings Supplements* 78.1-3 (1999), pp. 695–702.

[203] Yu Bagaturia et al. "Studies of aging and HV break down problems during development and operation of MSGC and GEM detectors for the inner tracking system of HERA-B". In: *Nuclear Instruments and Methods in Physics Research Section A: Accelerators, Spectrometers, Detectors and Associated Equipment* 490.1-2 (2002), pp. 223–242.

[204] Andrea Bressan et al. "High rate behavior and discharge limits in micro-pattern detectors". In: *Nuclear Instruments and Methods in Physics Research Section A: Accelerators, Spectrometers, Detectors and Associated Equipment* 424.2-3 (1999), pp. 321–342.

[205] L. Guirl et al. "An aging study of triple GEMs in Ar-CO-2". In: *Nucl. Instrum. Meth. A* 478 (2002). Ed. by M. Jeitler et al., pp. 263–266. DOI: 10.1016/S0168-9002(01)01768-5.

[206] M. C. Altunbas et al. "Aging measurements with the gas electron multiplier (GEM)". In: *Nucl. Instrum. Meth. A* 515 (2003), pp. 249–254. DOI: 10.1016/j.nima.2003.09.006.

[207] A Kozlov et al. "Development of a triple GEM UV-photon detector operated in pure CF4 for the PHENIX experiment". In: *Nuclear Instruments and Methods in Physics Research Section A: Accelerators, Spectrometers, Detectors and Associated Equipment* 523.3 (2004), pp. 345–354.

[208] A. Magnon et al. "Tracking with 40x40-cm**2 MICROMEGAS detectors in the high energy, high luminosity COMPASS experiment". In: *Nucl. Instrum. Meth. A* 478 (2002). Ed. by M. Jeitler et al., pp. 210–214. DOI: 10.1016/S0168-9002(01)01759-4.

[209] J. Galan et al. "Ageing studies of resistive Micromegas detectors for the HL-LHC". In: (Apr. 2013). arXiv: 1304.2053 [physics.ins-det].

[210] M. Capeans. "Aging and materials: Lessons for detectors and gas systems". In: *Nucl. Instrum. Meth. A* 515 (2003), pp. 73–88. DOI: 10.1016/j.nima.2003.08.134.

[211] DW Hess. *Plasma chemistry in wire coating*. Tech. rep. 1986.

[212] T. Akesson et al. "Aging studies for the ATLAS transition radiation tracker (TRT)". In: *Nucl. Instrum. Meth. A* 515 (2003), pp. 166–179. DOI: 10.1016/j.nima.2003.08.145.

[213] *RD-10: a study to improve the radiation hardness of gaseous detectors for use at very high luminosities*. Tech. rep. Geneva: CERN, 1992. URL: https://cds.cern.ch/record/290974.

[214] M Capéans-Garrido et al. *RD-10: a study to improve the radiation hardness of gaseous detectors for use at very high luminosities*. Tech. rep. Geneva: CERN, 1993. URL: http://cds.cern.ch/record/291083.

[215] Guy Turban and Michel Rapeaux. "Dry Etching of Polyimide in O 2 - CF 4 and O 2 - SF 6 Plasmas". In: *Journal of The Electrochemical Society* 130.11 (1983), pp. 2231–2236. DOI: 10.1149/1.2119558. URL: https://doi.org/10.1149/1.2119558.

[216] M Alfonsi et al. "Studies of etching effects on triple-GEM detectors operated with CF/sub 4/-based gas mixtures". In: *IEEE transactions on nuclear science* 52.6 (2005), pp. 2872–2878.

[217] T Kawamoto et al. *New Small Wheel Technical Design Report*. Tech. rep. ATLAS New Small Wheel Technical Design Report. 2013. URL: https://cds.cern.ch/record/1552862.

[218] F Fallavolita, D Fiorina, and J A Merlin. "Aging studies of the triple-GEM detectors for future upgrades of the CMS muon high rate region at the HL-LHC". In: *Journal of Instrumentation* (). to be published.

[219] *CAEN N1470 module manual*. CAEN. URL: https://www.caen.it/products/n1470/.

[220] *Lecroy 428F module maual*. Lecroy. URL: https://teledynelecroy.com/lrs/dsheets/428.htm.

[221] *Lecroy 1182 module maual*. Lecroy. URL: https://teledynelecroy.com/lrs/dsheets/1182.htm.

[222] *CAEN V1718 module maual*. URL: https://wwwusers.ts.infn.it/~rui/univ/Acquisizione_Dati/Manuals/CAEN%20V1718%20rev9.pdf.

[223] M Brice and S Morier-Genound. *New Scanning Electron Microscope Used for Cryogenic Tensile Testing*. unpublished. URL: https://cds.cern.ch/record/1504773.

[224] URL: http://cisric.unipv.it/index.php/8-laboratori/20-laboratorio-arvedi-pavia.

[225] Joseph I Goldstein et al. *Scanning electron microscopy and X-ray microanalysis*. Springer, 2017.

[226] URL: https://www.amptek.com/resources/periodic-table-and-x-ray-emission-line-lookup-chart.

[227] F Fallavollita, D Fiorina, and JA Merlin. "Advanced aging study on Triple-GEM detectors". In: *Journal of Physics: Conference Series*. Vol. 1498. 1. IOP Publishing. 2020, p. 012038.

[228] D Fiorina. "Comparative aging studies on a single wire proportional chamber". In: *Journal of Instrumentation* 15.07 (2020), p. C07008.

[229] F Fallavolita, D Fiorina, and J A Merlin. "Comparative aging studies on triple-GEM and wire chambers". In: *Journal of Instrumentation* (). to be published.

[230] Martin J Berger. "ESTAR, PSTAR, and ASTAR: Computer programs for calculating stopping-power and range tables for electrons, protons, and helium ions". In: *Unknow* (1992).

[231] James F Ziegler, Matthias D Ziegler, and Jochen P Biersack. "SRIM–The stopping and range of ions in matter (2010)". In: *Nuclear Instruments and Methods in Physics Research Section B: Beam Interactions with Materials and Atoms* 268.11-12 (2010), pp. 1818–1823.

[232] M Danilov et al. "Aging studies for the muon detector of HERA-B". In: *Nuclear Instruments and Methods in Physics Research Section A: Accelerators, Spectrometers, Detectors and Associated Equipment* 515.1-2 (2003), pp. 202–219.

[233] G. Bencivenni et al. "Measurement of GEM parameters with X-rays". In: *IEEE Transactions on Nuclear Science* 50.5 (2003), pp. 1297–1302. DOI: 10.1109/TNS.2003.818234.